Investigations of gaseous electrochemical reactions on zirconia electrolytes using amperometric sensors

Robert Charles COPCUTT

A thesis submitted to Middlesex University in partial fulfilment of the requirements for the degree of Doctor of Philosophy

November 1993

The work was carried out in the Energy Technology Centre at Middlesex University, Bounds Green Road, London, N11 2NQ.

Summary

Sensors incorporating zirconia electrolytes have been widely used for monitoring oxygen concentration and the air-to-fuel ratio of combustion systems. The aim of this work was to investigate the extension of this technology to other gases and to gas mixtures.

Initial work was done on single zirconia discs with porous metal electrodes on each face. Platinum, silver and gold electrodes were tested in controlled atmospheres at temperatures between 300°C and 850°C. It was shown, as expected, that in O_2/N_2 mixtures electrode activity/conductance decreased as oxygen concentration and temperature were reduced. In $CO/CO_2/N_2$ atmospheres reproducibility was poor. Interestingly, an increase in electrode conductance of 1-2 orders of magnitude was observed as the temperature was reduced through around 700°C which does not appear to have previously been reported. Is is thought to be related to the corrresponding change in the thermodynamic stability of CO at this temperature, ie $2CO \rightleftharpoons C\downarrow + CO_2$.

Zirconia pump-gauges with small enclosed volume (< $1mm^3$) and laser drilled diffusion holes were constructed with the novel addition of reference electrodes. These were operated with current-interruption circuitry and rapid subsequent data aquisition. This enabled, for the first time, the overvoltage due to charge transfer on the internal pumping electrode to be isolated: interesting behaviour was revealed. The overvoltage increased as oxygen-containing gases were reduced and then, in the case of NO, decreased as the reduction reached completion. The gauge EMF remained remarkably stable while NO was being reduced. Reduction of SO_2 was shown to generate electronic conductivity in the yttria-stabilised zirconia.

A potentially important result was obtained when operating a sensor in $CO/CO_2/O_2/N_2$ mixtures where there was sufficient O_2 present to oxidise all the CO present to CO_2. With the application of zero pumping current the gauge EMF showed a substantial, non-zero, value. It was suspected that a mixed potential developed on the external electrode while the diffusion hole prevented its formation on the internal electrode.

Based upon the results obtained, two sensor designs are proposed. The first is a lean-burn combustion sensor eliminating the possibility of an ambiguous response in rich- and lean-burn conditions. By reducing the activity of the external pumping electrode while maintaining a highly active internal pumping electrode the response in rich-burn conditions would be insignificant while the response in lean-burn conditions would be maintained.

The second design concerns multi-gas sensing; it is based upon previous designs but the need for minimising electrochemical leakage was pinpointed by this work. Because overvoltages on the internal electrodes were shown to reach high values electrode activitity should be high and a gauge cell should be incorporated to provide information about the oxygen partial pressure within the sensor. If operated by sweeping the voltage applied it was shown that because of the slow electrode response the sweep rate would need to be less than 0.2mV/s. Consequently, it is proposed that an array of sensors operating at a range of fixed pump voltages would greatly reduce the response time.

A computer-controlled apparatus was built with which to perform the experimental work. The apparatus controlled the furnace temperature, gas mixing apparatus and a potentiostat/galvanostat. The latter was purpose built so that all current and voltage ranges could be selected by the computer and current interruption performed automatically. Using software written in Turbo Pascal the apparatus was capable of performing a wide range of tests, unattended over periods of months.

Acknowledgements

The help of the following people and institutions is gratefully acknowledged.

They have enabled me to make this small contribution to the world-wide program for reducing air pollution, which I believe is very important.

Dr. W.C. Maskell for initiating the project and for his consistent and valuable support throughout its duration.

Prof. B.C.H. Steele for his supervision and advice. Also to many members of staff in his department at Imperial College for the use of their sputtering machine, cutting tools and their advice and help.

Prof. F.L. Tye for his advice and support.

The National Advisory Board for funding the project.

Dr. P.T. Walsh at the Health and Safety Executive for his role as External Adviser.

My colleagues at Middlesex University; Mr. D. Malpas for his help particularly with the construction of the glass sealed sensors, Mr. J. Jones, Dr. A. Iaonnou, Dr. M. Benammar, Dr. J. Larcin, Dr. E. Gehain, Dr. L. MacLean and many others for their help and friendship.

Other staff at Middlesex University who have helped, including the staff in the Mechanical Engineering workshop, Mr. M. Hart for preparing ceramics, and Mr. P. Kershaw for use of the SEM.

To Margaret and my many other teachers on the shamanic path.

To Carola and Eric and the rest of my family for their support.

Table of contents

Nomenclature

A	=	chemical activity
A_e	=	area of electrode
A_i	=	constant for conductivity
A_p	=	cross section area of pore
C_X	=	concentration of gas X
C_{gb}	=	capacitance of grain boundary
D	=	diffusion coefficient
e'	=	free electron in electrolyte
E_{WR}	=	potential difference between WE and RE
E(t)	=	potential difference as a function of time
F	=	Faraday constant or farad
G	=	Gibb's free energy
$h^{\cdot}$	=	hole
H	=	enthalpy
i	=	current density
i_0	=	exchange current density
I_L	=	limiting current
I_{lk}	=	leakage current
k	=	equilibrium constant
K	=	rate constant
ℓ	=	length of diffusion pore
L	=	thickness of electrolyte
M	=	molecular mass
n	=	number of electrons transferred
N	=	number of moles
pX	=	partial pressure of gas X

P	=	barometric pressure
O_O^x	=	normal oxygen atom in metal oxide
R	=	gas constant
RE	=	reference electrode
R_{el}	=	electrode resistance
R_{gb}	=	resistance of grain boundaries
R_z	=	resistance of electrolyte
S	=	entropy
t_{ion}	=	transport number
T	=	temperature
V	=	volume
$V_O^{\cdot\cdot}$	=	oxygen vacancy with effective double + charge
WE	=	working electrode
X	=	mole fraction
z	=	distance
Z	=	impedance
α	=	power function of gas diffusion rate
α_a	=	anodic charge transfer coefficient
α_c	=	cathodic charge transfer coefficient
β	=	symmetry coefficient
γ	=	activity coefficient
Γ	=	leak conductance of diffusion pore ($DA/T\ell$)
η	=	overpotential
θ_p	=	diameter of diffusion pore
λ	=	air to fuel (stoichiometric) ratio
μ	=	chemical potential
σ_e	=	electrode conductance
σ_i	=	ionic conductance of electrolyte
σ_n	=	n type electronic conductance
σ_p	=	p type electronic conductance

Chapter 1

Introduction

"We must make the rescue of the environment the central organizing principle for civilization"

Senator Albert Gore 1992

1.1) General

There is growing concern regarding the environmental and human health impact of gases such as NO/NO_2, SO_2/SO_3 and CO/CO_2. These gases are being generated in large quantities by numerous processes: mainly combustion. The problem is not helped by the lack of low-cost instrumentation available for monitoring these gases at source and in the atmosphere.

An interesting device that might help fill this gap in the market is an amperometric oxygen sensor made from zirconia that has been extended to measure other oxygen-containing gases. These sensors are based on the principle that oxygen-containing gases can be reduced by 'pumping the oxygen out of them' with a zirconia electrochemical pump. By restricting access of the gas to the pump with a diffusion pore, and monitoring the current, the concentration of the gases can be estimated. These have been called zirconia multi-gas, or polarographic, sensors.

Numerous other sensors have been reported in the literature but for a sensor to be commercially viable it must be cheap, simple, rugged, reliable, easy to use and have a fast response. Zirconia potentiometric sensors have a thirty year history in industry where they have convincingly displayed some of the above properties (Fray (1992)). Their cost is not at present low enough for applications such as domestic central heating units and their output is proportional to the log of the oxygen partial

pressure which makes them difficult to use for lean-burn control. Also, difficulty has been experienced adapting them to measure gases other than oxygen. Amperometric sensors have the advantage that they provide a linear output with respect to oxygen concentration and low-cost designs have been demonstrated (Ioannou and Maskell (1992)). The Energy Technology Centre at Middlesex University has substantial experience and expertise in the design and construction of amperometric oxygen sensors made using zirconia. It was therefore decided that zirconia amperometric sensor technology was the most appropriate one to pursue in this work.

One application envisaged for the Energy Technology Centre's oxygen sensors was the monitoring of the gaseous environment in industrial plants, mines, aircraft and other places where the oxygen concentration might be depleted to dangerous levels. Another was for air-to-fuel ratio (or λ) control systems in engines, furnaces and central heating systems. A difficulty with combustion control applications was that the sensors gave a response of the same sign when the flue gases were rich or lean (Copcutt and Maskell (1992) and Benammar and Maskell (1993a)). They therefore did not allow the two sides of stoichiometry to be distinguished unless additional features were added to overcome this problem.

1.2) Background to solid electrolytes

The sensors studied in this work relied upon the solid electrolyte properties of zirconia, so in this section the theory of solid electrolytes relating to zirconia was examined.

1.2.1 History

Michael Faraday in 1839 was the first to notice that some solids conduct an electric current ionically. In 1899 Nernst did further work with his Nernst glower made of yttria-stabilised zirconia (YSZ). In 1937 Baur and Preis used YSZ again to

make the first solid oxide fuel cell. The recent increased interest in solid electrolytes has been widely attributed to the papers published in 1957 by Wagner (Fray (1992)).

Modern solid electrolytes can be broadly classified into 3 classes. Zirconia is an example of an extrinsic conductor. This is because pure zirconia is a poor conductor and it is only when it is doped with an aliovalent oxide such as yttria or calcia that it becomes a good ionic conductor. δ-Bismuth oxide (BiO_3) is an example of an intrinsic conductor which has a high concentration of oxygen vacancies in the crystal structure of the pure compound. It therefore has good oxygen ion conduction without any stabilizers being introduced. Stabilizers are, however, helpful in improving several properties of the compound such as strength and conductivity. The third class contains amorphous conductors which includes a wide range of glasses and polymers (see eg. Tuller and Moon (1988)).

The conductivity of zirconia is almost entirely due to oxygen ion conduction when the applied voltage is less than about 2V and hence the interest in using this property for a number of practical applications. For instance zirconia is used in electrolysis cells for the production of very pure oxygen and in a range of sensors sensitive to oxygen only. The first oxygen sensors using zirconia were potentiometric devices described in papers by Kiukkola and Wagner in 1957 and Peters and Mobius in 1958 (see eg. Steele et al (1981)).

Solid electrolytes are now widely studied, but considering their potential for helping to improve the quality of the world's atmosphere, it can be argued that even the present level of research is too little. A wide range of gas sensors can be made from them but because of a lack of development only the potentiometric zirconia oxygen sensor for car exhausts has been widely used. A number of solid electrolyte fuel and storage cells have been developed but more work is required to reduce the price and increase reliability. Electrolysis cells and systems for cogenerating chemicals and power also hold considerable promise for reducing pollution if they were to be sufficiently developed.

1.2.2 Zirconia versus other electrolytes

Zirconia has a number of advantages over other solid electrolytes.

- It is relatively cheap since zirconium is the 20th most abundant element on the earth's crust (Weast (1988)).
- It is chemically stable.
- It has a relatively high conductivity particularly when stabilized with yttria or scandia.
- The electronic conductivity is substantially lower than the ionic conductivity in a wide range of oxygen partial pressures. This makes it ideal for many applications requiring reliable operation in extreme oxygen partial pressure conditions.
- It is strong and tough and tetragonal zirconia polycrystal (TZP) has such remarkable mechanical properties that it has created great interest from materials scientists for that reason alone.
- Zirconia has proved reliable for many applications such as for oxygen sensors for gases (Anthony et al (1984)), molten metals (Fray (1992)), and fuel cells (Steele (1985)). It is therefore well understood and trusted.

Zirconia was used exclusively in this work but there is room for improvement and many workers have devoted time to finding better electrolytes (eg. Fouletier and Henault (1983)).

Thoria has even better resistance to reduction and to the onset of n-type electronic conductivity at high temperatures and low oxygen partial pressures. It has been estimated that for a given low oxygen partial pressure thoria has an n-type conductivity 3 to 5 orders of magnitude lower than that of zirconia (Etsell and Flengas (1970)). The disadvantages are that thorium is radioactive, more expensive, and it has significant p-type electronic conductivity in air.

A few other electrolytes have shown less electronic conductivity at low oxygen partial pressures than zirconia. Recently Wang et al (1988) claimed that $CaZrO_3$ was more shock resistant and more resistant to reduction than zirconia.

However, Yajima et al (1991) showed that it is a proton conductor which could complicate its use. However, there is speculation that zirconia is also a proton conductor under extreme conditions (Usui et al (1989c)). Etsell and Flengas (1972) found that CO/CO_2 mixtures gave an accurate Nernst voltage at low oxygen partial pressures on calcia-stabilised zirconia (CSZ), while it had been reported that H_2/H_2O mixtures did not. This could suggest proton conduction in zirconia although phenomena such as mixed potentials could also explain these results.

Another possibility for high temperature, low oxygen partial pressure applications is mullite ($3Al_2O_3 \cdot 2SiO_2$) (Nagatani et al (1992)).

There is an intensive search for electrolytes with better conductivities particularly at lower temperatures. One of the best reported to date is an oxide of bismuth, copper and vanadium (BICUVOX) (Abraham et al (1990)). $Bi_2V_{0.9}Cu_{0.1}O_{5.35}$ has an ionic conductivity of $0.42(\Omega m)^{-1}$ at 300°C and $0.047(\Omega m)^{-1}$ at 200°C (more than 2 orders of magnitude higher than YSZ) and is therefore promising for low temperature work. Unfortunately, as with all bismuth based oxides, it is more easily reduced than zirconia and is not as strong. Bismuth is also toxic while there are no reports of zirconia being toxic.

1.2.3 The Kroger-Vink notation and nonstoichiometry.

Zirconia is often represented by the chemical formula ZrO_2 but the ratio of zirconium to oxygen atoms is rarely in the exact ratio of one to two. Most metal oxides are slightly nonstoichiometric. For pure zirconia the deviation from stoichiometry, x (in ZrO_{2-x}), is only 10^{-8} at 0.1MPa oxygen partial pressure (Kofstad (1983)). x increases as the oxygen pressure decreases. The crystal structures of metal oxides usually contain a variety of imperfections or disorders. Kroger and Vink devised a system for describing nonstoichiometric solids that has become widely used. It is outlined below but for more details the reader is referred elsewhere, e.g. Kofstad (1983).

An oxygen atom in a metal oxide has 2 extra electrons associated with it because it is far more electronegative than the metal atoms in the crystal. It is assigned the symbol O_O^x where the superscript x indicates that the atom is treated as neutral even though it is negatively charged. This is because it is "effectively" neutral. If the structure is missing a neutral oxygen atom the electrons that would have been associated with the oxygen move away from the vacancy leaving it with an effective positive charge. Dots are used instead of + signs to distinguish between effective and actual positive charges. Such an oxygen vacancy is given the symbol $V_O^{\cdot\cdot}$. The dash in the symbol e′ for an electron indicates an effective negative charge.

The concentration of oxygen vacancies in zirconia can be increased by partially reducing it. Since the overall structure must remain neutral the result is to increase the concentration of vacancies with a effective double positive charge ($V_O^{\cdot\cdot}$). Another method to increase the vacancy concentration is to add an aliovalent compound (or dopant) such as yttria (Y_2O_3) or calcia (CaO). It is also known as the stabilizer because it stabilizes the cubic or tetragonal crystal structure at moderate temperatures.

The overall electrochemical reaction between gaseous oxygen and zirconia can then be expressed as:

$$O_2(g) + 4e' + 2V_O^{\cdot\cdot} \rightleftharpoons 2O_O^x. \qquad (1.1)$$

1.2.4 Mechanism of ionic conduction

The mechanism of ionic conduction in solid ionic conductors is not fully understood. In the search for better solid electrolytes, much work has been done in attempting to predict the conductivity of compounds but so far the results are qualitative and not quantitative (eg. Kilner and Brook (1982)). Tuller and Moon (1988) present a good general summary of recent understanding. Ionic conductivity is temperature dependent and follows an Arrhenius type behaviour. This suggests that the process is thermally activated and involves ions hopping from site

to site. At higher temperatures the mobile ions have more kinetic energy and can move more easily between the sites. The sites in zirconia are oxygen-ion vacancies in the crystal structure created by aliovalent oxides. Ionic conductivity approximately follows the relation:

$$\sigma_i = \frac{A_i}{T} \exp\left(\frac{-\Delta H_i}{RT}\right) \qquad (1.2)$$

R is the gas constant, T the temperature and A_i is the ionic conductivity constant. The activation enthalpy ($-\Delta H_i$) is sometimes quoted in electron volts (eV); to convert to J mol^{-1} multiply by the Faraday constant (F = 96485 [C $equiv^{-1}$]). ΔH_i often increases as the temperature decreases (eg. see Suzuki et al (1981)). The constant A_i is therefore temperature dependent and many authors use A_i by itself instead of A_i / T. Both A_i and ΔH_i are complex functions of the composition and crystal structure.

It has been shown that a phenomena called 'jump relaxation' or 'dielectric relaxation' is important in determining the conductivity of many solid electrolytes (Funke (1988)). Bates and Wang (1988) showed that relaxation explains their experimental results with zirconia. The theory in essence states that an ion that has just jumped to a new vacancy site has a large probability of jumping back in the direction it came from. When an ion occupies a vacancy in the crystal structure it helps to create a field or 'defect cloud'. If it jumps to a neighbouring site the cloud created by nearby ions will tend to pull it back. If it manages to stay in the new site long enough, other nearby ions will jump in the same direction and 'relax' the cloud. In the relaxed cloud it has a reduced chance of jumping backwards and may even jump forwards again. Ratner and Nitzan (1988) explain how this model is similar to the Debye-Huckel theory for liquids but also mention other models that have been proposed.

1.2.5 Zirconia crystal structure

A study of the crystal structure of YSZ reveals a little about the optimum level of yttria doping. YSZ can exist in any of 3 different crystal structures; monoclinic, tetragonal or cubic. Fig. 1.1 shows the phase diagram for YSZ using averaged data from Nowotny et al (1988) and Yoshimura (1988). The exact location of the phase boundaries is uncertain below 2000°C because of the slow approach to equilibrium, continuous transformations, and significant influence from minor impurities.

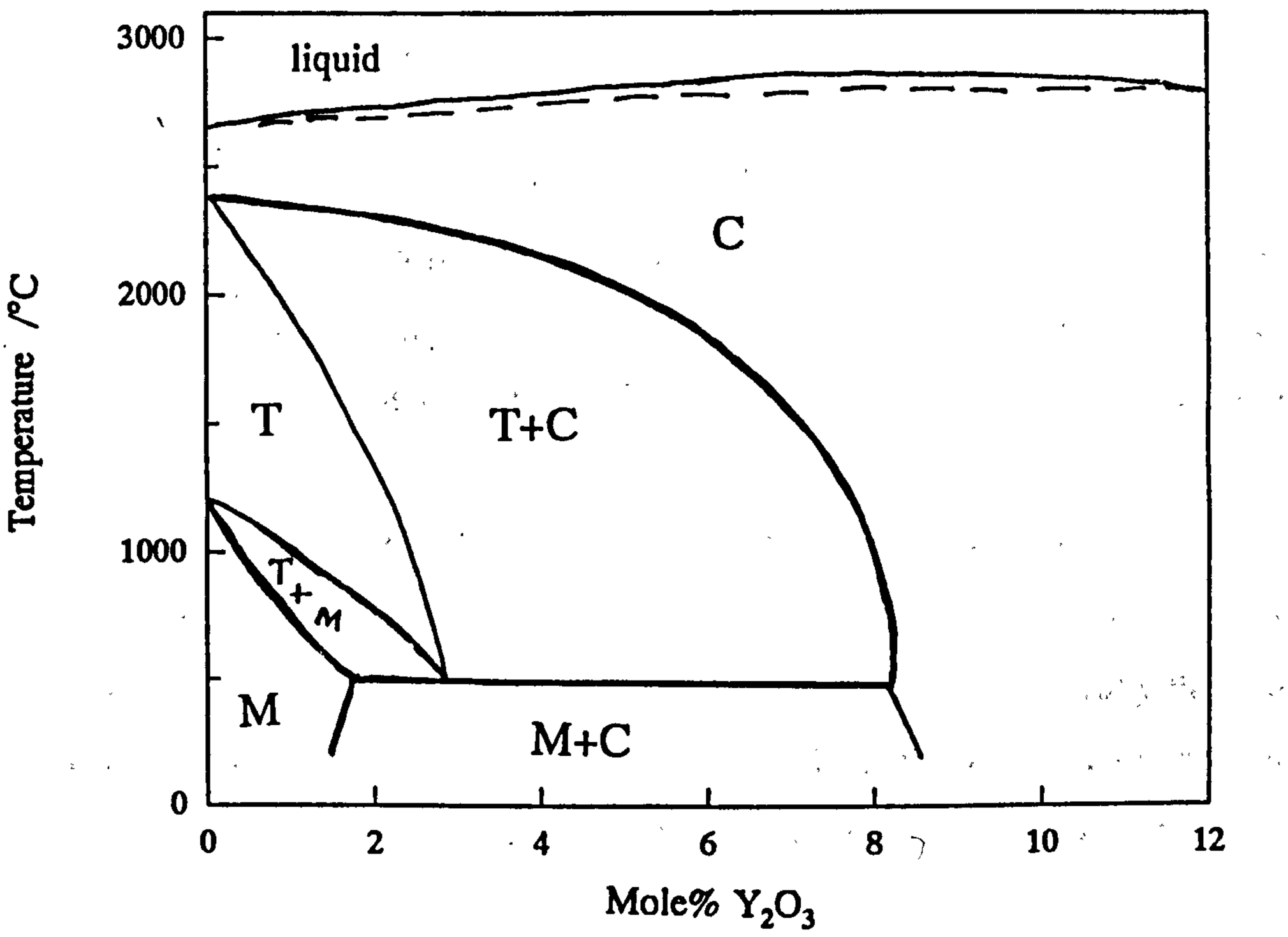

Fig. 1.1: Phase diagram of yttria-stabilised zirconia (Nowotny et al (1988) and Yoshimura (1988)). C-cubic, M-monoclinic, T-tetragonal.

Zirconia stabilized by oxides other than yttria displays similar characteristics. Monoclinic zirconia has the least desirable physical and electrical properties and is avoided for most purposes. The cubic phase has the best ionic conductivity and has

been the ceramic used for most oxygen sensors. Tetragonal zirconia polycrystal (TZP) can be made with between 2 and 5mole% Y_2O_3 in ZrO_2 and is a very promising material. TZP is extremely strong and tough and it has been found that if the size of the grains is small enough the transformation to the monoclinic phase is greatly inhibited. The grain size must be below about 0.2μm for 2% Y_2O_3 but at higher concentrations there is disagreement. (Badwal and Nardella (1989)) claim 0.6μm grains are needed for 5% Y_2O_3 while Nettleship and Stevens (1987) claim 1μm for 3% Y_2O_3. The small grain size required for TZP means that it must be made by sintering very fine powders.

The conductivity of cubic zirconias increases as the percentage of dopant is reduced until the limit of stability of the purely cubic structure is reached (7 to 9mole% Y_2O_3). Formation of the tetragonal phase with further decrease in dopant concentration can cause a large decrease in conductivity at high temperature (Nakamura and Wagner (1986)). However, zirconia with the cubic and the tetragonal structure (partially stabilized) is widely used because its conductivity is still good, particularly at low temperatures. It is also tougher than purely cubic zirconia (fully stabilized).

With calcia-stabilized zirconia (CSZ) a maximum in conductivity is reached at 12% CaO when there are about 6% anion vacancies, yet the conductivity is lower (Etsell and Flengas (1970)). Kilner and Brook (1982) showed theoretically that the difference in ionic radius between zirconium and the dopant cation has an important influence on the conductivity. With Zr and Ca the difference is large which is unfavourable.

While the constant A_i (in eqn.(1.2)) reaches a definite maximum when the tetragonal crystals are just beginning to form in the cubic structure, the trend in ΔH_i is more complex. It tends to increase with increased dopant concentration but may decrease in the low concentration range (Baumard et al (1988)). Sørensen et al (1985) suggested that the vacancies created by the dopant in zirconia cause defects in the crystal structure and as the concentration of vacancies increases the defects tend to aggregate which reduces the mobility of the charge carriers. A number of

theories involving the interaction of vacancies have been proposed eg. Nakamura and Wagner (1986) and Ratner and Nitzan (1988). Whatever the mechanism, the result is that ΔH_i is so much lower in 3Y-YSZ (3mole% Y_2O_3) than in 8Y-YSZ (8mole% Y_2O_3) that the former can have better conductivity below about 400 or 500°C.

1.2.6 Grain boundaries and ageing

When solid electrolytes are sintered they form grains. Many of the impurities tend to diffuse to the grain boundaries. These impurities alter the conductivity of the electrolyte, so the grain boundaries have different electrical properties to the bulk of the grain and cause a measurable effect.

In a pioneering paper Bauerle (1969) used complex impedance measurements or frequency response analysis (FRA) to study the conductivity of 10Y-YSZ with platinum electrodes. He devised an electrical equivalent circuit that explained some of the impedance results and clearly separated the contribution of the electrodes and the electrolyte. His equivalent circuit for the electrolyte included a parallel resistor and capacitor in series with another resistor (shown below).

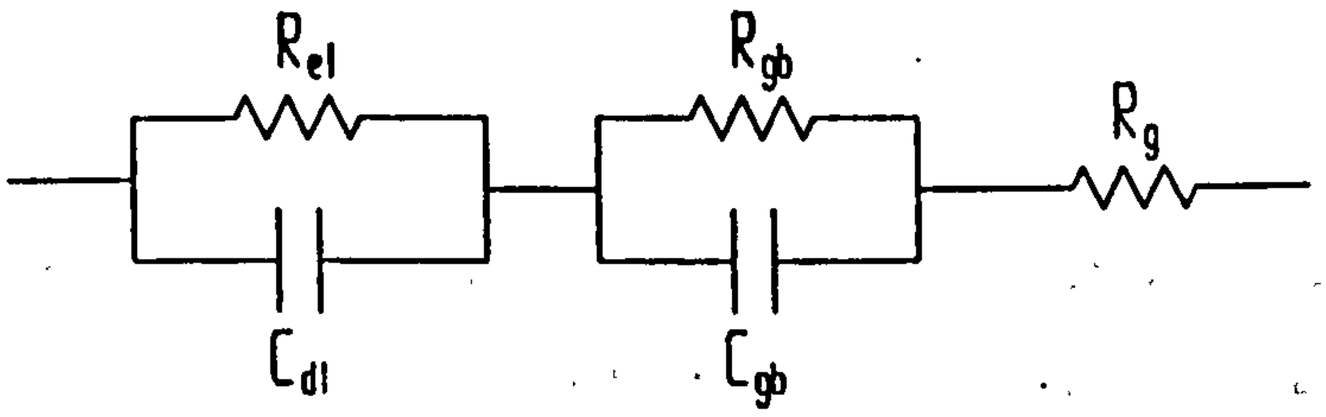

He proposed that the series resistor might represent the intra-grain resistance (R_g) and that the parallel RC network might represent the grain boundary impedance. However, he thought that vacancy trapping was a more likely explanation for C_{gb}. Because R_{el} and C_{dl} changed with the gaseous atmosphere in which the test was performed he concluded that they were associated with the electrode.

By going to higher frequencies and lower temperatures subsequent workers showed an extra capacitance in parallel with R_g (as shown below) provided a more accurate representation of many solid electrolytes.

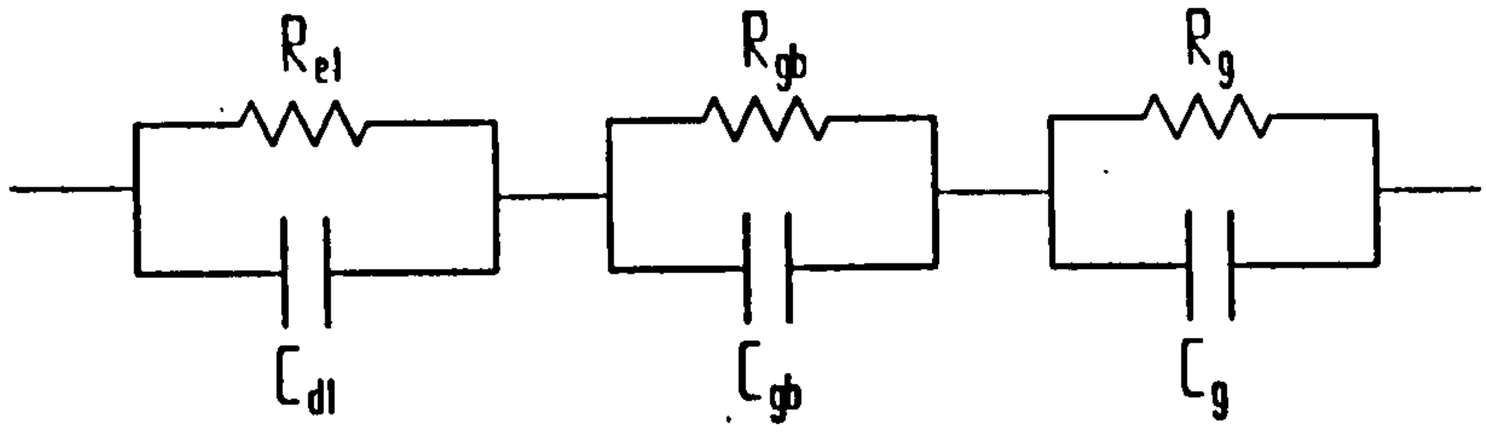

It is generally accepted that the high frequency network represents intra-granular phenomena and the mid-frequency network represents grain boundary phenomena. However, the situation is not simple. While C_g is often orders of magnitude smaller than C_{gb}, this is not always the case (partly because they are frequency dependent) and they sometimes cannot be clearly distinguished. FRA sometimes does not clearly indicate a bulk and a grain boundary network and a more complex equivalent circuit is indicated.

Dielectric relaxation mentioned in section 1.2.4 is the most likely explanation of C_g. It explains the magnitude of C_g and the fact that it increases with decreased frequency.

Impurities diffuse out of the oxide particles during sintering of the ceramic and play a key role in the formation of the grains and the general sintering process. Grain boundaries in zirconia are usually very thin (2-10nm) so their chemical analysis is difficult. The evidence is that the phase is composed of glassy silicates with a liquidus at about 1450°C and that their ionic conductivity is poor. Theunissen et al (1989) found that the grain boundary phase of YSZ contained 30-34% yttria independent of the bulk concentration, and Hughes and Sexton (1989) found a composition of $1.5Na_2O{:}0.5Y_2O_3{:}3.0SiO_2$. Badwal and Drennan (1987) found that the grain boundaries in the fired ceramic contained silica as the main component even when using a high purity zirconia powder with 20µg/g of silica in it. Baumard et al (1988) reported that R_{gb} increased as the Si content increased. Badwal (1990)

compressed zirconia held at 1200°C and found that R_{gb} decreased as the pressure increased. The pressure reduced the thickness of the glassy grain boundary phase by pushing it into the triple junctions and out of the way of the current flow. He (following Leach et al (1986)) found that a similar effect could be produced by rapid cooling from the sintering temperature.

Alumina is also an aid to sintering (Radford and Bratton (1979a)) and causes a decrease in C_{gb} (Radford and Bratton (1979b)). Steele and Butler (1985) proposed that the alumina causes a mullite type grain boundary to form which has improved conductivity compared to the usual grain boundaries which have a high silicon content. A number of authors have reported that R_{gb} is inversely related to the grain size in zirconia (Bonanos et al (1984), El Barhmi et al (1988a), Badwal (1990), and Slotwinski et al (1985)). R_g was hardly affected by these alumina additions which adds support to the initial assumption that the total electrolyte impedance is equal to the sum of the bulk and grain boundary impedances. However, much of the above work was done with TZP and the results are not so clearly defined for partially (PSZ) and fully stabilized zirconia (FSZ) which form grains approximately an order of magnitude larger (Steele et al (1981)).

Doubt has been thrown on the interpretation, used above, of the impedance spectra by Nafe (1984). He examined the DC resistance of CSZ, YSZ and yttria-stabilized thoria over the very wide temperature range of 300 to 2000K. He concluded that at high temperatures the total conductivity was dominated by the grains and at temperatures below about 300°C by the grain boundaries. He proposed that a parallel RC network is not an accurate equivalent for the grain boundary impedance: it is an over-simplification and consideration needs to be given to grain boundaries parallel to the current flow.

Ceramics usually have residual porosity and this porosity is usually concentrated at the grain boundaries. This porosity was suspected of contributing to C_{gb}. However, Kleitz et al (1981a) found that porosity had little effect on C_{gb} and that high porosity only increased R_g.

One possible cause for confusion in some conductivity results is ageing (Vlasov and Perfiliev (1987)). Ageing is characterised by a slow decrease in conductivity. All zirconias are prone to high temperature ageing which becomes significant above 800°C and reaches a peak near 1200°C. In some cases it is due to continued diffusion of impurities such as SiO_2 into the grain boundaries. Formation of the monoclinic phase, with its low ionic conductivity, may also be a factor. Ordering of the crystal lattice or formation of micro-domains has also been suggested (Vlasov and Perfiliev (1987)).

Ageing is slow (days to months) and has been correlated with the slow diffusion of cations. Typical diffusion coefficients are: 10^{-21} to $10^{-22}m^2s^{-1}$ for Zr^{4+} and 10^{-11} to $10^{-12}m^2s^{-1}$ for O^{2-} at 1000°C (Etsell and Flengas (1970)).

In addition to high temperature ageing TZP can also be affected by a severe low temperature degradation. It is particularly severe around 200-250°C and Yoshimura et al (1987) have shown how it is probably due to the diffusion of OH^- into the crystal structure. The OH^- causes a tetragonal to monoclinic transformation (t-m) starting at the surface, creating cracks that grow into the bulk. The process can be reversed at 1400°C. This theory is supported by Badwal and Nardella (1989) who showed that t-m transformation is prevented if the water concentration is very low but is promoted by anodic conditions. With these 2 ageing processes the long-term use of TZP is restricted to near room temperature and between about 500°C and 800°C (Badwal (1990)).

Small grains, hot isostatic pressing and small alumina additions all help reduce ageing of TZP (Nettleship and Stevens (1987)). Badwal and Nardella (1989) found that a high silicon content caused inhomogeneous grain growth and thus enhanced proneness to ageing.

The surface of the electrolyte has features in common with internal grain boundaries and Nowotny et al (1988) showed that Al and Ca migrate to the surface of YSZ and form a very thin but concentrated layer. This layer took more than 100 hours to form at 780°C. Hughes and Badwal (1991) showed a similar result with silicon migrating to the surface and taking yttria with it. They also found marked

changes in behaviour from small variations in impurity concentration. The use of high purity material is therefore important for minimizing ageing effects and generally increasing the reproducibility of results.

1.2.7 Electronic conduction

The total conductivity is the sum of the conductivities of all the different charge carriers. The only significant charge carriers in zirconia are oxygen ion vacancies, electrons, holes (electron vacancies) and in some circumstances possibly protons. Holes tend to form at high oxygen partial pressures by the reaction

$$\tfrac{1}{2}O_2(g) + V_O^{\cdot\cdot} \rightleftharpoons O_O^x + 2h^{\cdot}. \qquad (1.3)$$

p-type semiconductivity is thus created by the holes formed and the conductivity follows the relationship:

$$\sigma_p = \sigma_p^0 \, pO_2^{1/4}, \qquad (1.4)$$

where σ_p^0 is the conductivity due to holes at unit oxygen partial pressure.

At low oxygen partial pressures zirconia is partially reduced, the equilibrium goes the other way and free electrons are formed generating n-type conductivity.

$$O_O^x \rightleftharpoons \tfrac{1}{2}O_2(g) + V_O^{\cdot\cdot} + 2e'. \qquad (1.5)$$

The conductivity due to electrons is also oxygen pressure dependent and follows a similar relationship:

$$\sigma_n = \sigma_n^0 \, pO_2^{-1/4}. \qquad (1.6)$$

Fig. 1.2 shows a plot of conductivities of zirconia as a function of oxygen partial pressure using data from Kleitz et al (1981c). This group was one of the few to study the n-type conductivity of YSZ - most work has been done on calcia-stabilized zirconia. Palguev et al (1975) found the p type conductivity of YSZ to be lower than that reported by Kleitz et al while Beresnev (1991) found it to be slightly higher.

The presence of electronic conductivity causes electrochemical semipermeability which is considered in more detail in section 1.6.3.

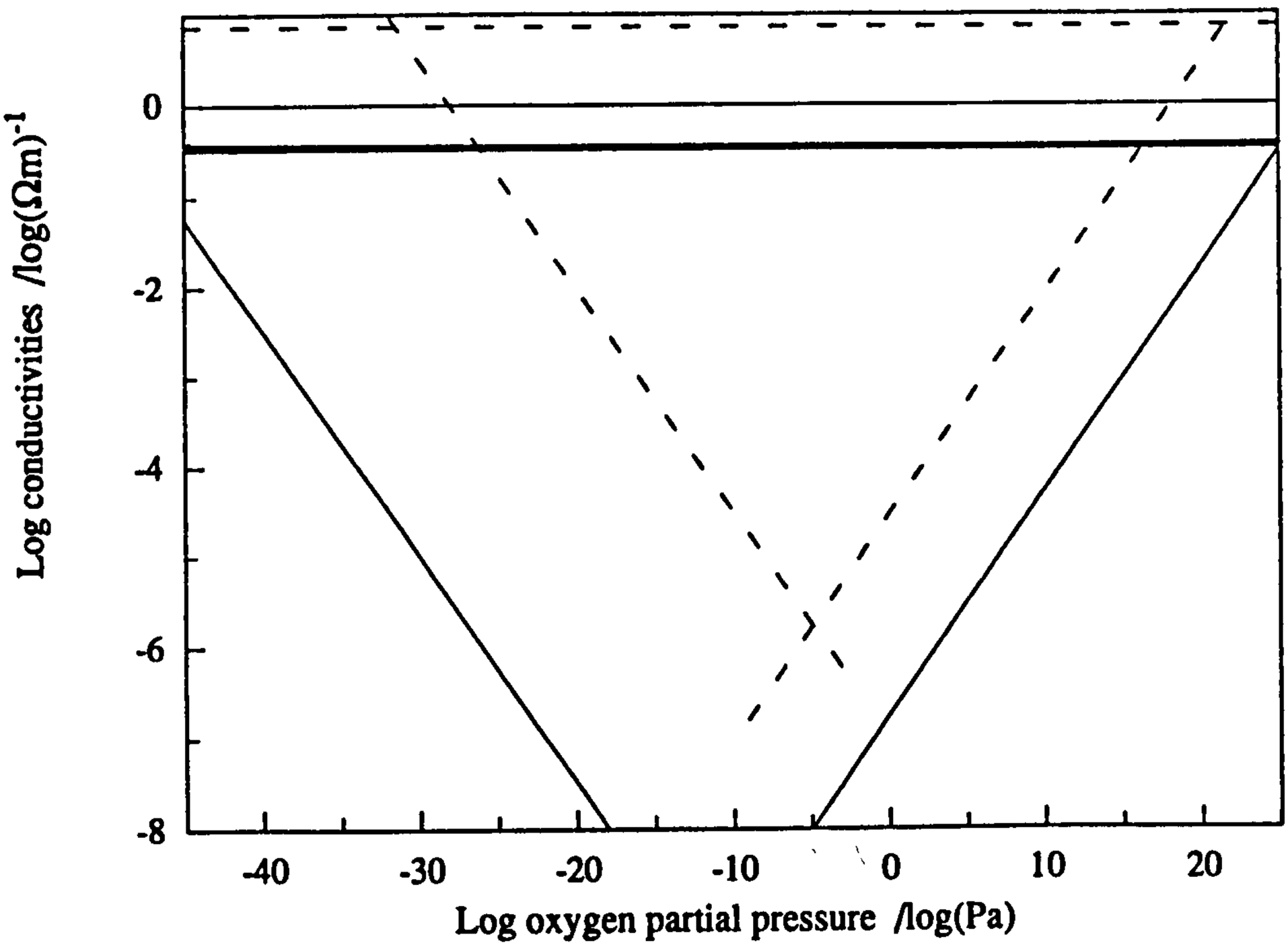

Fig. 1.2: Conductivity of YSZ. The horizontal lines represent ionic conductivity which is independent of oxygen potential. The lines with slope -¼ and +¼ represent n-type and p-type conductivity respectively. ———, 650°C; - - -, 950°C. Data from Kleitz et al (1981c).

Using an electrode consisting of a point of various metals pressed onto zirconia Kleitz et al (1981b) showed that partially reduced zirconia is reoxidised in 4 stages. The phenomena could only be observed with a point electrode because the effect diffuses rapidly with distance. The first stage is probably associated with trace impurities of Fe which is readily reduced from a valence of 3 to 2. The second and third stages could be due to trace impurities of Ti and Ce which also have variable valencies and can thus promote electronic conductivity. Reetz et al (1984) and Levy et al (1988) also concluded that trace impurities such as Fe and Ti play a role in the electronic conductivity of partially reduced zirconia.

1.3) Solid electrolyte oxygen sensors

In order to develop new sensors, existing sensors need to be thoroughly understood. The range of sensors being investigated is huge so this section has been severely restricted to the theory of sensors directly related to this work. Azad et al (1992) recently reviewed a wider range of sensors. Although the sensors described in this section are sometimes made from solid electrolytes besides zirconia, they have been described from the perspective of zirconia.

1.3.1 Potentiometric sensors

A typical potentiometric sensor can be represented as:

$$pO_2,Pt \mid YSZ \mid Pt,p'O_2$$

Fig. 1.3 shows such a sensor. One electrode is exposed to a gas with an oxygen partial pressure of pO_2 and the other electrode is exposed to a gas with an oxygen partial pressure of $p'O_2$. This difference in oxygen partial pressure causes a potential to develop between the two electrodes. This potential is given by the well known Nernst equation:

$$E = \frac{RT}{4F} \ln \frac{p'O_2}{pO_2} \qquad (1.7)$$

The constant R/4F is 2.15433×10^{-5} [VK^{-1}]; at 735°C the Nernst voltage is 50.0mV per decade of oxygen partial pressure ratio.

Minimal current should be drawn from potentiometric sensors to prevent any significant overpotentials from developing on the electrodes. If the oxygen pressures involved are extreme enough to cause significant electronic conductivity an error will be caused by three factors.

a) The electronic conductivity will cause a flux of oxygen ions in the electrolyte from high pressure to low pressure (to compensate for the flux of

electronic carriers). This will create an overpotential on the electrodes that will reduce the EMF.

b) The leakage of oxygen will increase pO_2 on the low pO_2 side. Fouletier et al (1976) and Iwase et al (1984) showed that this was not nearly as important as the overpotential factor.

c) The Nernst equation as shown above was derived assuming an ionic transport number (t_{ion}) of close to 1. If $t_{ion} < 1$ then the voltage drop across the two electrodes is equal to the Nernst voltage multiplied by t_{ion}. The value of t_{ion} used is found by integrating across the thickness of the electrolyte (Etsell and Flengas (1970)).

$$E = t_{ion} \frac{RT}{4F} \ln \frac{P'O_2}{pO_2} \qquad (1.8)$$

In commercial sensors one electrode is often exposed to air and the other immersed in the medium where the oxygen partial pressure is to be measured. The air acts as a reference with a known oxygen partial pressure so that the Nernst equation can be used to calculate the unknown pO_2. A common application for these sensors is the air to fuel ratio control of engines with catalytic convertors (Maskell (1987)). The sensor shown in Fig 1.3 is a typical example. They are also used for testing the oxygen levels in molten steel. Because of the high temperatures involved sensors for steel can have a lifetime of a few seconds. Sometimes steel sensors use a Cr/Cr_2O_3 mixture as an oxygen partial pressure reference instead of air (Fruehan et al (1969)). The low pO_2 created by the chromium means that the difference in oxygen partial pressures is reduced and this decreases the leakage due to semipermeability. The accuracy is therefore increased.

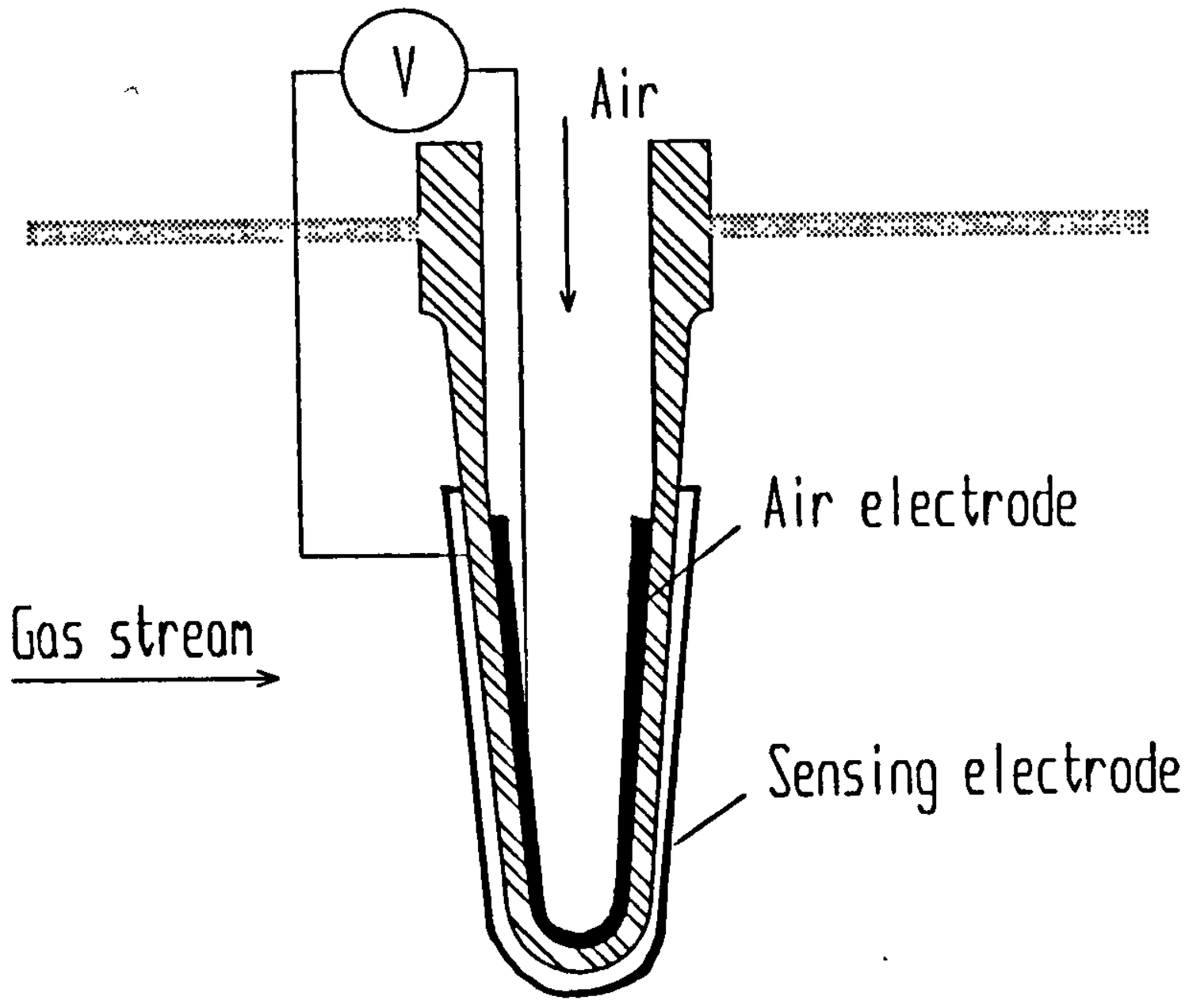

Fig. 1.3: A typical potentiometric oxygen sensor made using a zirconia thimble.

More detail about potentiometric sensors can be found in numerous papers eg. Maskell and Steele (1986), Fouletier (1974) and Anthony et al (1984).

1.3.2 Amperometric sensors

These are not yet widely used but hold promise for many applications including the sensing of gases other than oxygen. Recent work in the Energy Technology Centre has included development of thick film heaters for attachment to sensors and of control electronics (Benammar and Maskell (1989)). These developments have enabled lower cost devices to be produced which are now being incorporated into prototype domestic boilers (Hargreaves and Ovenden (1990)). Sensors made by screen printing layers of platinum and zirconia have also been produced (Ioannou and Maskell (1992)) enabling a further reduction in cost.

Fig. 1.4 shows an amperometric sensor with a reference electrode (RE) and a schematic diagram of the circuit used to operate it. Oxygen is pumped out of the internal chamber so that the oxygen partial pressure within the chamber is very low. The electrochemical reaction involved in the operation of these sensors is simply:

$$O_2(g) + 4e^- \rightleftharpoons 2O^{2-} \qquad (1.9)$$

Oxygen is consumed at the cathode inside the sensor and released by the anode on the outside surface.

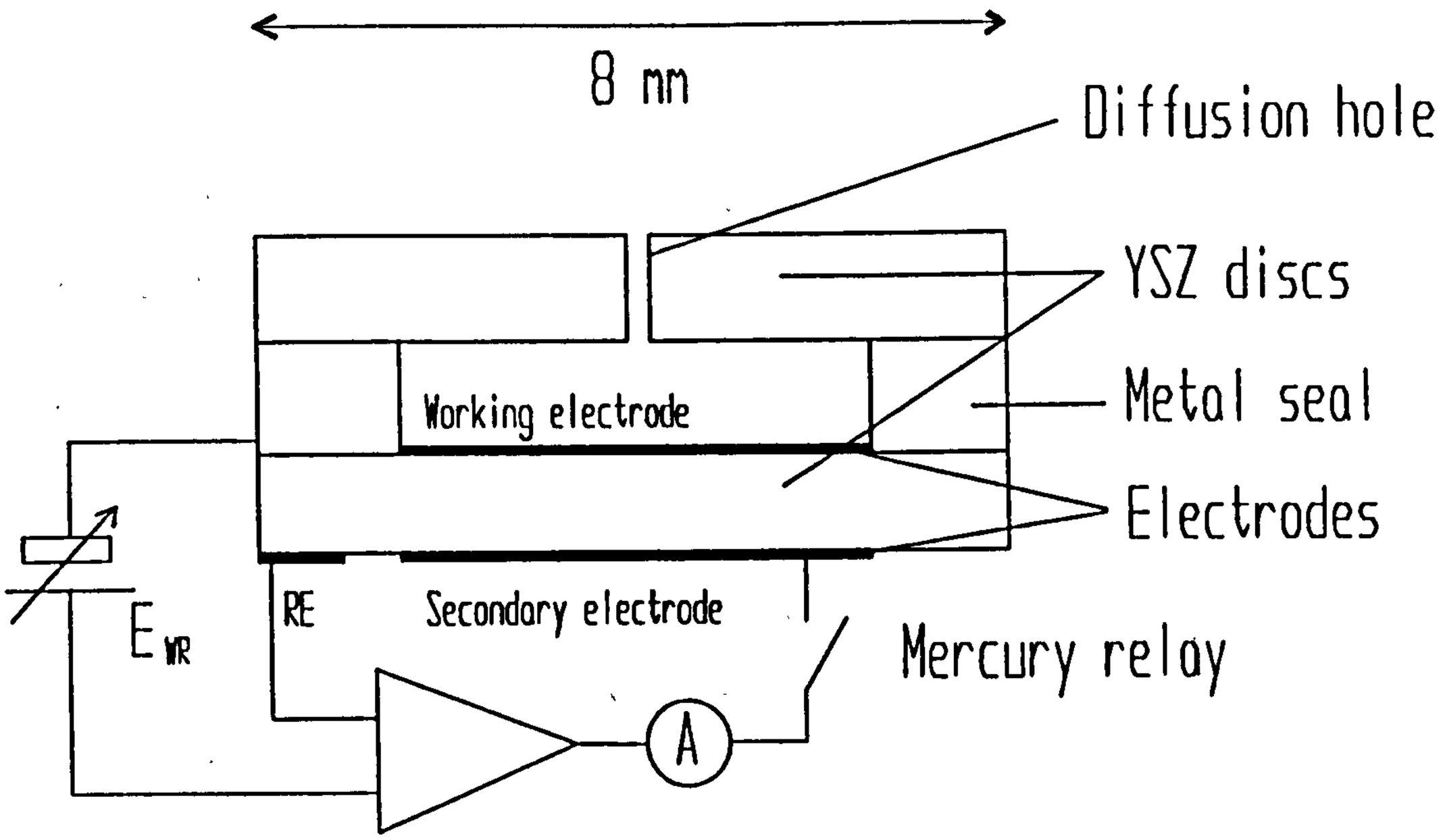

Fig. 1.4: A zirconia amperometric oxygen sensor with metal seal.

Normally a pumping potential of about 500mV is applied to the electrodes. This potential leaves the enclosed volume with a minimal oxygen partial pressure and creates a limiting current situation. An equation for the limiting current (I_L) of a sensor can be derived by doing a mass balance on a small length (dz) of the diffusion pore. The balance is (Saji et al (1984) and Usui et al (1989)):

$$J_{O_2} = -D\frac{dC_{O_2}}{dz} + X_{O_2}J_{O_2} \qquad (1.10)$$

where J_{O2} is the oxygen flux and D is the diffusion coefficient of oxygen in nitrogen. C_{O2} is the oxygen concentration and X_{O2} is the mole fraction of oxygen.

The first term on the right hand side of the balance comes directly from Fick's first law of diffusion. The second term in the equation accounts for the oxygen carried with the flow of gas through the diffusion pore caused by the pumping of the oxygen. Using the ideal gas law it can be seen that:

$$C_{O2} = X_{O2}\, P / RT.$$

P is the total ambient pressure. The result of substituting this into eqn.(1.10) and rearranging is:

$$J_{O_2} = \frac{-DP}{RT}\frac{1}{(1-X_{O_2})}\frac{dX_{O_2}}{dz} \qquad (1.11)$$

The boundary conditions for solving this differential equation are:

i) at $z = 0$, $X_{O2} = X_{O2}$ external

ii) at $z = \ell$, X_{O2} = zero (in the limiting condition).

where ℓ is the length of the diffusion pore.

The result is:

$$J_{O_2} = -\frac{DP}{RT\ell}\ln(1-X_{O_2}) \qquad (1.12)$$

If t_{ion} is unity Faraday's law can be applied to obtain the limiting current (I_L):

$$I_L = \frac{4FDA_pP}{RT\ell}\ln(1-X_{O_2}) \qquad (1.13)$$

where A_p is the cross sectional area of the diffusion pore.

The term $\ln(1-X_{O2})$ approaches $-X_{O2}$ as X_{O2} approaches zero so eqn(1.13) can be simplified to eqn(1.14) for low oxygen concentrations.

$$I_L = -\frac{4FDA_pP}{RT\ell}X_{O_2} = -\frac{4FDA_p}{RT\ell}pO_2 \qquad (1.14)$$

Eqn(1.14) can be derived directly from eqn(1.10) if the second term of the right hand side is removed. For air, eqn(1.13) gives a result 11% higher than eqn(1.14). For 10% and 1% oxygen the errors in eqn(1.14) are 5.1% and .51% respectively. It is difficult to measure accurately the diffusion pore size and the diffusion coefficients. Therefore, by finding a pore size that gives a best fit to eqn(1.14) at about 10% oxygen the error would never be greater than about 5% for all concentrations up to 21%. Greater accuracy was desired in this work so the $-\ln(1-X_{O2})$ correction was used.

Eqn(1.13) and (1.14) are applicable whether the type of diffusion is bulk or Knudsen. Bulk diffusion dominates when the size of the diffusion pore is greater than the mean free path length of the diffusing gas (Dietz (1982)). The mean free path length in air at 0.1MPa and 15°C is 6.63×10^{-8}m (Weast (1988)). Under the conditions considered here the ideal gas law can be used with little error. Therefore the mean free path length is proportional to the inverse of the absolute temperature and at 700°C it is 2.24×10^{-7}m which is 100 times smaller than the smallest diffusion hole used in this work. For bulk diffusion the relationship between the diffusion coefficient (D) and temperature and pressure is (Reid et al (1987)):

$$D \propto \frac{T^{\alpha}}{P} \qquad (1.15)$$

where α is a constant dependent upon the gases in the mixture.

α is usually in the range 1.5 to 1.75 as can be seen by examination of the formulae for estimating D in Appendix 1. It can be seen from eqns. 1.13, 1.14 and 1.15 that I_L is proportional to $T^{(\alpha-1)}$ (Dietz (1982)) and therefore amperometric sensors are expected to show a temperature dependence of between $T^{0.5}$ and $T^{0.75}$. It can also be seen than I_L is approximately independent of the total pressure. The current is therefore a measure of oxygen concentration rather than partial pressure (Dietz (1982)).

The estimated value for D for oxygen in nitrogen at 700°C is 164 mm^2s^{-1} (Perry (1984)). Therefore, a sensor with a 25μm pore 0.7mm long should give a limiting current in air of 116μA at 700°C.

At total ambient pressures below about 1kPa Knudsen diffusion would be expected to dominate assuming a 25μm pore and 700°C. Knudsen diffusion follows the relationship (Dietz (1982));

$$D = \frac{\theta_p}{3}\sqrt{\frac{8RT}{\pi M}} \qquad (1.16)$$

θ_p is the diameter of the diffusion pore, and M is the relative molecular mass of the diffusing species.

When Knudsen diffusion dominates, I_L should be proportional to the oxygen partial pressure and to $T^{-0.5}$. The 'Knudsen sensor' therefore differs from the 'bulk sensor' in being pressure sensitive and having an output that decreases with increasing temperature. Usui et al (1989b) verified the absolute pressure dependence using a 22μm pore. Above 40kPa I_L was independent of pressure but below that pressure Knudsen diffusion started to show an influence and I_L decreased. Kamo et al (1985) using a 500μm pore found I_L to be slightly dependent on the total pressure down to about 5kPa when it became directly dependent. Kamo et al (1985) and Usui et al (1989b) both found a temperature dependence of $T^{0.73}$ in the bulk diffusion region indicating an α value of 1.73.

The limiting currents reported in the above equations are negative. This is because international convention has chosen cathodic currents to be negative and anodic ones positive. The working electrode in this work was always the internal pumping electrode which must be cathodic in order to pump oxygen out of the internal volume. Limiting currents for amperometric oxygen sensors are therefore negative in this work.

1.3.3 Pump-gauge sensors

A number of devices come under the general heading pump-gauge. They share several features with amperometric sensors but also include a Nernstian gas sensing cell in addition to a pump cell. Early examples were made with zirconia tubes by Fouletier et al (1975). Flow into the sensor, of the gas to be analyzed, was controlled by some external arrangement. Later designs used two discs of electrolyte, one acting as a pump, and the other as a gauge (Haaland (1977) and Hetrick et al (1981)) see fig. 1.5. 'Flow' was controlled by the size of the diffusion pore.

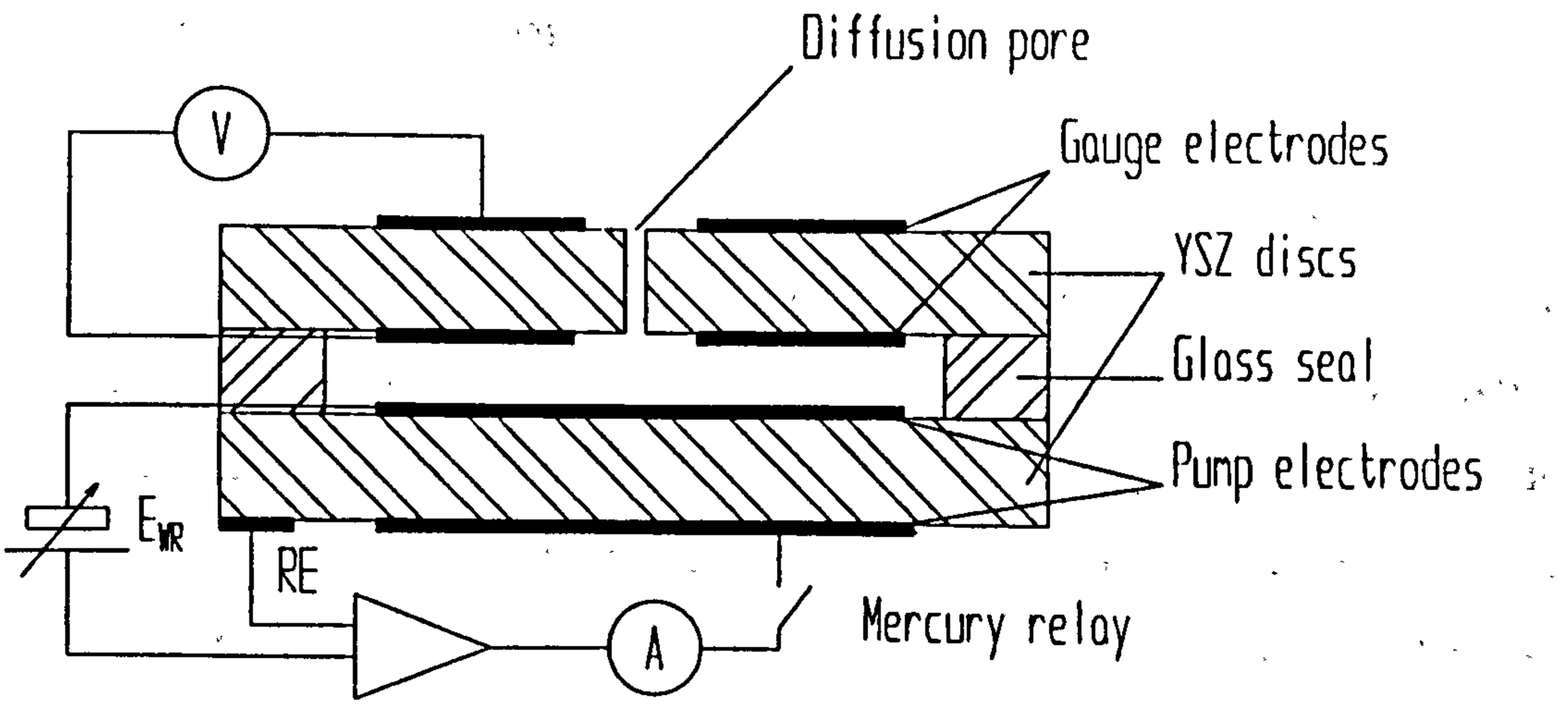

Fig. 1.5: A pump-gauge oxygen sensor made with a glass seal.

Two modes of operation are commonly used.

a) Constant E_g mode. If the pump current is adjusted so that the gauge voltage is constant and large (eg. 150mV indicates a 1000 fold decrease in oxygen pressure) then the current follows the relation given by eqn. 1.14 above. However, there are advantages in using lower gauge voltages as discussed later. The equation describing the pumping current can be obtained by combining eqn(1.7) (Nernst equation) and (1.14) to give (Hetrick et al (1981)):

$$I = -\frac{4FDA_p}{RT\ell} pO_2 \left(1-\exp\left(\frac{-4FE_g}{RT}\right)\right) \qquad (1.17)$$

where E_g is the voltage on the gauge cell.

b) AC mode. If a sinusoidal current is applied to the pumping electrodes, the gauge voltage will also vary with an approximate sinusoidal waveform. The peak amplitude of E_g indicates the oxygen partial pressure. This mode of operation has several advantages such as removing the need for an oxygen partial pressure reference. Several enhancements to the basic idea have been described (Benammar and Maskell (1992a & b, 1993b).

1.3.4 Coulometric sensors

These sensors derive the oxygen partial pressure from the charge required to pump the oxygen out of an enclosed volume. They are constructed on the same principle as the pump-gauge sensor except that the diffusion pore is not necessary. Oxygen is pumped into the small enclosed compartment until pO_2 is the same inside and out. This is measured with the gauge cell and a zero Nernst potential indicates equality of the internal and external oxygen pressures. Faraday's law then defines the charge required to remove the oxygen from the compartment. They have the disadvantage of requiring complex control circuitry and the response is slow. Heijme et al (1975) patented a coulometric sensor that was a small intellectual step from being the first amperometric sensor. It used the charge required to empty the chamber of oxygen and/or the time required to replenish it via a diffusion barrier to determine the oxygen concentration. More details can be found in Haaland (1977) and de Jong (1983).

1.4) Extending the application of solid electrolyte sensors

Gas sensors made using solid electrolytes have the advantages that they are heat resistant, miniaturisation is straightforward and they can be robust and long lived. All the sensors described in section 1.3 can be made with electrolytes that conduct ions other than oxygen and their application can therefore be extended to the corresponding gases. At present viable electrolytes are available only for the following gases: hydrogen, the halogens and carbon and sulphur oxides.

Glass is a hydrogen conductor and the pH probe is a well known example of a potentiometric sensor. NASICON is a sulphur ion conductor but it also conducts oxygen ions. This means that the oxygen concentration must be known in order to calculate the concentration of the sulphur oxides. Sensors using it therefore need to be used in conjunction with oxygen sensors. Although this adds complication, a combined oxygen and NASICON sensor could simultaneously determine the concentration of oxygen and all the sulphur oxides (assuming equilibrium conditions) (Gauthier et al (1977) and Skeaff and Dubreuil (1993)).

If the sensing electrode is made of a compound containing both the ionic species of interest and the ionic species mobile in the electrolyte, a sensor can be made for a very wide range of species. For instance a phosphorus sensor has been made using a sodium phosphate electrode on β-alumina. Sodium ions are mobile in β-alumina and a potentiometric sensor made from it therefore measures the sodium activity of the electrodes. The sodium phosphate electrode produces a sodium activity that is related to the phosphorous activity of the fluid (eg. molten metal) that surrounds it. It is therefore possible to calculate the phosphorus concentration using the cell potential and a knowledge of the thermodynamic stability of sodium phosphate (Fray (1992)).

The same principle has been used to detect oxygen at room temperature using fluorine ion conducting electrolytes (Alcock et al (1992)). Rao et al reviewed NO_x sensors and described a device for NO/NO_2 detection using β″-alumina. Azad et al (1992) recently reviewed a wide range of solid electrolyte sensors.

As mentioned in section 1.2.2, zirconia has a number of advantages and therefore it has been used wherever possible. Some of the reported work is discussed below.

1.4.1 Lean-burn control sensors

Combustion processes of all kinds produce many of the air pollution and atmospheric problems suffered today. Lean-burn (excess of air) combustion has a number of important advantages over stoichiometric combustion including:

- Reduced emission of carbon monoxide.
- Reduced proportion of fuel that passes through the system unburnt or only partially oxidized.

However, if a gas concentration sensor in the exhaust gases is not used to provide feed-back control of the combustion a relatively large excess of air is required to ensure that excess fuel conditions do not occur. A sensor in a feed-back control loop allows the fine control required to maximize the advantages of lean-burn.

- The emission of nitrogen oxides can be reduced by accurate dynamic control of the air to fuel ratio (Matsushita et al (1984)). Together with the previous 2 points it might be possible to achieve tolerable emission levels from petrol engines without any catalytic convertor with its associated use of precious metals.
- If the excess of air is kept to an optimum level the efficiency of the combustion can be maximised. A 10-15% improvement compared to operation at stoichiometry can be achieved for petrol engines (Kobayashi et al (1984)).

The problem with potentiometric sensors is that they have low sensitivity to changes in the air-fuel ratio in lean-burn conditions. This could be partly overcome using costly temperature control to negate the temperature sensitivity, but the output signal would still need to be linearized and amplified. The output is also sensitive to the presence of gases such as CO and NO_x at temperatures below 400 or 500°C

which could be a problem when the engine is starting from cold. Attempts have been made to overcome some of these problems by several workers including (Subbarao and Mati (1983)). These sensors have not been successful.

Zirconia amperometric sensors hold promise for lean-burn control but the simple designs described above cannot distinguish the two sides of stoichiometry. In lean-burn conditions the potential on the external pumping electrode (anode) is typically less than 100mV negative with respect to air. The pump voltage of typically 500mV therefore creates a potential of 500-600mV negative relative to air on the internal pumping electrode (cathode). This is insufficient to reduce either CO_2 or H_2O. The problem during rich-burn conditions is that the anode potential increases to more than 700mV negative with respect to air which means that the cathode potential becomes more than 1200mV negative relative to air. This is sufficient to reduce CO_2 and H_2O. The result is a current during rich-burn conditions in the same direction as the current during lean-burn conditions (Benammar and Maskell (1993a)).

Several authors have proposed solutions to this problem. Dietz (1982), Soejima and Mase (1985) and Ueno et al (1986) describe sensors that use an air reference. By holding the Nernst potential between the air electrode and an electrode within the pumping potential at about 400mV, they found that lean-burn always gave a negative current and rich-burn always gave a positive current. Logothetis et al (1985) describe a similar device but the air reference is only used to detect on which side of stoichiometry the system is. Kobayashi et al (1984) described the development of a lean-burn engine that used an adapted thimble sensor. By adding a ceramic diffusion layer they turned it into an amperometric sensor with an air reference.

Suzuki et al (1985) and Maskell (1991) both described double chamber devices that did not need air references. Benammar and Maskell (1993q) have demonstrated the feasibility of one possible mode of operation for double chamber devices.

1.4.2 Non-Nernstian sensors

These sensors can be used to detect reducing gases such as carbon monoxide, methane and hydrogen in air (Haaland (1980)). The sensor consists of two electrodes of different materials on a zirconia disc. One electrode is made of a metal such as platinum which catalyses the oxidation of the reducing gas. The other is made of a non-catalytic metal such as gold. The reducing gas reacting on the platinum electrode makes the oxygen concentration on that electrode lower than on the non-catalytic electrode. A Nernst potential is therefore developed. These sensors are not specific because a wide range of gases and volatile organic compounds can produce a response. They are useful for such applications as fire hazard alarms. Haaland (1980) has studied various electrodes with different gases and has also investigated creating electrodes with low catalytic activity by poisoning them with sulphur or lead.

Moseley (1988) gave "non-Nernstian sensors" a broader classification to include the anomalous EMF sensors discussed in the next section.

1.4.3 Anomalous EMF CO sensor

Okamoto et al (1980) reported a CO sensor that used an anomalous EMF generated on platinum electrodes at temperatures below 450°C. Several previous workers had noticed that low concentrations of CO caused an anomalously large decrease in the oxygen potential as measured on a platinum electrode (Steele et al (1981)). Later work using infra-red spectroscopy showed that this effect was due to the very strong adsorption of CO on Pt at these temperatures (Okamoto et al (1981) and Kudo and Fueki (1990)). The rate of oxidation of CO on platinum dispersed on zirconia or alumina reinforced this conclusion (Okamato et al (1981)). Presumably the CO excludes oxygen from the electrochemical reaction sites and causes an anomalously low O_2 potential on the platinum electrode.

By coating one of the platinum electrodes on a zirconia disc with a CO oxidizing catalyst, Okamoto et al (1980) were able to measure an EMF. This was because the uncovered electrode had a very low oxygen activity because of the competitive adsorption of CO. The catalyst over the other electrode oxidised all the CO and the oxygen activity on that electrode was equivalent to the partial pressure of the oxygen in the surrounding atmosphere (with a slight reduction due to that consumed by the CO). Note that this mechanism is different to that of a non-Nernstian sensor. The other difference is that non-Nernstian sensors generally operate above 500°C while anomalous emf sensors generally operate below 400°C (de Velasco et al (1993)).

The response of Okamoto et al's sensor was largest at temperatures below 350°C giving a sensor response of 30mV for 100ppm of CO and was insensitive to oxygen concentration. A non-Nernstian sensor in air at 600°C would produce 4.5μV for 100ppm CO in air, and the EMF would increase with reduced oxygen concentration.

The EMF of the CO sensor was found to oscillate when the CO concentrations were between 10% and 70% of the oxygen concentration. The sensor response remained at a fixed level for CO concentrations higher than this, which could be an indication that the surface of the platinum was saturated with adsorbed CO.

Hydrogen probably also causes a mixed potential because the CO sensor of Okamoto et al was found to have a cross sensitivity with it. The sensor was modified by adding a selective H_2-oxidation catalyst to remove this cross-sensitivity. Fig 1.6 illustrates the final design of the sensor. A very similar sensor was recently reported by Li et al (1993). They used a porous layer of CuO and ZnO over one of the Pt electrodes as a CO oxidizing catalyst. The other electrode had no over-layer of catalyst so their sensor would probably also suffer from cross-sensitivity.

Gessner et al (1988) noticed a similar effect with NO_x and showed that the electrochemical activities of NO and NO_2 caused a mixed potential. de Velasco et

al (1993) reported a hydrogen sensor that made use of the mixed potential on a SnO_2 electrode on zirconia.

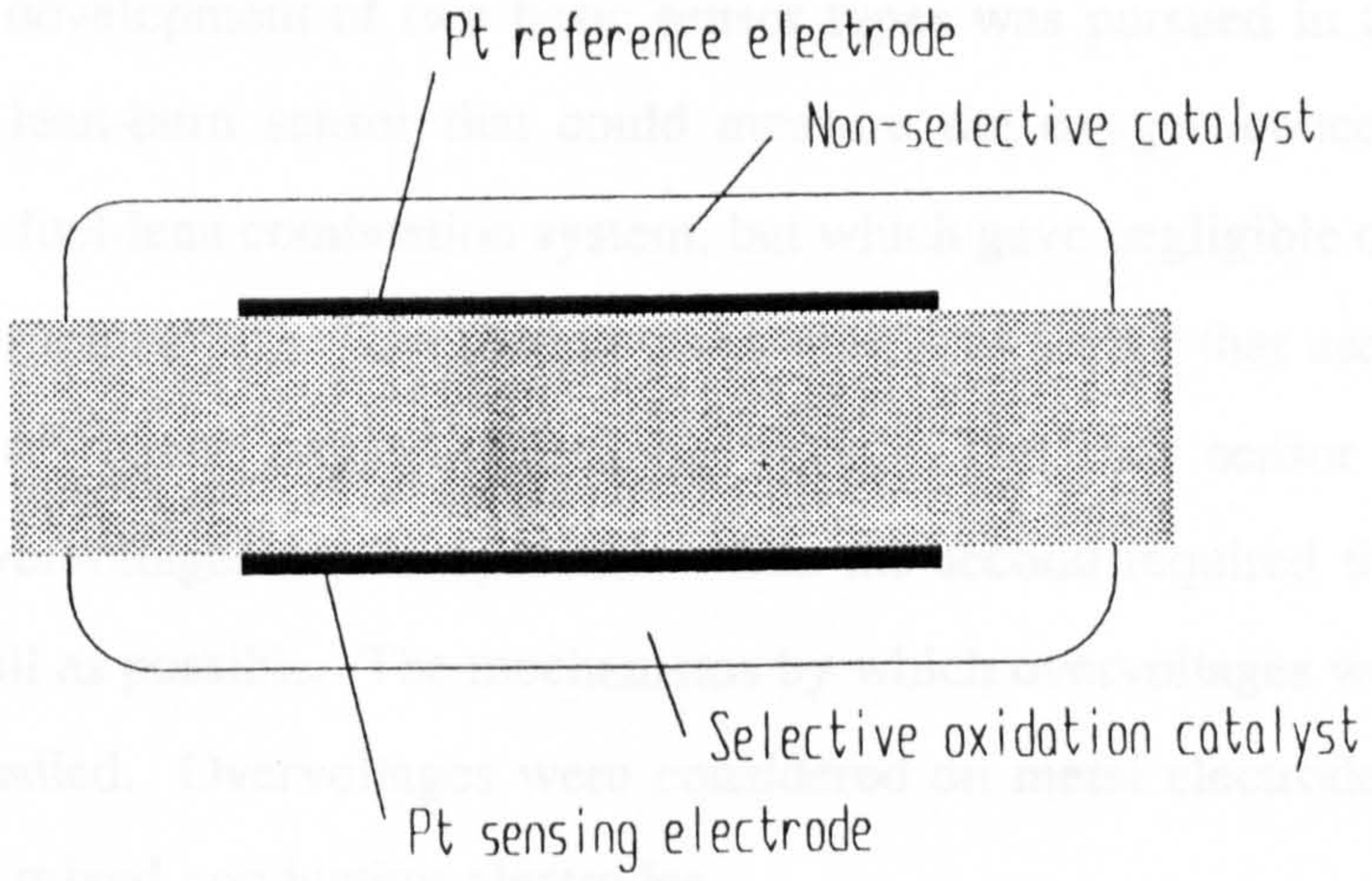

Fig. 1.6: The anomalous CO sensor of Okamoto et al (Kudo and Fueki (1990)).

1.4.4 Amperometric multi-gas sensors

The potential applied to the pump of an amperometric sensor causes removal of oxygen from the enclosed chamber of the sensor. Progressive increases of the pump potential causes the oxygen partial pressure to be reduced to the point where other oxygen containing gases are reduced. The reduction of these gases causes additional current to flow compared to the current resulting from free oxygen reduction only. By analysing the current-voltage characteristics of the sensor it is possible to detect the presence of reducible gases. Dietz (1982) showed that H_2O or CO_2 could be determined in this way. Usui et al (1989d & 1991) have achieved success in differentiating between free oxygen and H_2O, using this method, while Saji et al (1988) had limited success detecting CO_2.

1.5) Theory for designing and optimizing sensors: overvoltages

The development of two basic sensor types was pursued in this work. The first was a lean-burn sensor that could measure the oxygen concentration in the exhaust of a fuel-lean combustion system, but which gave negligible output when the system was running rich. The second was a multi-gas sensor that used the ability of the sensor to reduce oxygen-containing gases. The first sensor required large electrode overvoltages for its operation while the second required the overvoltages to be as small as possible. The mechanisms by which overvoltages were formed was therefore studied. Overvoltages were considered on metal electrodes only and not on oxide or mixed conducting electrodes.

Despite intensive study by many workers over the past 2 decades the processes are still not clearly understood. For an oxygen electrode acting as a cathode, the oxygen enters the zirconia from the bulk gas via a number of steps. It must first diffuse through a boundary layer in the gas to the electrode surface. If the electrode is porous the oxygen also has to diffuse through the pores. It must then adsorb onto the surface of the electrolyte and/or the metal of the electrode. Any oxygen not adsorbed onto the surface at an electrochemical reaction site (ERS) must then diffuse along the surface it is on until it reaches such a site. If the oxygen is adsorbed as a molecule it must also dissociate into adsorbed atoms at some stage. Wang and Nowick (1981) proposed that imperfect adhesion of the platinum to the zirconia created a small space between the Pt electrode and the zirconia. They suggested that diffusion of adsorbed oxygen in this space could be rate limiting. Oxygen may also diffuse through the bulk of the metal electrode. Having finally reached an ERS the oxygen atoms can undergo electrochemical reaction and enter the electrolyte as oxygen ions.

To develop a mathematical model of the process the important rate limiting steps need to be isolated. At gas-solid electrolyte interfaces, gas phase diffusion of oxygen to the electrode has been shown not to be rate limiting. Firstly if it were, the exchange current density would be inversely proportional to the oxygen partial

pressure which has never been observed (eg. Sakurai et al (1989)). Secondly, overvoltages would probably decrease with increased gas flow rate. Most studies reported no dependence of overvoltages on flow rate although Etsell and Flengas (1971) did report a small (but unspecified) effect. Where flow rate sensitivity has been observed it was often associated with temperature or pressure effects (Anthony et al (1984)). Thirdly, the diffusion coefficient of gases is around $10^{-4}m^2s^{-1}$ which is 5 orders of magnitude greater than that in liquids. The development of a diffusion layer in gases like that in liquids is therefore not possible at the current densities that can be achieved with solid electrolytes.

Electron micrographs of metallic electrodes indicate that their structure is so open that gas phase diffusion in the pores is also unlikely to be limiting.

Gur et al (1980) and others have considered dissociation of adsorbed oxygen molecules as limiting but there is little experimental evidence for this. Also, recent work by Gillan (1993) suggests that bimolecular gases will not adsorb unless they strike the metal surface with a particular orientation and simultaneously dissociate. This simultaneous adsorption and dissociation may therefore be rate limiting.

The other possible rate controlling mechanisms cannot be so easily eliminated, although diffusion of oxygen through metals such as platinum and gold was considered very unlikely (Wang and Nowick (1981)). The theory of electrochemical exchange reaction was considered first.

1.5.1 The Butler Volmer equation

The Butler-Volmer equation was derived using considerations of the activation energy of the electrochemical exchanges. For a complete derivation see Bockris and Reddy (1970). The most general form of it is:

$$i = i_0[e^{\alpha_a F\eta/RT} - e^{-\alpha_c F\eta/RT}] \qquad (1.18)$$

i is the current density flowing for a give overvoltage (η) and i_0 is called the exchange current density. α_a and α_c are respectively the anodic and cathodic transfer coefficients which are made up of the following components:

$$\alpha_a = \frac{n-\gamma}{s} - r\beta \qquad \alpha_c = \frac{\gamma}{s} + r\beta \qquad (1.19)$$

where γ is the number of charge transfer steps before the rate determining step in the cathodic direction, and β is the symmetry factor. r is the number of electrons transferred in the rate determining step and n is the total number of steps in the electrochemical transfer. s is the number of times the rate determining step (RDS) is repeated.

At high overvoltage the Butler Volmer equation simplifies to the Tafel equation.

$$i = i_0 e^{\alpha c F \eta/RT}$$

for cathodic conditions and

$$i = i_0 e^{\alpha a F \eta/RT}$$

for anodic conditions. At an overvoltage of 50mV at 700°C the error in the current given by the Tafel equation is about 10% while at 100mV it is less than 1%. A Tafel plot is made by plotting ln(i) vs. η and the slope of the curve at large η is $\alpha F/RT$.

van Hassel et al (1991b) found that for gold electrodes the apparent charge transfer coefficients (α_a and α_c) were 2.08 and 0.66 respectively at 769°C in 0.1MPa partial pressure of oxygen. The coefficients decreased at lower temperatures to values closer to 1.5 and 0.5. They also found that α_a increased at lower oxygen partial pressures. They partially explained their results with a model that assumed competition between charge transfer and surface diffusion of adsorbed oxygen. Diffusion is discussed further in section 1.5.4. while charge transfer is considered in section 1.5.3.

1.5.2 Electrode resistance - exchange current density

When an electronic conductor such as a metal is in contact with an electrolyte, an exchange of electrons and ions continuously takes place. When no net current flows through the electrode, the rate of electrochemical exchange is the same in both directions. ie. the anodic and cathodic reactions proceed at the same rate. The rate of this exchange is called the exchange current density (i_0). It cannot be measured directly because it is a dynamic equilibrium process occurring on a molecular scale but can be calculated from the electrode resistance (R_{el}). R_{el} is given by: $d\eta/dI$ in the limit as η approaches zero. i_0 is then given by (eg. Bockris and Reddy (1970) p 1007 or Liu and Khandkar (1990)):

$$i_o = \frac{1}{R_{el}} \frac{RT}{F(\alpha_a+\alpha_c)} = \frac{1}{R_{el}} \frac{RT}{F} \frac{s}{n} \qquad (1.20)$$

This equation is only valid at low overvoltages. The error in i_0 from eq. 1.20 compared to the value derived from the full Butler-Volmer equation depends upon the values of α_c and α_a. For values of R_{cl} measured using values of η between +2mV and -2mV it varies between 1 and 5% for α_c and α_a between 0 and 4. For ±10mV the error is 6 to 26%.

1.5.3 The three phase boundary

The three phase boundary (TPB) is the line where the metal of the electrode, the electrolyte and the gas phase meet. A number of recent workers have shown that with most metal electrodes on zirconia the TPB is where most, if not all, of the electrochemical reaction sites are found (Schouler (1983)). All research that has studied the result of changing the length of the TPB has found that the current carrying capacity of the electrode increases with increased length of the TPB (Brook et al (1981)).

Some interesting insights have come from attempts to measure the width of the TPB. Brook and Markin (1973) used doped indium oxide particles of various sizes as electrodes. They estimated the TPB to be about 2μm wide under moderate conditions (<100mV) but wider under extreme overvoltages (>1V). The TPB can achieve this width by 2 mechanisms. Either oxygen diffuses through the electrode material or electronic carriers in the zirconia allow electrochemical reactions to take place a short distance from the electrode.

Tannenberger and Siegert (1969) noted what Wang and Nowick (1981) have called constriction resistance. Using silver electrodes on zirconia discs of different thicknesses Tannenberger and Siegert found that a plot of electrolyte resistance against electrolyte thickness did not pass through the origin. They found that their results predicted that even an infinitely thin electrolyte would have the resistance equivalent to 100 to 200μm of electrolyte. van Heuveln et al (1993) found that constriction resistance caused a large increase in the measured electrolyte resistance when using $La_{.85}Sr_{.15}MnO_3$ electrodes on thin zirconia sheets. They found that increasing the length of the TPB reduced the constriction resistance and the electrode resistance.

Kleitz et al (1981a) found evidence for the importance of the width of the TPB from experiments using gauze electrodes. Electrolyte conductivities measured using gauze electrodes were lower than those measured with sputtered electrodes. The measured values increased as the oxygen partial pressure was increased. This suggested that the increased p-type conductivity at higher pressures allowed electrons in the zirconia to move further from the real TPB and create a wider effective TPB. Fig. 1.7 illustrates this mechanism.

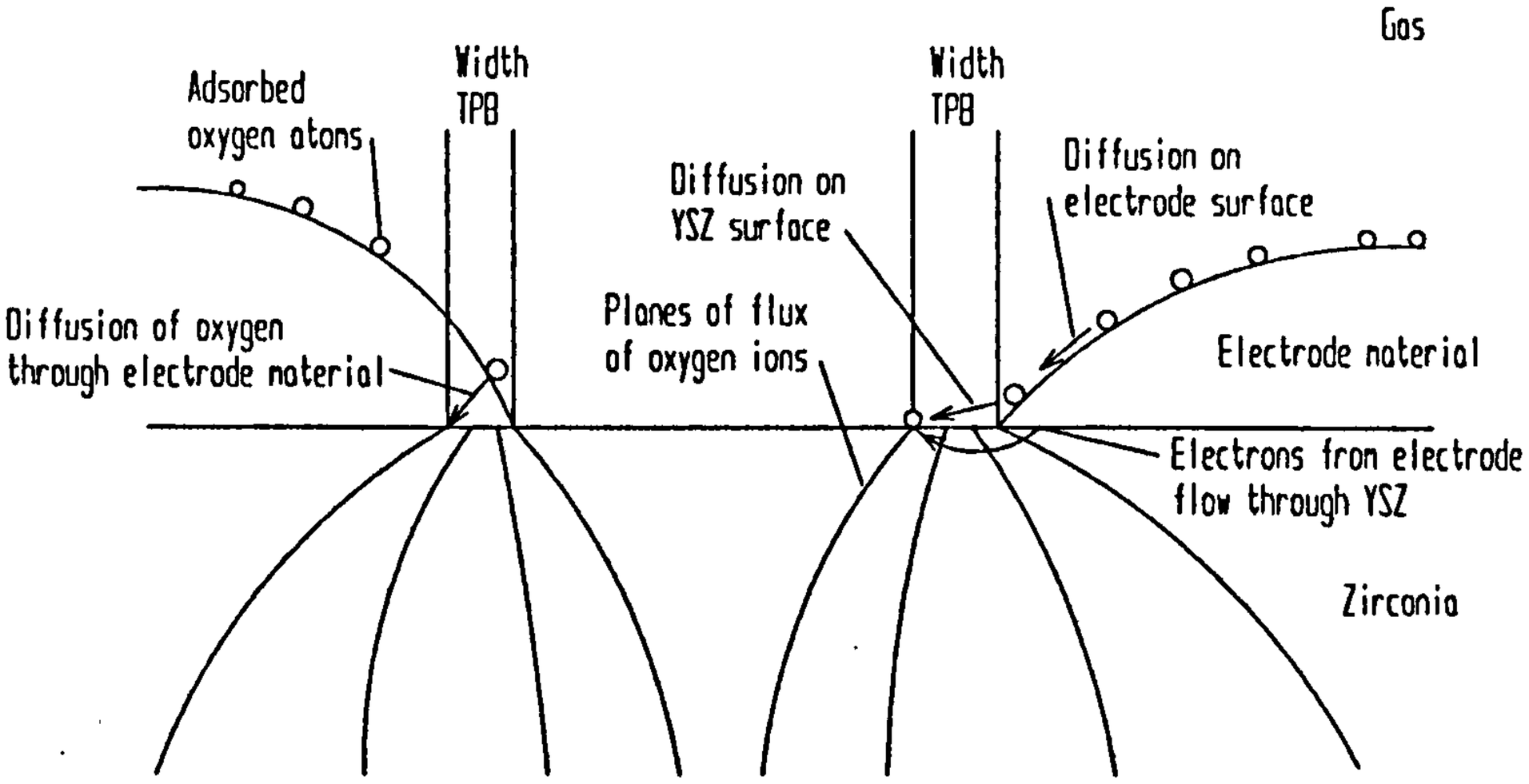

Fig. 1.7: Cross section of an electrode on zirconia in cathodic operation showing the TPB and the route taken by oxygen approaching and leaving it.

Further evidence for the mechanism suggested above is the large increase in exchange current densities observed when the surface of the zirconia is deliberately given a higher electronic conductivity. van Hassel et al (1992) and van Hassel and Burggraaf (1992) did this by inserting iron into the surface of zirconia with an ion-beam implanter and found an increase in i_0. Nguyen et al (1986a) increased i_0 by partially reducing the zirconia to promote electronic conductivity. Obayashi and Okamoto (1981) immersed zirconia into hydrofluoric acid and observed an increase in i_0 which they attributed to fluorine diffusion into the surface. However, it is more likely that it dissolved the glassy phase on the zirconia surface.

Fig. 1.7 also shows how diffusion of oxygen through the metal can increase the TPB thickness. Oxygen diffuses more rapidly through silver than other metals used for electrodes (Kontoulis and Steele (1991)) which could explain the high exchange current density found with silver electrodes (Wang and Nowick (1981)). Diffusion through other metals is probably not fast enough to make a significant difference to the TPB.

1.5.4 Surface diffusion resistance

A plateau has been widely observed in the cathodic current-voltage characteristics of platinum electrodes (Brook et al (1971)). It is most apparent at low oxygen concentrations. This is strong evidence that diffusion of adsorbed oxygen across the surface of the electrode and/or electrolyte to the TPB can be rate limiting. It is not so clear if the adsorption of oxygen onto the electrode or electrolyte surface may also be rate limiting; most studies have assumed it is not. However, if neither gas phase diffusion nor the adsorption process are limiting, it is difficult to explain why the rate of oxygen adsorption directly onto the TPB is not fast enough to eliminate the need for surface diffusion. It has also not been clarified if diffusion is only important at high overvoltages or at low overvoltages as well. Nguyen et al (1986b) showed theoretically that if diffusion on the zirconia surface were rate controlling then i_0 should be proportional to $pO_2^{5/8}$. If diffusion on the metal surface were controlling then i_0 would be proportional to $pO_2^{3/8}$. Their results showed a 0.53 dependence (3/8 is 0.375 and 5/8 is 0.625). They suggested that diffusion on zirconia was controlling because Au and Pt had widely different capacities for adsorbing oxygen but behaved similarly as electrodes. Also, the amount of oxygen that adsorbs onto the zirconia has been shown to be negligible when compared to platinum (eg. see van Hassel et al (1992)).

Isotope studies by Steele et al (1986) on zirconia without any electrodes showed that the surface exchange rate was 3 orders of magnitude lower than that observed in electrochemical work. Adding platinum to the surface doubled the surface exchange rate but it was still much lower than typical exchange current densities. Park and Blander (1991) tested the weight gain of zirconia exposed to H_2O^{18}. They found surface diffusion rates much higher than those found by Steele et al, but still lower than i_0 values would indicate. With Bi_2O_3 Steele et al found the surface exchange rate to correspond to i_0. The surface of Bi_2O_3 is therefore probably

active in electrochemical exchange (as confirmed by diverse studies) while that of zirconia probably plays very little part.

1.5.5 Arriving at the total steady-state overvoltage

Numerous models have been proposed using different groupings of the possible rate limiting steps discussed above. However, no model has been reported that assumes all three of the following steps simultaneously: adsorption followed by surface diffusion to a TPB with a width dependent upon t_{ion} followed by electrochemical reaction at the TPB.

For details of models that have been reported the reader is referred to Sakurai et al (1989), Nakagawa et al (1990, 1991 & 1993), van Hassel et al (1991a & b) and Robertson and Michaels (1991).

Overvoltages are affected by many factors including electrode morphology, trace surface impurities, electrolyte surface roughness, and previous treatment (high temperatures or current densities) to mention a few (see above references). Results are therefore difficult to reproduce. Progress with understanding this complex phenomenon has therefore been slow and much work remains to be done.

1.6) Sensor design: leakage mechanisms

The major problem encountered with making a sensor that behaved ideally (i.e. according to eq. 1.13 and 1.17) was the construction of the seal. Therefore, in this section the theory behind the different mechanisms by which oxygen could enter the sensor were examined.

1.6.1 Physical leakage

Diffusion is caused by the process of molecules constantly mixing due to their random motion in the bulk of a fluid. Fick's first law has generally been found to describe this accurately. As discussed in section 1.3.2. bulk diffusion dominates in a gas if the diameter of the diffusion pore is greater than the mean free path length between collisions of the molecules, and Knudsen diffusion dominates when it is less. It was also shown in section 1.3.2. that the sensor output shows different absolute pressure and temperature dependence characteristics when the different diffusion mechanisms dominate. Small unintentional physical leaks could therefore create a problem under the following circumstance. Assuming the sensor output was required to be independent of absolute pressure, it would be relatively simple to assure that the diffusion pore was large enough. However, if there was a leak in the sensor due to porous ceramic or small gaps in the seal, then diffusion through that leak would probably be of the Knudsen type. This could make the sensor pressure sensitive if there were enough of these leaks. If it was important, sensors would have to be tested for pressure dependence.

1.6.2 Electrochemical leakage

The report by Kaneko et al (1987) is the most detailed study of the phenomenon of electrochemical leakage. However, that study only considered small oxygen partial pressure differentials (applied voltages up to 40mV). For small gauge voltages (E_g) they found that:

$$I_{lk} = E_g/(R_L + k_1 p'O_2^{-1/4} + k_2 pO_2^{-1/4}) \qquad (1.21)$$

where I_{lk} is the current due to electrochemical leakage.

$k_1 p'O_2^{-1/4}$ is the ohmic resistance of internal electrode and $k_2 pO_2^{-1/4}$ is the ohmic resistance of the electrode formed by the interface between the metal seal and the external electrolyte surface. R_L is the effective resistance of the leak circuit

(electrons flowing through the metal seal and O^{2-} ions flowing in the opposite direction through the electrolyte).

At gauge voltages higher than those considered by Kaneko et al (40mV) it can no longer be assumed that the electrode current-voltage characteristics are linear so a more detailed study was thought necessary.

1.6.3 Semi-permeability

Electrochemical semi-permeability results from a flux of electrons or holes flowing through the electrolyte (caused by electronic conductivity) and a compensating flux of ions also flowing through the electrolyte in response to an electric field. Semipermeability puts constraints on the conditions of use of electrolytes and has been well studied (Kleitz et al (1981c). In zirconia, n-type dominates over p-type conductivity when the oxide is in equilibrium with a gas with an oxygen partial pressure below about 10^{-10} Pa. Fig 1.2 (section 1.2.6) shows more clearly how the different conductivities are related.

Kleitz et al (1981c) and Iwase et al (1984) studied semi-conduction in zirconia. They came to a common conclusion using different methods and found that the flux of oxygen due to electronic conductivity was given by:

$$J_{O2} = RT/4F^2L[\sigma_p^0(pO_2^{1/4} - p'O_2^{1/4}) - \sigma_n^0(pO_2^{-1/4} - p'O_2^{-1/4})] \qquad (1.22)$$

where L is the thickness of the electrolyte, σ_p^0 is the p-type conductivity at unit oxygen partial pressure and σ_n^0 is the n-type conductivity at unit oxygen partial pressure. The above was derived theoretically by making some simplifying assumptions, but was found to model the experimental results accurately. The equation can be simplified if p-type conductivity dominates to:

$$J_{O2} = RT/4F^2L[\ \sigma_p^0\ (pO_2^{1/4} - p'O_2^{1/4})] \qquad (1.23)$$

If $p'O_2 \ll pO_2$ then it can be further simplified to:

$$J_{O2} = RT/4F^2L[\ \sigma_p^0\ (pO_2^{1/4})] \qquad (1.24)$$

At low oxygen pressures a similar relation was found to hold for oxygen flux due to n-type conductivity. It is given below for the case where $p'O_2 \gg pO_2$.

$$J_2 = RT/4F^2L[\ \sigma_n^0\ (pO_2^{-1/4})] \qquad (1.25)$$

The current due to semipermeability was derived from eqn(1.25) using Faraday's law and is:

$$I_{lk} = RTA_e/FL[\ \sigma_n^0\ (pO_2^{-1/4})] \qquad (1.26)$$

where A_e is the area of the electrodes.

Equation 1.26 is applicable for most situations studied in this work and Fig. 1.8 shows the predicted leakage current as a function of pumping voltage. The electronic conduction was estimated using data from Kleitz et al (1981c):

$$\sigma_n = 9.81x10^6 \exp(-359000/RT)\ pO_2^{-1/4} \qquad [\Omega cm]^{-1}$$

where the units required for pO_2 and T are pascals and kelvin respectively. R is 8.3144. In the example taken, the predicted leakage at 40mV is 10^{-8}A (using eqn(1.22)), and so it is clear why Kaneko et al (1987) found no evidence for semipermeability.

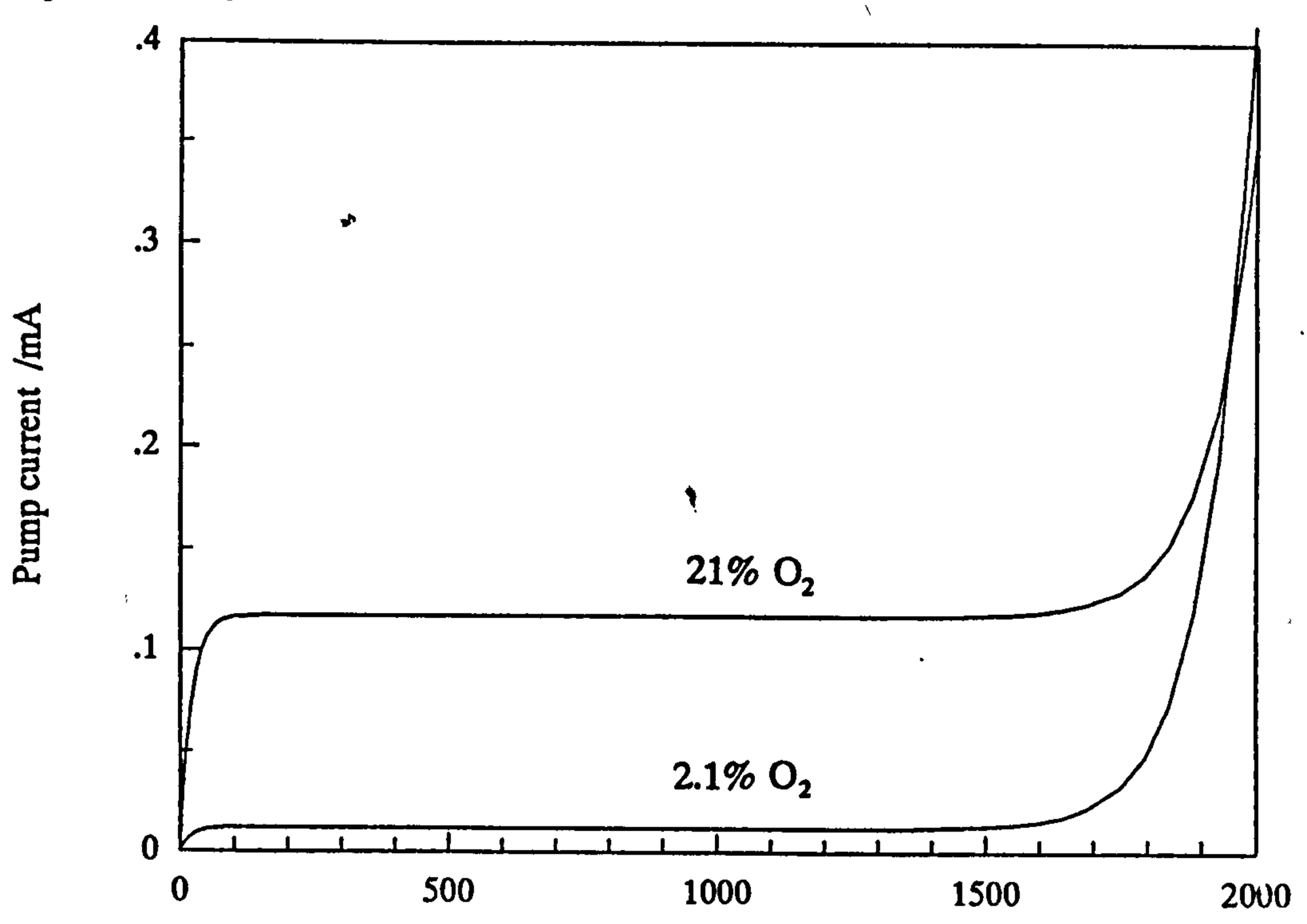

Fig. 1.8: Theoretical current curves due to semipermeability leakage and diffusion through the diffusion hole as a function of pumping voltage. A sensor with a 25μm diameter pore 0.7mm long operated in an oxygen / nitrogen mixture at 700°C was assumed.

Dou et al (1985) have suggested that oxygen migrates on the surface of any pores (closed or open) within the ceramic. This effectively increases semipermeability (and changes the pO_2 dependence). It becomes more noticeable as the thickness of the ceramic decreases. This could partially explain the wide range of electronic conductivity results reported in the literature as noted by Kleitz et al (1981c).

1.7) Sensor design: response rates

For a new zirconia gas sensor to be viable for many commercial applications it would need a response time shorter than a few minutes. For a lean-burn control sensor in car engine exhausts the response time would need to be less than a second. The factors influencing the response time of amperometric sensors and their gauge cells are reviewed below.

1.7.1 Rate limitation due to dead volume

(Hetrick et al (1981)) made an estimate of the response time of an amperometric sensor by using the basic formula:

$$\tau = \text{Volume / Flow rate into volume.}$$

They used the diffusion rate of oxygen into the sensor at steady state as a flow rate which is $DA_p pO_2/RT\ell$ mole/s (from eq. 1.14). Using the ideal gas equation this translates to DA_p/ℓ m^3/s. Therefore:

$$\tau = V\ell/DA_p$$

where V is the internal volume of the sensor. For a typical sensor using a 50μm thick seal and 5mm diameter electrodes, 25μm diffusion pore 0.7mm long τ is 8.5 seconds assuming $D = 164mm^2s^{-1}$. This is longer than the observed response times which are typically 0.5s (Benammar and Maskell (1991), (Soejima and Mase (1985) and Ueno et al (1986)). Saji et al (1984) and Suzuki et al (1986) found even shorter

response times of 200 and 20ms respectively. The difference is not surprising since these tests were done by changing the external oxygen partial pressure while the internal oxygen partial pressure was held at a low and almost constant level.

1.7.2 Rate limitation due to diffusion

Another estimate of the response time can be made by calculating the time that it takes to establish a new concentration profile through the diffusion pore. The theoretical time for a 90% response to a step change in oxygen concentration is (Maskell (1987)):

$$\tau = 0.3\ell^2/D$$

where ℓ is the length of the diffusion pore.

For a 0.7mm long pore at 700°C (where $D = 164mm^2s^{-1}$) the result is 0.9ms. It is difficult to test for such a rapid response rate but the evidence is that this estimate is too fast (Suzuki et al (1986)). One reason is that the oxygen cannot all be reduced by the part of the electrode adjacent to the pore entrance. The oxygen must diffuse inside the sensor to a part of the electrode that has the capacity to reduce it.

1.7.3 Electrode capacitance

Many studies have been done on the response rate characteristics of electrodes. It is not clear yet how much of the capacitive response observed is due to the double layer and how much is due to factors such as the build-up or consumption of electro-active species adsorbed on the electrode. Kleitz et al (1981a) reported that between about 500 and 700°C the overvoltage is composed of a fast and a slow relaxing part. Robertson and Michaels (1991) also found two components to the overvoltage and attributed the fast relaxing component to the double layer capacitance of the electrodes. Fig. 1.9 from Kleitz et al (1981a) summarises typical

relaxation frequencies assigned to the different components of the response of a zirconia cell with platinum electrodes. They found that the rapid response of the zirconia grains varied only with temperature. The slower response of the grain boundaries varied over a narrow band depending upon the zirconia sample. The fast component of the electrode overvoltage (labelled as the double layer) only depended upon temperature while the slow component showed a strong dependence upon the oxygen partial pressure.

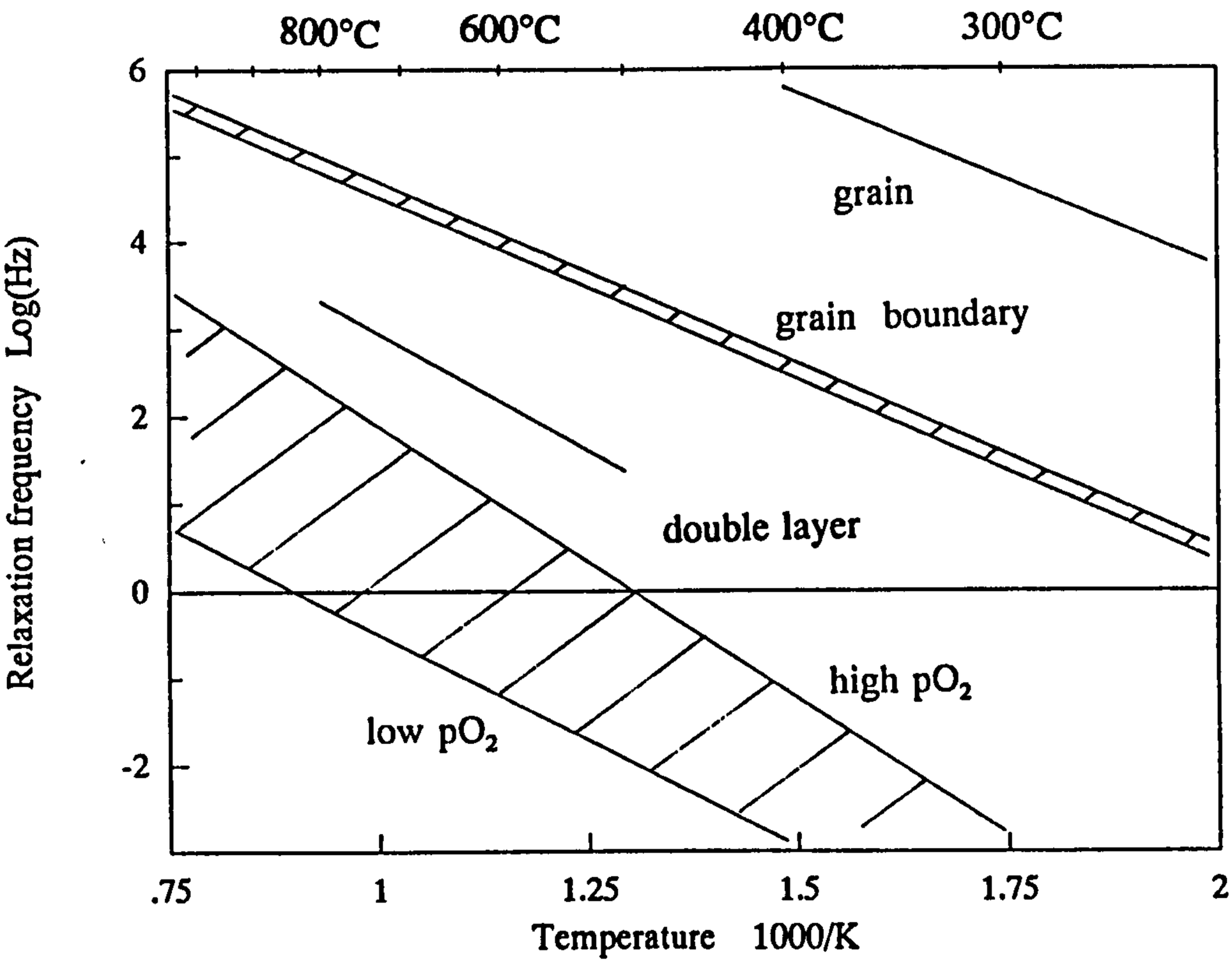

Fig. 1.9: Relaxation frequencies due to the different components of platinum electrodes on zirconia (Kleitz et al (1981a)).

1.7.4 Response delay due to electronic conduction

Heyne and den Engelsen (1977) did a theoretical study in which they showed that a layer of electronically conducting substance ($t_{ion} < 1$) in an otherwise ionically

conducting electrolyte ($t_{ion} \approx 1$) would cause a transient error in the Nernst voltage. This error can take many hours to diminish because it requires that the oxygen activity within the electrolyte reaches steady state. It is possible that grain boundaries display enough electronic conduction to cause a noticeable error (Steele et al (1981)).

Although this phenomena may not have an important effect on the pumping cell of a sensor it could have significant influence on the gauge cell.

1.8) Thermodynamics

The thermodynamics of gaseous reactions needs to be understood to predict the current due to reduction of a gas in an amperometric sensor. Considering water as an example, the reduction reaction on the electrode is:

$$H_2O + 2e^- \longrightarrow H_2 + O^{2-}. \qquad (1.27)$$

Fouletier et al (1984) showed that at temperatures between about 700 and 900°C the Nernst potential on platinum electrodes provides an accurate indication of the oxygen partial pressure in the gas phase which reaches equilibrium at these temperatures. The oxygen activity on the electrodes can therefore be calculated by assuming that it was in equilibrium with the gas phase. The equilibrium for the gas phase reaction:

$$H_2O \longrightarrow H_2 + \tfrac{1}{2}O_2 \qquad (1.28)$$

is:

$$K_{H2O} = \frac{pO_2^{1/2}\, pH_2}{P^{1/2}\, pH_2O} \qquad (1.29)$$

where P is the total (ambient) pressure and is included in the equation to ensure that the equilibrium constant K_{H2O} is dimensionless.

K_{H2O} can be determined from the well know thermodynamic relationship:

$$K_{H2O} = \exp(-\Delta G/RT). \qquad (1.30)$$

where ΔG is the Gibb's free energy of formation of water at temperature T.

Another well known equation can be derived from eqn.(1.30) by making the following substitutions into the Nernst equation (1.7).

$$p'O_2 = K_{H20}^2 P p H_2O^2 / pH_2^2 \text{ (from eqn (1.29) and } pO_2 = P.$$

If $pH_2O = pH_2$ the result is:

$$E = RT/4F \ln(K_{H2O}^2).$$

By substituting eqn(1.30) into this equation the result is:

$$E = -\Delta G/2F$$

or:

$$nFE = -\Delta G. \qquad (1.31)$$

where n is the number of electrons transferred.

The free energy of formation of oxides (MO_x) can be determined by measuring the oxygen potential created by a mixture of the oxide and its corresponding cation in its elemental form. With solid and liquid systems care needs to be taken to ensure that minimal oxygen diffuses to the M-MO_x mix because an insulating oxide layer can form which will change the results (Anthony et al (1984) and van Manen et al (1992)).

It is interesting to compare the redox potentials (derived from eqn(1.31)) as a function of temperature for a number of oxides (Fig. 1.10). The data in Fig. 1.10 was calculated using Gibbs free energy of formation data from Barin (1989) (tabulated in Appendix 6). The data from Barin used the convention that the ambient pressure was 0.101MPa. Therefore the potentials shown in Fig. 1.10 are for a cell with the species shown at an ambient pressure of 0.101MPa on one side and an oxygen partial pressure of 0.101MPa on the other side. Also the oxidized and reduced species must be at equal partial pressures.

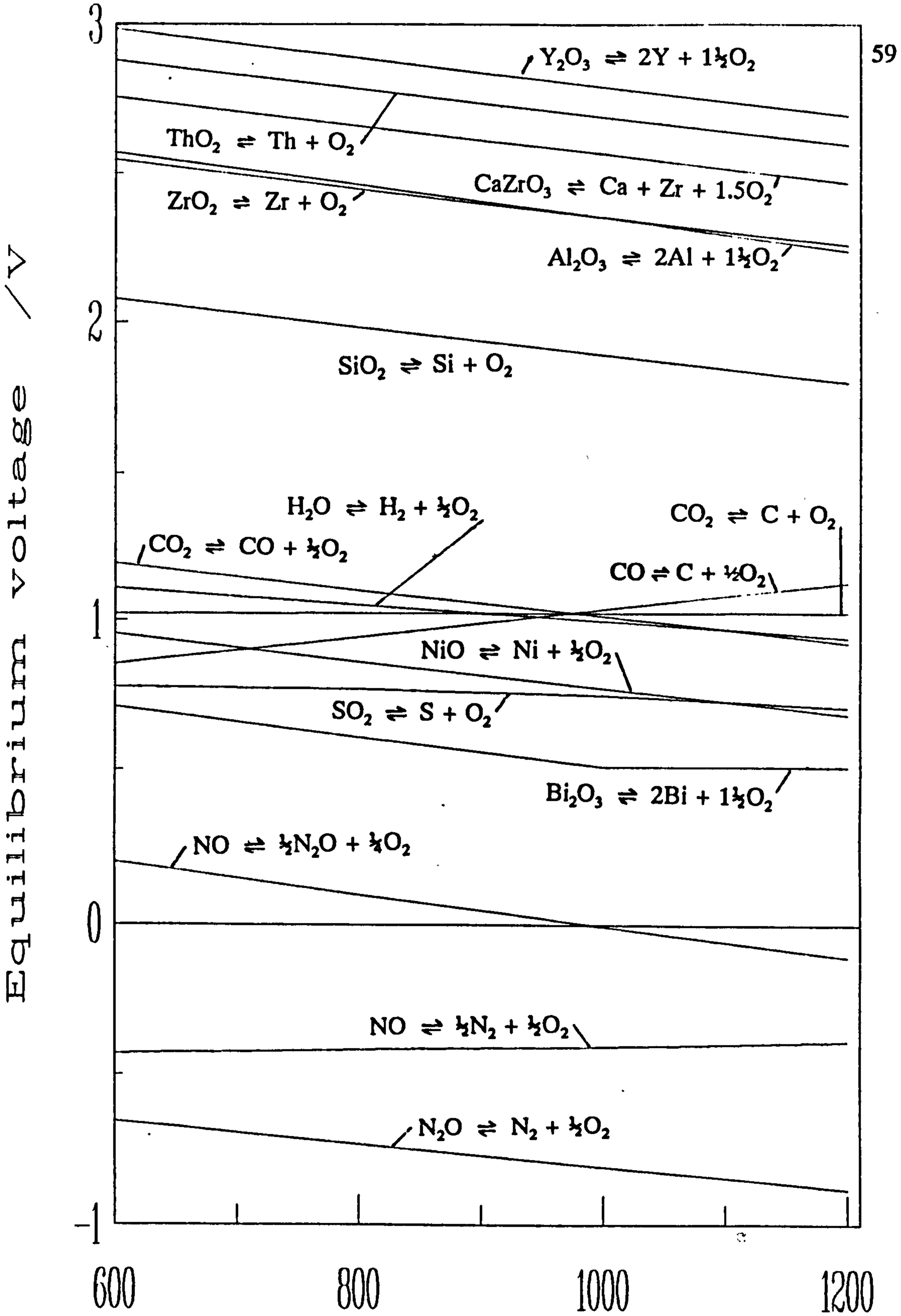

Fig. 1.10: Oxygen potentials created by various redox couples compared to O_2 at 0.101MPa as a function of temperature.

1.9) Aims and objectives

The main aim of this work was to investigate sensors for a range of oxygen-containing gases. After reviewing the available sensor technology it was decided to concentrate on extending the existing design of zirconia pump-gauge sensors.

Initially experiments were done to determine the current-voltage characteristics of electrodes made of platinum, gold and silver. Single YSZ discs with no diffusion barrier were used in O_2/N_2 and $CO/CO_2/N_2$ mixtures. This was to provide an insight into the behaviour of complete sensors. The next objective was to find a method for making these sensors with a gas-tight seal that had the minimum electrochemical leakage.

Unique amperometric sensors with gauge cells and reference electrodes were made and tested in O_2/N_2 mixtures to confirm their satisfactory operation. The importance of the overvoltage on the internal pumping electrode was demonstrated at this stage. To determine which gases these sensors were capable of detecting tests were performed in mixtures containing CO, CO_2, NO and SO_2. A method for compensating for electrochemical leakage had to be developed in order to optimize the interpretation of the results obtained. Based on this work the designs for two sensors were proposed; one for a lean-burn sensor and the other for a multi-gas sensor.

Another objective was to assemble instrumentation for testing electrodes and sensors within the Energy Technology Centre. A computer controlled potentiostat/galvanostat with the ability to continuously perform a range of electrochemical tests was built. To enable continuous unattended operation the control of the furnace and the gas flow valves was integrated into the system.

Chapter 2

Experimental equipment and methods

"The years of anxious searching in the dark, with their intense longing, their alternations of confidence and the final emergence into the light - only those who have experienced it can understand it"

Albert Einstein

2.1) Manufacture of sensors and cells

2.1.1 Preparation of zirconia discs

Zirconia discs 7.8 mm in diameter and with thicknesses between 0.25 and 0.8mm were prepared by 3 methods.

a) Cutting from large presintered pellets:

6Y-YSZ (6mole% Y_2O_3 or 9.8wt%) and 8Y-YSZ powder from Toya Soda was pressed into pellets at a pressure of approximately 30MPa. They were then fired by heating at 300°C/hour to 1550°C for 2 hours and then cooled at 300°C/hour. The 8Y-YSZ had a density of 5790kg/m^3. 7.8mm cores were drilled from these sintered pellets with a hollow diamond drill. The cores were then cut into slices 0.7mm thick with a Capco diamond saw.

The surfaces of the discs were then ground so that they were almost flat. This was done by gluing them to a special holder, using Lakeside cement, which was then mounted in a drill. By carefully controlling the pressure on the drill it was possible to grind concentric rings onto the discs with silicon carbide paper. The

concentric rings were an important feature which enabled a gas-tight seal to be formed between two disc with a metal ring (Maskell (1992)). It was found that the quickest way to do the polishing was to start with a coarse paper and finish with fine (1000 grit) paper. A very short grind under low pressure was all that was required on the coarse paper. Plenty of water was needed, particularly with the coarse paper, to prevent the Lakeside cement from softening with the heat from the grinding.

b) Using ceramic sheet prepared by ICI:

Zirconia powder was mixed with suitable plastics and dispersing agents and rolled into sheets of various thickness by ICI. 9.4mm discs were punched out of these sheets with a steel punch tool. The green discs were then immediately fired or else dried at about 60°C before grinding concentric rings with silicon carbide paper. No water was used for the grinding and an extremely light pressure was used. The discs (ground or unground) were then fired on a high purity alumina plate. To minimize the buckling of the discs, the heating rate up to 400°C was kept to below 180°C/hour (usually 60°C/hour).

c) Isostatic pressing.

Isostatic pressing has the advantage that the stress is distributed more evenly through the pellet compared to the linear pressing technique used in method a). Therefore higher pressures can be applied which produces pellets that can be fired into zirconia with lower porosity and fewer flaws. It was found to be very difficult to make a mould from which a well shaped pellet would emerge after pressing. The method originally used was to put a rubber bung into the end of a short piece of flexible rubber hose. A weighed sample of 6Y-YSZ powder was put into the tube and another rubber bung forced into the open end. The trapped zirconia was then pressed to 140MPa in an isostatic press. Most samples crumbled when removed from the mould. By using softer rubber for the bungs and the tube and using 190MPa pressure, green discs were finally prepared. They were fired at 1550°C for 2 hours. None of the resulting discs were judged to be of sufficient quality for further testing.

2.1.2 Sintering the zirconia

The sintering program chosen for the ceramic is important. If the temperature is too low or the time too short the ceramic does not reach full density and the conductivity is low. If it is too hot or too long the grains become too large which decreases the strength of the ceramic. Grain growth in TZP makes it vulnerable to low temperature ageing or can cause spontaneous transformation to the monoclinic structure if the critical grain size is exceeded. Ageing in TZP can occur even if the ceramic is at the critical temperature for a short period during temperature cycling (Wen et al (1988)).

Most ceramics in this work were sintered at 1550°C for 2 hours and heating and cooling rates were between 300 and 600°C/hour.

2.1.3 Fabricating a hole in the zirconia

Amperometric sensors required small holes to act as diffusion barriers, the production of which presented a considerable challenge. For discs cut from fired pellets, laser drilling was the only method considered practical (Maskell and Steele (1988)). However, experience showed that the holes were tapered and the diameter varied markedly between batches. It was also found to be difficult to achieve a small hole size, although in one batch 15µm diameter holes were achieved (Malpas (1992)).

With the ICI ceramic, there were several options. The easiest method found was to drill holes in the green ceramic with micro drills with diameters of 250µm or 150µm. During firing the holes shrank to 170µm or 100µm respectively. With a disc 0.8mm thick these holes would give limiting currents of about 2.5 and 0.9mA respectively in air at about 700°C. A lower limiting current was often desired, so other methods were investigated.

One technique tried was to place a 40µm platinum wire in the holes drilled in the green ceramic. A small drop of zirconia powder and 400 solvent (from ESL)

was mixed into a paste which was then placed on the disc so that it flowed down into the hole and surrounded the wire. The discs were heated to 100°C twice (to increase the flow rate) and more paste was added after each heating. The discs were then heated to 900°C to sinter partially the zirconia and then cooled so that the platinum wire could be removed. Some zirconia paste came away with the platinum wire because it was not sufficiently sintered to resist this damage. A second test was done where the discs were heated to 1000°C. Two of the three wires broke on attempting to remove them because the zirconia had sintered too much. Therefore, a temperature of 950°C would seem reasonable for this process but a third test was not performed.

An attempt was made to use this last method using 7μm carbon fibres but was not successful. The delicate fibres would not stay in the drilled hole while the zirconia paste was added.

2.1.4 Preparation of electrodes

Electrodes were prepared by three methods

a) painting on a paste or slurry with a pin.

Painting has the advantage that it wastes less material than the other methods used. This is especially true when dealing with small numbers of discs. The other 2 methods are quicker and more accurate once set-up, but set-up time required is much larger than for painting.

For platinum electrodes a commercial flux-less platinum paste (no. 5542 from Electro-Science Limited (ESL)) was used. For gold and silver a paste was made by mixing about 0.5g of the metallic powder (1.5-3μm and 5-8μm respectively from Aldrich) with 400 solvent from ESL. The solvent was added slowly and the mixture was continuously stirred (with a small metal rod in a glass bottle) until it had a viscosity suitable for painting. It was then mixed more until there was no visible sign of inhomogeneity.

The pastes were then spread carefully onto the zirconia surfaces using a very light touch with a pin. A pin was found to be much better for this than a brush. It allowed more accurate control of where the paste was painted and of how thickly it was applied. Care had to be taken to prevent the zirconia abrading the surface of the pin and leaving unwanted iron/nickel/chromium deposits. Great care was also taken to ensure that the paint was applied evenly. With gold it was also important to insure that the paint layer was thin because thick layers peeled off due to the mismatch in thermal expansion coefficients.

b) Sputtering

Only platinum electrodes were sputtered. A holder was made from aluminium to enable up to 76 discs to be sputtered in the Nordiko sputtering machine in the Department of Materials at Imperial College.

c) Screen printing

Pure platinum electrodes, using the 5542 paste, and cermet platinum electrodes were screen printed. The cermet paste was made by mixing the 5542 paste with a the 3Y-YSZ powder (Toya Soda) and the 400 solvent. This mixture was blended on a triple roll mill.

d) Sputtering plus screen printing

Pure platinum electrodes were prepared by first sputtering as in method b) and then screen printing the 5542 paste as in method c).

2.1.5 The need for reference and gauge electrodes

In this work a single disc with two or three electrodes on it was called a cell. A sensor referred to an amperometric sensor consisting of at least two discs (or cells) sealed together with metal or glass and including a diffusion pore (see Fig. 1.4 or 1.5).

A reference electrode (RE) is an electrode in the same environment as the working electrode (WE) and/or the secondary electrode (SE) (also called counter electrode). The difference is that essentially no current flows through the RE and so

no overvoltage develops on it. The voltage on it therefore reflects the chemical potential of the oxygen in the gas in which it is placed. If the uncompensated resistance in the electrolyte can be determined by a technique such as current interruption, the overvoltage on the WE can be calculated. If the RE shares the gaseous environment of the SE and not the WE, some method is needed for determining the chemical potential of the oxygen in the gas around the WE. The amperometric sensors used in this work had this problem because the internal pumping electrode was the WE (because the overvoltage on it was of particular interest). Putting a reference electrode inside the sensor on the same electrolyte as the pumping electrode would have reduced the area of the later. This was considered undesirable. The RE was therefore put on the outside of the sensor next to the external pumping electrode. The voltage between the working and reference electrodes (E_{WR}) consequently included a contribution from the difference in oxygen potentials: ie. the Nernst potential. The solution was to put electrodes, that carried no current, on the electrolyte with the diffusion hole in it to measure this Nernst potential. These were called the gauge electrodes and their addition enabled the calculation of the overvoltage on the WE.

An amperometric sensor with a reference electrode was first reported in Copcutt and Maskell (1992) and Fig. 1.4 illustrates a cross section of such a sensor. A five electrode pump-gauge sensor with diffusion pore was first reported by Copcutt and Maskell (1993) and Fig. 1.5 illustrates its cross section. Fig. 2.1 is a view of the outside of a glass-sealed sensor facing the external pumping and reference electrodes and illustrating their relative positions.

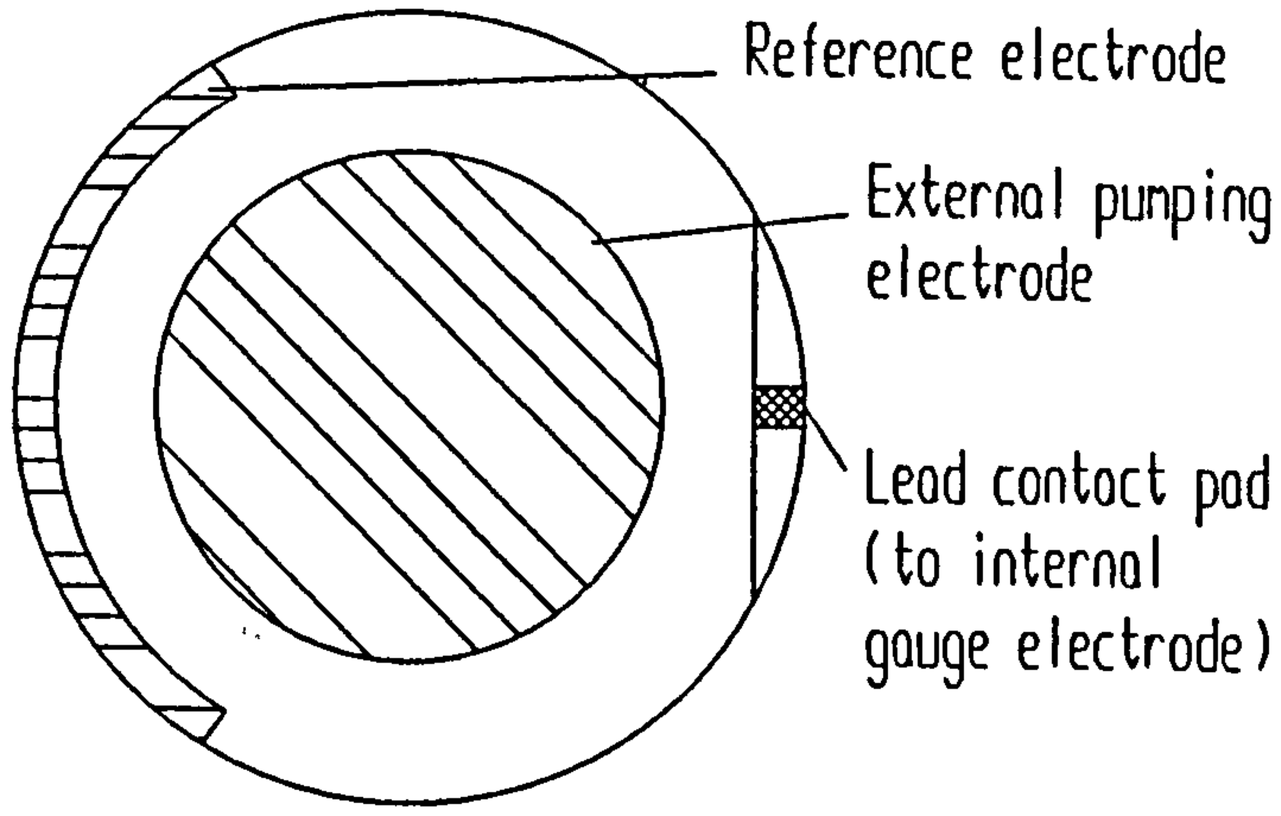

Fig. 2.1: A glass-sealed pump-gauge sensor showing the positions of the external pumping electrode and the reference electrode.

2.1.6 Assembling an amperometric sensor

a) Metal-sealed sensors:

The jig used for testing the sensors was built so that the sensors could be assembled in it. It was based upon a design previously described (Benammar and Maskell (1992b) and is discussed further in section 2.2.1. A metal ring was made by first punching a 5mm hole in a 100μm thick sheet of the same metal as the electrodes. The metal was then cut with scissors so that a 1mm wide ring was left with a 2mm wide tag for attaching to the connecting wires. This ring was placed between the two zirconia discs and the 7.5mm OD alumina tube (see Fig. 2.3) was used to press them together by tightening the spring-loaded nut. The furnace was then heated while applying a voltage to the pump electrodes and monitoring the resultant current as the temperature rose. The current decreased when the metal seal deformed sufficiently to close the physical leaks. Seals could be formed using silver

foil by firing at 750°C for 1 hour under a pressure of about 100N. Gold seals required 1000 to 1030°C for at least 2 hours at 100N; Kaneko et al (1987) used 3 hours and Malpas (1992) used 16 hours. Platinum seals required even more severe conditions with pressures of 250N and temperatures of 1100°C over 5 hours being barely sufficient.

The furnace was then cooled and the sensor removed so that the external edge of the metal seal could be covered with glass (see next section). It was found that the glass seal was more effective if the edge of the metal was recessed below the edge of the ceramic. This made it difficult to position the metal rings in the rig ready for assembly. The solution was to glue the ring to the one of the ceramic discs with a very small spot of acrylic glue. A minimum quantity of powerful glue was used to minimize the residue it might leave after firing. The two discs were then placed in the rig and all the components of the sensor could be easily and accurately aligned.

b) Glass-sealed sensors:

A single attempt was made to assemble a sensor by holding two zirconia discs together and painting glass paste around the circumference. The sensor made this way gave abnormally low currents, possibly because glass diffused onto the electrodes, and was not considered useful.

The last two (and best) sensors tested were made by screen printing and firing platinum electrodes with an extra track leading to the edge of the disc (Fig. 2.2). Both had cermet platinum electrodes with about 67wt% Pt, but the cermets used were not from the same batch. A ring (not circular) of glass paste (LZ1/R012 ground to 200/325 mesh from Ceramic Developments) was then screen printed onto the 6Y-YSZ discs. The discs were then fired at 970°C and the process repeated. The discs then had a double layer of glass on the outer 0.5mm of their surfaces. Fig 2.2 illustrates the surface of a disc at this stage in the process. To assemble a sensor, two discs were pressed lightly together and fired to 850°C. Pt leads were attached to the exposed pads and a final firing at 950°C was performed with no pressure being applied. The temperatures were held for 20 minutes in each case.

The first sensor made this way (sensor G1) had a hole tapering down to just over 40µm into which a 40µm platinum wire had been lodged. The second glass-sealed sensor (G2) had a laser drilled hole with a mean diameter of 22µm.

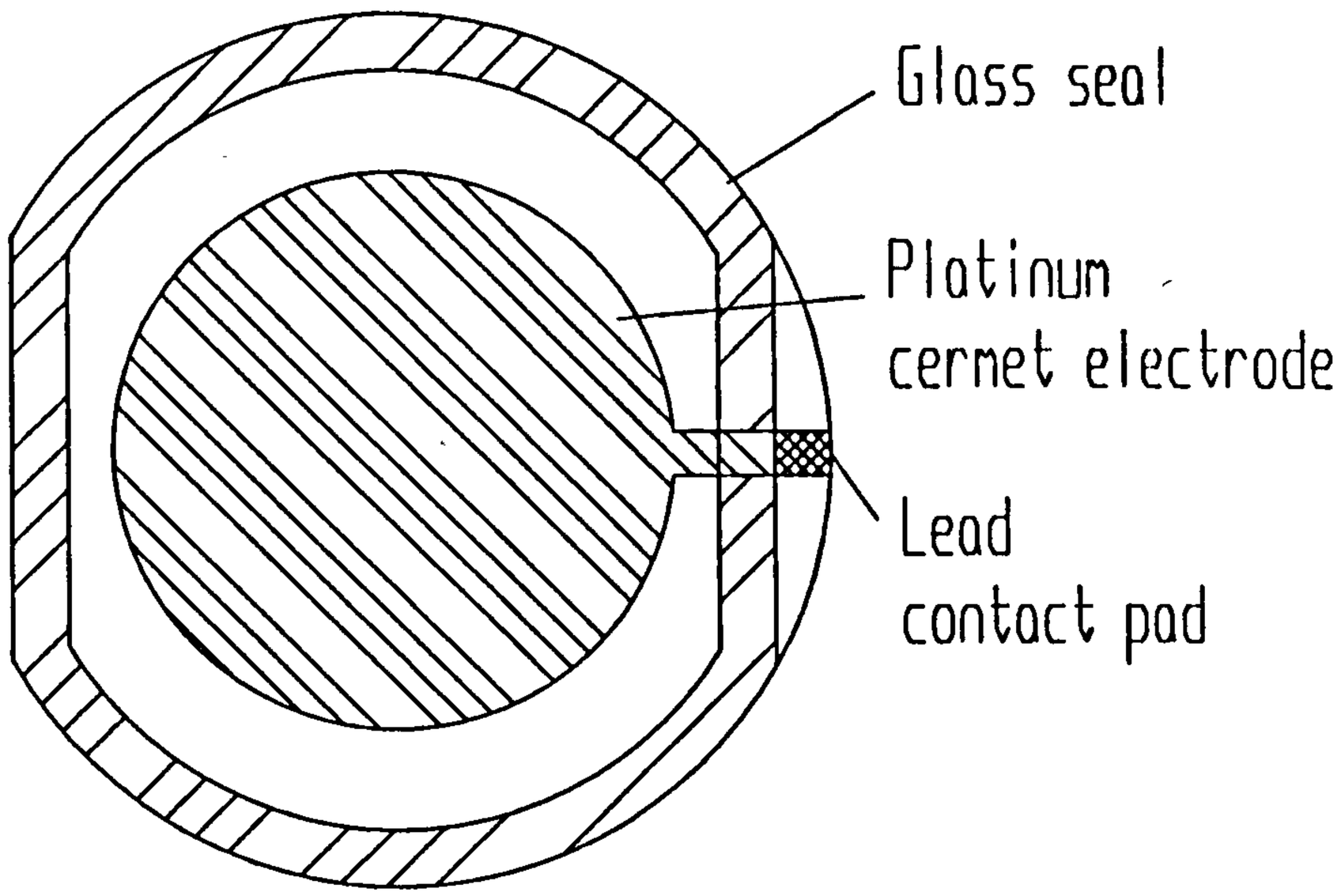

Fig. 2.2: A YSZ disc with a platinum electrode and deposit of glass ready to be sealed to another similar disc.

2.2) Miscellaneous apparatus

2.2.1 Mounting the sensor

The rig for holding the sensors is shown in Fig. 2.3. The 7.5mm OD alumina sealing tube was spring-loaded either to hold the sensor in place or to force the YSZ discs together during the process of forming metal seals between the discs. It slid inside a 12mm OD alumina tube. A 3mm OD alumina tube was used to feed gas to the sensor and the end nearest the sensor was supported by a 50mm length of 5mm OD tube. Earlier rigs used Mullite and aluminous porcelain tubes but all tubes in the

final rig were alumina to prevent differential expansion from changing the position of the end of the inner-most tube and to keep the spring pressure constant with varying temperature.

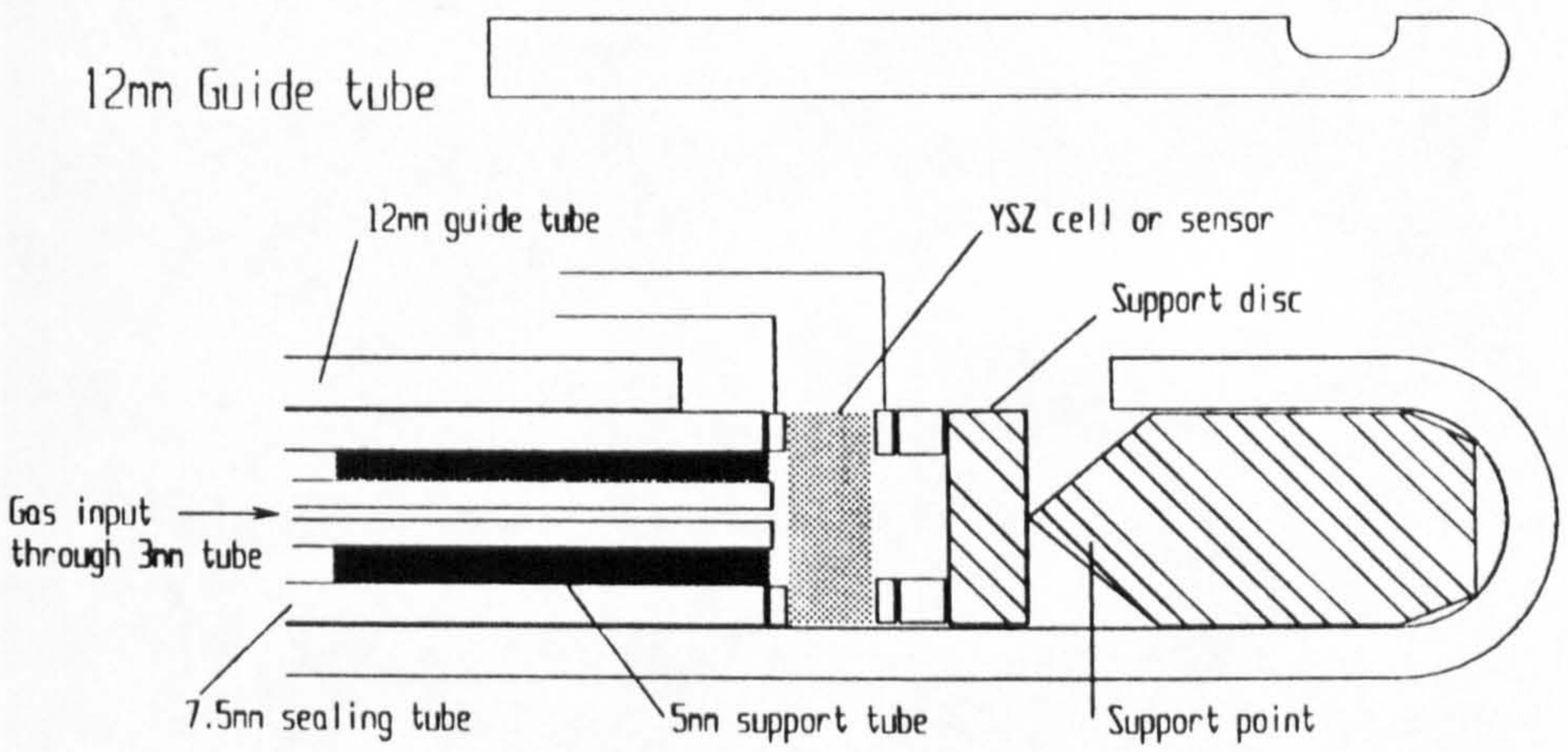

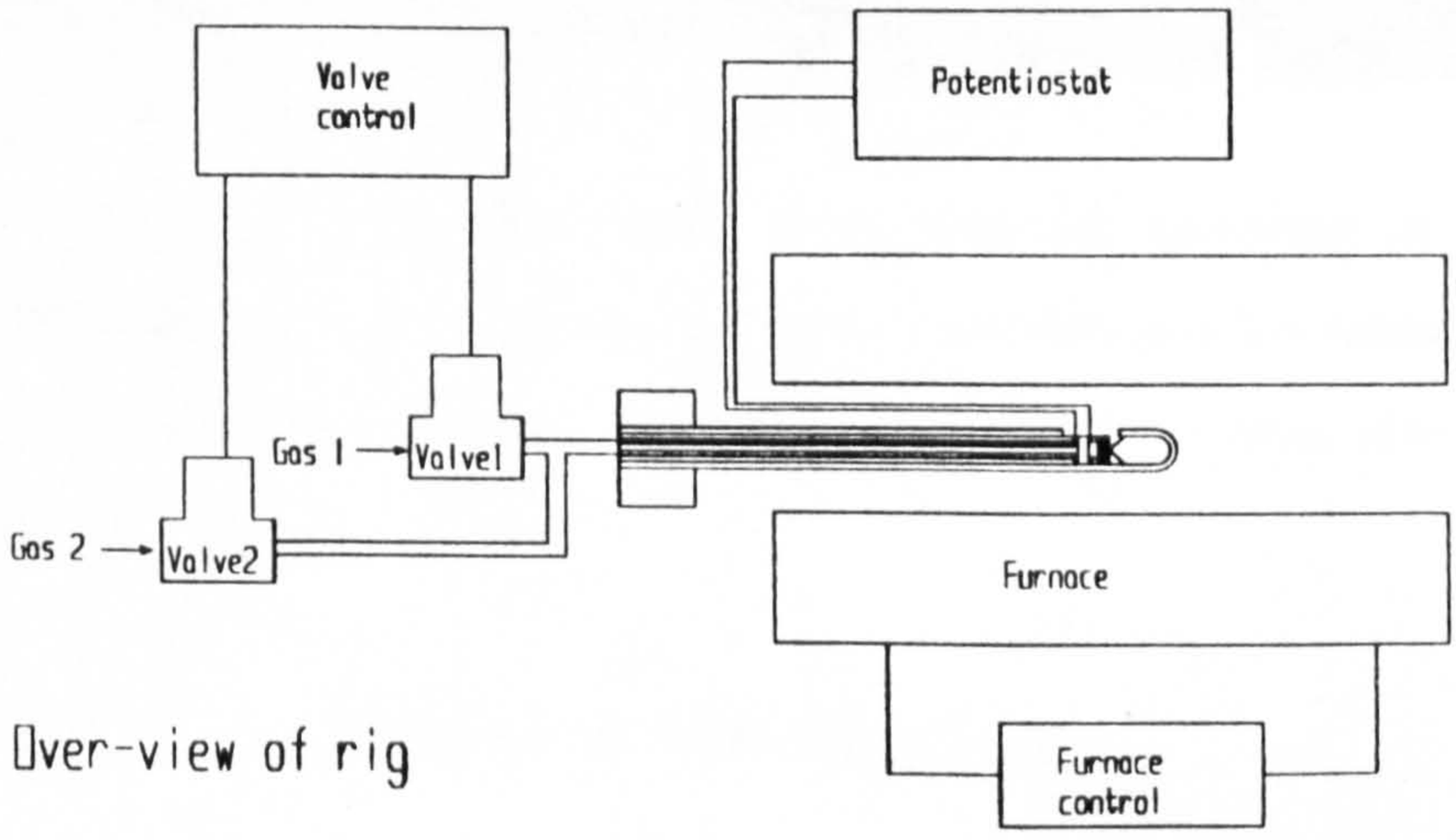

Fig. 2.3: The rig for mounting, constructing and testing the sensors.

Fig. 2.4: Photograph of a sensor in position for mounting in the rig and connecting with the platinum wires emerging from the shielded tubes. The lower tube is the thermocouple and top tube is a sealed zirconia tube used as a potentiometric sensor.

2.2.2 The silica tube enclosing

The original idea was to seal the sensor or cell to the end of the 7.5mm OD alumina tube so the each side could be exposed to a gas of different composition. However, it was found to be very difficult to form a satisfactory hermetical seal between the alumina of the tube and the zirconia. A system using a large silica tube similar to the system used previously (Kaneko et al (1987)) was therefore built. Fig. 2.5 shows the apparatus. The silica tube was purchased from Quadrant Glass, and the brass holder was machined in the Mechanical Engineering workshop. All the guides around the central guide for the sensor-holding rig were tapered inwards so

that the electrical lead wires emerged from their shielded tubes as close as possible to the sensor. The fibre insulation within the silica tube shown in the photograph Fig. 2.5 was necessary because the brass holder had no provision for water cooling. It also reduced heat loss from the furnace. Without the insulation within the silica tube, the temperature of inside was up to 15°C below that of the furnace heating elements. With it in place the thermocouples inside and outside the tube agreed to within 5°C.

The supports for the brass holder were designed to conduct heat away. Although provision for a heat shield to be added was made it was found to be unnecessary for furnace operating temperatures up to 950°C.

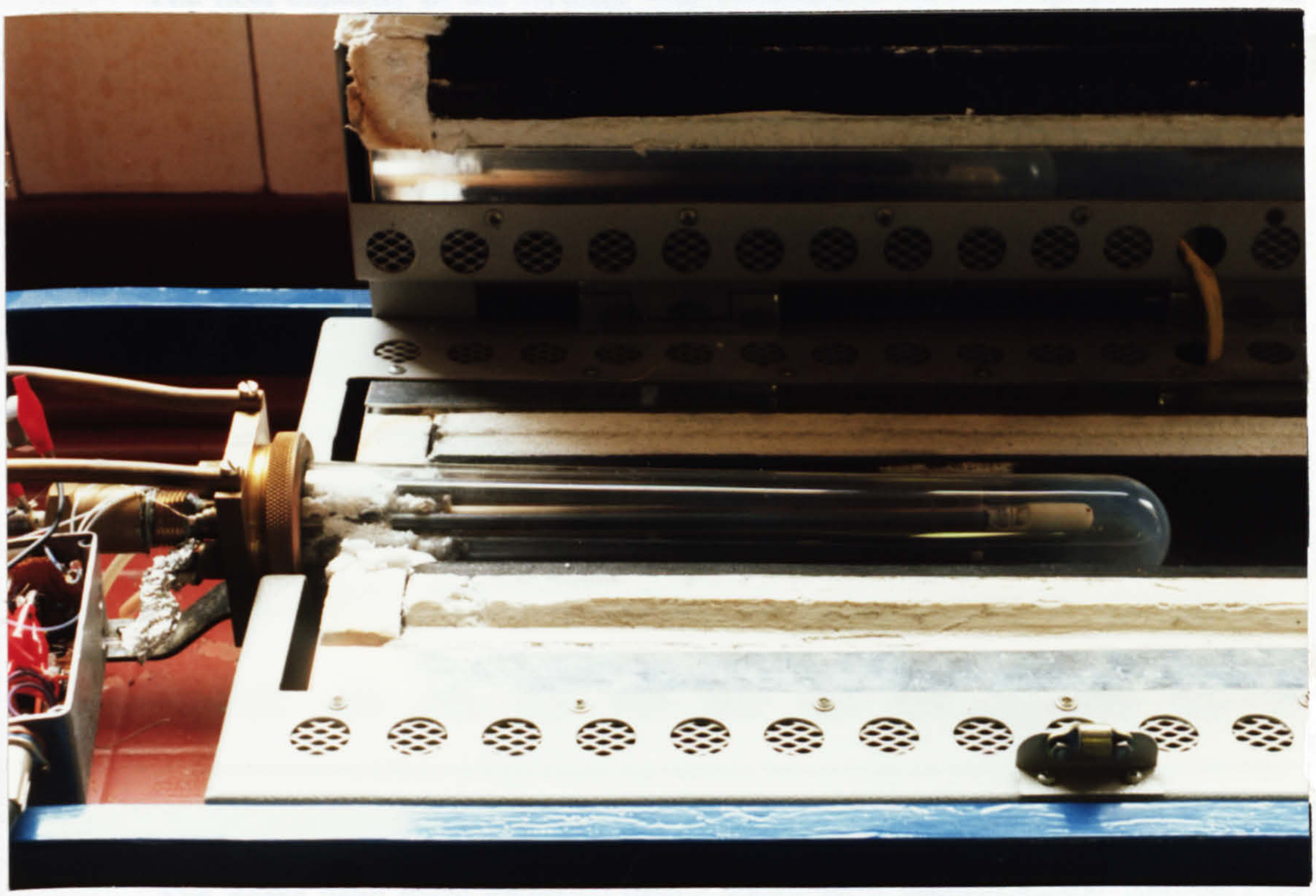

Fig. 2.5: Photograph of the brass holder which formed a gas-tight seal with the silica tube and supported the sensor mounting rig and the electrical leads to the sensor.

2.2.3 The furnace

The furnace used was a Carbolite CST10/75. It was fitted with two thermocouples. The thermocouple fitted by the manufacturer was K type and was sealed into the inner surface of the furnace. A second R type (Pt,Pt13%Rh) thermocouple was mounted close to the cell and was used for primary control of the heating rate and operating temperature by the computer. A switch was used to change between using the factory-supplied controller or the computer as the primary means of furnace control. A circuit built for furnace control is described in Appendix 2.

The heat capacity of the furnace was estimated to help set the parameters in the program for its temperature control. It was approximately 700J/K at 500°C. The loss of heat to the atmosphere was also measured and found to be 0.5W per Kelvin difference in temperature between the furnace and the atmosphere at 500°C.

The accuracy of both thermocouples was tested against the melting point of silver (961.93°C) (Weast (1988)). A piece of silver was attached to platinum wires near the R thermocouple. A voltage was applied across the silver strip and the current constantly monitored. The furnace was rapidly heated to 930°C and then at 120°C/hour until the current stopped flowing. Both thermocouples were found to be accurate to within 5°C.

2.2.4 Gas supply

The gases used were standard purity supplied in high pressure cylinders by British Oxygen. The compositions used were dry air, white spot (oxygen-free) nitrogen, 4% CO_2 in N_2, 4% CO in N_2, pure CO_2, pure SO_2 and 0.01% NO in N_2. The gases were fed to flow control valves and then to the furnace in PTFE or stainless steel tubing with 1/4" Swagelok fittings. This was to ensure that oxygen and water vapour could not diffuse into the supply from the surrounding air.

Mass flow control valves type 5850TR from Rosemount Brookes were used to control the flow of gas from the cylinders into the apparatus. These valves were interfaced to the computer with the circuit shown in Appendix 2. Valves with full scale flow rates of 5, 15, 75 and 150ml/minute were used. These flow rates were for nitrogen at 0°C and 101.3kPa. The valves monitored the cooling of a heated wire so a correction factor was needed for other gases. The factor was 1 for all gases used except for CO_2 and SO_2 for which the readings were multiplied by 0.78 and 0.73 respectively to arrive at the flow rates.

0.5µm filters were kept connected up-stream of the valves at all times to prevent microscopic pieces of extraneous material entering the valves and altering their calibration. The calibration of the valves was checked with a soap bubble flow meter and found to be within the 1.0% accuracy and 0.2% repeatability limits claimed by the manufacturer. A potentiometric oxygen sensor was used on a regular basis to ensure that the valves were supplying the desired oxygen concentration in air/N_2 mixtures.

Warm-up time for the valves was recommended to be 45 minutes and the response time to within 2% of the set value was claimed to be 6 seconds. The claimed temperature sensitivity was 0.09%/°C between 5-65°C, and the leak integrity was claimed to be less than 0.06 ml/minute of helium.

The volume of gas between the flow control valves and the sensor under test was kept to a minimum so that the sensor would experience the fastest change in concentration possible when the valve setting were changed (Danckwertz (1953)). A 3mm OD, 1.6mm ID alumina tube was used to feed the gas to the sensor in the furnace. It was delicate so a short piece of 5mm OD alumina tube was put over the end nearest the furnace centre to support it within the 7.5mm OD alumina tube (Fig. 2.3). This short spacer tube was also designed to prevent back-diffusion of gas flowing away from the sensor.

2.2.5 Potentiometric sensors

a) Thimble sensor:

A potentiometric oxygen sensor was used to monitor gas flows into or out of the main test rig. It was acquired ready-made and was manufactured by applying Pt electrodes to the inside and outside of a zirconia thimble. The thimble was then mounted in a holder which enabled gas to be piped to the inner electrode. Contacts were made to the electrodes and the completed sensor was mounted in a small furnace. The furnace was controlled by a dedicated unit that held the temperature at 735°C. This resulted in a Nernst output of 50mV per decade of oxygen partial pressure.

b) Zirconia tube:

A 300mm long 6mm OD zirconia tube with one end closed was mounted within the silica tube. Platinum electrodes were applied to both sides of the closed end. The open end was exposed to air so that the oxygen partial pressure inside the silica tube could be monitored. This was useful as a check on the gas flow apparatus and as a guide to the oxygen potential achieved by platinum electrodes in CO/CO_2 mixtures (relative to air). The closed end is visible in the photograph of Fig. 2.4.

2.2.6 ±15 volt power supply

A power supply capable of supplying 3A at +15V and 2 x 1A at -15V was built to supply a regulated voltage to the potentiostat/galvanostat, the gas flow control valves, and related devices. The circuit diagram is shown in Appendix 2.

2.3) The computer-controlled apparatus

2.3.1 Theory of potentiostat/galvanostat

The basic idea of a potentiostat is illustrated in Figs. 1.4 and 1.5 while Fig. 2.6 shows more detail of the circuit built for this work. Full details are in Appendix 2.

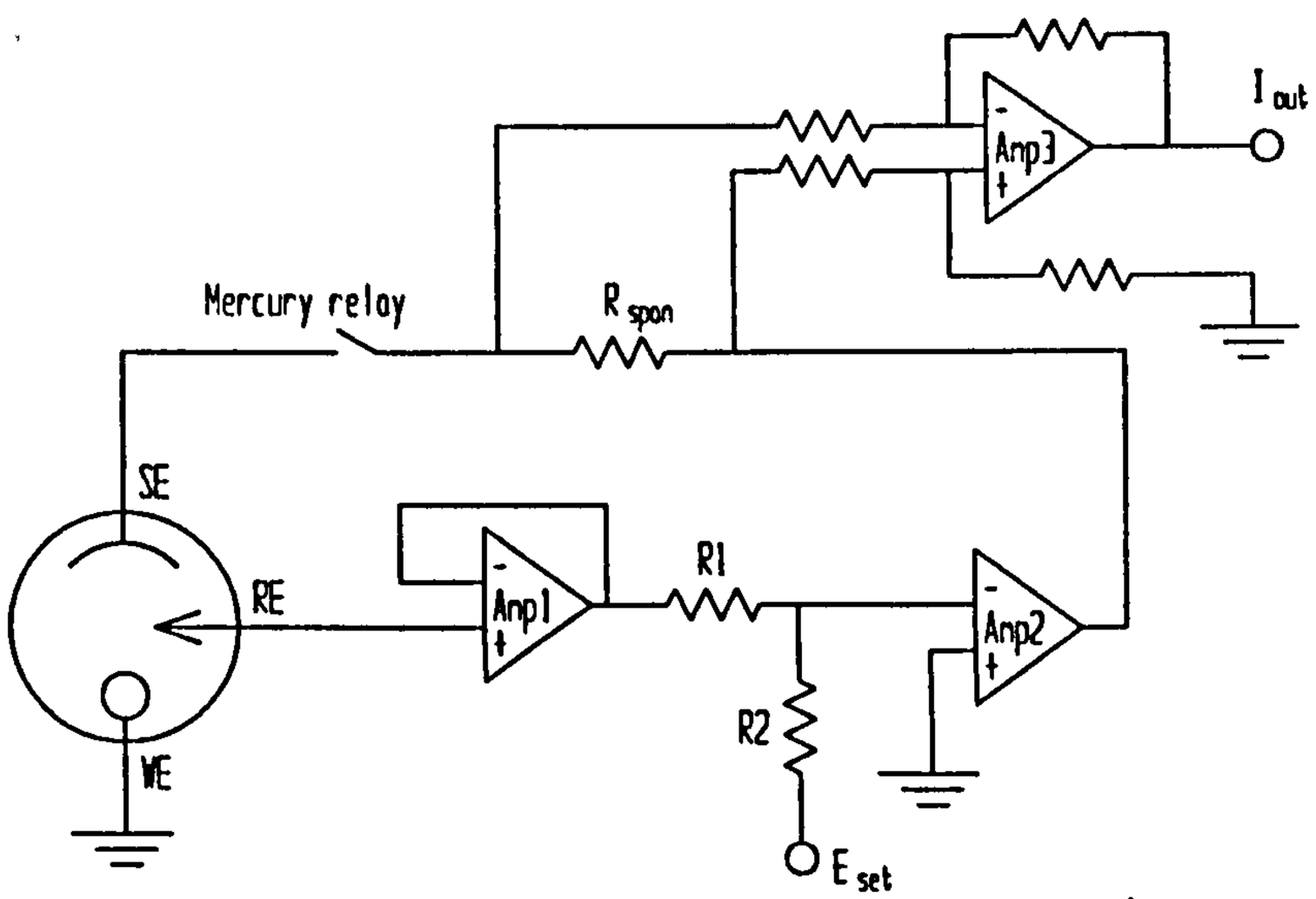

Fig. 2.6: The basic potentiostat circuit.

Very little current was drawn from the reference electrode to ensure that there was negligible overvoltage on it and that its potential approached equilibrium with the gas in which it was immersed. It was connected to the non-inverting input of op-amp 1 which was chosen for its high input impedance ($>10^{13}\Omega$). This op amp was connected as a voltage-follower and fed into a second op amp through resistor R1. The ADDA card applied a potential E_{set} to resistor R2 which fed into the same input. The other input terminal of op amp 2 was connected to earth. Op amp 2

therefore passed whatever current was required through the secondary electrode so that the voltage between RE and WE (E_{WR}) was given by:

$$E_{WR} = -V_{set}\, R1 / R2.$$

Four ratios of R1 and R2 could be selected by the computer to provide a wide range of possible settings for E_{WR} (98mV full scale to 4490mV full scale).

The voltage drop across the span resistor (R_{span}) was proportional to the current flowing through it. This voltage was amplified to a level suitable for the ADDA card by op amp 3 which was connected as a differential amplifier.

The basics of a galvanostat are illustrated in Fig 2.7 while full details are in Appendix 2.

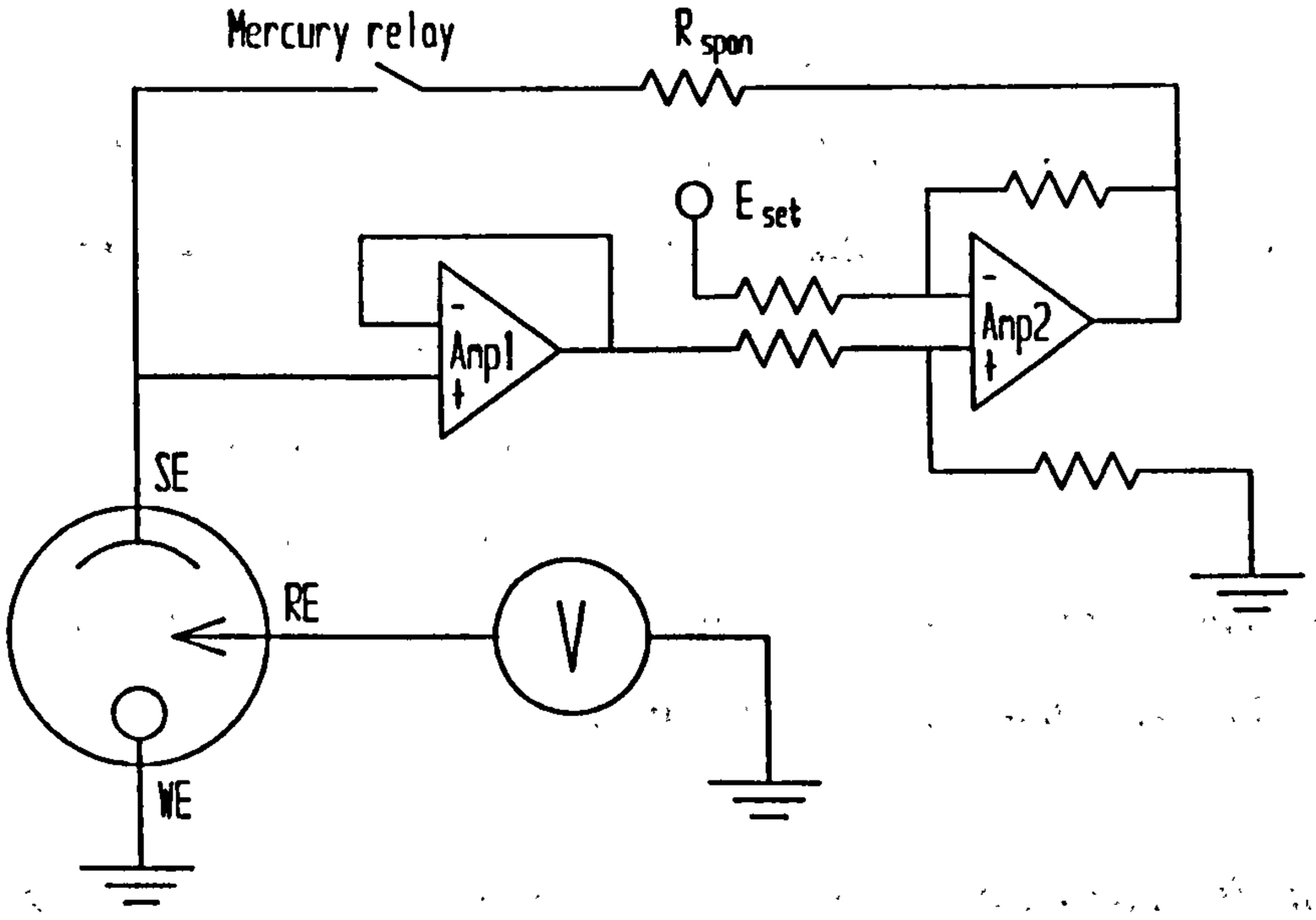

Fig. 2.7: The basic galvanostat circuit.

A galvanostat does not rely on a reference electrode and simply drives a set current through the cell. The current was set by the ADDA card which applied potential E_{set} to one arm of the resistor array connected to the differential amplifier (Amp2).

A mercury relay was added in series with the R_{span} in both circuits so that current interruptions could be performed. Both circuits also had a range of 8 values

that could be selected for R_{span} so that a wide range of current readings could be taken (3.65μA full scale to 1.41A full scale).

2.3.2 Auxiliary circuitry

Four voltmeters were included to measure the potentials of the various electrodes on the amperometric sensor and the potentiostatic sensor. The primary voltmeter, which was usually attached to the reference electrode, had 4 switchable ranges that closely matched the ranges that could be set by the potentiostat. It was built to have a fast response to accurately amplify the voltage change after current interruptions (the op amp had a slew rate of 30V/μs). Two more voltmeters were built with full scale readings of 1.2 and 2.2V. All these voltmeters had input impedances greater than $10^{12}\Omega$ as recommended for accurate measurement of electrode voltage on zirconia by Anthony et al (1984). They also recommended a resolution of 1 - 10μV, but only the most sensitive range on the primary voltmeter came close to this (12.3μV). However, they, and others including Verkerk et al (1983b), noticed an unexplained offset of up to 1mV on some potentiometric sensors so such great precision was hard to justify.

A fourth voltmeter was permanently connected to read the secondary electrode voltage. It was connected directly to the ADDA card and only had a resolution of 1mV.

An amplifier was also required to amplify the signal from the R type (Pt/Pt13%Rh) thermocouple. Circuit details of all the above are in Appendix 2.

2.3.3 The digital interface

A digital (on/off) interface was required to switch the relays that controlled the furnace and the current and voltage ranges. It was also needed to select the gas

flow control valve to which a flow setting was being sent. A total of ten digital outputs were needed.

It was decided to use the parallel printer port, supplied as standard with the computer, as the digital interface to save on the cost of the ADDA interface card. This has the disadvantage that the computer cannot be used for printing unless a second parallel port is fitted. All connections to the parallel port were buffered with a resistor and an op amp as added security against voltage spikes damaging the control chip on the computer's mother board (Fig. A2.7 in Appendix 2).

2.3.4 Analogue input signals

An ADDA conversion card with 14 bit resolution and capable of 10 000 readings per second was connected to the expansion bus of the computer. It was found that the ADDA card did not give a totally linear response. The response was most linear (within 2mV) when the full scale voltage was adjusted to 9.5V. It was therefore decided to build all the rest of the apparatus to use this value. It was also found that if one of the inputs to the card was at a voltage greater than about 11V it caused the card to misread all inputs. Zener diode limiters were therefore included in the electronic circuits so that all inputs to the ADDA card stayed below this value.

2.3.5 Analogue output signals

Analogue outputs were required to set the voltage on the potentiostat, the current on the galvanostat and the flow settings for the four gas flow control valves. Six outputs were therefore needed but only two were available. The interface circuitry was therefore designed so that the potentiostat and galvanostat could share the output from the second card and the gas valves shared the output from the first card.

2.3.6 System overview

Fig 2.8 is an overview of the complete computer interface to all the external equipment. The full circuit description is in Appendix 2. An analogue to digital and digital to analogue (ADDA) conversion card was used to receive and send all the analogue signals. All digital signals were sent by the centronics printer port. Fig. 2.9 is a photograph of the system.

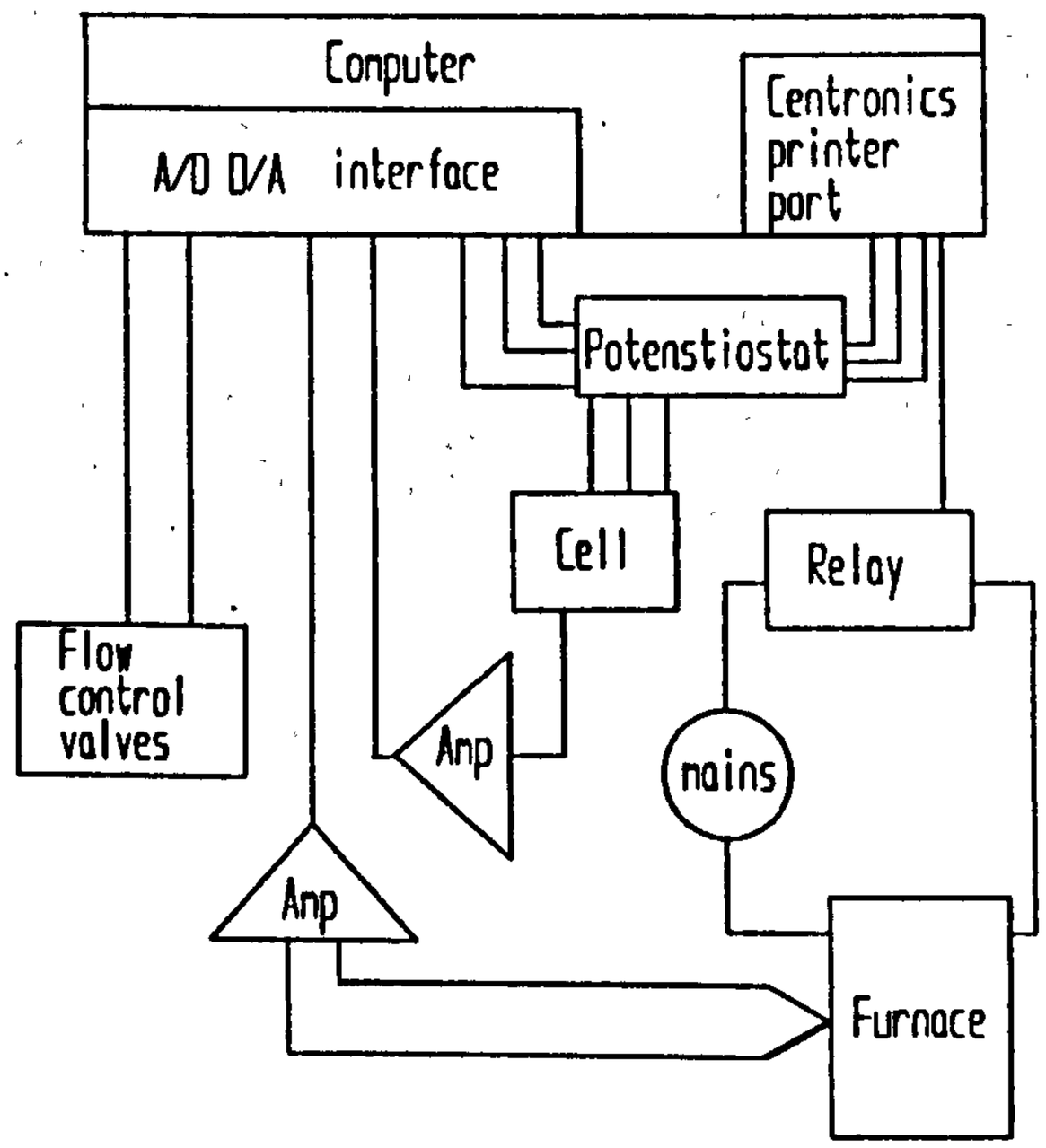

Fig. 2.8: Over-view of the computer interface system.

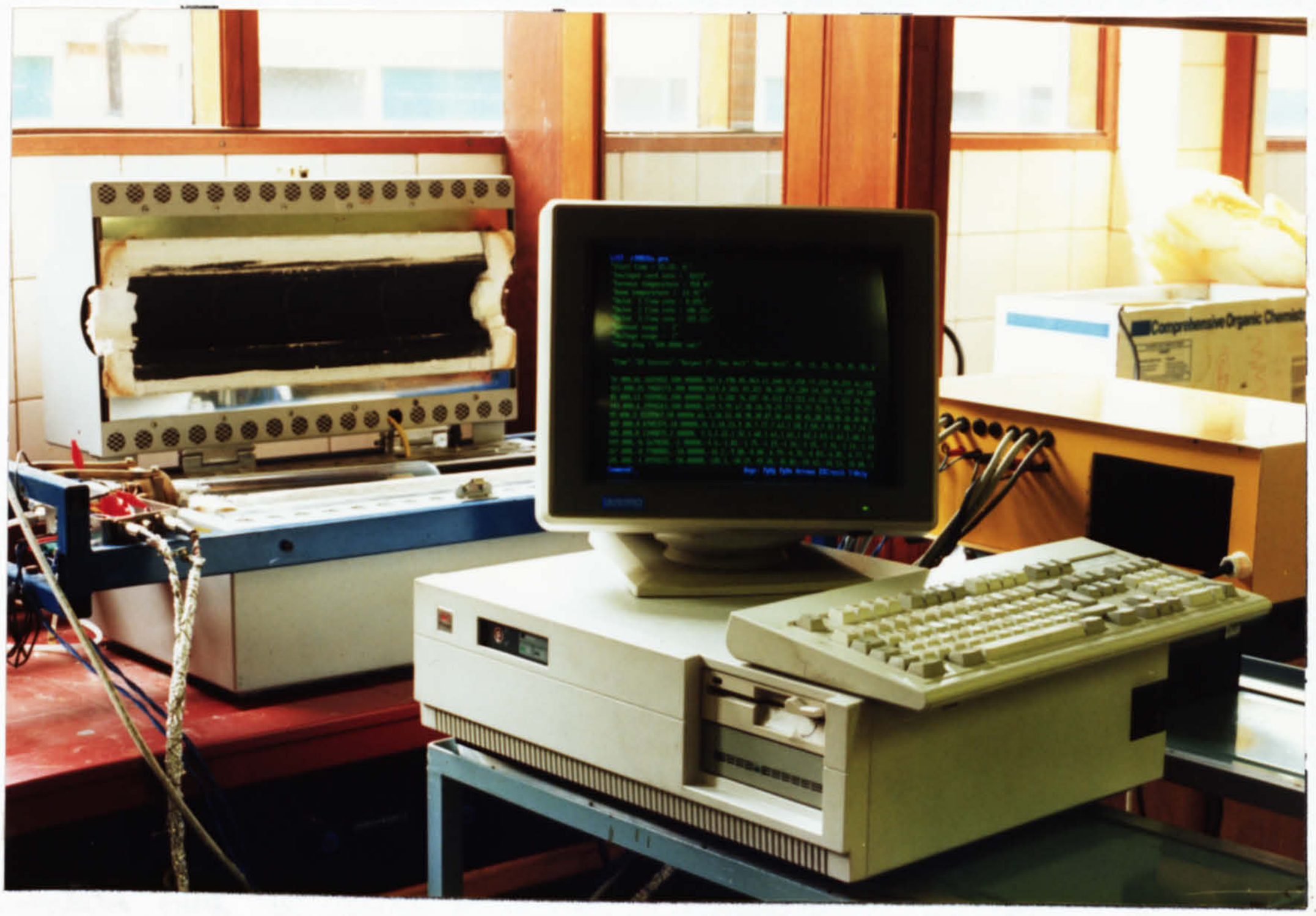

Fig. 2.9: Photograph showing the computer with a screen full of results, the furnace, and the main power supply with the potentiostat/galvanostat unit in the yellow box behind the computer.

2.3.7 Calibration procedure

The calibration of the potentiostat and other interface circuits was performed in conjunction with the calibration and testing of the ADDA card and the controlling computer program.

Most calibrations and tests were performed by connecting accurately known resistances in place of the cells or sensors. Single resistors accurate to within 0.1%, and resistance boxes were used. The voltages were measured with a number of digital voltmeters (some displaying 6 significant figures) and the results compared. Each voltage and current range was calibrated and tested at several points within its measurement range. After these tests there was a high degree of confidence that all

current readings were accurate to within 0.5% or 0.02μA. The primary voltmeter was also accurate to within 0.5% or 0.02mV. A.C. interference (mostly 50Hz from the mains) was the major source of error. A sampling oscilloscope was used to measure it and the results were used to judge the effectiveness of steps taken to reduce it. Another important residual source of error was the computer feeding an A.C. signal directly into the ADDA card. The oscilloscope was also used to calibrate the sampling speed of the ADDA card and to confirm that the current interruption procedure was operating correctly.

2.4) The computer control program

By far the most critical and complex part of the whole computer-controlled apparatus was the software. The program had to handle the details of operating the ADDA card, the timing of various operations, the performance of various electrochemical experiments, and then the collection and presentation of the results. A number of options were investigated before construction of the computer controlled potentiostat was begun.

The first task was to decide on what computer to use. There were a number of BBC's and Apple computers available. It was decided that neither was powerful enough to run efficient software for collecting and analyzing the data. Also ADDA interface cards for these computers were more difficult to obtain than cards for PC compatible computers. To protect the system from obsolescence, a 80386DX based IBM PC compatible operating at 20MHz with a colour VGA screen was chosen.

More options had to be considered before development could begin.

a) Commercial or self-built potentiostat.

There were a few computer-controlled potentiostats available complete with software but they had two major problems. The first was a very high cost at about £10 000. The second was that the software and the interface would have been difficult to adapt to do all that the present system can do.

b) Development software:

Several software options were available for developing the control program. Asyst is a powerful package for writing computer control software, but the price was high. There were a few lower budget packages available but they did not have the required versatility.

General purpose programming languages such as C, C++, Pascal, Forth or Assembler offered the greatest versatility and were also the least expensive. The main disadvantage was that the effort required to develop the software was much greater.

Partly as an educational exercise, a self-built potentiostat with control software written in Turbo Pascal was chosen.

2.4.1 Furnace temperature control

This and subsequent subsections of section 2.4 are an outline of the control program and how it was used. It was called CONTRL. The details of the code for CONTRL came to almost 4000 lines so they have not been included in this report. A more detailed explanation of the program structure is included in Appendix 3 and the operating instructions can be found in Appendix 4.

CONTRL enabled the user to set the furnace heating rate and the final desired temperature. It also displayed a plot of the furnace temperature over the previous 20 minutes so that possible problems with the furnace could be isolated. The plot demonstrated that the program could control the furnace temperature without overshoot or oscillation.

Anthony et al (1984) warn that zirconia tubes may crack if they are cooled at more than 150°C/hour. This seems a bit extreme; but care is required. Heating and cooling rates were normally set to 600°C/hour although rates of twice this were allowed over small temperature spans.

2.4.2 Gas flow control

During a series of experiments the usual procedure was to set a gas flow rate on all the gas flow control valves in use and then to heat the furnace to the highest temperature to be used. The gas composition in the apparatus therefore had time to come to steady state while the furnace heated up. The high temperature also aided the desorption of any gases used in previous experiments. After the readings were taken at the highest temperature, the temperature was decreased to the next level without changing the gas flow rate. After finishing the readings for a given gas flow rate at all temperature levels to be tested, the flow was changed to the next setting and the furnace again heated to the highest temperature.

2.4.3 Cyclic voltammetry

A cyclic voltammogram (CV) was performed by applying a triangular voltage waveform to a cell and recording the current that flowed. Because of the digitized signal the potentiostat had to approximate the triangular waveform with a staircase waveform. With 14 bit resolution, the approximation was accurate. An additional precaution was taken to ensure accurate simulation of pure CV by paying attention to the timing of the current measurements relative to the steps in the voltage. Middleton (1990) found that the results were accurate if the current was measured after $0.5t_{step}$ where t_{step} was the time between voltage steps. CONTRL measured the current just before stepping the voltage.

A voltammogram was usually started by making the working electrode anodic first. This was done to oxidise any reduced species remaining on the electrode from previous experiments. CV was often used to perform a quick test on a new cell or sensor to see how well it was operating. On the basis of this it was either modified or else tested at length while unattended with one of the procedures described below.

CV mode was also used to test the response rate of cells and sensors. If the current during the return sweep closely followed that measured during the original sweep the CV was assumed to be slow enough to measure equilibrium current-voltage characteristics. If the electrolyte resistance was known the overvoltage on the working electrode could also be determined from these results. The electrode resistances were sometimes measured in this way by only sweeping between about +20mV and -20mV. Where possible the electrode resistance was calculated using linear regression on the overvoltage results between -2 and +2mV. However, noise was often a factor at such low voltages and it was sometimes considered more accurate to use values between ±5mV or greater.

2.4.4 Current interruption

Interruption of the current flowing through the cell or sensor was simply performed by setting the mercury relay to open. The relay had a delay of about 2ms so it was not possible for the computer to know the exact time at which it opened. The ADDA card was therefore set to read the primary voltmeter at the maximum rate after the relay was set to open. It was possible to judge when the relay opened because the voltage readings were steady while the relay was closed and changed rapidly as soon as the relay opened.

The operation of this circuit was carefully checked with the oscilloscope. It was found that the ADDA card took readings every 0.1ms and that the relay produced a clean break in the current.

2.4.5 Steady state readings

In this mode (called SS mode) a fixed voltage or current was set to flow through the cell until a steady reading of the resultant current or voltage respectively was obtained.

The reading could be monitored on the screen and the test ended by typing 'b'. This caused a current interruption and all the relevant results could be saved to the hard disk. However, the ability to perform these tests unattended was desired.

A routine was therefore written which tested the value that needed to come to a steady state. When this value did not change by more than 0.1% during a preset time scale (typically 30 to 200 seconds), a current interruption was performed, the results were recorded and then the new experimental values were set; all automatically. Up to 30 consecutive SS tests could be pre-set and performed at a given temperature and gas composition.

Problems were encountered with this method for determining when steady state had been reached because of the large range of time-scales required. A number of checks were therefore added to provide more control. The ability to set minimum and maximum time for each run was added. Difficulty was also caused by oscillations which disguised the arrival of steady state. A test was added to the program that detected oscillations and ended the run after 5 changes in direction.

As with CV mode, anodic readings were generally made first to reduce oxidized species on the working electrode. A typical sequence would be +50, +20 and +10mV to oxidize adsorbed species. This would be followed by +5, +2, +1, -1, -2, and -5mV to enable the electrode resistance to be determined. Up to 22 increasingly cathodic potentials would then be applied to obtain the full current-voltage curve.

2.4.6 Macro mode for continuous operation

Despite the high degree of automation already described, an even greater level was desired. After extensive tests to confirm that all aspects of CONTRL and the electronic system performed well, a macro facility was added to it. The macro facility enabled any number of tests to be pre-set and run unattended. Any tests that CONTRL had been written to perform could be run in any combination.

2.4.7 Saving the results

If the program was set to do so, it wrote the results to a file on the hard disk. The file was written as a coma separated values (CSV) file so that it could be easily imported into a spreadsheet program for further processing. The processing of the results is described in chapter 3.

Chapter 3

Results of experiments on single electrodes

Our doubts are traitors and make us lose the good

we oft might win by fearing to attempt.

William Shakespeare

3.1) Interpreting the current interruption results

3.1.1 Separating the overvoltages and the IR drop

The simplest solid electrolyte cell consists of a working (WE) and a secondary (SE) or counter electrode on either side of a layer of electrolyte. Many processes occur when a voltage is applied across this cell. The current that flows creates an overvoltage (η) on each of the two electrodes and the resistance of the electrolyte causes an IR drop or potential difference (E_z) across the electrolyte. Some method is needed to separate these three main components of the total potential difference (E_{WS}). By adding a reference electrode (RE) it is possible to isolate partially the overvoltage on the working electrode (η_W). The potential on the RE lies somewhere between the potential of the WE and the SE. The potential difference between the working and reference electrodes (E_{WR}) therefore includes a portion of the total IR drop called the uncompensated IR drop (E_u). Therefore:

$$E_{WR} = \eta_W + E_u, \tag{3.1a}$$

while

$$E_{WS} = \eta_W + E_z + \eta_S \tag{3.1b}$$

where η_S is the overvoltage on the secondary electrode. (Only conditions where there was negligible Nernst voltage are considered in this section). The ratio between E_u and E_z depends upon the geometry of the cell (Pizzini et al (1974) and van Heuveln et al (1993)) but the ratio is difficult to predict (Van Herle and Thampi

(1993)). Therefore, while E_u can be estimated from an indepedent measurement of the electrolyte resistance it is more accurate to measure E_u directly by frequency response analysis or current-interruption. Both methods require analysis of the results to distinguish between the contribution from E_u and the overvoltage on the working electrode (η_W).

As explained in section 1.2.6 the electrolyte and the electrode can be approximately modelled by parallel resistor capacitor pairs. When the current flowing through such a pair is interrupted the charge stored in the capacitor discharges through the resistor. The voltage E(t) at time t across this RC network is simply:

$$E(t) = E(0) \exp(-t/RC) \qquad (3.2)$$

where E(0) is the voltage across the network at time (t) = 0 (ie. the time when the interruption occurred). If ln[E(t)] is plotted against time the result is a straight line with intercept ln[E(0)] and slope of -1/RC.

Current-interruption is useful for separating η_W and E_u because the potential difference across the electrolyte (E_u) decays significantly faster than that across the electrode (η_W). Bauerle (1969) showed this using frequency response analysis (FRA) and subsequent workers have confirmed his conclusions using FRA and current-interruption.

Various voltages $E_{WR}(0)$ were applied to a cell (a 0.7mm thick disc of 6Y-YSZ (9.8wt% yttria) with two sputtered and screen printed platinum electrodes and a painted reference electrode) for between 2 and 15 minutes before the current was interrupted. Fig. 3.1 shows the results for current-interruptions performed at 800°C on this cell. All runs were performed with all three electrodes exposed to the same gas composed of 0.07%O_2 in N_2. The sign of the voltages from the cathodic runs have been reversed for the log plot. The voltage was sampled every 0.1ms so it was assumed that the first reading where $E_{WR}(t)$ was appreciably below $E_{WR}(0)$ was taken 0.05ms after the mercury relay actually opened.

Examining data from the same experiment but over a longer time period in Fig. 3.2 shows that in all cases there was a purely exponential relaxation (or decay) from times between 1 to 15ms, as confirmed by the line drawn through the data points. More rapid relaxation of E_{WR} was evident at $t < 0.5$ms. A line was drawn

through the data points to help illustrate this. During the the first 0.05ms there was a step change in E_{WR} which was more evident on the anodic results where the current was greater. Kleitz et al (1981a) and Robertson and Michaels (1991) found that there was a fast and a slow relaxation process on platinum electrodes under certain conditions. Robertson and Michaels proposed that the faster relaxation was due to discharge of the double layer and that the slower one was due to the electroactive species adsorbed on the electrode. Although this theory has not been conclusively proven it was used in this section to explain the three relaxation processes observed in Figs 3.1 to 3.4. The fast relaxation (before 0.05ms) was mainly due to E_u, the next (between 0.05 and 0.5ms) due to the double layer and the last (>0.5ms) to diffusion of adsorbed species.

Fig. 3.3 and Fig. 3.4 represent the results for similar experiments to the above except that the temperatures were at the lower values of 700 and 600°C respectively. By 600°C the electrode relaxation was generally slower than at 800°C as expected, but the relaxation rate showed a strong dependence upon the current before interruption if the current was anodic. Relaxation rates from cathodic currents were more consistent. In Fig. 3.4, after interrupting a current of +0.80mA E_{WR} decreased for 2ms and then increased in magnitude. This is characteristic of an inductive effect which has been widely observed before. Schouler and Kleitz (1987) suggested that it is caused by increased p-type conductivity in the surface layer of the zirconia. van Hassel et al (1991b) attributed the effect to a change of the charge of the adsorbed oxygen atoms.

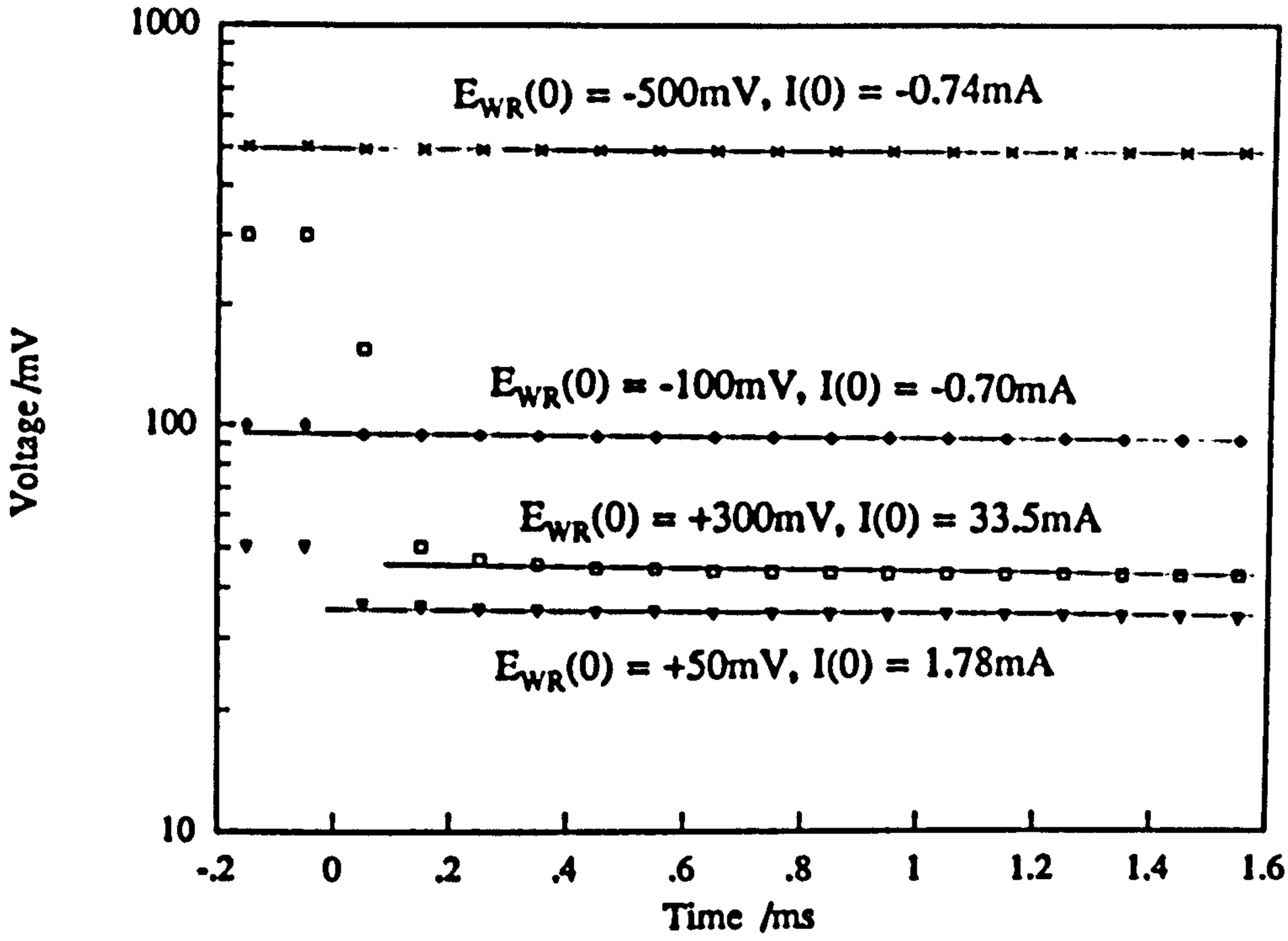

Fig. 3.1: Change of E_{WR} before and after current interruption at time zero. Pt electrodes on 6Y-YSZ at 800°C in 0.07%O_2 in N_2.

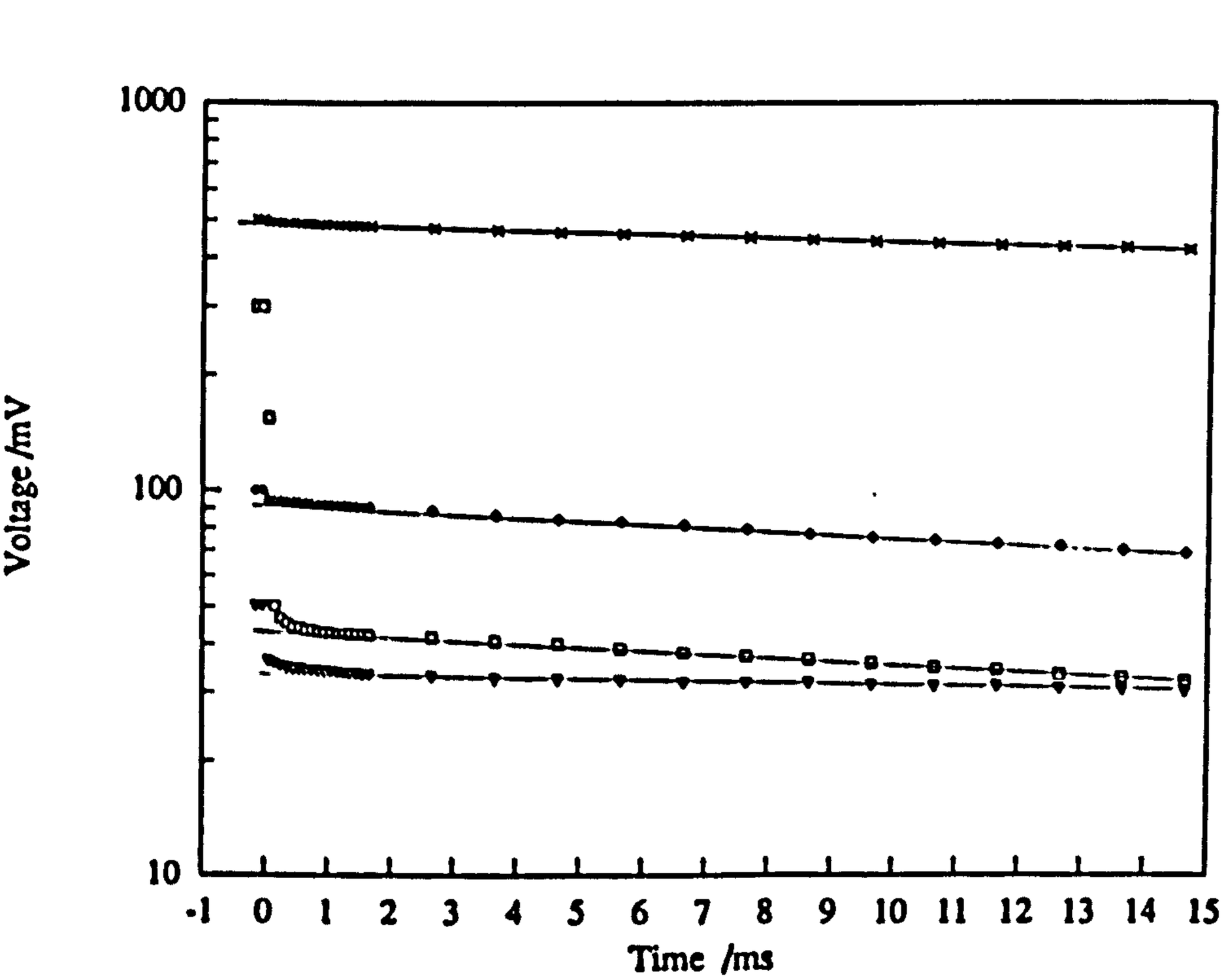

Fig. 3.2: As Fig 3.1 but over a longer time scale.

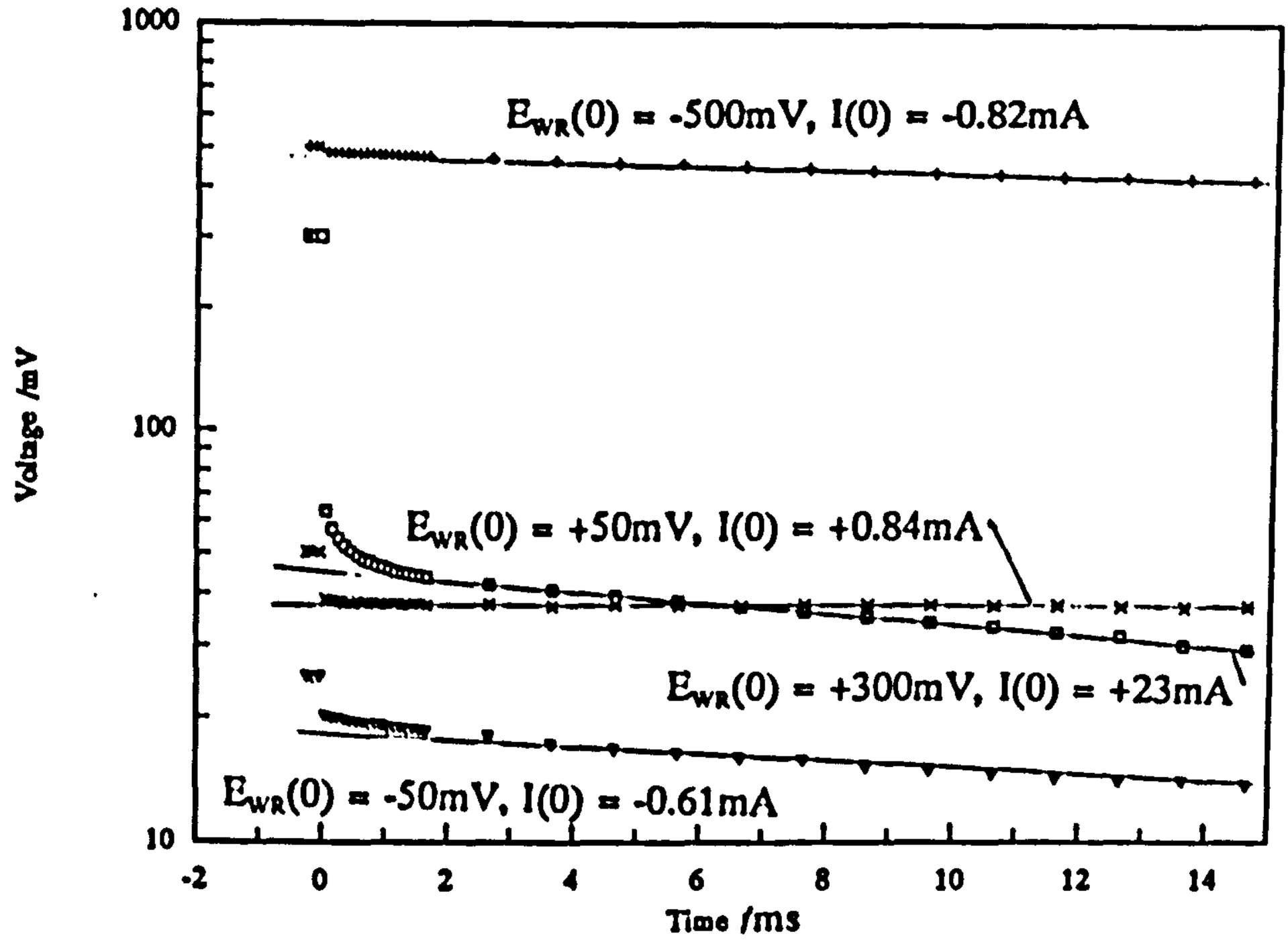

Fig. 3.3: E_{WR} as a function of time. Pt electrodes at 700°C in 0.07%O_2 in N_2.

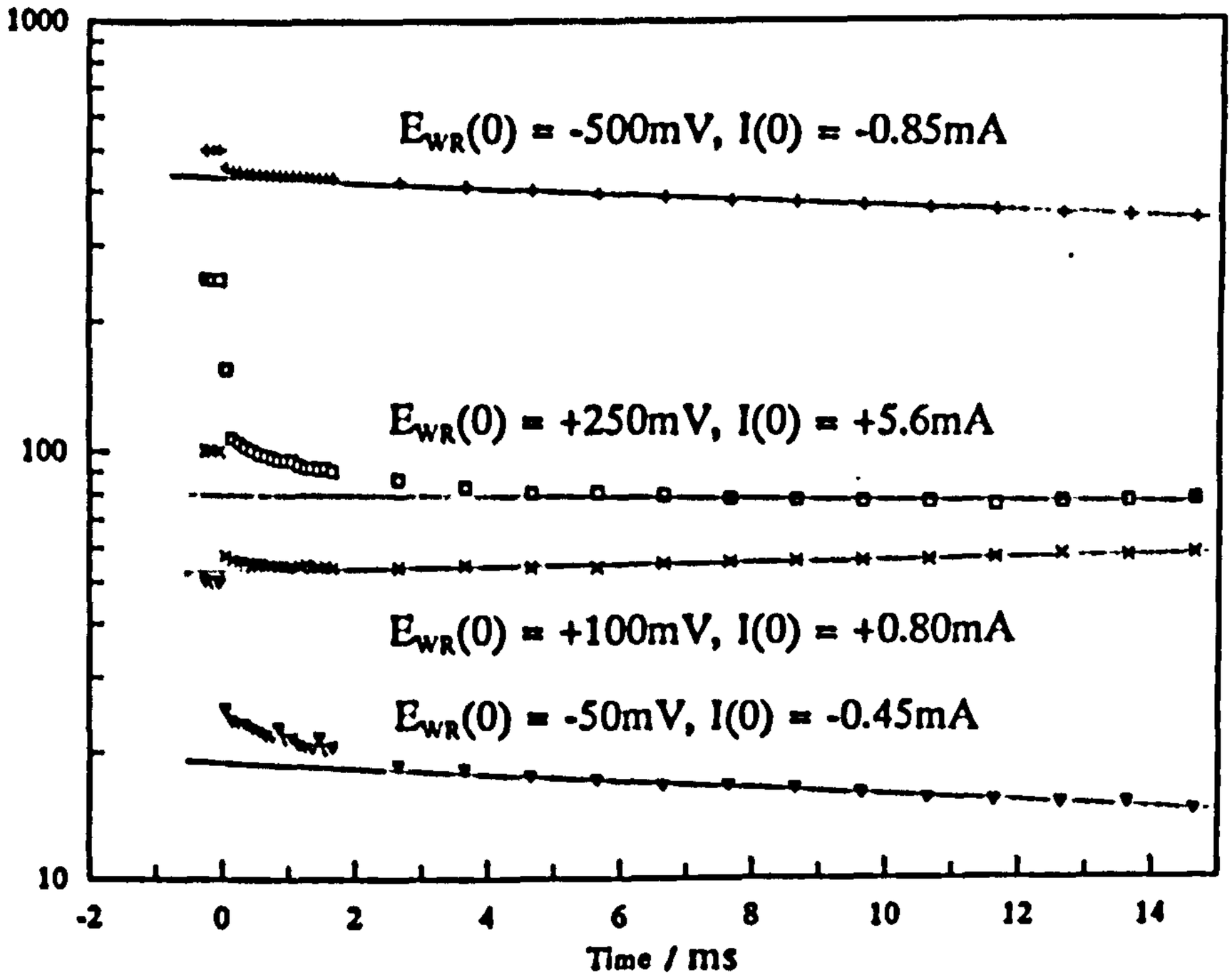

Fig. 3.4: E_{WR} as a function of time. Pt electrodes at 600°C in 0.07%O_2 in N_2.

The observed relaxation rates were compared with literature results. The equivalent circuit for a zirconia cell, assumed for the analysis of the current-interruption results, is presented in Fig. 3.5.

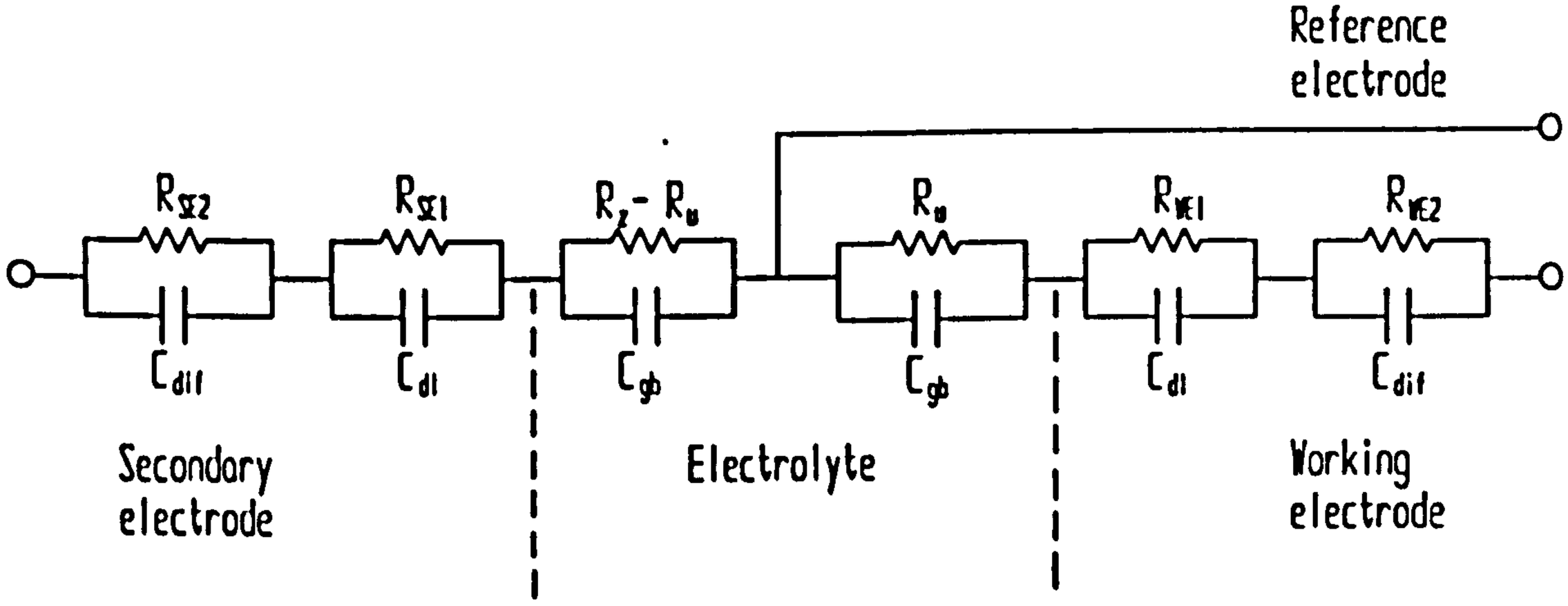

Fig. 3.5: Equivalent circuit of cell consisting of a zirconia disc with three electrodes. R_u is the uncompensated resistance ($E_u = I(0)R_u$) in parallel with the grain boundary capacitance of the zirconia associated with it: C_{gb}. R_z is the total electrolyte resistance of the cell so R_z-R_u is the part of the electrolyte resistance compensated out by the reference electrode. It is also in parallel with a grain boundary capacitance. The two capacitors C_{gb} do not have the same value but the RC products are equal: ie. $(R_z-R_u)C_{gb1} = R_uC_{gb2}$. $I(0)R_{WE1} = \eta_1$ is the potential difference across the double layer capacitance of the working electrode: C_{dl}. C_{dif} is the capacitance caused by the surface diffusion of electroactive species and R_{WE2} is the resistance associated with this diffusion: $I(0)R_{WE2} = \eta_2$ and $\eta_1 + \eta_2 = \eta_W$. R_{SE1} and R_{SE2} have corresponding meanings for the secondary electrode.

The voltage across RC pairs connected in series is the sum of the voltages across each pair. Therefore, the voltage E_{WR} at any time (t) after current-interruption follows the relation:

$$E_{WR}(t) = E_{WR}(0)\left[\frac{R_u}{R_T}\exp\left(\frac{-t}{R_u C_{gb}}\right)+\frac{R_{WE1}}{R_T}\exp\left(\frac{-t}{R_{WE1} C_{dl}}\right)+\frac{R_{WE2}}{R_T}\exp\left(\frac{-t}{R_{WE2} C_{dif}}\right)\right] \quad (3.3)$$

R_T is the total resistance between the reference and working electrodes ($R_T = R_u + R_{WE1} + R_{WE2}$) where $R_{WE1} = \eta_1/I(0)$ and $R_{WE2} = \eta_2/I(0)$ are the two components of the total overvoltage η_W. The voltage across the RC pairs associated with the SE can be ignored when considering E_{WR}.

Fig. 3.6 shows how eqn(3.3) was able to model the experimental results. The six unknown R and C values were determined by testing different values until the total of the absolute errors of the predicted voltages was minimized. The following was used to convert the RC values to relaxation frequencies for comparison with the literature data.

$$1/RC = 2\pi \times \text{relaxation frequency.} \quad (3.4)$$

The relaxation frequencies used of 31 600, 500 and 5Hz at 700°C and 10 000, 126 and 1.3Hz at 600°C agreed with the data from Kleitz et al (1981a) (their diagram was reproduced in Fig. 1.9).

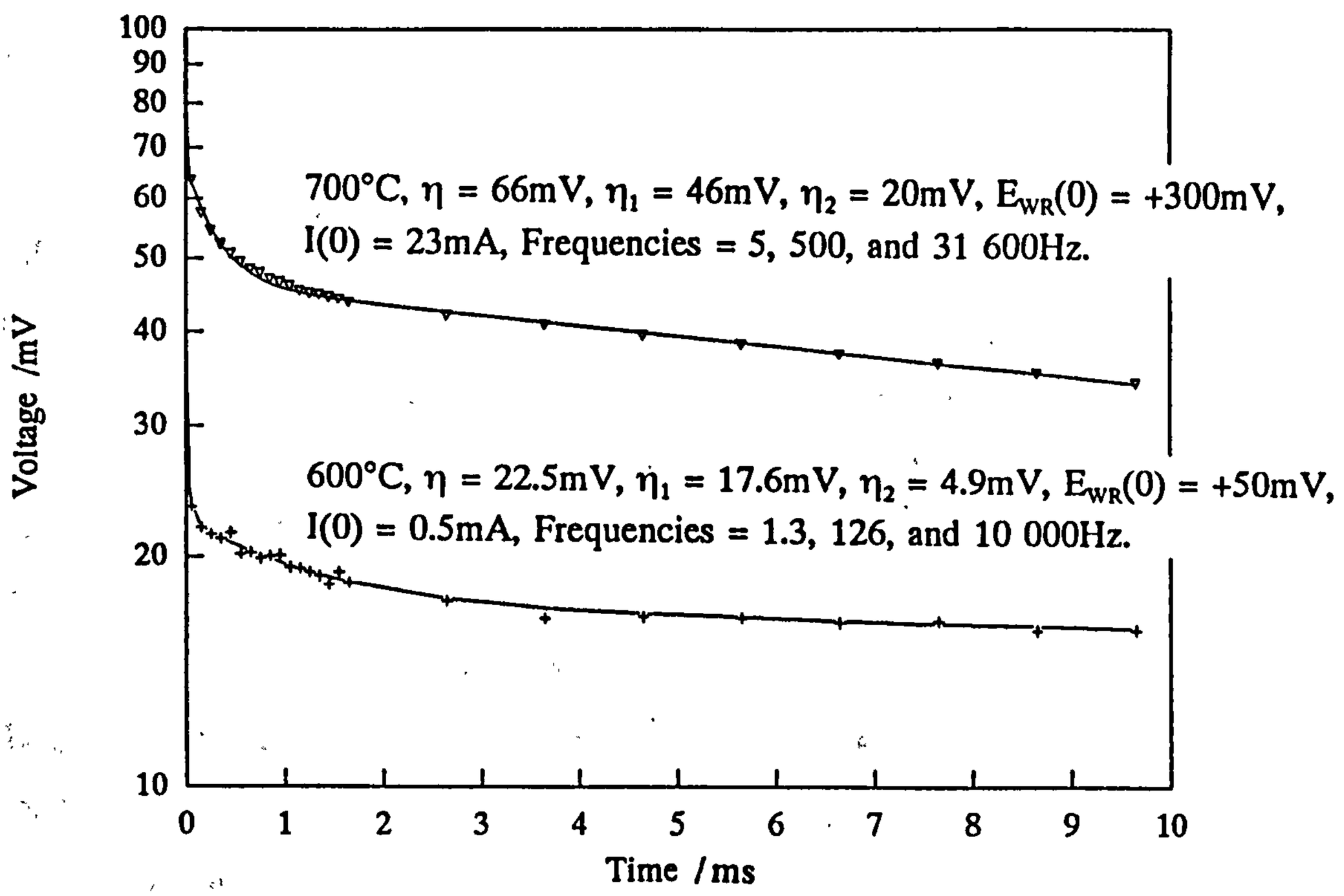

Fig. 3.6: E_{WR} as a function of time. ——, theoretical curves using eqn(3.3) and overvoltages and relaxation frequencies shown on figure. I(0) is the current flowing immediately before current-interruption.

Finding 6 unknown values using the above method was time consuming. If the available apparatus had been able to read the voltages faster than every 0.1ms a method based on the above simulation would have produced accurate estimates of the overvoltages. However, considering the speed limitations of the equipment available, a simpler and quicker method for estimating overvoltages was justified. Using the above simulation and experimental results over a range of temperatures, the time after the interruption at which $E_{WR}(t) = \eta_W$ was calculated. All subsequent overvoltage results in this work were derived by assuming that E_{WR} was equal to η_W at the time shown in Table 3.1.

Table 3.1.

Estimates of the time at which $E_{WR}(t) = \eta_W$
for various commonly used temperatures on Pt electrodes on YSZ.

Temperature /°C	>700	600	550	500	450	400	350
Time /ms	0.025	0.1	0.2	0.3	0.9	2	5

The response rates of electrodes made from gold and silver were probably different to those for platinum. However, there was insufficient data from experiments or the literature to estimate these response rates so Table 3.1 was still used to derive the relative contributions of η_W and E_u to the $E_{WR}(t)$ readings. Since the relaxation of the slowest process in the electrolyte was about 2 orders of magnitude faster than the fastest on the electrode (Pt) the error in the above method probably never exceeded 5% of $E_{WR}(0)$ at temperatures below 650°C.

If the potential between the SE and the WE (E_{WS}) was monitored instead of E_{WR} then the above procedure separated the sum of the two overvoltages and the total potential difference across the electrolyte (E_z). The conductivity of the electrolyte could then be determined from:

$$\sigma_i = I(0)\, L / E_z\, A_e \qquad (3.5)$$

where L is the electrolyte thickness and A_e is the electrode area.

3.1.2 Lead wire resistance

Because of the design of the circuit, the measured uncompensated resistance included the resistance of the lead connecting the working electrode to the zero voltage reference point. Most of this resistance came from the platinum wire running to the middle of the furnace. This lead resistance therefore depended upon the furnace temperature. To measure it, all the lead wires were shorted together where the sensor would normally be located. The furnace was then set to various temperatures before using the potentiostat to apply small voltages across the working electrode lead and to measure the resultant current.

The result was:

$$R_{lead} = 1.50 + 0.0025T\ \Omega \quad (\pm 0.05\ \Omega)$$

T is the furnace temperature [°C]. The result represents a thermal coefficient of 0.00167 which is lower than the coefficient for platinum of 0.00393 (Weast (1988)) because almost half the wire was at room temperature and only a short length was close to the measured temperature.

3.2) Conductivity of the zirconia discs

η_W was determined as explained above and E_u was determined using eqn(3.1a): $E_u = E_{WR} - \eta_W$. Alternatively if no RE was used then: $E_z = E_{WS} - \eta_w - \eta_S$. The sum $\eta_W + \eta_S$ was determined in the same way as η_W.

Three factors limited the accuracy of the conductivity results.

a) Sampling speed

The limited speed of the ADDA card meant that the contributions of E_u and η_W to E_{WR} could not be accurately distinguished.

b) Uneven current distribution

It was shown by Pizzini et al (1974) that if the electrodes did not cover the whole area of the disc then the conductivity results (based on electrode area) would be high. This is because the equipotential planes are not parallel to the electrodes when the electrodes only cover part of the disc.

c) Constriction resistance

Because of the limited width of the three phase boundary, the current flowing through the zirconia near the electrodes is concentrated towards the TPB. This uneven distribution of current increases the measured resistance.

Factors b) and c) had counteracting affects on the results but constriction resistance was probably dominant particularly with gold electrodes with their short TPB. Above 700°C the slow sampling probably caused most experimental error. The overall affect of the above was that electrolyte conductivity results tended to be too low.

Because $E_{WR} = \eta_W + E_u$ and η_W was usually much larger than E_u any errors in measuring E_{WR} and separating the two components of it were magnified in the E_u determination. Therefore, only measurements where η_W was relatively low were used to determine electrolyte conductivity.

The difficulties just described were not a problem in most of this work because the values of η_W and E_{WR} were usually of greater interest than E_u.

3.2.1 Relative size of uncompensated resistance

The primary voltmeter of the potentiostat could be attached to the reference or the secondary electrode to measure $E_{WR}(t)$ or $E_{WS}(t)$ respectively. The former was the usual arrangement since the overvoltage on the working electrode was the value of most interest. However, the latter was also used and a test was performed to compare the results.

The experiment was done on a 0.7mm thick 6Y-YSZ disc with sputtered and screen printed platinum electrodes 5.0mm in diameter and a small painted reference electrode next to one of the 5.0mm electrodes. By measuring $E_{WS}(t)$ at 600°C in air R_z was found to be 187Ω ($0.195\Omega^{-1}m^{-1}$). The voltmeter was then moved from the SE to the RE which was on the same side of the disc as the WE. $E_{WR}(t)$ was measured and the uncompensated IR drop (E_u) was determined. The uncompensated resistance (R_u) of the electrolyte for this cell arrangement is given by $R_u = E_u / I(0)$ and was found to be 133Ω. The lead connections were then changed by swopping the

electrodes connected to the WE and SE of the potentiostat. The WE was then on the opposite side of the disc to the RE. R_u for this cell arrangement was found to be 53Ω. The sum of the two R_u readings was 186Ω which was very close to the first measurement of R_z considering the estimated experimental uncertainty of 5Ω for each reading.

The result showing R_u to be 28% of R_z when the WE and RE were on opposite sides of the disc and 72% when they were close together on the same side is interesting. It shows that the common assumption of R_u being $0.5R_z$ (eg. Ong et al (1981)) is not necessarily correct. Recent work by van Heuveln et al (1993) and Van Herle and Thampi (1993) have shown that the relative size and position of the SE and WE are important in determining the ratio between R_u and R_z.

3.2.2 Low current results

Fig 3.7 shows the conductivity results for 3 zirconia discs measured without a reference electrode. The 3Y-YSZ (5.0wt% yttria) was obtained from ICI in the green state as plasticized sheet. The first 3Y-YSZ disc was sintered before painting on a calcined (coarse) 3Y-YSZ paste and re-resintering. This was done to roughen the surface and improve the poor adherence of the gold electrodes. The second 3Y-YSZ disc had the 3Y-YSZ paste painted on in the green state before co-sintering. Gold electrodes were then painted on the roughened surfaces in both cases. The 6Y-YSZ disc had platinum electrodes prepared by the usual method of sputtering followed by screen printing. The best fit to the data was found by linear regression and compared, in Fig. 3.8, with reported values.

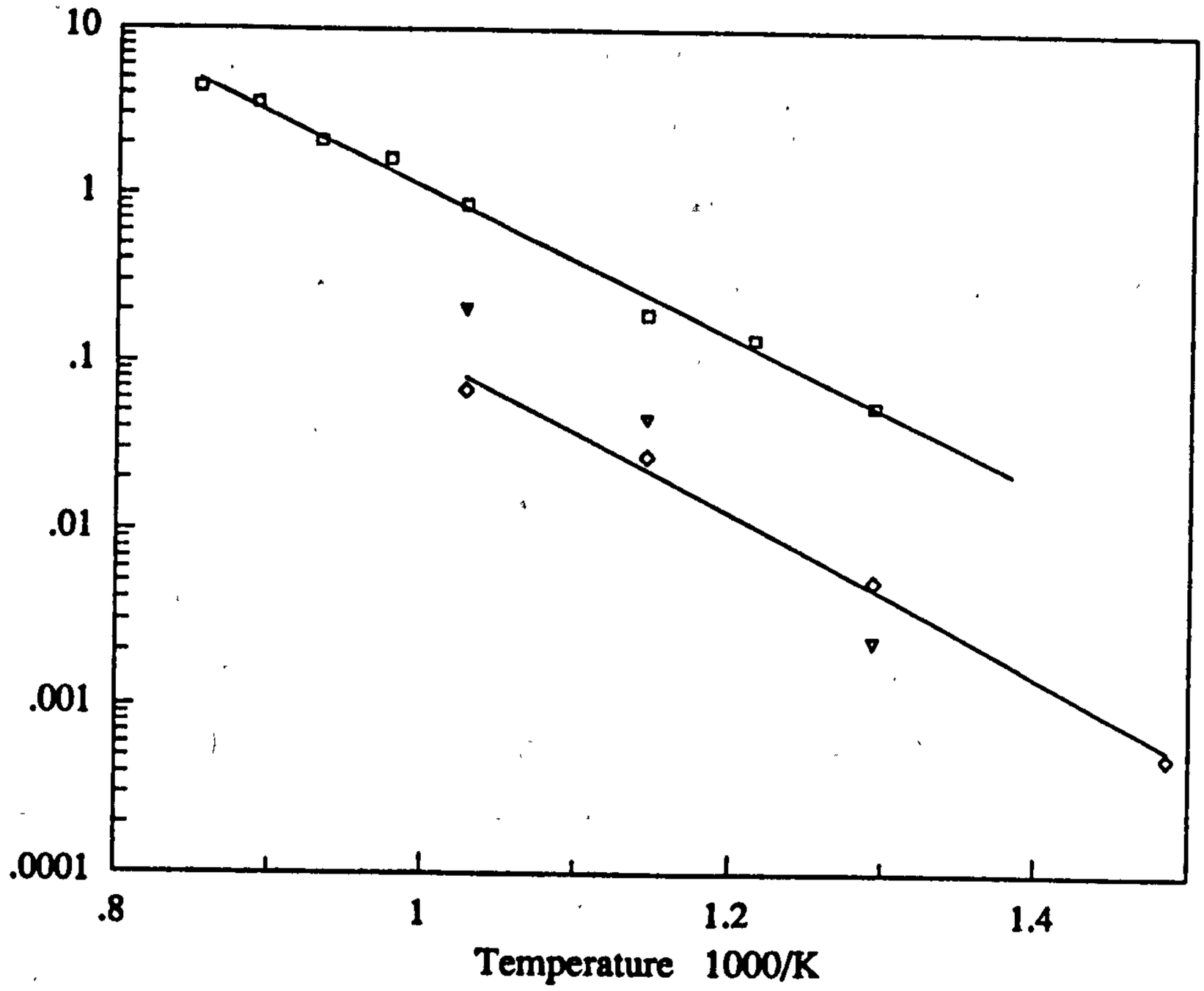

Fig. 3.7: Experimental results for the conductivity of three zirconia samples. □, 6Y-YSZ; ◇, pre-sintered 3Y-YSZ disc; ▽, co-sintered 3Y-YSZ disc.

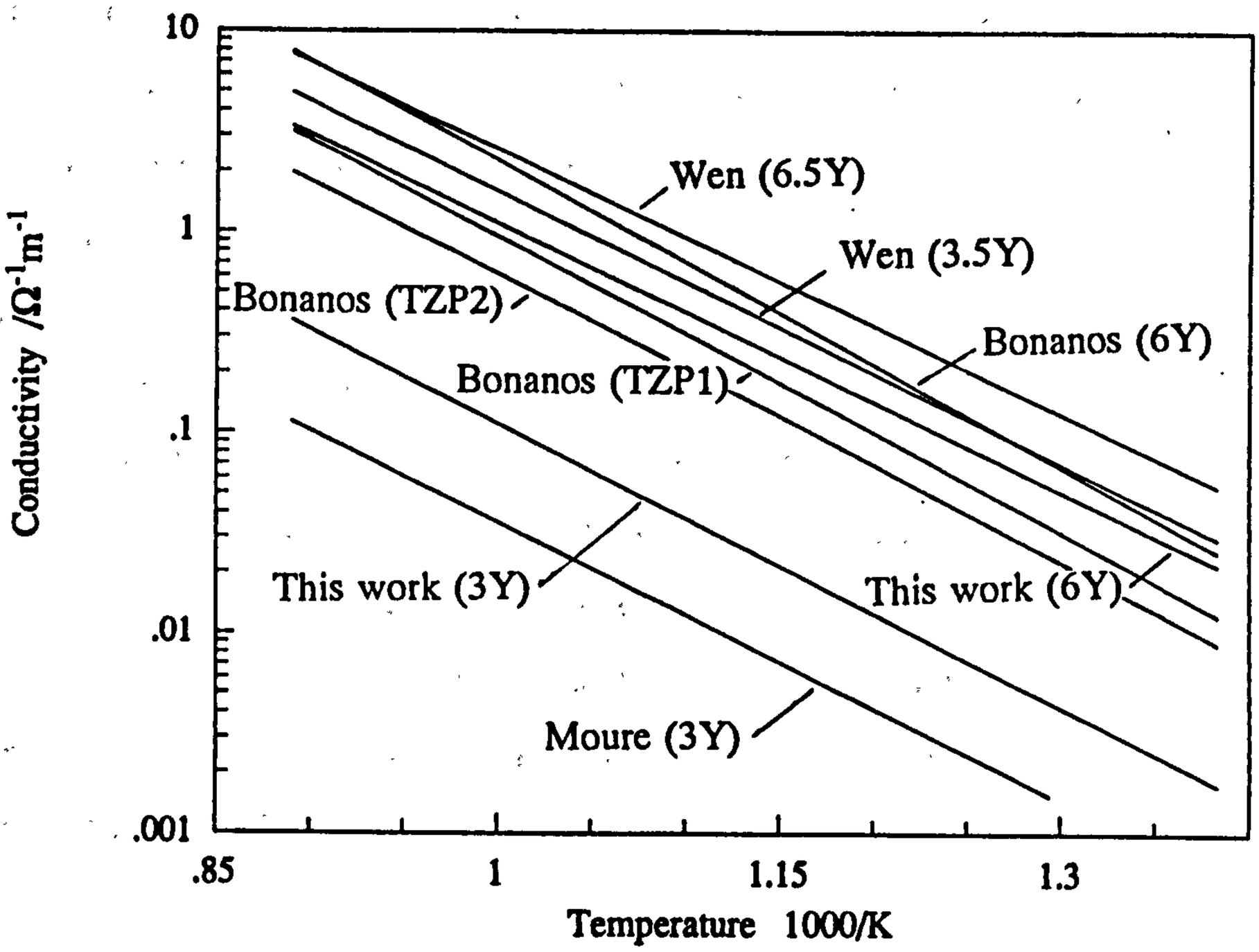

Fig. 3.8: Comparison of conductivity results of YSZ with data from Moure et al (1985), Bonanos et al (1984), and Wen et al (1988). Figures are mole% Y_2O_3.

The wide variation in conductivity results from the literature has already been discussed in chapter 1. The experimental results in this work are lower than the literature results particularly the 3Y-YSZ results; except compared to the results from Moure et al. Badwal (1990) tested the conductivity of 3Y-YSZ from the same source (ICI) and after sintering at < 1400°C found the conductivity at 350°C to be $1.6\times10^{-4}(\Omega m)^{-1}$. Extrapolating the experimental results from this work produced the same result. Badwal found that after reheating to 1500°C and quenching in air the conductivity increased to $8.3\times10^{-3}(\Omega m)^{-1}$. This clearly illustrates the importance of rapid cooling after sintering for some TZPs. El Barhmi et al (1988b) also found that rapid cooling after sintering improved the conductivity and that samples quenched to below 400°C were better than those quenched to 500°C. However, they found that the advantages of this harsh quenching to low temperatures were largely lost if the zirconia was heated above 760°C.

Moure et al (1985) used 2 types of gold electrode and their electrolyte conductivity results depended on the type of electrode used. Their results, used in Fig. 3.8, were obtained with sputtered gold electrodes, but they found that adding a thin gold foil gave them even lower conductivity results. This suggests that their results for the electrolyte included a contribution from the electrodes (the example complex impedance diagram they gave did not show a semicircle due to the gold electrode). Also the small TPB on the gold electrodes (particularly the foil) may have caused a large constriction resistance. Finally, they sintered their ceramic at the relatively high temperature of 1700°C.

While only 3 series of tests were performed where the voltage $E_{WS}(t)$ was monitored after current-interruption (no RE used), many series were performed where $E_{WR}(t)$ was measured. Fig. 3.9 shows some of the results based on the assumption that $R_u = 0.28R_z$. Although it cannot be certain that the factor of 0.28 was appropriate for the cells concerned, the results were generally higher than those reported in Fig. 3.7. They also showed less deviation from a straight line.

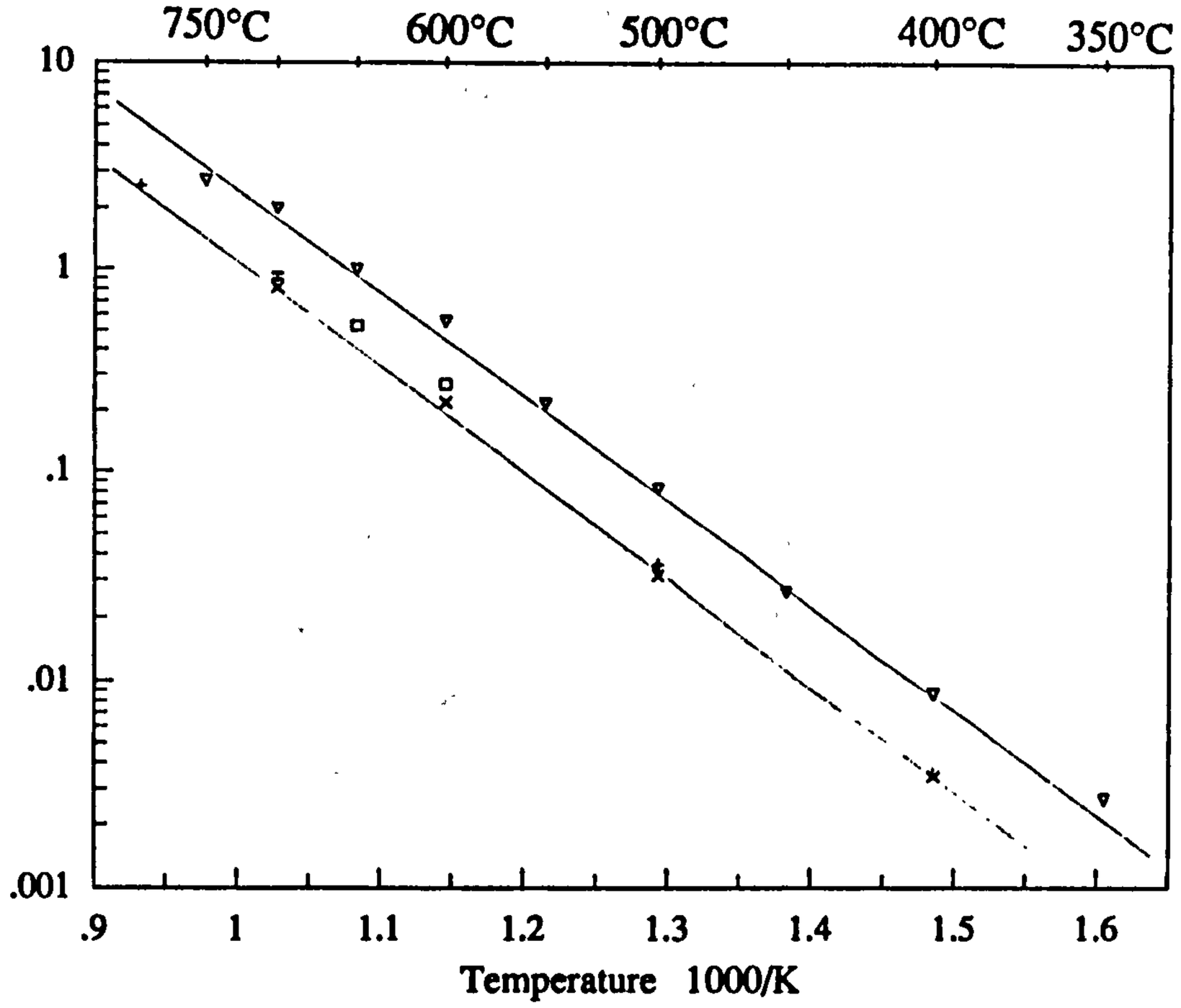

Fig. 3.9: Conductivity of YSZ determined by measuring E_{WR} and assuming $R_u = 0.28R_z$. □, 8Y-YSZ 0.7mm thick; +, ICI 8Y-YSZ 0.35mm thick; ×, ICI 3Y-YSZ 0.8mm thick; ∇, 6Y-YSZ 0.7mm thick.

3.2.3 High current results

The theory already outlined explains how a large voltage applied to a zirconia cell induces p-type electronic conductivity at the anode and the n-type equivalent at the cathode. The total conductivity therefore increases. Levy et al (1988) found that large enough voltages caused the zirconia to display the conductivity characteristics of a metal.

Experiments were performed to observe the relationship between the conductivity and the voltage E_{WS} applied to a zirconia cell. Fig. 3.10 shows results where the conductivity of a 0.8mm thick ICI 3Y-YSZ disc with gold electrodes was measured (without an RE) by current-interruption. There is no evidence of a clear transition between ionic and mixed conductivity as might be expected. The scatter in the results indicates that the accuracy was low so it is possible that the

experimental error masked this transition. However, it is believed that the width of the TPB increased and caused a gradual reduction in the constriction resistance with increased voltage. The increased total conductivity due to the electronic contribution is clearly evident at the highest voltages.

Fig 3.11 shows the results obtained using cyclic voltammetry (CV) on a 6Y-YSZ disc with platinum electrodes (an RE was used). At low anodic voltages the current was greater when the voltage was increasing than during the return scan. However, at higher voltages the opposite occurred; ie. the cell changed from capacitive behaviour to inductive behaviour. This change was often observed (see also Schouler and Kleitz (1987)) and seemed to correspond with the onset of significant electronic conductivity but this correlation was not accurately checked. The solid line in Fig. 3.11 represents a resistance of 15Ω which was the uncompensated resistance (R_u) found for this cell at 700°C using current-interruption at low voltages (<100mV). At high anodic voltages the current flowing was greater

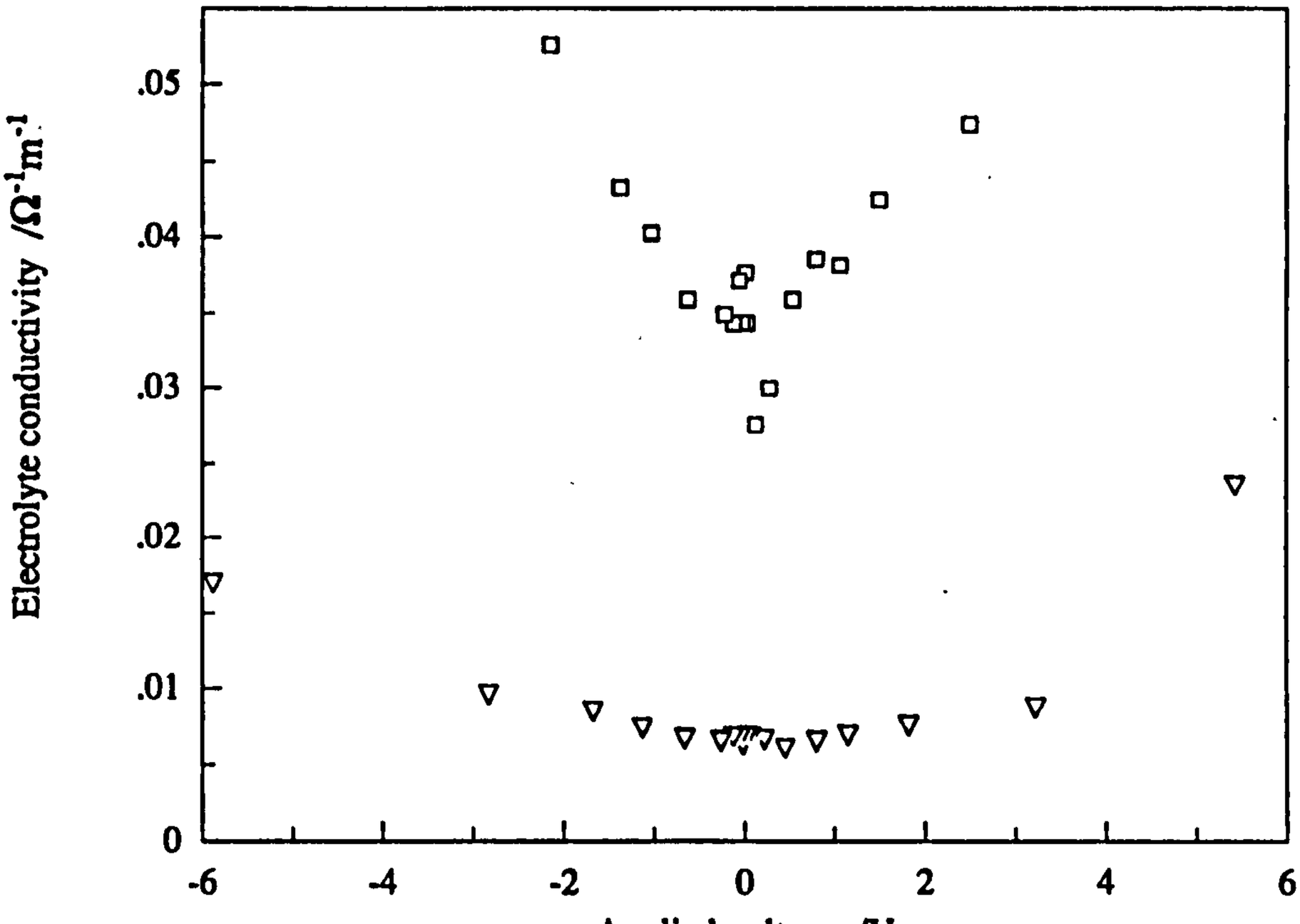

Fig. 3.10: Conductivity of 3Y-YSZ at high applied voltages. Measured in air using 5.0mm diameter electrodes on disc 0.8mm thick. □, 600°C; ∇, 500°C.

than that possible through a 15Ω resistance so it was assumed that the electrolyte resistance decreased and that the anodic overvoltage asymptotically approached a maximum value. An asymptotic approach to a maximum η_a value was observed using current-interruption but currents no greater than 10mA were used. Fig. 3.12 shows the electrolyte conductivity calculated assuming the maximum values of η_a to be 65mV at 800°C and 130mV at 700°C. These values were determined by first assuming R_u to be 15Ω and finding the maximum η_a predicted by this assumption. The values found were 63 and 117mV respectively. Similar results were obtained at 600°C but are not shown. These CV results are also discussed in section 3.4.

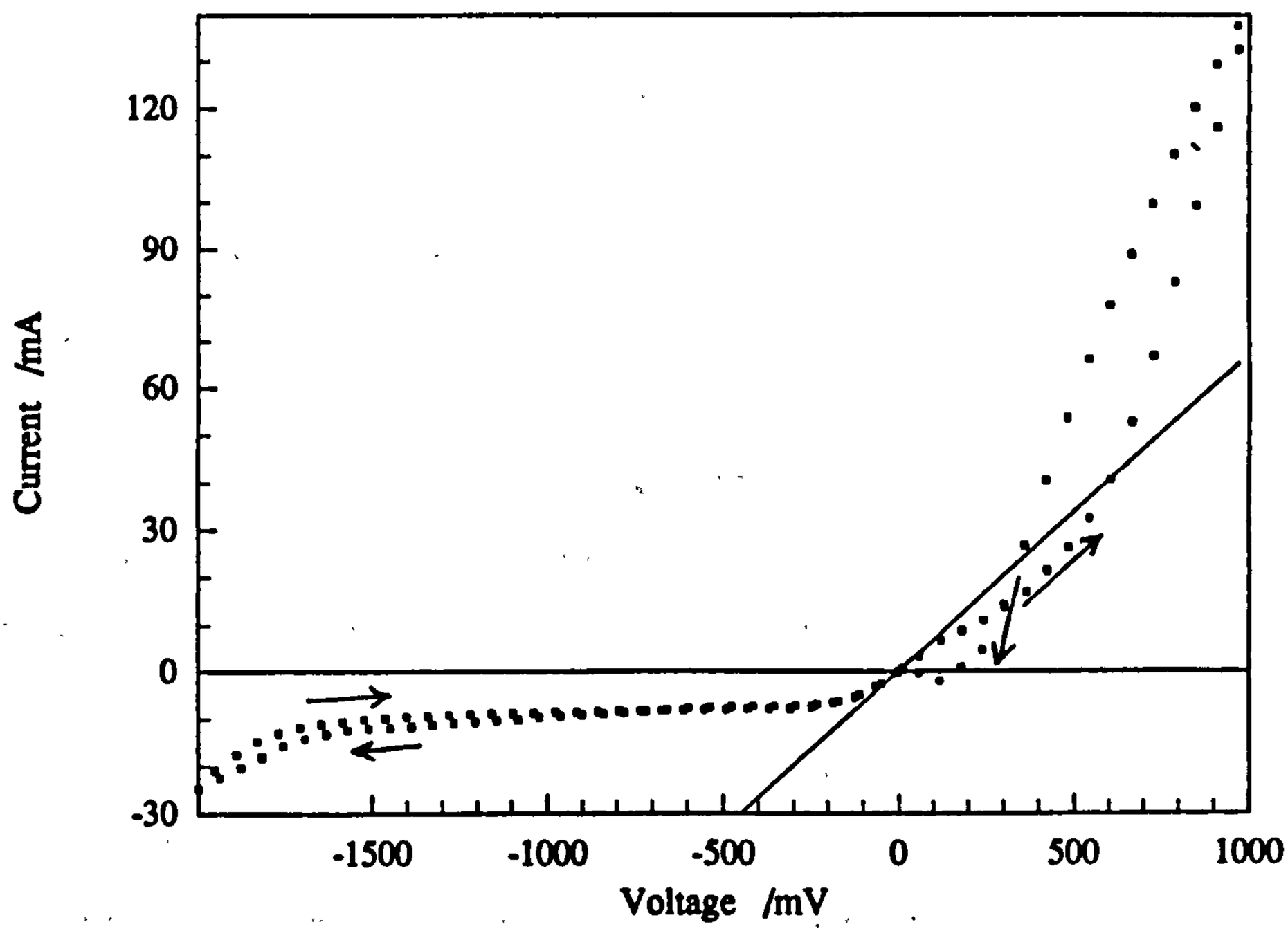

Fig. 3.11: CV scan at 2mV/s (of E_{WR}) on 5.0mm diameter working electrode on 6Y-YSZ disc 0.7mm thick at 700°C in 0.8%O_2 in N_2.

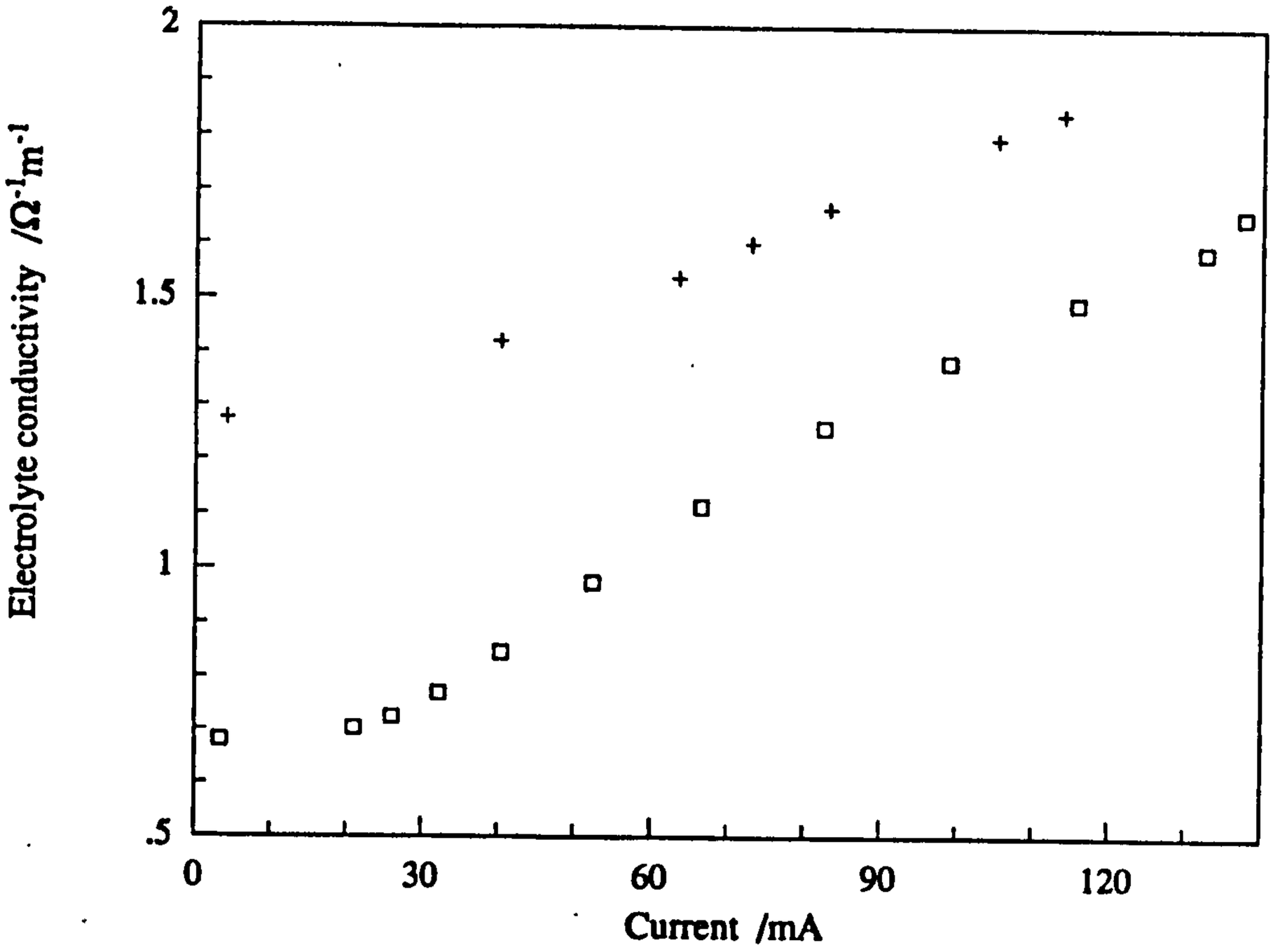

Fig. 3.12: Conductivity of 6Y-YSZ cell at high applied voltages derived from CV scans. □, 700°C; +, 800°C.

A single experiment was done where current was passed through a zirconia disc held within the silica tube and a nitrogen/air mixture of constant composition was fed into this enclosed space. Both platinum electrodes were in the same atmosphere surrounding the disc. The oxygen concentration of the gas flowing out of the silica tube was monitored with a potentiometric sensor (the thimble sensor). The results illustrated by Fig. 3.13 show how the oxygen concentration of the exiting gas increased as the current flowing through the zirconia disc increased. This clearly illustrates that the YSZ disc was being reduced. The measured oxygen concentration returned to its original value when the current flow through the disc was stopped. The corresponding applied voltages (E_{WS}) (due mainly to the cathodic overpotential) are also shown in Fig 3.13 and it can be seen that they are at a level where n type electronic conduction would be expected.

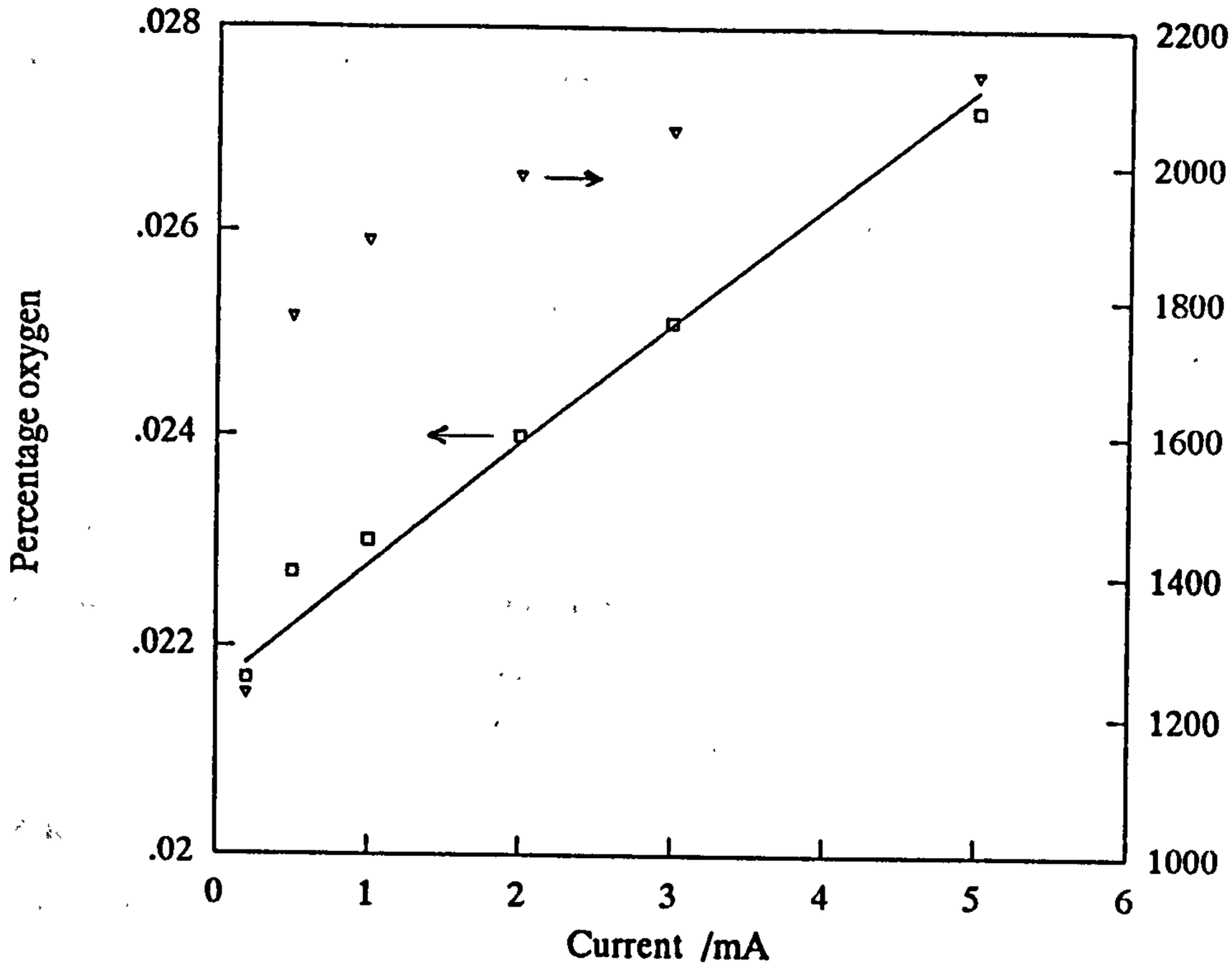

Fig. 3.13: Percentage oxygen leaving enclosed volume in which zirconia cell was operated at 700°C. $\%O_2$ and applied voltage (E_{ws}) plotted against current.

The solid line in the graph represents 8 electrons for every molecule of excess oxygen in the exiting stream (4 are expected). The agreement is remarkably good but, without further experimental work, it is not possible to say if this was a coincidence. The detailed calculations used to produce Fig. 3.13 are presented in Appendix 5.1.

The experiment was performed to measure conductivity and not the reduction of zirconia so the length of time each current setting was held was not accurately recorded but was between 1 and 4 minutes. This was not long enough to bring the exiting oxygen concentration to steady state. The time constant (τ) for a system where fluid flows into a vessel of fixed volume is: volume/flow rate. The gas volume inside the silica tube was 200ml and the flow rate was 2.5ml/s which means the time constant was 80s and the fractional response to a step change in oxygen reduction rate would be: $\exp(-t/\tau)$ where t is the time since the step change. If each current setting had been held for about 60s the increase in exiting oxygen concentration would have been half the steady state value which in turn would have corresponded to 4 electrons per mole of oxygen reduced.

3.3) Electrode conductances

Electrode conductance (σ_e) is related to the kinetics of the electrochemical reaction and reflects the electrode activity: it is defined by:

$$\sigma_e = \lim_{I \to 0} dI/d\eta \qquad (3.7)$$

Where possible, electrode resistances or conductances were calculated using results where the overvoltages were less than 10mV. In this section only electrode resistances and not exchange current densities (i_0) were calculated. This was because i_0 could not be determined until the values of the transfer coefficients (α_a and α_c) were known (eqn(1.20)) and as shown in section 3.4 these varied over a wide range and no fixed values could be assumed for them.

3.3.1 Stability of electrodes

The electrode resistance (measured at low overvoltages) has been widely used as an indication of the quality or activity of an electrode. However, results are notoriously difficult to repeat. The resistance of two electrodes prepared by the same method using identical batches of chemicals and fired under identical conditions can be a factor of 2 different. It is therefore best to do a series of tests on a single electrode and to compare the trends.

Even using a single electrode, experimental results can be misleading because of aging and attention must be given to this. Verkerk et al (1983) found that platinum electrodes were stable if they were used at least 150 to 200°C below the temperature at which they were sintered. Platinum and gold electrodes were generally initially fired at 1000 - 1025°C, in this work, and used at or below 800°C. In section 4.2.7 it is shown that the activity of platinum electrodes changed very little with over 4 weeks of use at temperatures up to 750°C.

A gold electrode was found to have a resistance of 167Ω at 800°C in air and after nearly 20 hours at 800°C and about 60 hours at lower temperatures (500 to 700°C) its resistance was 212Ω. After heating to 1021°C for 5 minutes its resistance rose to 504Ω at 800°C in air. However, this electrode gave different results when

tested twice under the same conditions. Its resistance was measured at 700°C in 0.07% O_2 before being cooled to room temperature and then reheated to 700°C: results of 14 and 19kΩ respectively were obtained. This suggests either an error of up to 50% in the measurements or a high degree of sensitivity of the electrode to its history and test conditions. Despite this difficulty in measuring electrode conductances, the conclusion from these and other results was that temperatures above 800°C caused significant degradation of gold electrodes within 24 hours.

Silver melts at 961.9°C and firing at 900°C was shown to produce electrodes with lower activity than electrodes fired at lower temperatures. Silver electrodes fired at 850°C for 3 hours were tested before and after being held at 750 and 725°C for 5 hours each. The resistance in air at 700°C increased from 47 to 86Ω indicating clearly that 750°C was too hot for these electrodes. Similar electrodes were used at 700°C for over 13 hours and at lower temperatures for 3 days. The resistance in air increased from 52 to 65Ω at 600°C and 270 to 350Ω at 500°C. Silver was found to adhere extremely well to zirconia even when fired at 500°C so it would be worth investigating in more detail for applications involving temperatures not exceeding about 650°C.

3.3.2 Platinum electrodes

A range of tests were performed on sputtered and screen printed platinum electrodes. It was found that the conductance at temperatures near 650°C in gases with a low CO/CO_2 ratio was an order of magnitude lower after the WE was held at cathodic voltages compared to the value after being held at anodic voltages. This suggests blocking of the 3-phase boundary by reduced species (CO or C). All results discussed in this section refer to measurements made by starting with the most anodic potential and then stepping to more cathodic values.

Initial tests in various $CO/CO_2/N_2$ mixtures reported by Copcutt and Maskell (1992) showed a marked change in electrode conductance at around 700°C. The results on a second electrode (Fig. 3.14) show a similar trend in some $CO:CO_2$ ratios but not when the ratio was 1:100 (×). The lines drawn on Figs. 3.14 to 3.21 are to guide the eye only. Fig. 3.15 is a presentation of the results obtained in similar

$CO/CO_2/N_2$ mixtures using a third similar electrode. The most obvious trend is that the electrode conductance (σ_e) is much greater and more temperature dependent in O_2/N_2 mixtures where the O_2 concentration is relatively high (4.3%). Fig. 3.16 presents the results using a 4th platinum electrode. Only relatively high CO concentrations were used and no transition near 700°C was evident. One clear feature in Fig. 3.15 and 3.16 is that the conductance is much more temperature dependent in O_2/N_2 mixtures than in CO/CO_2 mixtures.

The conductance of Pt electrodes on YSZ in O_2/N_2 mixtures has been widely studied. Two important trends have been noticed. Firstly the conductance as a function of pO_2 reaches a maximum. The maximum conductance value decreases with decreased temperature and the pO_2 where this maximum occurs decreases with decreased temperature. (Mizusaki et al (1987a & b) and Verkerk et al (1983a & b)). Secondly at pO_2 values significantly less than the maximum just mentioned the conductance is proportional to $pO_2^{1/4}$ (Schindler et al (1989)). Kuzin and Komarov (1990) showed that this relationship continues down to very low pO_2 values. Electrode conductance on single cells (ie. without a diffusion barrier) was not extensively tested in this work but the few results obtained did not conflict with the reported trends. Fig. 5 of Copcutt and Maskell (1992) shows a line representing the $pO_2^{1/4}$ proportionality.

Fig. 3.17 presents the conductance results of the second electrode plotted against the oxygen partial pressure. Fig. 5 in Copcutt and Maskell (1992) presents the results using the first electrode tested. As the $CO:CO_2$ ratio became increasingly CO rich the electrode conductance decreased, particularly at the lower temperatures. The electrode conductance reached a minimum and then increased as the CO concentration increased. The $CO:CO_2$ ratio where this minimum in σ_e occurred became increasily CO rich as the temperature decreased. Mizusaki et al (1990 & 1992) did very similar studies and reported a similar effect in the later paper. In the earlier paper they only reported an increase in σ_e as the CO concentration increased. This could be because they did not go to low enough CO concentrations at the relatively high temperatures used.

Drawing conclusions from this work was difficult because the reproducibility of the conductance measurements in $CO/CO_2/N_2$ mixtures was poor. This may have

been caused by a very slow (many hours) drift in electrode potential that was sometimes observed. For instance the voltage of the Nernst sensor connected to the gas outflow sometimes changed slowly over a period of many hours. Also the potential of the reference electrode drifted slowly relative to the other two electrodes (in the same atmosphere) and sometimes a difference of over a hundred mV would be maintained even though no current had been passed through any of the three electrodes for several hours. Passing a current through the reference electrode also did not help. It is therefore likely that there was a slow adsorption/desorption process occurring that sometimes masked the other more rapid electrochemical processes on the electrodes. Yentekakis et al (1988) suggested that the formation of PtO_2 might cause similar effects.

Most measurements reported in this section were performed galvanostatically. The computer program was designed to maintain each setting until the value being monitored (E_{WR} in this case) did not change by more than 0.1% during the selected time period. A minimum time was also set and testing for steady state was not started until this minimum time had elapsed. Both time periods were varied for the tests on each cell. The result was that the average time for which each current setting was maintained varied. On the first electrode the average time was about 8 minutes, on the second about 15 minutes, 20 on the 3rd and 10 on the 4th.

It was concluded that CO is electrochemically active on the platinum electrodes for the following reasons. Firstly Kuzin and Komarov (1990) showed that σ_e in O_2/N_2 mixtures is very low at the pO_2 values comparable to those where CO is included in the mixture. Secondly tests in this work showed that σ_e is as low in O_2/CO_2 mixtures as it is in O_2/N_2 mixtures. Finally σ_e increased as pCO increased once pCO was above the level where the minimum in σ_e was observed. Mizusaki et al (1992) came to more detailed conclusions: essentially, CO adsorbed on the Pt surface reacts at the three phase boundary with O atoms adsorbed on the YSZ surface to form CO_2 on the Pt surface.

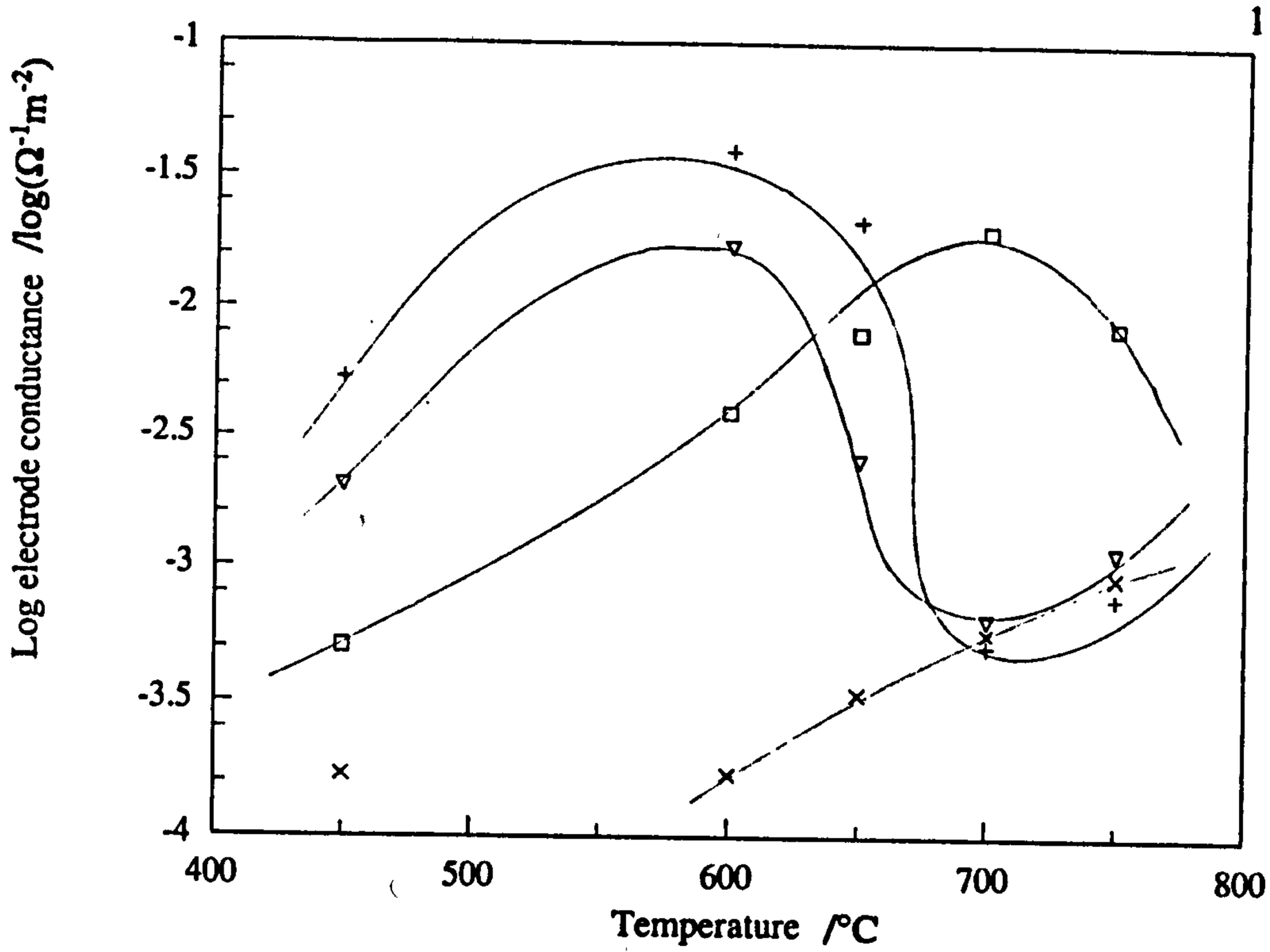

Fig. 3.14: Conductance of second platinum electrode in CO/CO_2 mixtures (balance N_2) as a function of temperature. □, 3.88% CO, 3.03% CO_2; ×, 0.135% CO, 13.5% CO_2; ∇, 0.124% CO, 96.9% CO_2; +, 0.0128% CO, 99.7% CO_2.

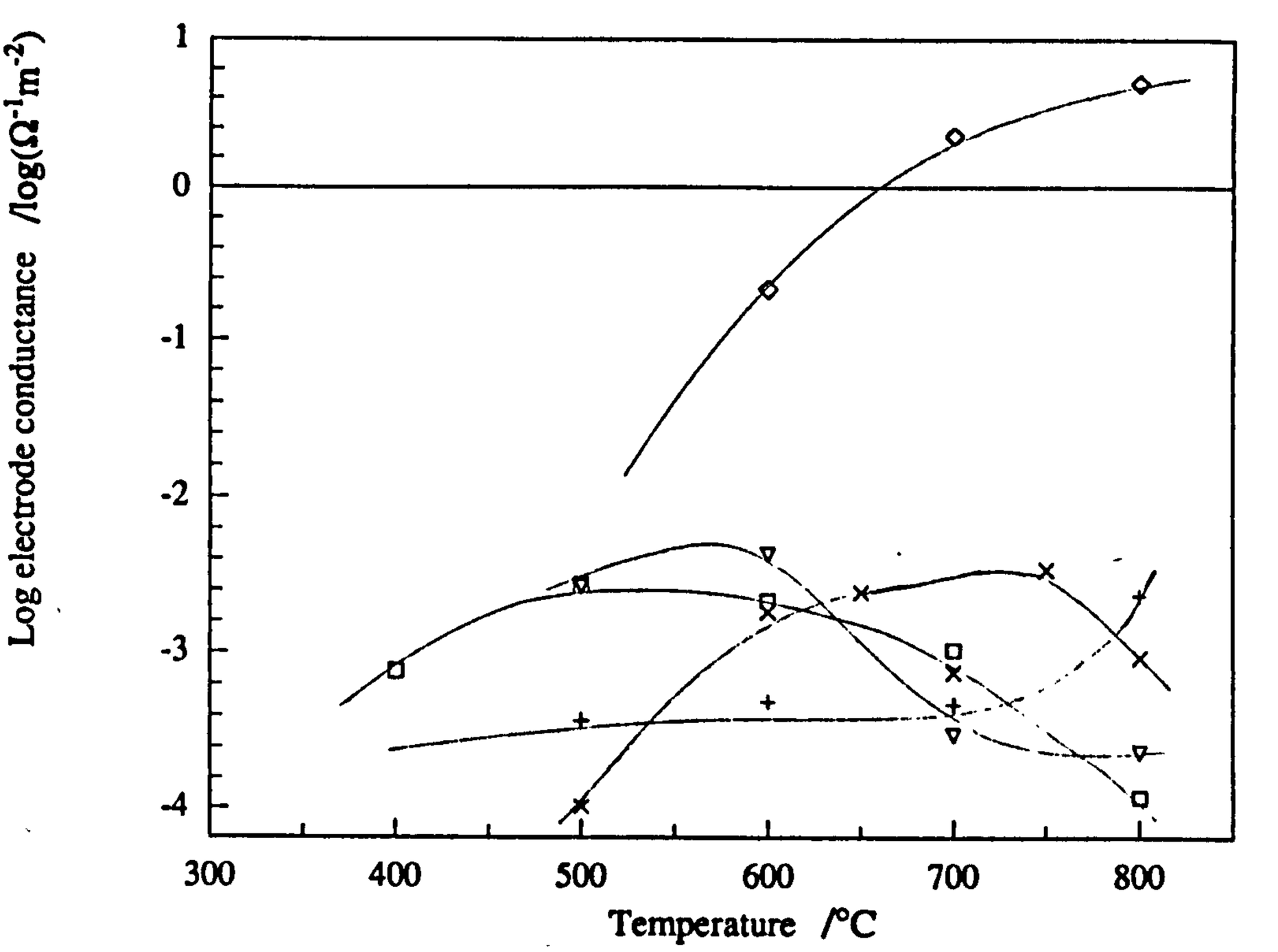

Fig. 3.15: Conductance of third platinum electrode in $CO/CO_2/N_2$ mixtures as a function of temperature. □, 3.88% CO, 3.03% CO_2; ∇, 3.66% CO, 8.63% CO_2; +, 3.03% CO, 23.8% CO_2; ×, 3.03% CO, 23.8% CO_2; and ◇, was 4.3% O_2 in N_2.

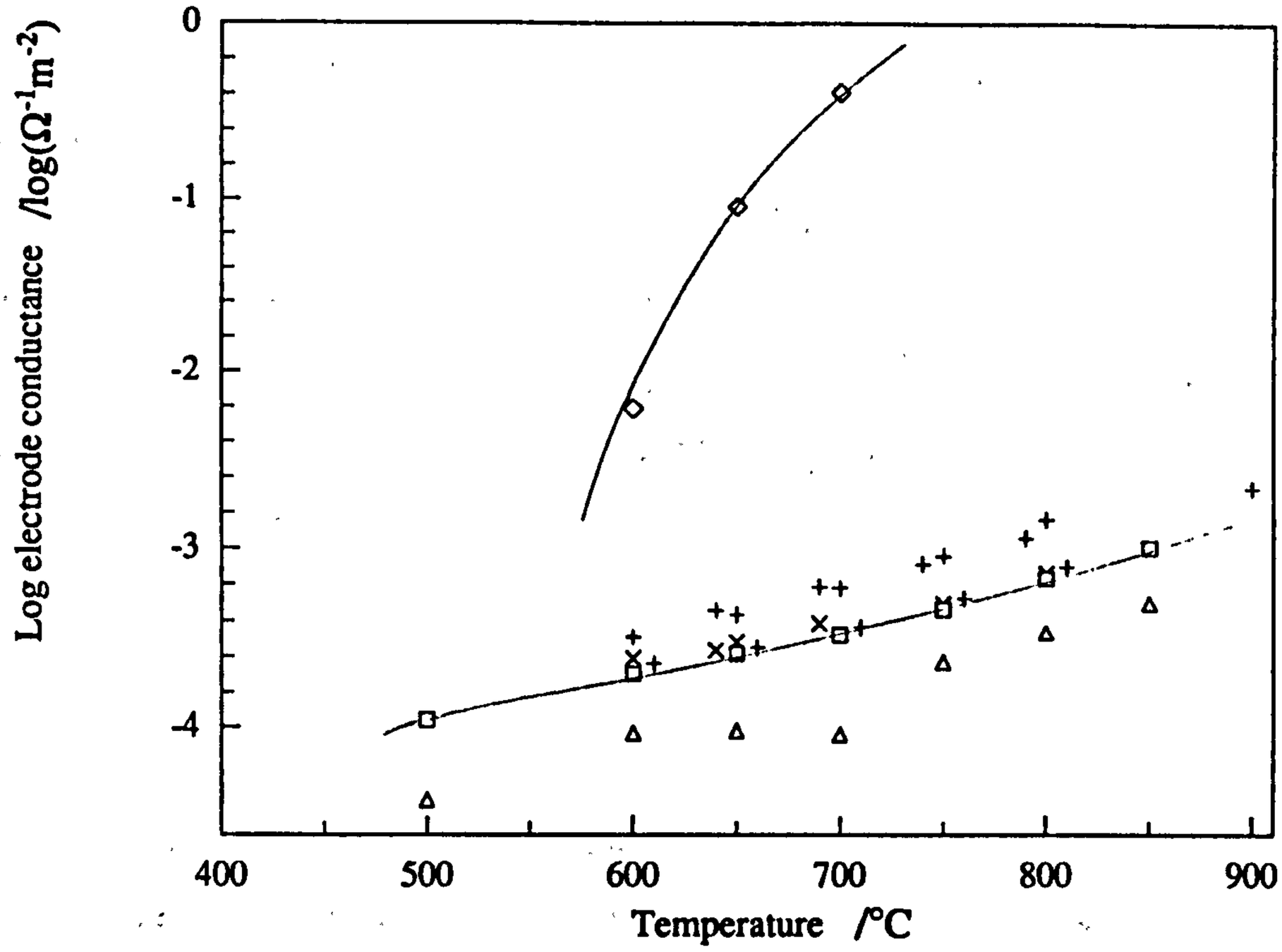

Fig. 3.16: Conductance of fourth platinum electrode in CO/CO_2 mixtures (balance N_2) as a function of temperature. +, 3.77% CO, 5.88% CO_2; ×, 3.46% CO, 13.5% CO_2; □, 3.05% CO, 23.8% CO_2; Δ, 0.97% CO, 75.7% CO_2; and ◇, was air.

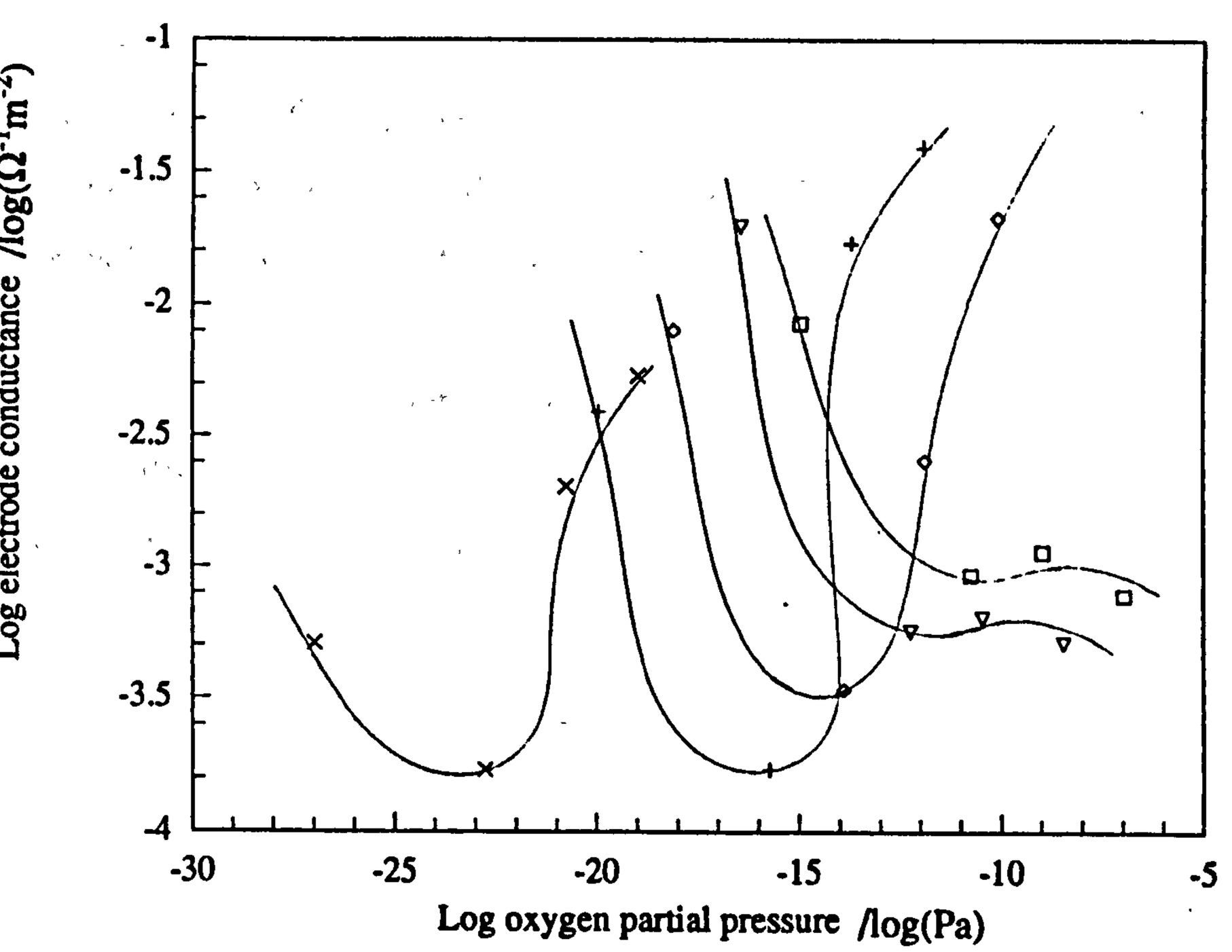

Fig. 3.17: Conductance of second platinum electrode in CO/CO_2 mixtures as a function of oxygen partial pressure. The temperatures were: □, 750°C; ∇, 700°C; ◇, 650°C; +, 600°C and ×, 450°C.

The major increase in electrode conductance sometimes observed in CO/CO_2 mixtures when the temperature decreased from 750°C to 650°C implicates disproportionation of CO. There is a corresponding change in the thermodynamic stability of CO at 700°C (see Fig. 1.10). It was suspected that the following process was important below 700°C: $CO_{ads} \rightleftharpoons C_{ads} + O_{ads}$, $O_{ads} + 2e^- \rightleftharpoons O^{2-}$, then either $C_{ads} + 2O^{2-} \rightleftharpoons CO_2 + 4e$ or $C_{ads} + O_{2(g)} \rightleftharpoons CO_{2(g)}$. The work of Yentekakis and Vayenas (1988) supports this conclusion as do the results in section 5.2.

3.3.3 Silver electrodes

The following results were taken from the low overvoltage measurements made using the internal pumping electrode of an amperometric sensor assembled with silver electrodes. Fig. 3.18 shows the electrode conductance as a function of temperature and Fig. 3.19 represents the same results as a function of oxygen partial pressure.

In O_2/N_2 mixtures the conductance generally decreased with decreasing pO_2 and temperature. In $CO/CO_2/N_2$ mixtures the conductance reached a minimum when the $CO:CO_2$ ratio was 1:10 to 1:100. As the CO concentration increased there was an increased trend for the conductance to decrease with increasing temperature at around 700°C.

Since the trends were similar to the trends shown by the platinum electrodes it was concluded that the mechanisms were the similar. The differences in behaviour could be accounted for by the differences in adsorption of the relavent gases on the two metals.

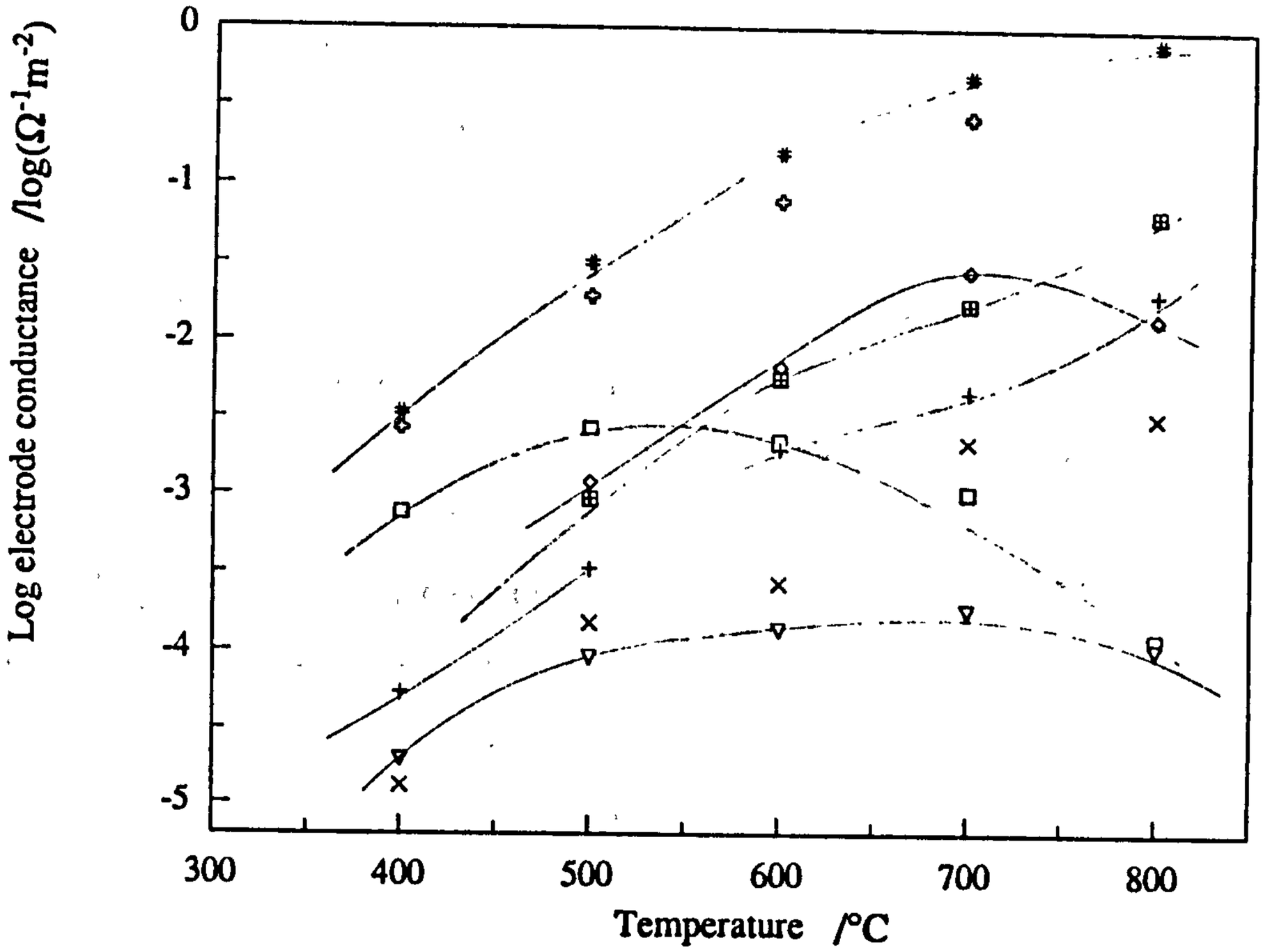

Fig. 3.18: Conductance of silver electrode in $CO/CO_2/N_2$ and O_2/N_2 mixtures as a function of temperature. □, 3.88%CO 3.06%CO_2 balance N_2; ∇, 3.05%CO 23.8%CO_2; ×, 0.65%CO 83.7%CO_2; +, 0.076%CO; 98.1%CO_2; ◇, 0.207%O_2; +, 2%O_2; #, 20.9%O_2; +, 100%O_2.

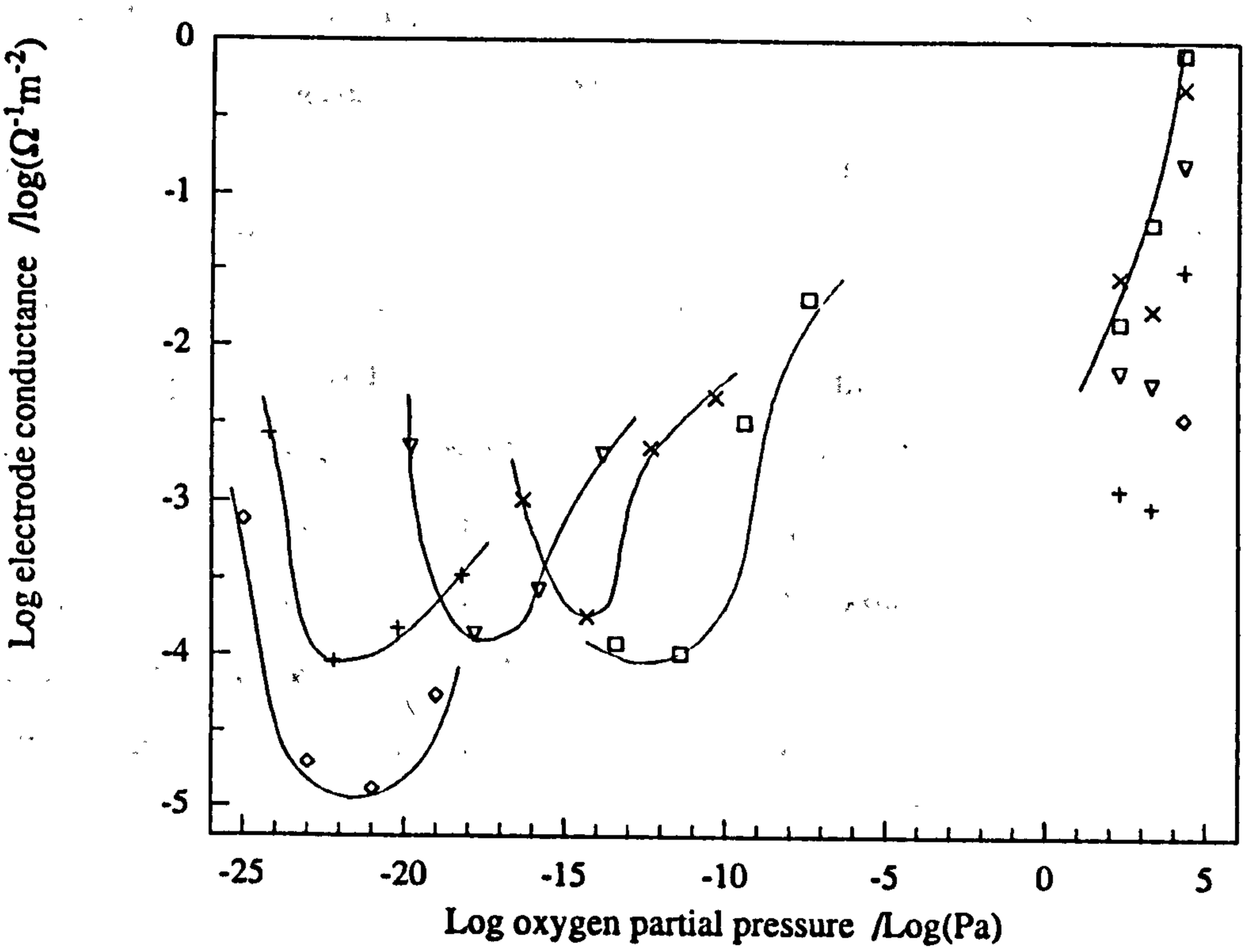

Fig. 3.19: Conductance of Ag electrode as a function of oxygen partial pressure. The temperatures were: □, 800°C; ×, 700°C; ∇, 600°C; +, 500°C; and ◇, 400°C.

3.3.4 Gold electrodes

The only gold electrode extensively tested was the internal electrode of an amperometric sensor. Electrode activity was relatively low so it was possible to calculate current vs. overvoltage characteristics up to several hundred mV before the gauge cell voltage became significant even at 800°C.

As with the previous electrodes it can be seen from Figs 3.20 and 3.21 that the conductance was more temperature-dependent in O_2/N_2 mixtures than in CO/CO_2 mixtures. In some CO/CO_2 mixtures there was a small increase in σ_e as the temperature decreased from 700 to 600°C, but the transition was not as large as it was with platinum.

Fig. 3.22 shows a very clear trend of reduced conductance with reduced oxygen partial pressure and then increased conductance with increased CO concentration. This suggested that CO was electrochemically active on gold electrodes as was concluded with silver and platinum electrodes. A minimum in σ_e may have been observed if low enough CO concentrations had been tested.

In previous figures (3.14 to 3.21) the lines were drawn to guide the eye but in Fig. 3.22 the line represented σ_e proportional to $pO_2^{1/4}$. The observed results followed this relation at low temperatures and low pO_2. van Hassel et al (1991) also observed this trend in σ_e with gold electrodes and it was the same behaviour as that observed on platinum at low pO_2 as discussed in section 3.3.2. Therefore, it was concluded that the mechanism of electrochemical reaction must have been very similar with all three metals tested. Different adsorption coefficients of the relavent gases on gold compared to the other metals probably explains the differences in the results. Comparing Fig. 3.22 with Fig. 3.19 and 3.15 it can be seen that the gold electrodes are less active than platinum or silver electrodes. This has been attributed to a shorter TPB on gold electrodes (Wang and Nowick (1981)).

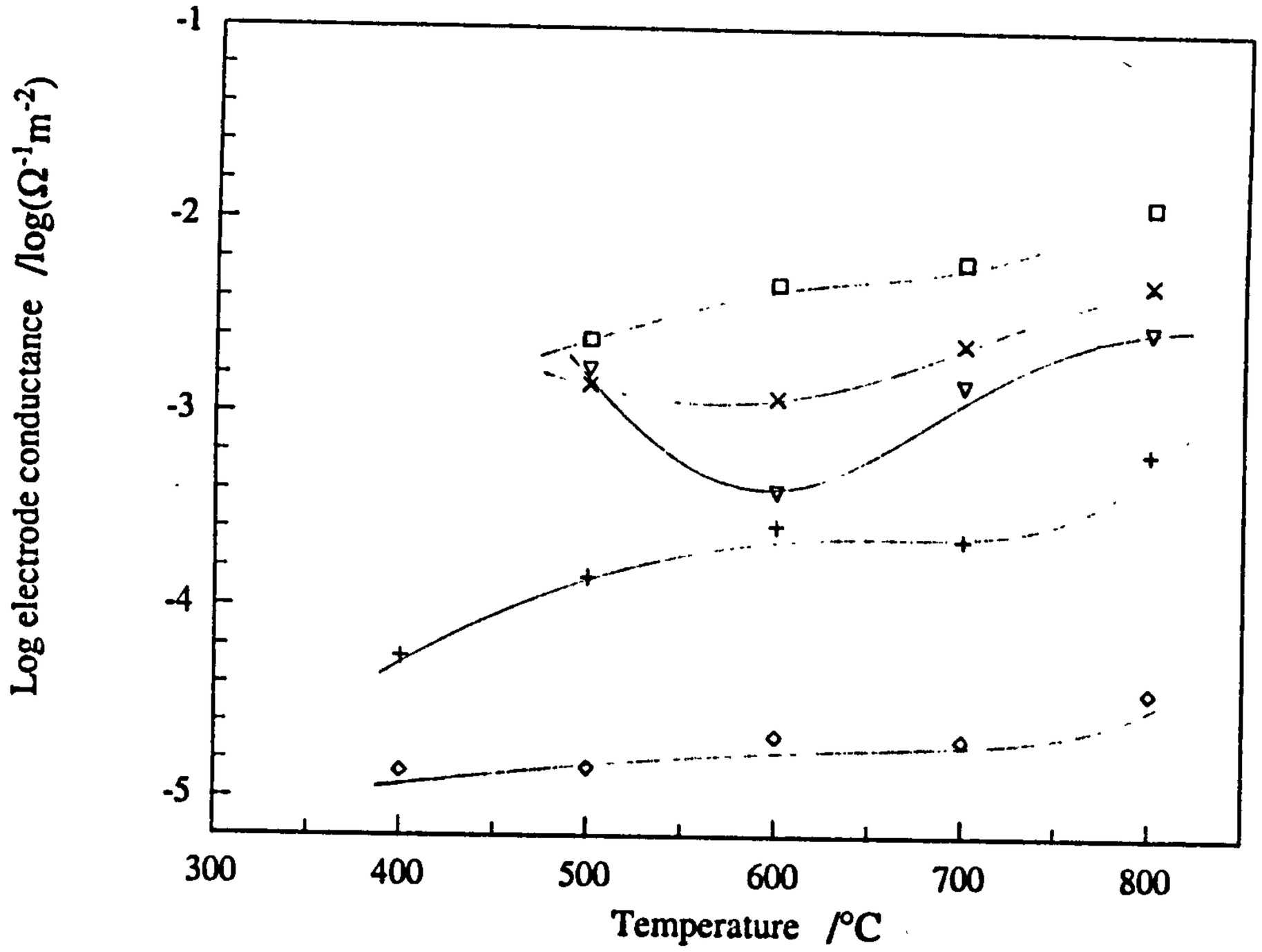

Fig. 3.20: Conductance of Au electrode in $CO/CO_2/N_2$ mixtures as a function of temperature. The $CO:CO_2$ ratios were: □, 1:1; ×, 1:10; ∇, 1:25; +, 1:100; ◇, 1:1000.

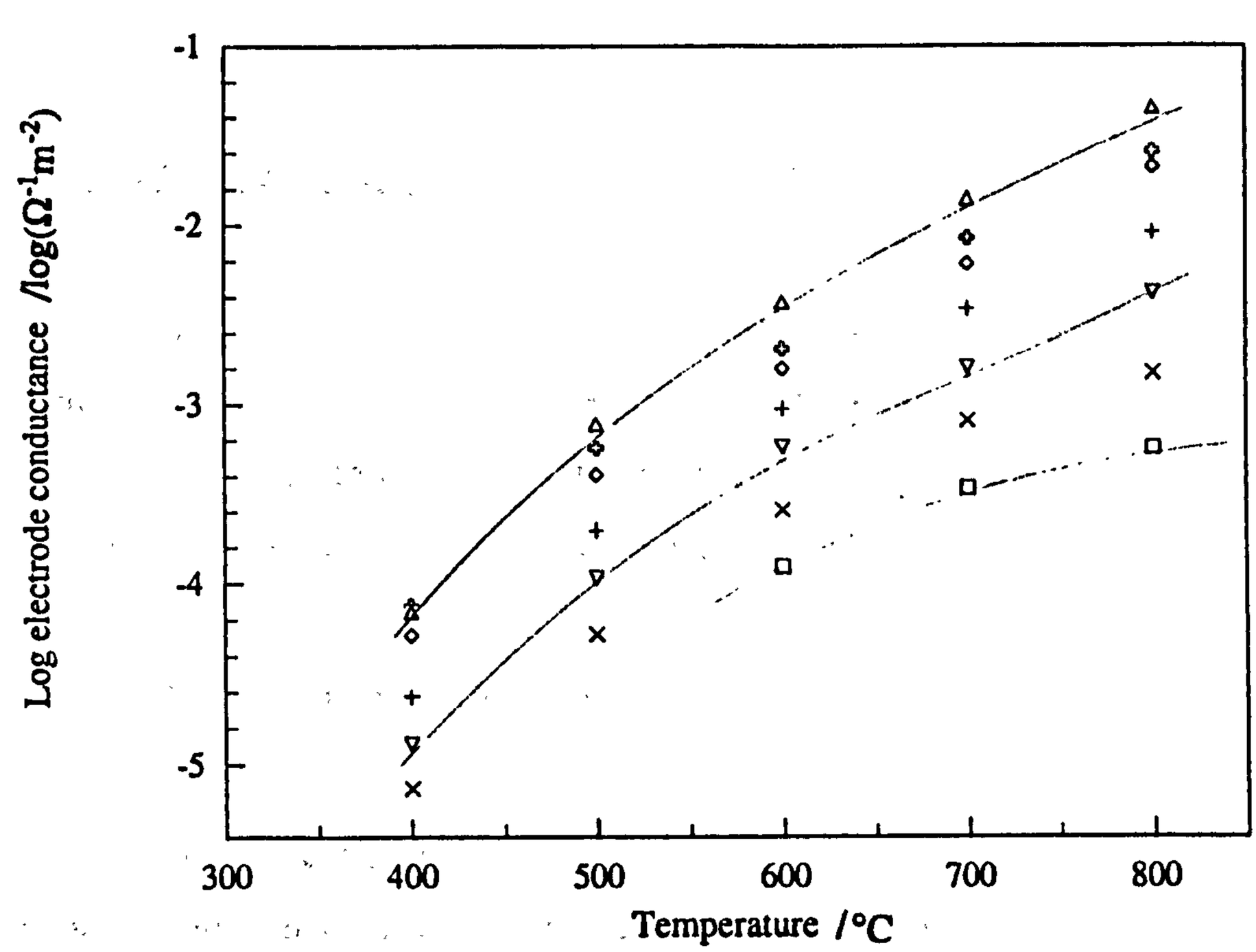

Fig. 3.21: Conductance of gold electrode in O_2/N_2 mixtures as a function of temperature. The oxygen concentrations were: □, 0.07%; ×, 0.21%; ∇, 0.7%; +, 2.1%; ◇, 5%; , 20.9%; Δ, 100% O_2 in N_2.

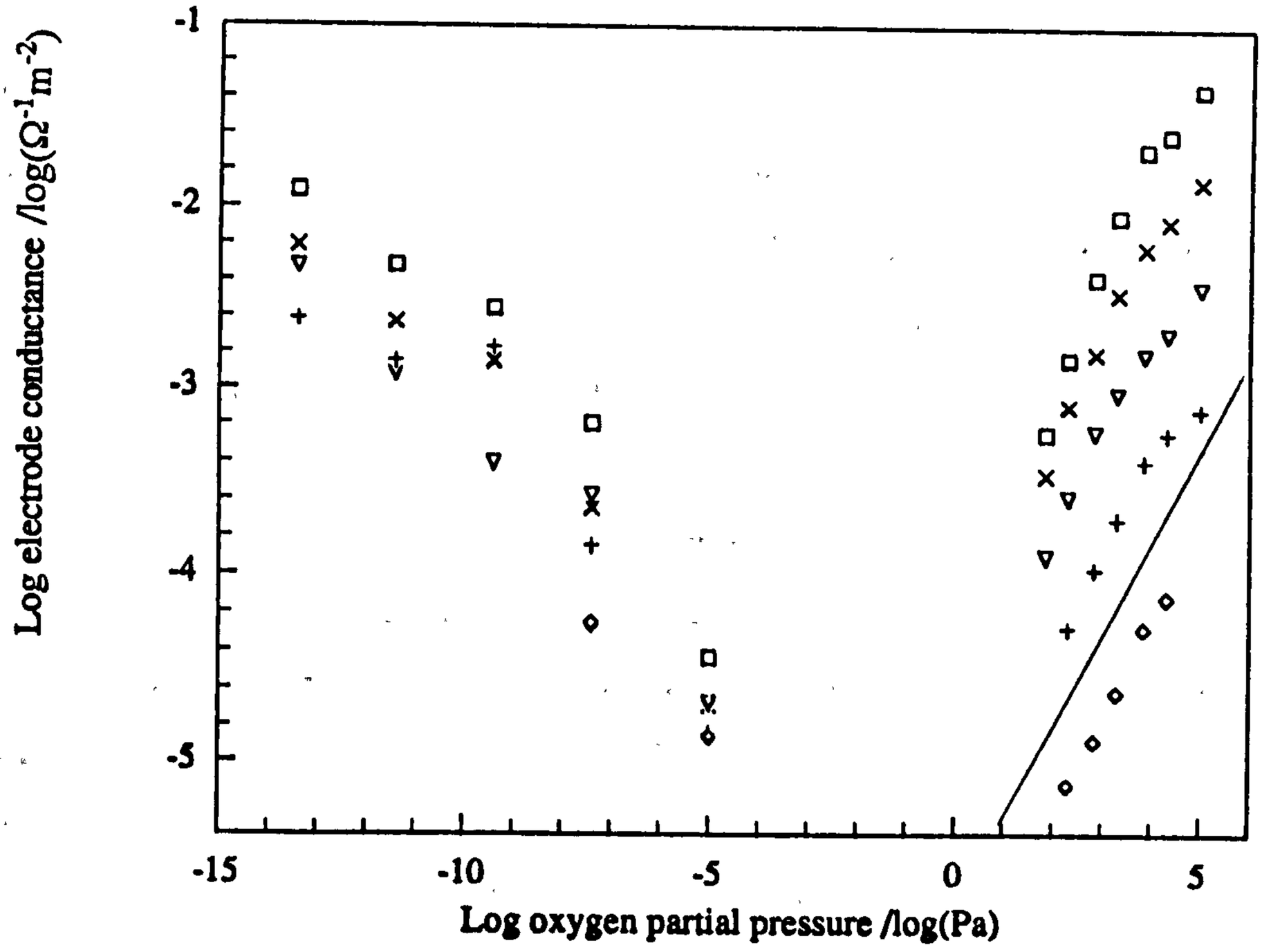

Fig. 3.22: Conductance of gold electrode as a function of oxygen partial pressure.

□, 800°C; ×, 700°C; ∇, 600°C; +, 500°C; ◇, 400°C.

3.4) High overvoltage characteristics in O_2/N_2 mixtures

The diffusion barrier of an amperometric sensor would have affected the concentration of the gas surrounding the test electrode at the overvoltages considered in this section. Therefore, only results using single disc cells with all electrodes freely exposed to the same atmosphere are reported in this section.

3.4.1 Platinum electrodes

An interesting feature of the results in Fig. 3.23 was the plateau in the cathodic current. This was modelled with the Butler-Volmer equation by assuming α_c to be zero and i_0 to be 0.98mAcm^{-2}. The exchange coefficients (α_a and α_c) that fitted the results best (using 0.25 steps) where determined first and then i_0 was found by linear regression of the low overvoltage results. These results were obtained

using CV mode. α_c of near zero is a strong indication that the resistance of the electrode is controlled by diffusion of an active species on the electrode surface (Bockris and Reddy (1970)). However, other mechanisms were also significant because the plateau was not flat and at high cathodic voltages the current increased significantly. A possible explanation for this was that n-type conductivity was induced by the low oxygen activity at the cathode and this broadened the effective TPB.

The large increase in anodic current while the overvoltage remained almost constant was a notable feature of the electrodes tested in O_2/N_2 mixtures (Fig. 3.23). The solid line represents the Butler-Volmer equation with $\alpha_a = 4$ but at the highest η_a values tested the current increased with almost no change in η_a. Widening of the TPB due to increased p-type electronic conductivity of the YSZ may explain this.

Currents greater than 10mA were not tested using current-interruption so Fig. 3.24 presents data measured using CV mode. Note that currents and not current densities were used so while the exchange current (I_0) was 6.15mA the exchange current density was 1.18mAcm^{-2}. The overvoltages had to be calculated by subtracting the estimated electrolyte IR drop (E_u) from E_{WR}. R_u was measured separately to be 15Ω so $E_u = 15 \times I$. The results for anodic currents greater that 60mA were not shown in order to magnify the scale. The full results (I vs. E_{WR} instead of η) were reported in Fig. 3.11. The results show that the value of R_u measured at low currents had decreased at high currents as discussed in section 3.2.3.

In Fig. 3.25 α_c was not rounded to the nearest ¼ (α_a was) and the value for α_c that best fitted the data was used in the Butler-Volmer equation. The conditions were similar to those of Fig. 3.23 with the cell at 800°C in 0.021% oxygen, and the value of α_c was 0.1.

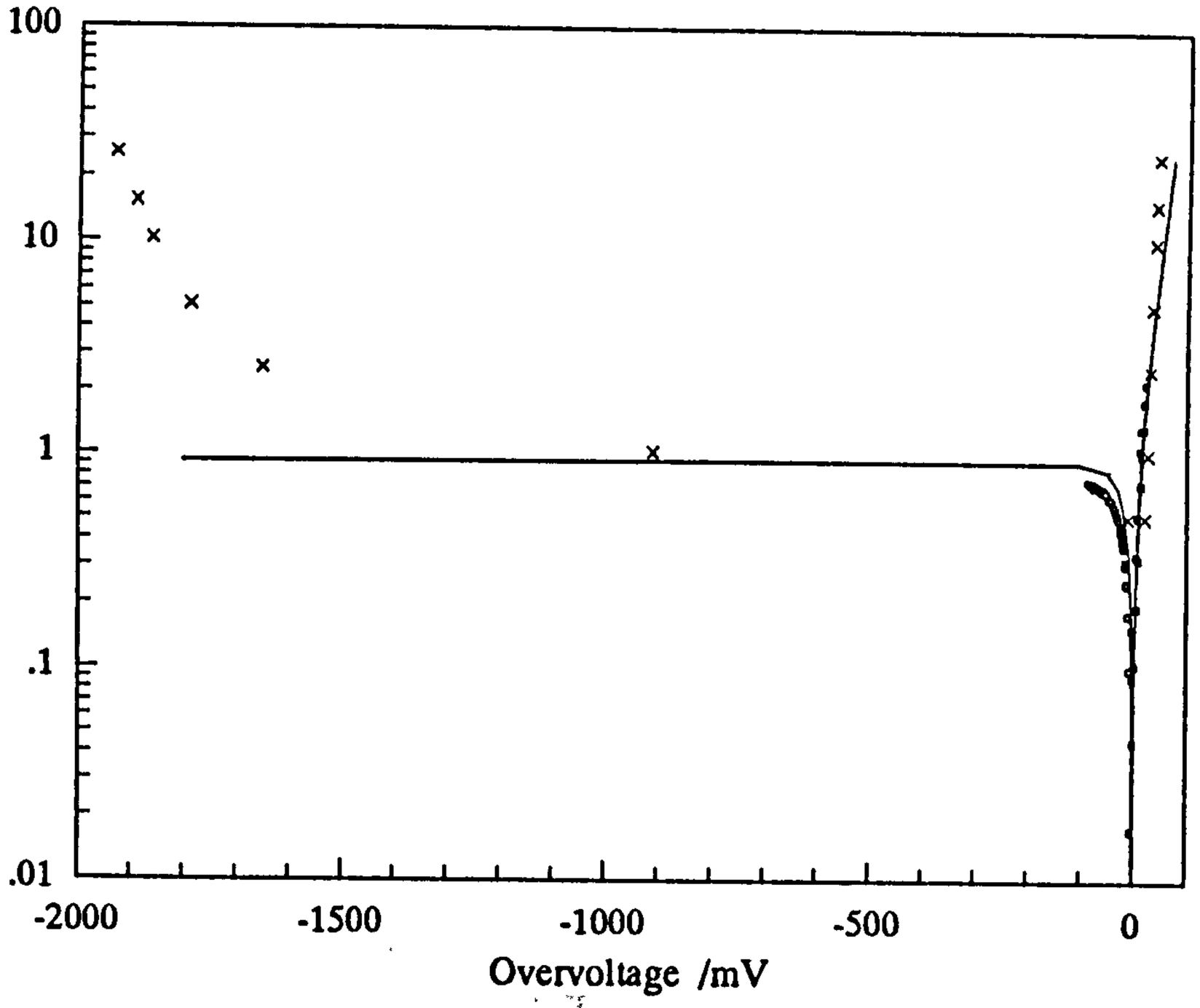

Fig. 3.23: Log of current density on a 6Y-YSZ cell with Pt electrodes in $0.021\%O_2$ at 700°C. ——, Butler-Volmer: $\alpha_c = 0$, $\alpha_a = 4$, $i_0 = 0.93 mAcm^{-2}$. ×, measured by steady state mode; □, measured by CV mode.

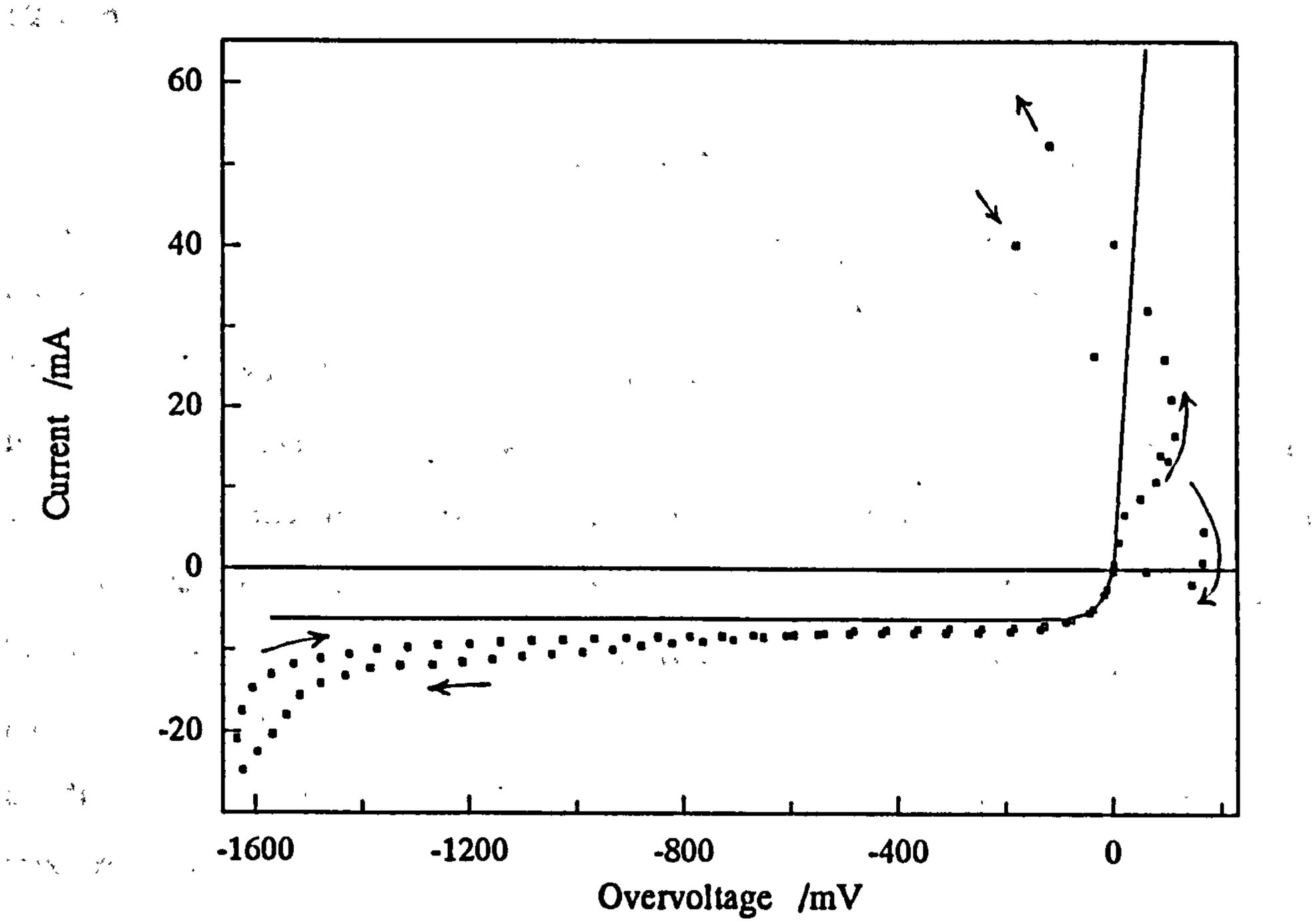

Fig. 3.24: Current vs. overvoltage on a 6Y-YSZ cell with Pt electrodes in $0.8\%O_2$ at 700°C measured by CV mode at 2mV/s. ——, Butler-Volmer equation with $\alpha_c = 0$, $\alpha_a = 4$, $I_0 = 6.15 mA$.

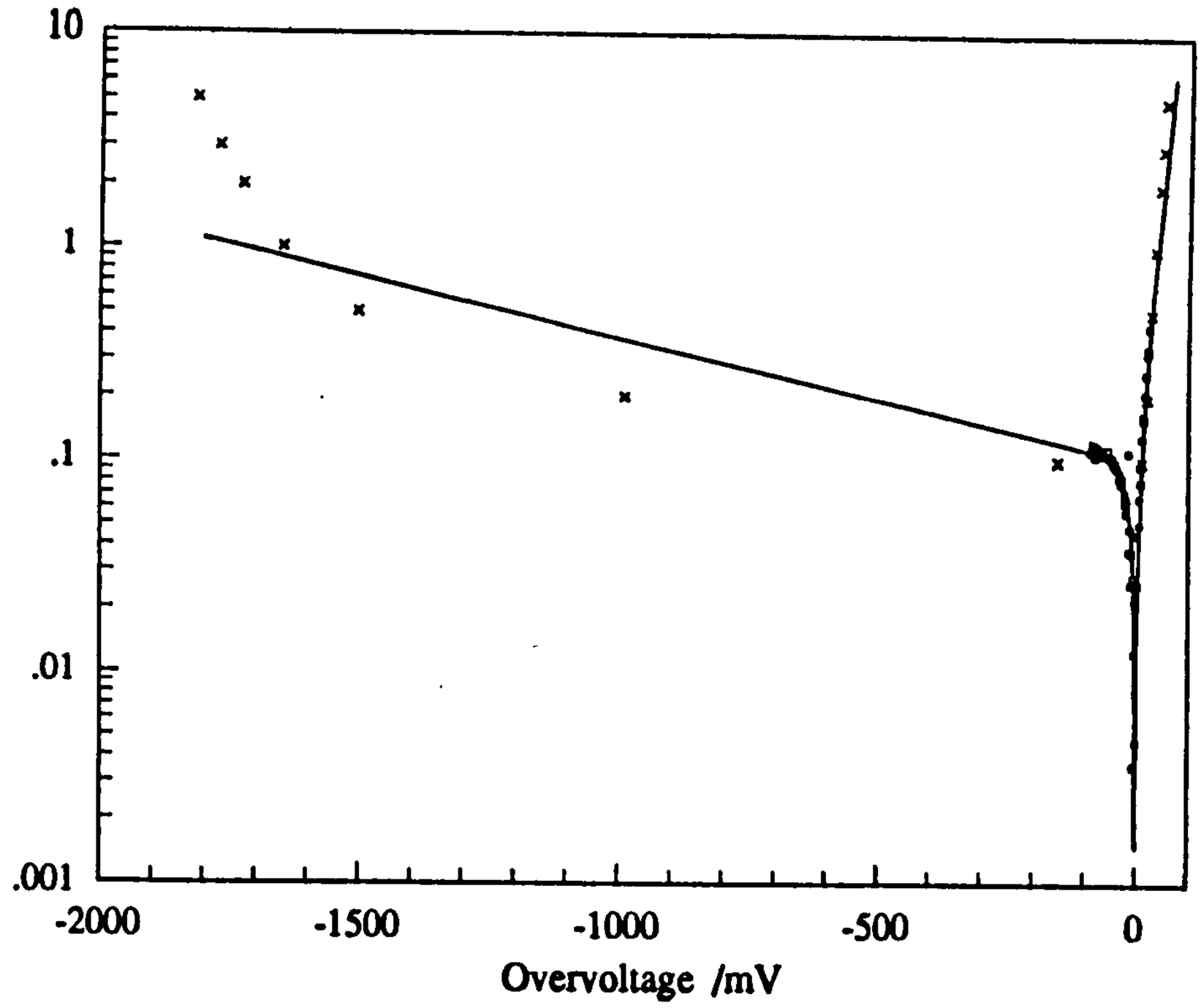

Fig 3.25: Log of current density on cell as Fig. 3.23 except at 800°C. ——, Butler-Volmer equation with $\alpha_c = 0.1$, $\alpha_a = 4.5$, $i_0 = 0.1$mA. ×, measured by steady state mode; □, measured by CV mode.

The above results do not conflict with the literature as a whole because there is very little agreement about the exact nature of current voltage characteristics of electrodes (Mizusaki et al (1987a & b) and Nakagawa et al (1993)). For instance Etsell and Flengas (1971) observed a plateau in the cathodic current at low pO_2 and found that the plateau current was proportional to pO_2. Schindler et al (1989) found the current plateau to be proportional to $pO_2^{½}$. Nguyen et al (1986b) observed a cathodic plateau at low pO_2 and found α_a and α_c to be 1.5 and 0.5 respectively at higher oxygen concentrations. Both coefficients approached unity in pure oxygen. However, the important conclusion for this work is that at currents above i_0, the anodic overvoltage was much smaller than the cathodic overvoltage in O_2/N_2 mixtures.

3.4.2 Silver electrodes

Silver electrodes on 8Y-YSZ were tested using steady-state mode in a range of O_2/N_2 mixtures. The data was fitted to the Butler-Volmer equation as before. Fig. 3.26 shows the results for the cell in air at 500 and 600°C. It can be seen that as with platinum, the electrodes only approximately obeyed the Butler-Volmer equation.

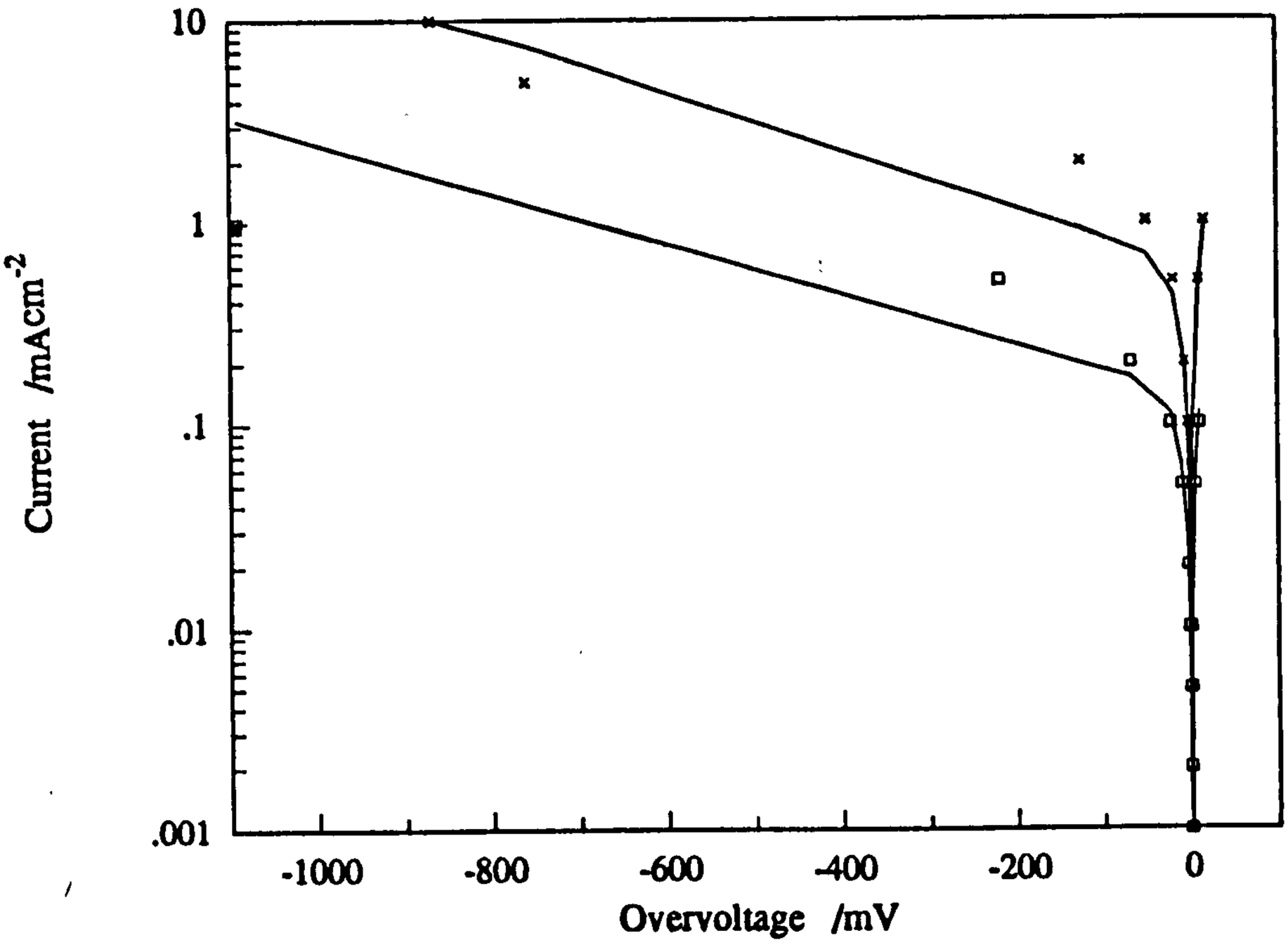

Fig 3.26: Log of current density on Ag electrodes on 8Y-YSZ at 500°C (□) and 600°C (×) in air. —, Butler-Volmer: α_c = 0.2 and 0.25, α_a = 4 in both cases, i_0 = 0.14 and 0.6mAcm^{-2} respectively.

3.5) Overvoltages in $CO/CO_2/O_2/N_2$ mixtures

3.5.1 Platinum electrodes

Some interesting results from cyclic voltammetry measurements in $CO/CO_2/N_2$ mixtures are illustrated in Figs 3.27 and 3.28. The results in Fig. 3.27

were obtained using a fixed $CO:CO_2$ ratio of 1:1000 and the temperature was increased as shown in the diagram. In Fig. 3.28 the temperature was held at 650°C and the gas concentrations were changed as illustrated. The peaks in the cyclic voltammograms indicate the presence of an oxidizable species (possibly CO or carbon) on the electrodes. At high temperatures this species seems to disappear leaving the electrode with a very high resistance. Increased CO concentrations seem to remove the peak which might suggest that the species responsible is carbon. Looking at Fig. 1.10 it can be seen that below 700°C the reaction $CO \rightarrow C + \frac{1}{2}O_2$ occurs most readily while above that temperature the reaction $CO_2 \rightarrow CO + \frac{1}{2}O_2$ is likely to be the first to occur as pO_2 is reduced. The problem with the proposed formation of carbon was that with the gas mixtures used for Figs 3.27 and 3.28 pO_2 was not low enough to make it thermodynamically possible. However, it is possible that CO strongly adsorbed onto the platinum did create conditions favourable for carbon formation locally on the electrode surface.

Another possibility is that CO was only electrochemically active when it did not completely cover the platinum surface. At high gaseous CO concentrations and at high temperatures it covered the platinum surface so thoroughly that there were few vacant surface sites left where electrochemical reaction could occur. This was not the favoured theory because adsorption usually gets weaker as temperatures are increased.

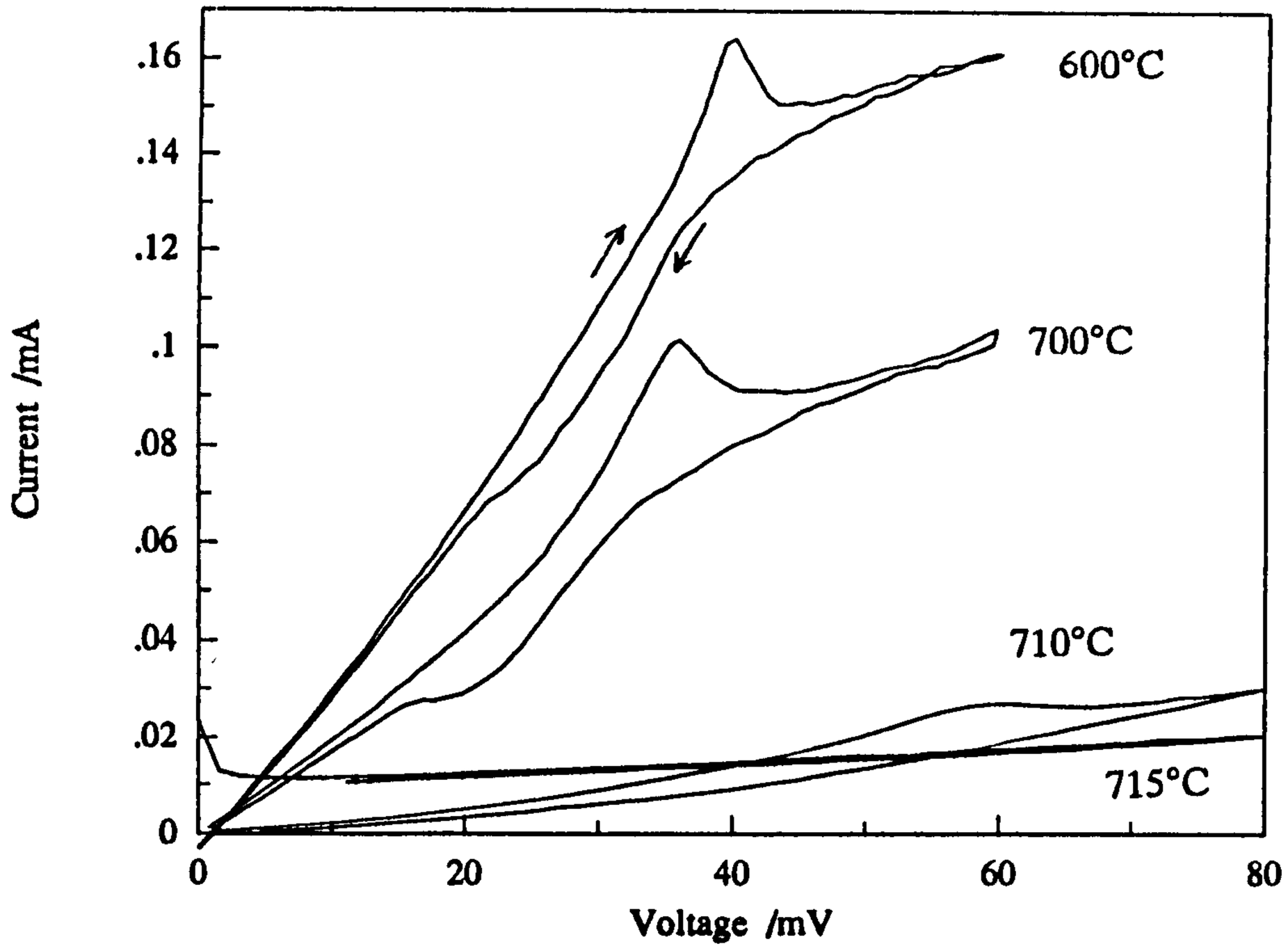

Fig 3.27: Current-voltage (E_{WR}) characteristics of Pt electrode in 0.014% CO, 14% CO_2, balance N_2 at temperatures shown. Measured using CV mode at 1mV/s.

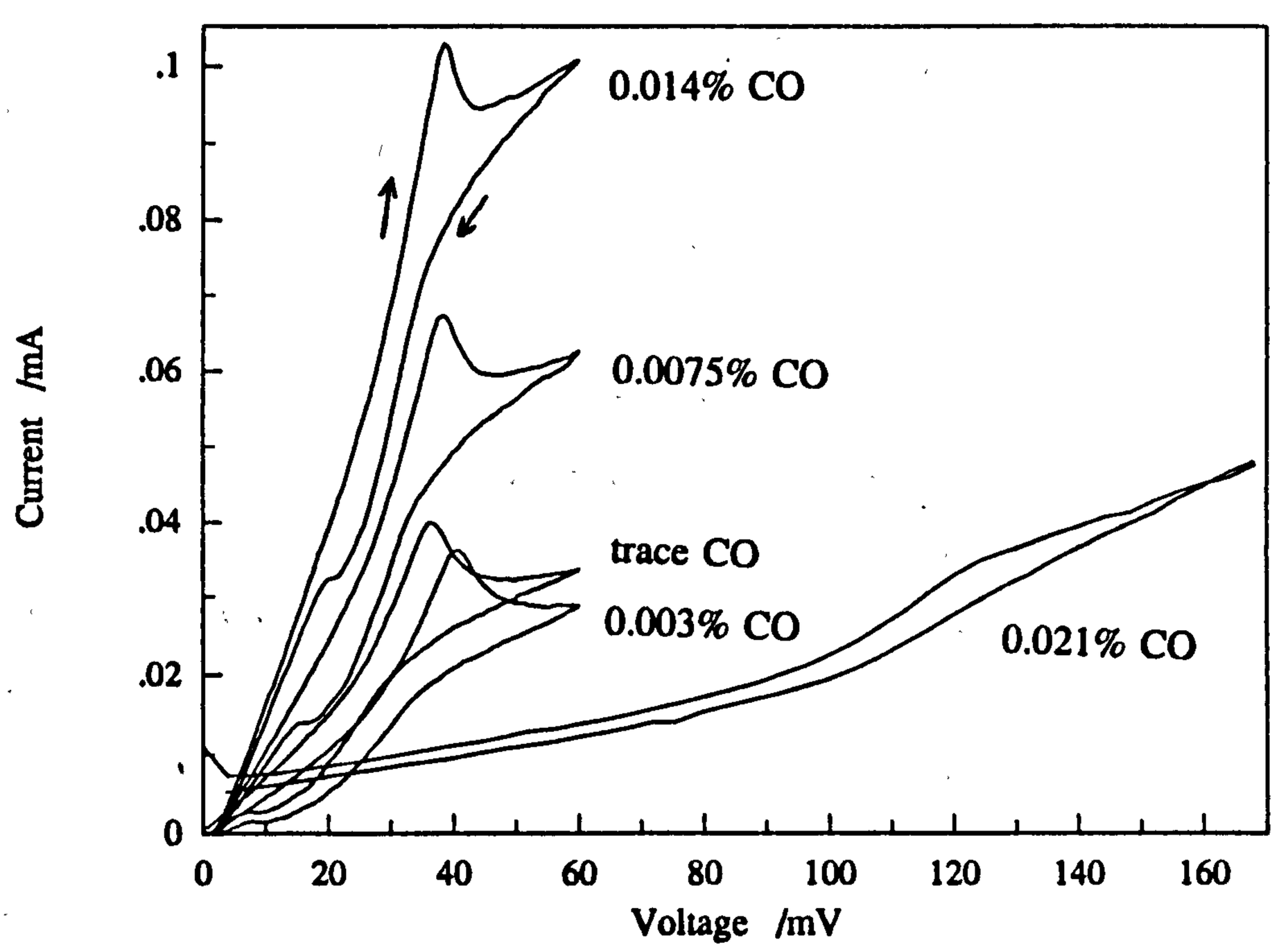

Fig 3.28: Current-voltage (E_{WR}) characteristics of Pt electrode in CO concentrations shown (balance 14% CO_2 and N_2) at 650°C. Measurements taken using CV at 1mV/s.

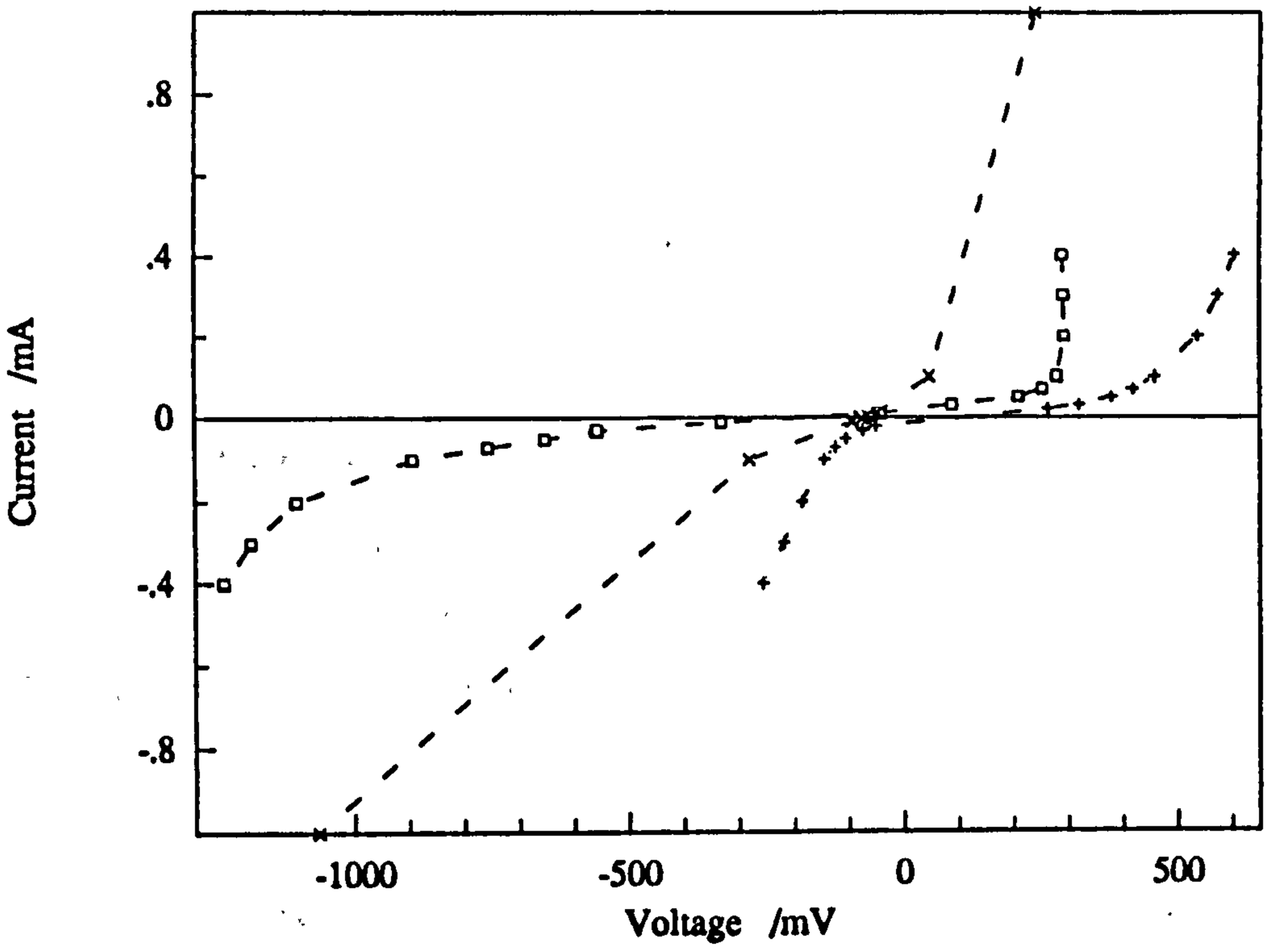

Fig 3.29: Comparison of measured overvoltage as a function of current during 3 tests at 700°C. □, 0.124% CO 96.9% CO_2 and balance N_2; +, 14% CO_2 0.014% CO and balance N_2; ×, 0.12% CO 99% CO_2. □ and + on same disc, × on second disc.

Fig. 3.29 shows 3 sets of results from tests where the CO:CO_2 ratio was about 1:1000 at 700°C. The results were expected to be similar because both cells used were 6Y-YSZ with sputtered and screen printed platinum electrodes and the CO:CO_2 ratio was similar in all cases. The expected oxygen partial pressure was therefore similar. A particularly bad example of non-reproducibility was chosen for Fig 3.29, but the problem was common with CO/CO_2 mixtures and, as discussed in section 3.3, was probably due to a slow responding process in parallel with more rapid processes.

If an attempt were made to fit the Butler-Volmer equation to the data it can be seen that $\alpha_a > \alpha_c$. However, the difference was not as great as it was in O_2/N_2 mixtures.

3.6) Conclusions

This chapter concentrated on experiments performed on single YSZ discs and provided background material for the following chapters on sensors. It was explained how the overvoltage on the working electrode was isolated from the total voltage between the working and reference electrode using current-interruption. This method was used throughout this work. Partly as a test for this method the conductivity of a number of YSZ discs was measured and the results were shown to be reasonable. It was concluded that using Table 3.1 as a guide for separating the overvoltage from the IR drop produced an error of no more than 5% of the applied voltage at temperatures below 650°C. A larger error was possible at 700°C or above because of the limited speed of the ADDA card.

The current voltage characteristics of electrodes made from platinum, silver and gold were then examined. Generally the electrode conductance decreased as pO_2 decreased in O_2/N_2 mixtures. In CO/CO_2 mixtures electrode conductance tended to increase as pCO increased but the opposite trend was sometimes observed at low pCO. It was noticed that for currents greater than i_0 in O_2/N_2 mixtures η_a was significantly smaller than η_c while in $CO/CO_2/N_2$ mixtures the difference was not so large.

Chapter 4

Amperometric sensors in O_2/N_2 mixtures

4.1) Causes of non-ideal response

If an amperometric sensor could be made with no electrochemical leakage it would draw a current independent of pumping voltages above 200mV in O_2/N_2 mixtures. Semipermeability would cause the current to rise at voltages greater than 1600mV at 700°C as seen in Fig. 1.8. It is important to quantify these two leakage mechanisms in order that the sensor output can be more accurately interpreted.

4.1.1 Semipermeability

The theory for semipermeability was discussed in section 1.6.4. A number of measurements of the n-type conductivity of CSZ but only a few of YSZ have been reported in the literature. Kleitz et al (1981c) found up to a 60 fold variation for the reported values of σ_p and σ_n for CSZ so using literature values should be done with care.

Using equation 1.22, and data from Kleitz et al (1981c), it was shown that semipermeability was only a factor at higher pumping voltages. At 700°C the additional current due to n-type semiconductivity was 1μA for 1540mV total applied voltage and 10μA for 1740mV for a sensor with 5.0mm diameter electrodes on YSZ 0.7mm thick operated in air. It was therefore safe to say that electrochemical leakage was the only cause of non-ideal response below 1500mV at 700°C in air. The activation energy for σ_n is high so decreasing the temperature to just 600°C means 1770mV can be applied before leakage of 1μA and 1950mV for 10μA would be expected. At 400°C it is 2240mV for 1μA. Allowing for the uncertainty of the data used it can still be claimed that in this work the amperometric sensors were not

operated in regimes where semipermeability would have been significant. This was done to prevent possible damage to the devices.

4.1.2 Electrochemical leakage

Electrochemical leakage (Kaneko et al (1987)) was the most persistent problem encountered with the sensors used in this work. Any metallic (or electronically conducting) contact between the inside and the outside of a sensor that creates a three phase boundary (TPB) between the zirconia, the metal, and the surrounding atmosphere causes electrochemical leakage. To minimize leakage these external three phase boundaries (ETPB) needed to be kept as short as possible. Alternatively they could be isolated from any substance that could be reduced: ie. any oxygen-containing gas, or any solid containing an easily reduced oxide.

Sensors made using metal ring seals were manufactured in two stages. The first stage was to bond the two zirconia discs together with a ring of the same metal used for the electrodes. This metal seal also served to make the contact between the electrodes and the platinum wires leading to the potentiostat. The second stage was to cover the exposed part of the metal seal with glass paste which was then fired (Benammar and Maskell (1992c)). This helped isolate most of the ETPB and reduced but did not eliminate electrochemical leakage.

To reduce leakage further, glass-sealed sensors were made using glass alone to seal the two YSZ discs together. However, metal tracks were needed to make contact to the internal electrodes. The small area of track exposed to the outside atmosphere caused a small amount of leakage. Fig. 4.1 shows a glass-sealed sensor sectioned through the seal and facing the internal pumping electrode. The small contact pad where the external lead was attached is marked and a possible path through the YSZ taken by the oxygen ions originating at the pad is also illustrated.

In Fig 4.2 the paths taken by the oxygen ions are illustrated on a section cut through the zirconia discs of the sensor. Note that each of the two cells comprising a pump-gauge sensor make their own contribution to the leakage. Negligible current flows between the electrodes of the gauge cell so the electrochemical leakage on it essentially lets more oxygen into the chamber. The potential on the external

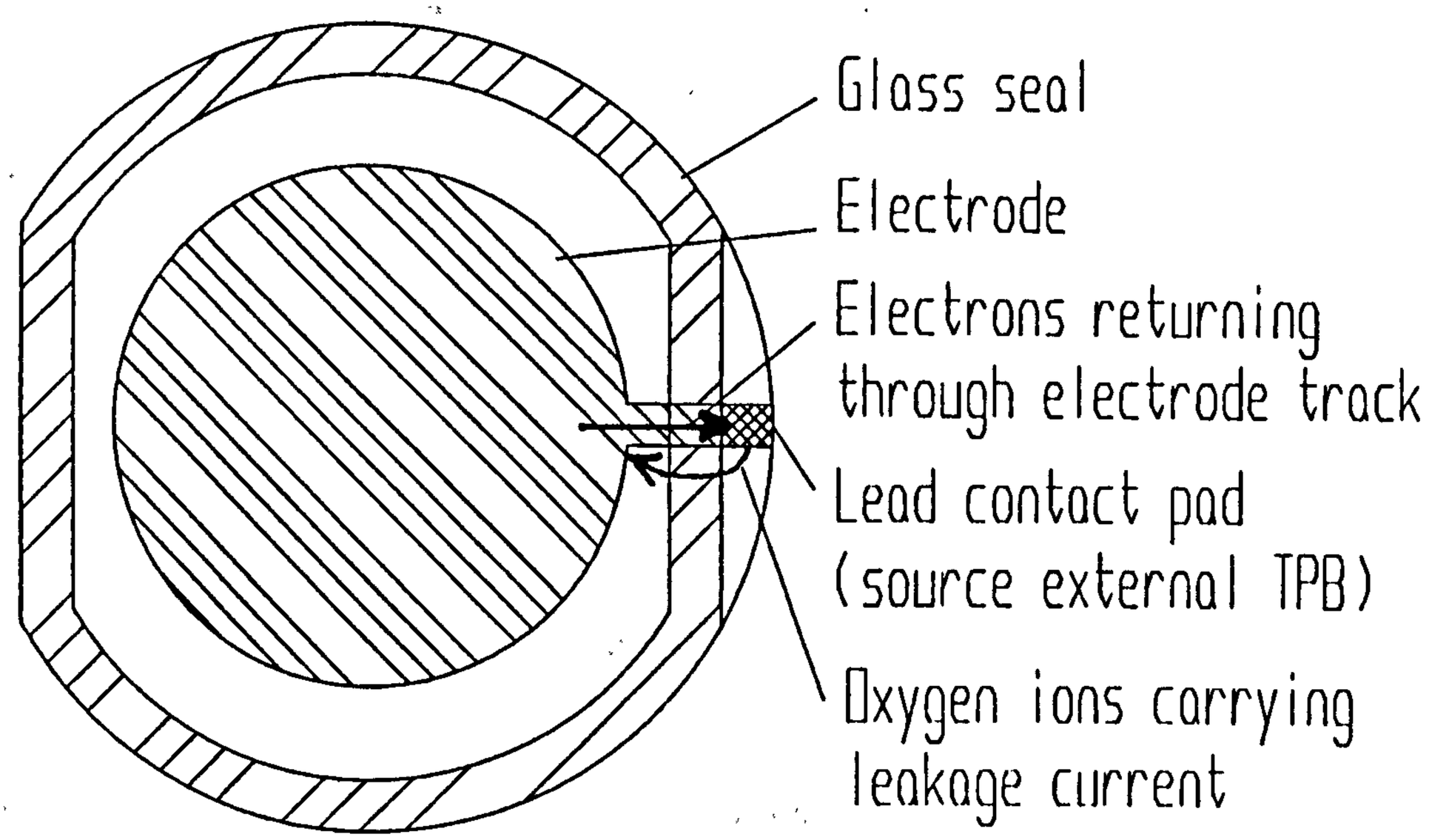

Fig. 4.1: **Section through the seal of a glass-sealed sensor showing the sub-cell that caused electrochemical leakage.**

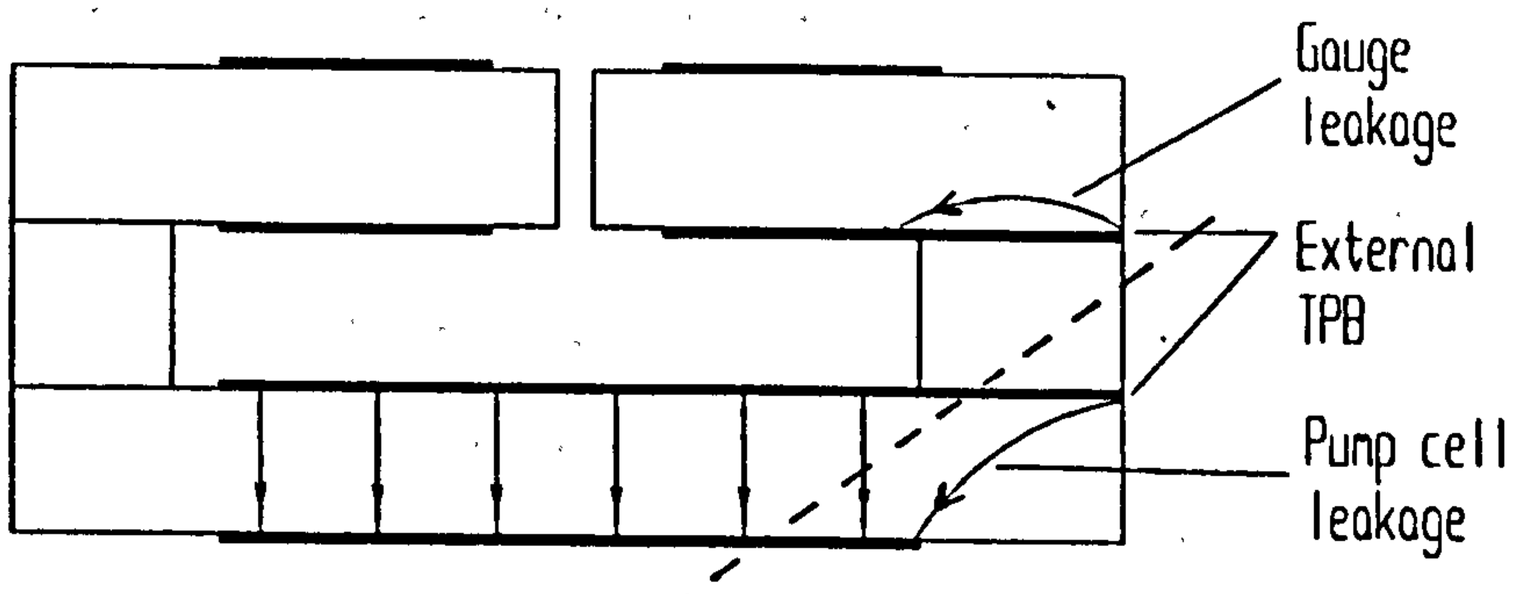

Fig. 4.2: **Section through the YSZ discs of a sensor showing the different paths taken by the oxygen ions in the gauge and the pumping cells.**

pumping electrode attracts all the oxygen ions so the ETPB on this cell acts as a second cathode from which extra oxygen is pumped. If only the part of the sensor below and to the right of the dashed line of Fig. 4.2 is considered it can be seen that a sub-cell is formed. It has a small cathode (the ETPB) and a large anode (the pump electrode), both of which are exposed to the same atmosphere.

Since the cathode (or the ETPB) was relatively very small it was assumed that the resistance to electrochemical leakage was predominantly located there. Therefore, on the gauge cell of the sensor, the overvoltage at the ETPB was equal to the potential between the internal and external electrodes.

On the pump cell the oxygen ions from the ETPB share the anode with the ions from the internal electrode. They therefore share the same anodic overvoltage. Consequently, the overvoltage on the ETPB was equal to the potential between the internal pumping electrode and the external reference electrode (E_{WR}).

To estimate electrochemical leakage it was assumed, as a first approximation, that both ETPB's would obey the Butler-Volmer equation (eqn(1.18)) with both having the same coefficients for this equation. Greater accuracy in interpreting the experimental results was obtained by using this method to compensate for electrochemical leakage (see section 4.2.3).

While the above method was useful it was only approximate for several reasons. Firstly, it was shown in chapter 3 that electrodes do not obey the Butler-Volmer equation. Secondly, when pO_2 inside the sensor is very low the electrode resistances of the internal electrodes increase by more than two orders of magnitude. The leakage current will therefore no longer be determined by the ETPB alone, and a small overvoltage could develop on the internal gauge electrode. Thirdly, the exchange currents of the two ETPB's will not be the same.

4.2) Results and interpretation

4.2.1 Approaching the limiting current state

The current that flows in an amperometric sensor obeys eqn(1.17) approximately. By using the gauge voltage (E_g) as an indication of $p'O_2$ (oxygen

partial pressure within the enclosed volume) any overvoltages on the pumping electrodes are eliminated from the equation. Therefore, the equation models the current voltage characteristics of sensors over a wide range of conditions. However, as discussed in chapter 1, the flow correction ($-\ln(1-X_{O2})$) needs to be included for accurate interpretation of results where the oxygen concentration is above a few percent. A more general and accurate equation was derived by substituting the Nernst equation (eqn(1.7)) into eqn(1.13). Thus:

$$I = \frac{4FDA_pP}{RT\ell}\ln\left(1 - X_{O_2}\left(1 - \exp\left(\frac{4FE_g}{RT}\right)\right)\right) \qquad (4.1)$$

Figs. 4.3 to 4.6 show the results of tests done on the two glass-sealed sensors, G1 and G2. Fig. 4.3 shows that eqn(4.1) could model the pump current (I_p) of sensor G1 as a function of the gauge voltage (E_g), but that I_p vs. the pump voltage (E_p) deviated from the predicted line. Fig. 4.4 presents results measured at the lower temperature of 450°C so the overvoltages on the pumping electrodes were larger as was the IR drop through the electrolyte. The figure shows I_p vs. the voltage between the internal pump electrode and the external reference electrode (E_{WR}) and I_p vs. the overvoltage on the internal electrode (η_c). η_c was calculated by subtracting the Nernst (gauge) voltage from the value of $E_{WR}(t)$ at the time when the IR drop had decayed to a negligible value (see Table 3.1). Therefore:

$$E_{WR}(0) = \eta_c + E_g + \text{IR drop.}$$

I_p vs. E_p ($E_p = \eta_c$ + full IR drop + η_a + E_g) was also plotted. Despite the large deviation between eqn(4.1) and I_p vs. E_p there was little deviation between this equation and E_g.

The gauge voltages shown in fig. 4.5 did not agree as well with eqn(4.1) as those shown in Fig. 4.4 because sensor G2 was only given about 7 minutes to stabilise at each pump voltage setting. This was too short a time for the gauge cell to reach equilibrium at the relatively low temperature of 500°C. The results reflected in Fig. 4.4 were taken after more than 20 minutes so closer agreement with the Nernst law was achieved, even at 450°C. At 400°C (Fig. 4.7) the error in E_g increased suggesting that 20 minutes was still not long enough for the electrodes to reach equilibrium at that temperature. Young (1983) and many others found large deviations from the Nernst law below 400°C although they did not say how long they

waited for equilibrium. The accuracy of E_g readings was assessed more carefully in section 4.2.4 after compensating for electrochemical leakage.

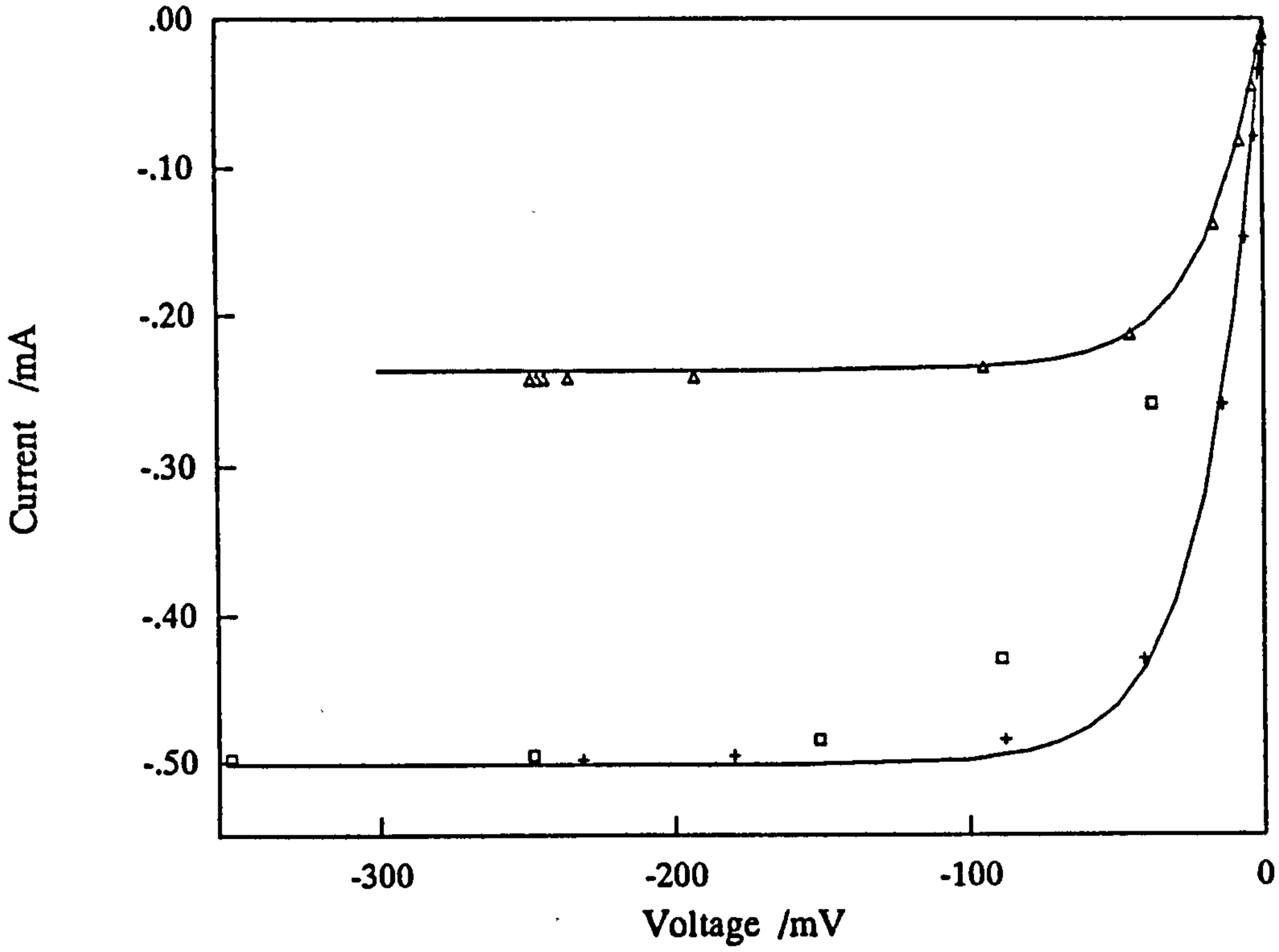

Fig. 4.3: Current - voltage characteristics of sensor G1 at 650°C. ——, theoretical responses (eqn(4.1)) for I_p vs. E_g assuming pore diameter (θ_p) of 50.0μm. +, I_p vs. E_g in air; Δ, I_p vs. E_g in 10.5% O_2; □, I_p vs. E_p.

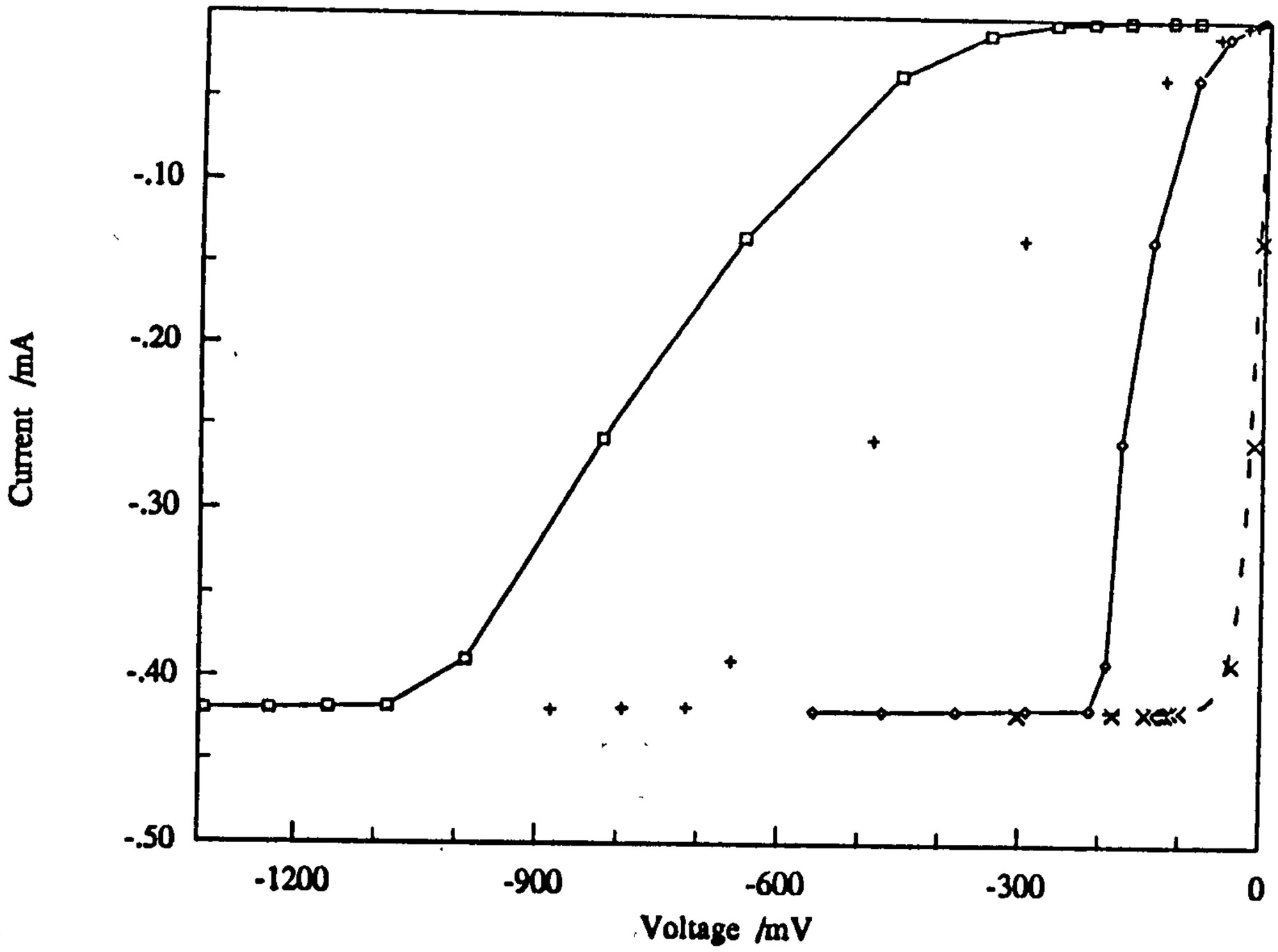

Fig. 4.4: Current - voltage characteristics of sensor G1 at 450°C in air. - - -, theoretical response assuming θ_p = 50.0μm; ×, I_p vs. E_g; .–◇–, I_p vs. cathodic overvoltage; +, I_p vs. E_{WR}; –□–, I_p vs. E_p.

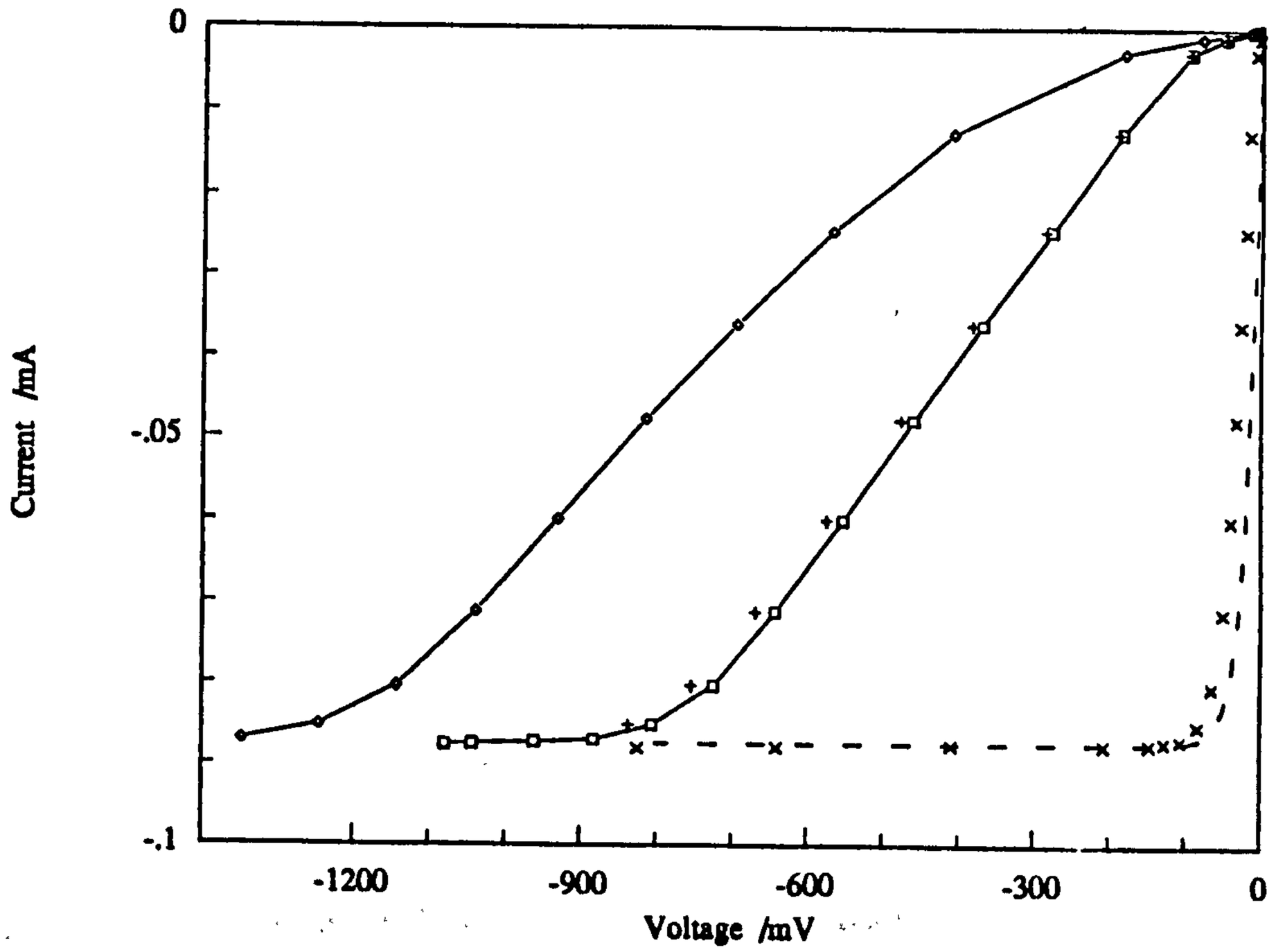

Fig. 4.5: Current - voltage characteristics of sensor G2 at 500°C in air. - - -, theoretical response assuming θ_p = 22.3μm; ×, I_p vs. E_g; –□–, η_c; +, E_{WR}; –◇–, E_p.

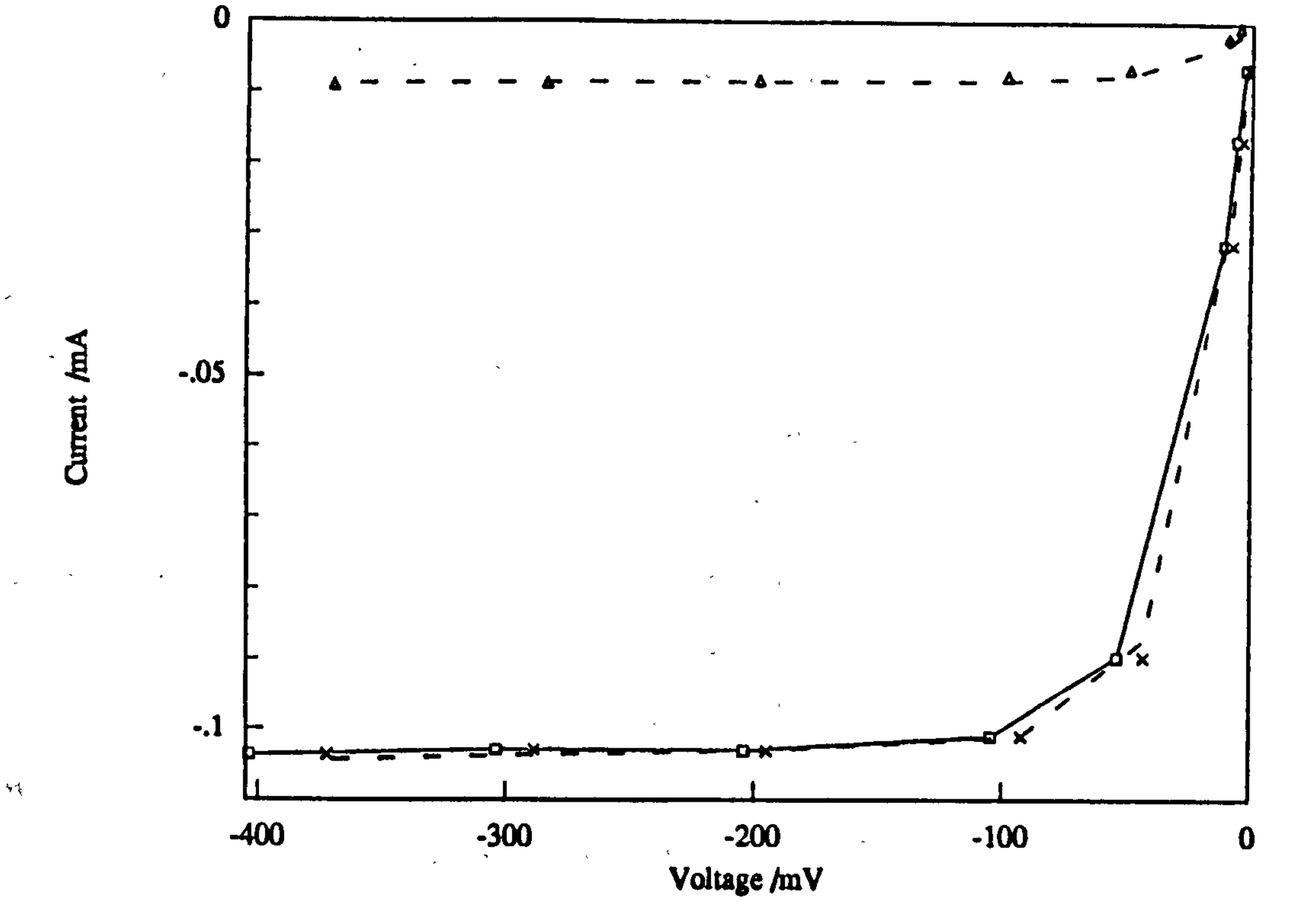

Fig. 4.6: Current - voltage characteristics of sensor G2 at 700°C and . - - -, theoretical responses assuming θ_p = 22.3μm; ×, I_p vs. E_g in air; –□–, I_p vs. E_p in air; Δ, I_p vs. E_g in 1.9%O_2.

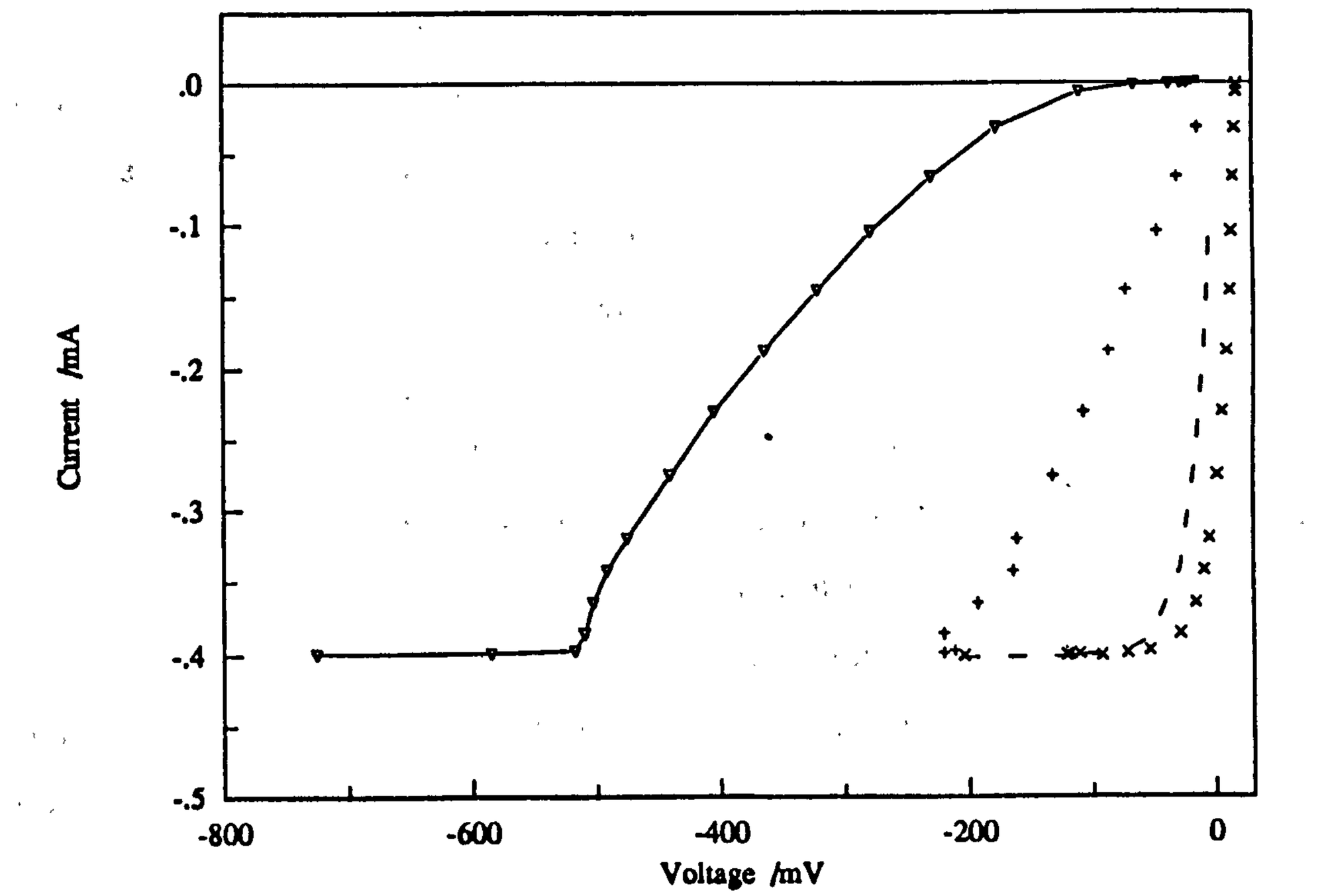

Fig. 4.7: Current - voltage characteristics of sensor G1 at 400°C in air. - - -, theoretical I_p vs. E_g assuming θ_p = 50.1μm; ×, I_p vs. E_g; –∇–, I_p vs. η_c; +, IR drop measured between WE and RE;

4.2.2 Electrochemical leakage on silver seals

An experiment was done to illustrate how the application of a glass layer over a metal seal reduced electrochemical leakage. A sensor made with a silver metal seal and silver electrodes was used. Figs. 4.8 and 4.9 show the results, at 600 and 750°C respectively, before and after glass was applied to the outside of the silver seals. The sensor was tested in air by cyclic voltammetry at 20mV/s with the applied voltage being made increasingly anodic initially. It was apparent that the cathodic currents were much lower after the application of the glass. The current also showed a greater inclination to form a plateau showing that the glass did not simply plug a leak where diffusion could occur.

The glass coating did not totally eliminate this leakage because the currents achieved showed a strong temperature dependence: 1mA at 750°C, 0,4mA at 600°C and 0,2mA at 500°C (measured at 450mV). Therefore, although putting a layer of glass over the external metal-zirconia interfaces of metal-sealed sensors helped a lot, it did not cure the problem. A likely cause was thought to be incomplete coverage of the zirconia-metal interface by the glass. It was also possible that the glass at the interface was partially reduced and that the oxygen from the reduction caused a small current. Another possibility was that electronic (and possibly ionic) conduction was induced in the glass by the reducing conditions.

An important compound in glass is usually silica. Fig. 1.10 shows that silica is more easily reduced than zirconia. It was therefore reasonable to assume that it would be partially reduced before zirconia and thus become an ionic and/or electronic conductor. Glasses contain many oxides and it is likely that many of these may be more easily reduced than silica. Therefore glass should not be allowed to come into contact with the electrode (which includes the metal of a metal seal) where the oxygen activity is the low.

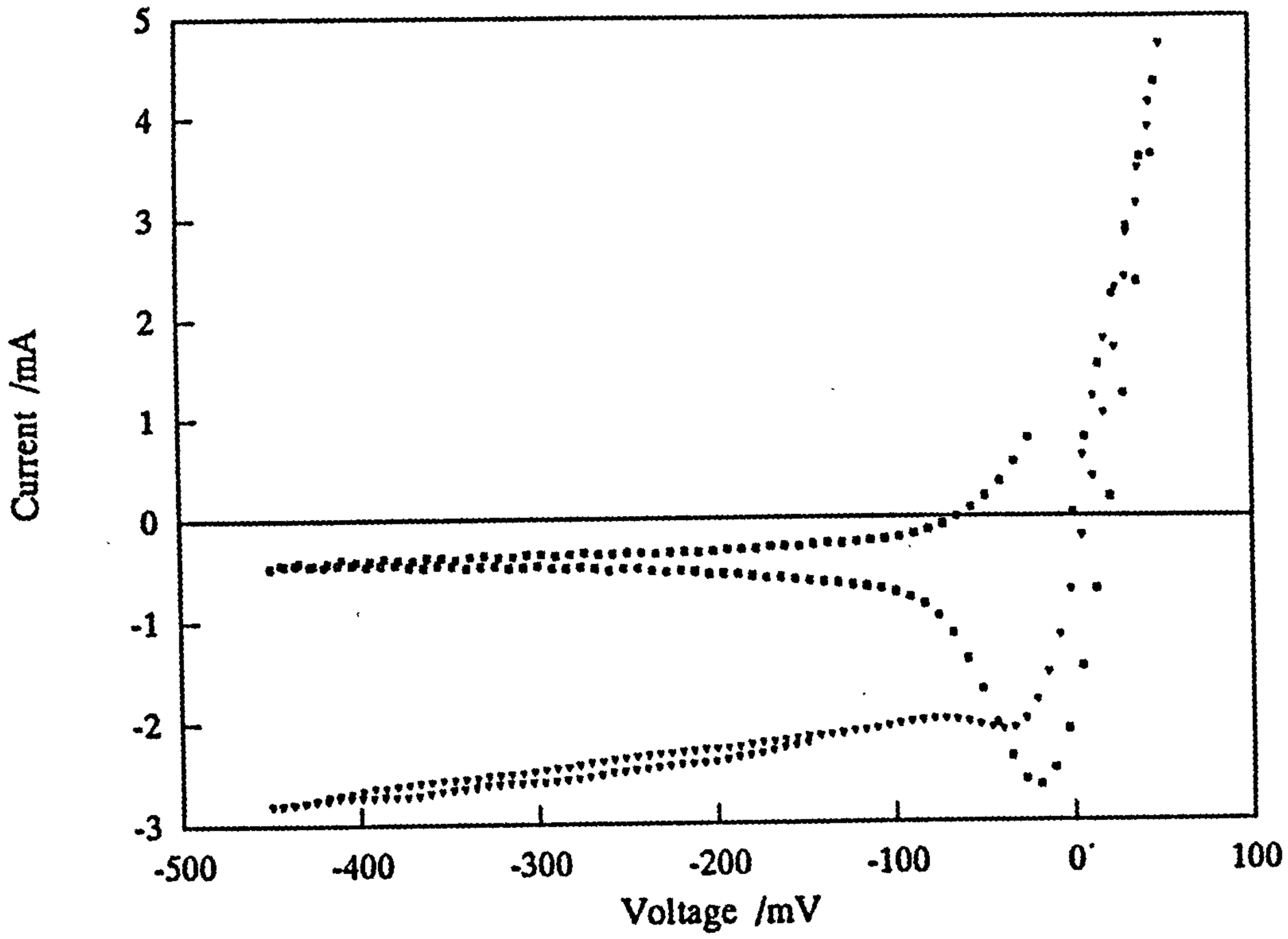

Fig. 4.8: Response of silver sensor to sawtooth voltage waveform 20mV/S. Sensor at 600°C in air. ∇, bare metal seal; □, glass covered seal.

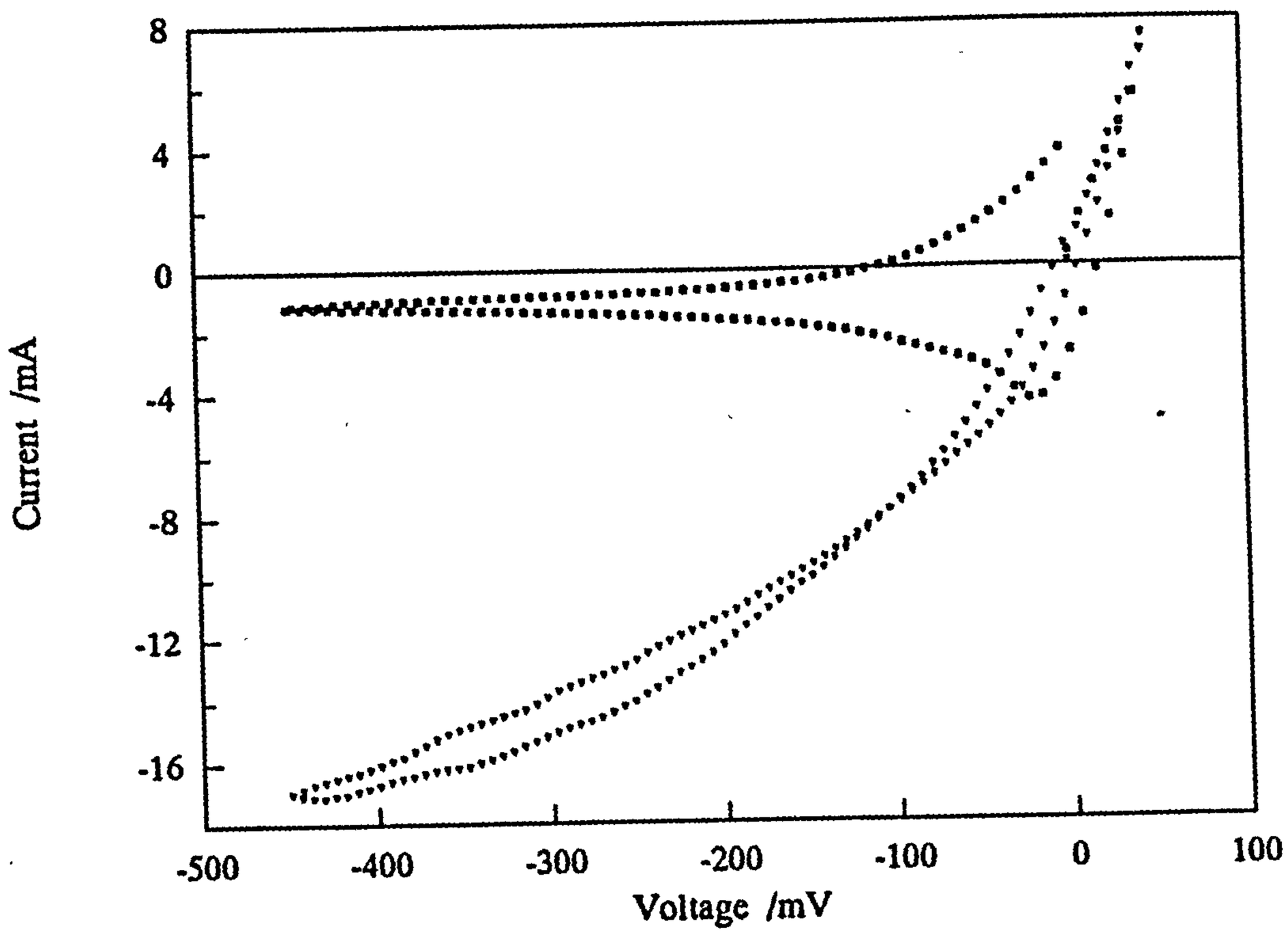

Fig. 4.9: As Fig. 4.8 but at 750°C.

A large peak in the cathodic current was apparent at low voltages presumably due to the removal of oxygen absorbed on or dissolved in the silver within the sensor (Haaland (1980)). This dissolved oxygen increased the response time of the sensor compared to one made from platinum which did not produce such large cathodic peaks (see section 6.2).

To determine the steady-state currents a much slower scan was needed but the sensor failed before these tests could be done. This was a repeated feature of silver sensors and was shown to be due to the formation of fine tracks of silver on the surface of the glass covering the seal (clearly visible under a microscope). The tracks grew between the tags of silver used for sealing the sensor and as electrode contacts. The tracks created a short circuit and their growth seemed to be associated with the applied voltage on the two tags between which they grew. If the tracks were ground away the short circuit problem disappeared for a while, but application of a voltage difference on the tags made it reform within tens of hours.

The silver electrodes tested produced current densities comparable with the better platinum electrodes. Silver was therefore considered a promising electrode material provided that the track formation problem could be solved.

4.2.3 Estimating the electrochemical leakage

Fig. 4.10 shows the results of operating sensor G1 in air at 750°C. The solid line with a plateau at I = -0.52mA represents the theoretical current (eqn(4.1)) assuming no electrochemical leakage and a pore diameter of 49.5μm. The dashed line is the sum of the previous result and an estimate for leakage assuming an exchange current (I_0) of 1.0μA on each cell and $\alpha_c = 0.30$. Since α_a had little affect on the results it was assumed to be 1.5 for all leakage estimations. The difference between the theoretical current (including leakage) and the actual current was multiplied by 10 to clarify the magnitude of this difference (plotted as (□) in Fig. 4.10).

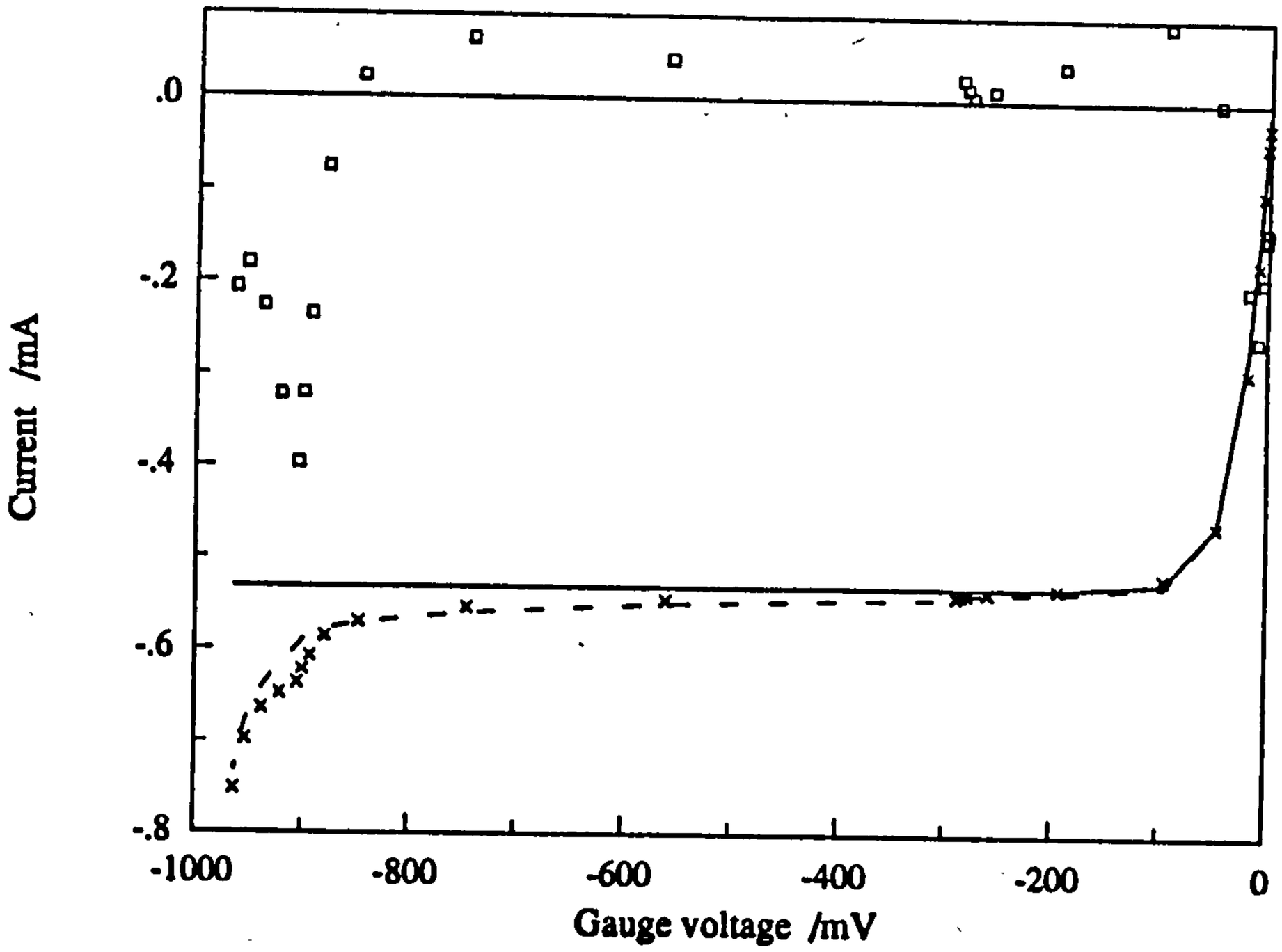

Fig. 4.10: Sensor G1 in air at 750°C. ×, measured current vs. gauge voltage; ——, theoretical current assuming no electrochemical leakage; - - -, theoretical current after adding contribution from leakage; □, deviation between results and theory multiplied by 10. θ_p = 49.5μm, I_0 = 1.0μA, α_c = 0.30.

An interesting feature of sensor G1 was that the gauge voltage would remain almost constant while the pump voltage was increased over a relatively wide range. Fig. 4.11 is similar to Fig. 4.10 except that G1 was at 700°C. While E_p increased from -260 to -680mV E_g only increased from -250 to -260mV. The difference was taken up by a large increase in the overvoltage on the internal pumping electrode also shown on Fig. 4.11. In chapter 3 it was demonstrated that the overvoltages, for a given current, increases as the oxygen partial pressure decreases. This was probably a partial explanation for the rapid increase in overvoltage seen on sensor G1.

While E_g remained almost constant during the above mentioned process the electrochemical leakage on the gauge cell changed little. However, E_p increased significantly so the leakage on the pumping cell also increased. Careful inspection of Figs 4.10 and 4.11 reveals how the above theory was able to account for the small step increase in current that occurred while the E_g was nearly constant. They also illustrate how well the theory was able to account for the rapid rise in current as the

E_g approached -1000mV. Again, this was due to E_g increasing much more slowly than E_p causing a rapid increase in electrochemical leakage on the latter cell.

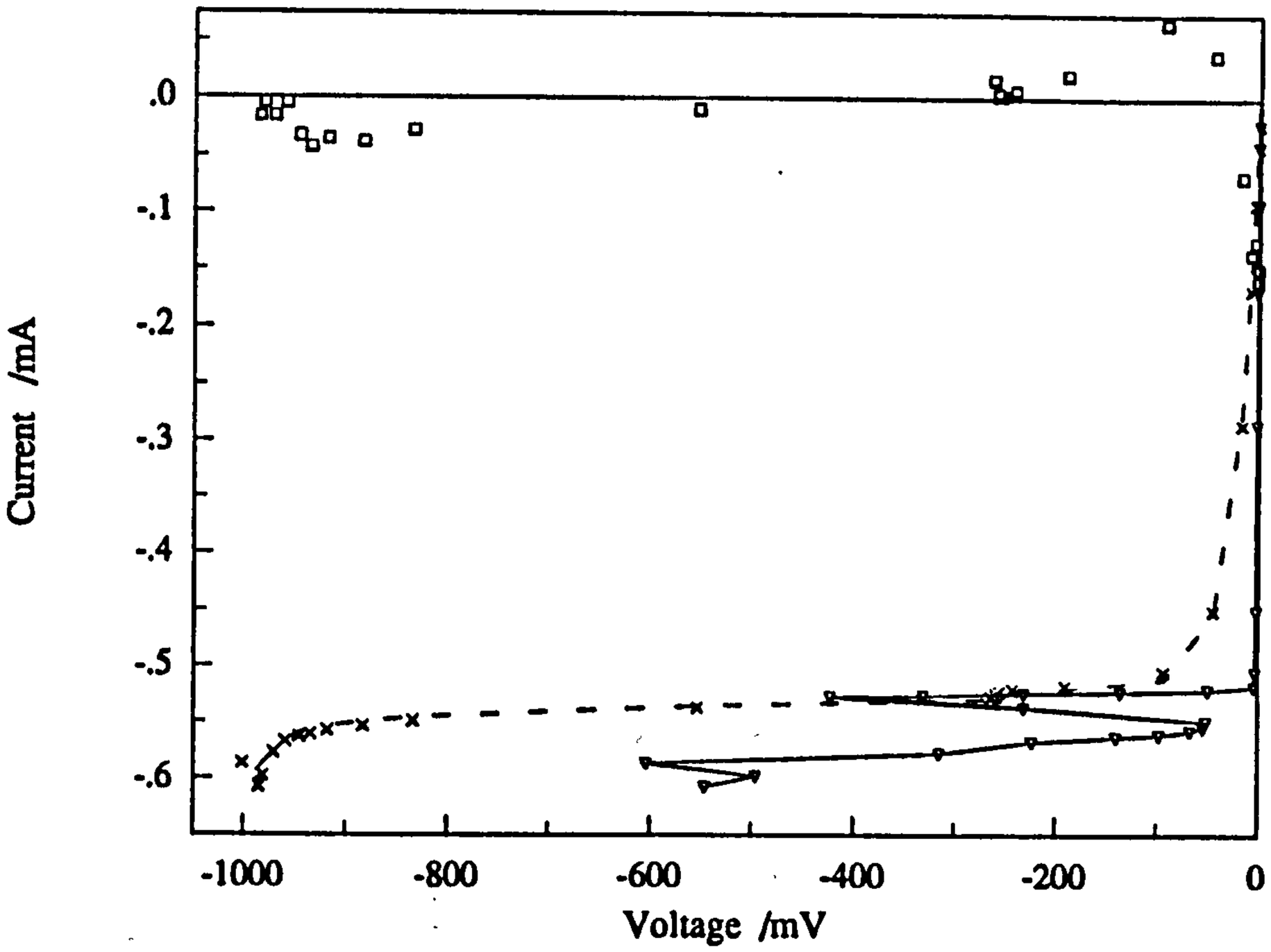

Fig. 4.11: Sensor G1 in air at 700°C. ×, measured current vs. gauge voltage; - - -, theoretical current including contribution from leakage; □, deviation between results and theory multiplied by 10; –∇–, overvoltage on internal pumping electrode. θ_p = 49.5μm, I_0 = 3μA, α_c = 0.17.

Fig. 4.12 illustrates the results from sensor G2 in air at 700°C. Summing the electrochemical leakages from each cell allowed the theory to account for the observed current within 1% between 100 and 700mV. Above 700mV the leakage current made a larger contribution to the measured current and deviated significantly from the fitting parameters of the Butler-Volmer equation. Below 100mV the source of error was the deviation between the gauge voltage and Nernst's law which is discussed below.

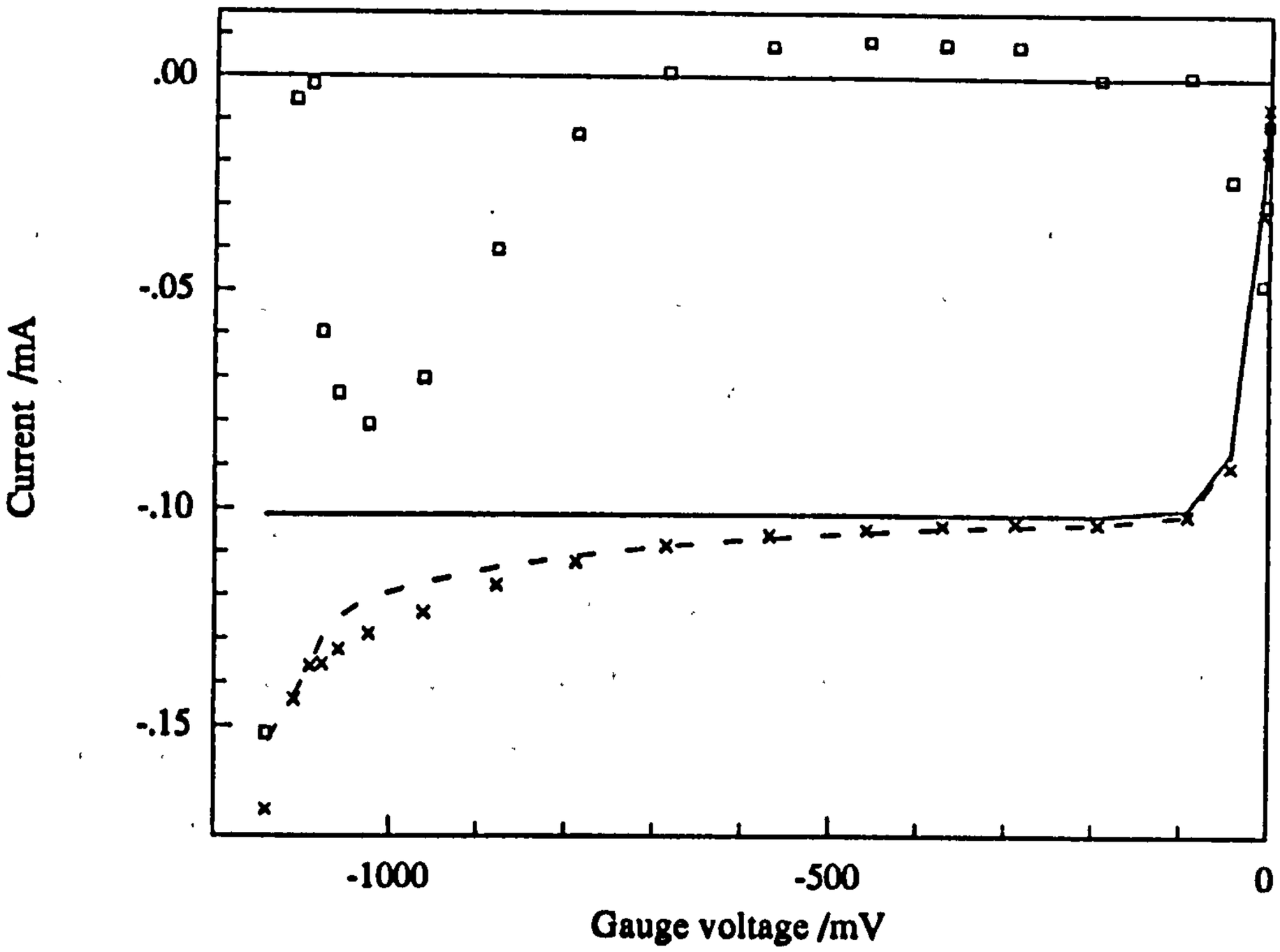

Fig. 4.12: Sensor G2 in air at 700°C. Symbols as Fig. 4.10. θ_p = 22.0μm, I_0 = 0.6μA, α_c = 0.22.

In chapter 3 it was explained how observed α_c values typically range from close to zero to 0.5. The α_c values in the above three examples are within this range. The I_0 values required to model the leakage provide an approximate indication of the size of the ETPB causing the leakage. The area equivalent of the ETPB was estimated using the data presented in Fig. 3.24 as a model for electrode activity. The current through the cell was -9.2mA when η_c was -500mV. Sensor G1 was not tested in the same O_2 concentration (0.8%) but it was tested at 1.9% and 0.41% O_2 in N_2. The coefficients used to model the leakage in these mixtures at 700°C were I_0 = 0.4μA and 0.17μA and α_c = 0.18 and 0.22 repectively. The predicted leakage currents on each cell at -500mV were 1.17 and 0.63μA respectively. These values are 4 orders of magnitude lower than on the 19.6mm^2 electrode used for the comparison. The equivalent area of the ETPB on each cell of G1 was therefore 2×10^{-3}mm^2. If the TPB was 2μm wide as suggested by Brook and Markin (1973) the TPB would have been 1mm long which was not unreasonable considering the sensor design.

4.2.4 Accuracy of the gauge cell

Having quantified the major source of non-ideal behaviour in the sensors it was possible to estimate the error in the gauge voltage. When the current is at a plateau and is almost independent of the pumping voltage, any error in the gauge voltage has little effect on the accuracy of eqn(4.1). At low voltages where the current is changing rapidly the gauge voltage error is the major source of total error.

To quantify this error it was assumed that the parameters (θ_p, I_0, and α_c) fitted as above were exact and that eqn(4.1) would have been exact if E_g had obeyed the Nernst law. The results in table 4.1 show how the error in E_g on sensor G1 increased as the temperature dropped below 500°C. The sensor was given an average of 20 minutes at each E_p setting to reach equilibrium. Above 500°C the estimated error in E_g was less than 3mV with no obvious temperature dependent trend. This agrees with Perfilyev and Fadeev (1984) who found that the lower limit for accurate compliance with the Nernst law was 500°C if 10 minutes was allowed to reach steady state. Etsell and Flengas (1972) proposed that the formation of oxides such as PtO, Pt_3O_4 and PtO_2 prevented platinum electrodes from giving an accurate Nernst potential below 500°C.

Table 4.1

Comparison of measured gauge voltage (on G1) with theory based on eqn(4.1) as a function of temperature and pO_2.

Temperature °C.	Oxygen concentration (percentage in N_2)					
	20.9% O_2		5.225% O_2		0.41% O_2	
	E_g measured	E_g theoretical	E_g measured	E_g theoretical	E_g measured	E_g theoretical
750	-8.02 -17.2	-9.69 -19.1	-4.37 -9.04	-4.88 -9.65	-4.52 -19.39	-3.85 -17.62
600	-8.75 -30.32	-10.68 -32.8	-7.33 -16.76	-8.57 -17.53	-4.23 -19.24	-3.47 -15.94
500	-1.46 -7.14	-2.87 -9.22	-3.94 -18.51	-6.29 -21.53	-3.35 -17.49	-4.28 -17.1
450	+3.06 -9.91	-1.5 -16.1	-3.21	-17.41	+3.94 -7.14	-4.96 -14.8
400	+8.75 -5.1	-9.99 -24.6	-0.44 -72.3	-39.9 -81.2	+20.99 -10.79	-13.2 -35.1
350			+80.9 -2.33	-3.98 -70	+63.55 +32.65	-5.1 -30.1

4.2.5 Current as a function of temperature

Sensor G1 was tested at temperatures between 750 and 350°C at 50°C intervals. The results using air were used to calibrate the effective pore diameter since the oxygen content of the dry (bottled) air used could be confidently taken to be 20.9%. Figs 4.10 and 4.11 above represent the results at 750 and 700°C respectively. Figs 4.13 and 4.14 below represent the results at 600 and 500°C

respectively.

The deviation from theory multiplied by 10 was plotted on all these graphs and it can be seen that the deviation was generally less than 1%. In order to reach this level of accuracy it was found that the assumed pore diameter had to be increased slightly as the temperature dropped. At 750°C it was 49.5μm and at 500°C it was 49.8μm. This adjustment may have been needed because the temperature dependence of the bulk gas diffusion coefficient of O_2/N_2 mixtures was slightly less than the value of $T^{1.75}$ actually used (see eqn(A1.29)). Usui et al (1989b) found a $T^{1.73}$ dependence in O_2/N_2 mixtures in agreement with the above observation. Alternatively, the shape of the diffusion pore (annular because of the platinum wire) could have caused Knudsen diffusion to make a small contribution to the bulk diffusion coefficient. The experimental results from sensor G2 were not as accurate because of the relatively larger contribution from the leakage current; compare Figs.

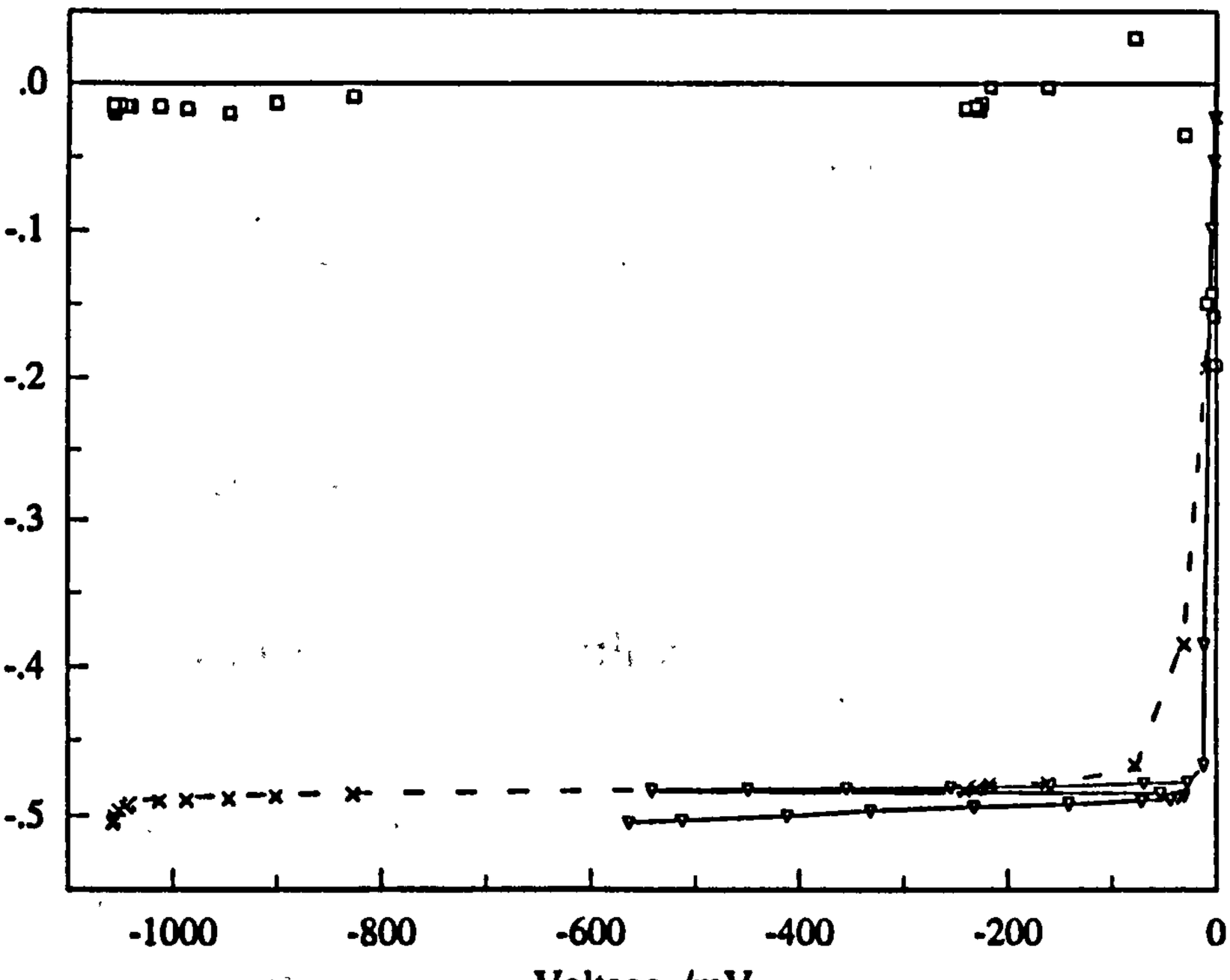

Fig. 4.13: Sensor G1 in air at 600°C. ×, measured current vs. gauge voltage; - - -, theoretical current including contribution from leakage, I_0 = 80nA, α_c = 0.13; □, deviation between results and theory multiplied by 10. –∇–, overvoltage on internal pumping electrode.

4.10 and 4.12. Less extensive results were also obtained so it was not possible to compare temperature dependence data. However, the same trend was observed because the pore diameter that fitted the data changed from 22.2μm at 500°C to 22.0μm at 700°C. The smaller pore could have caused a contribution from Knudsen diffusion.

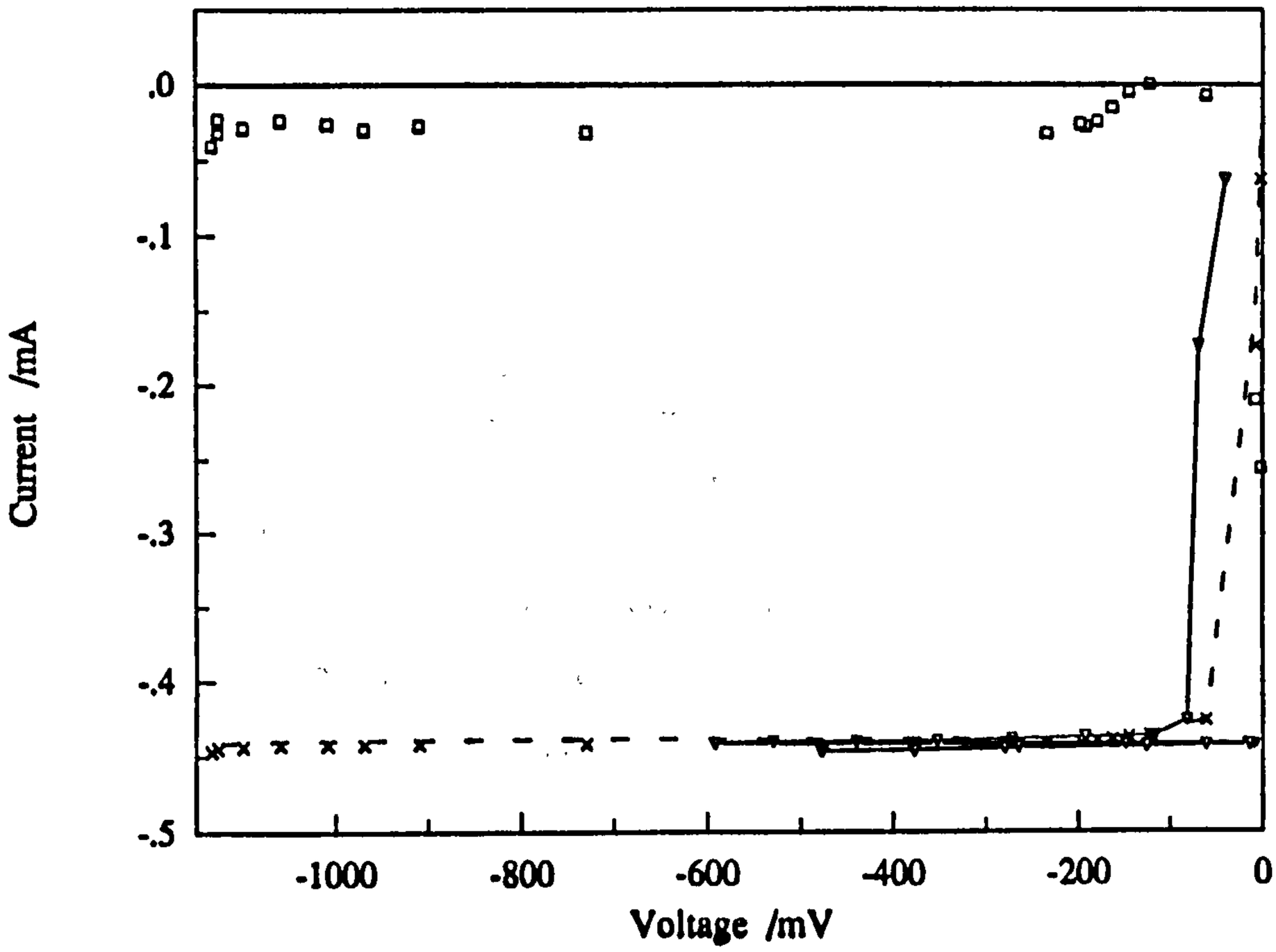

Fig. 4.14: Sensor G1 in air at 500°C. Symbols as Fig. 4.14.

4.2.7 Current as a function of pO_2

Sensor G1 was tested in oxygen concentrations ranging from 20.9% (air) to 0.1%. At all concentrations it was possible to find a value of I_0 and α_c that accurately modelled the results. No adjustment was needed to the pore size, used to model the air results, at any temperature. Figs. 4.15 to 4.18 below and 4.13 above show results using a range of oxygen concentrations; all at 600°C with sensor G1.

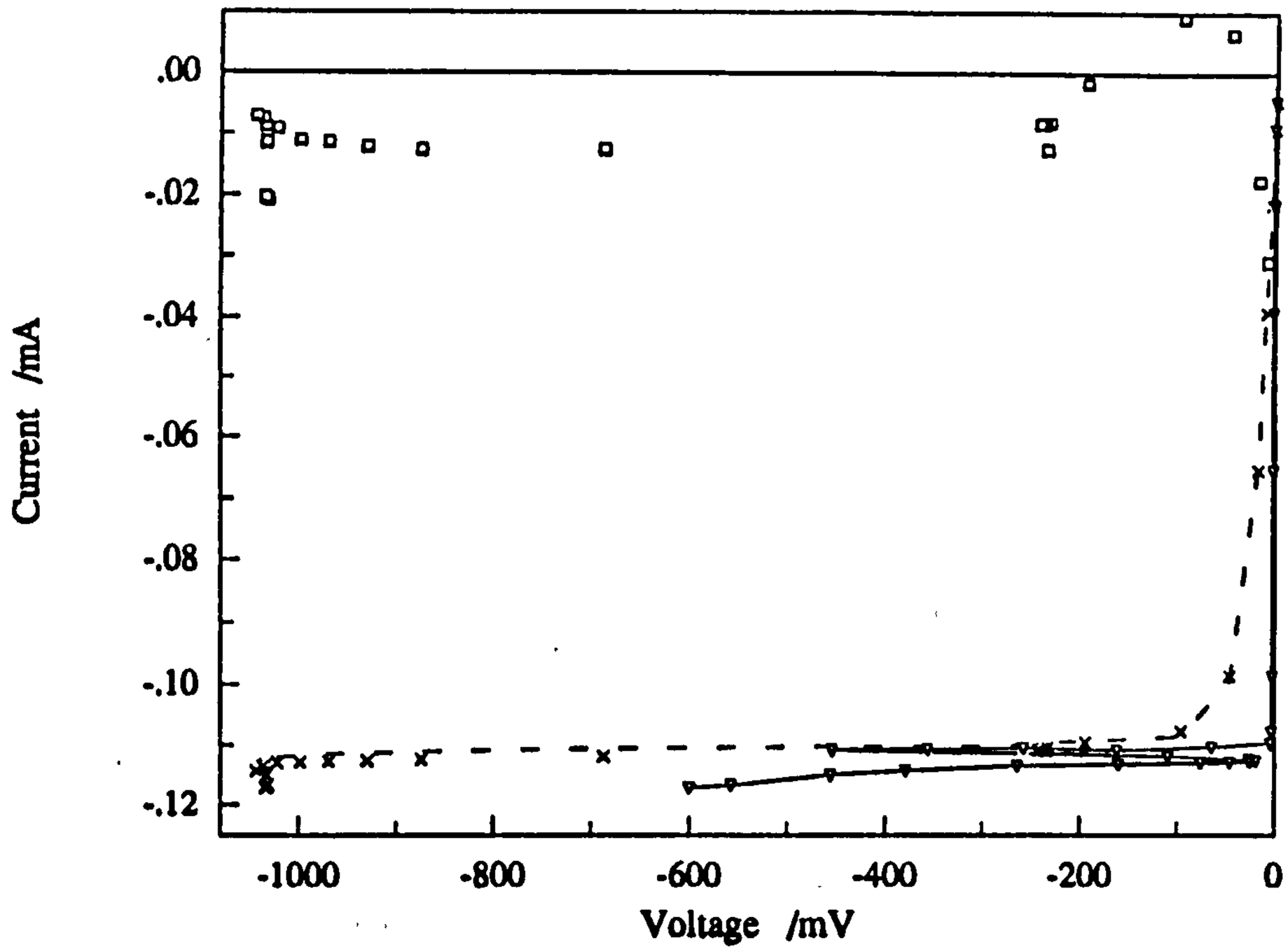

Fig. 4.15: Sensor G1 in 5.225%O_2 balance N_2 at 600°C. ×, measured current vs. gauge voltage; - - -, theoretical current including contribution from leakage, I_0 = 0.2μA, α_c = 0.14; □ deviation between results and theory multiplied by 10. –▽–, overvoltage on internal pumping electrode.

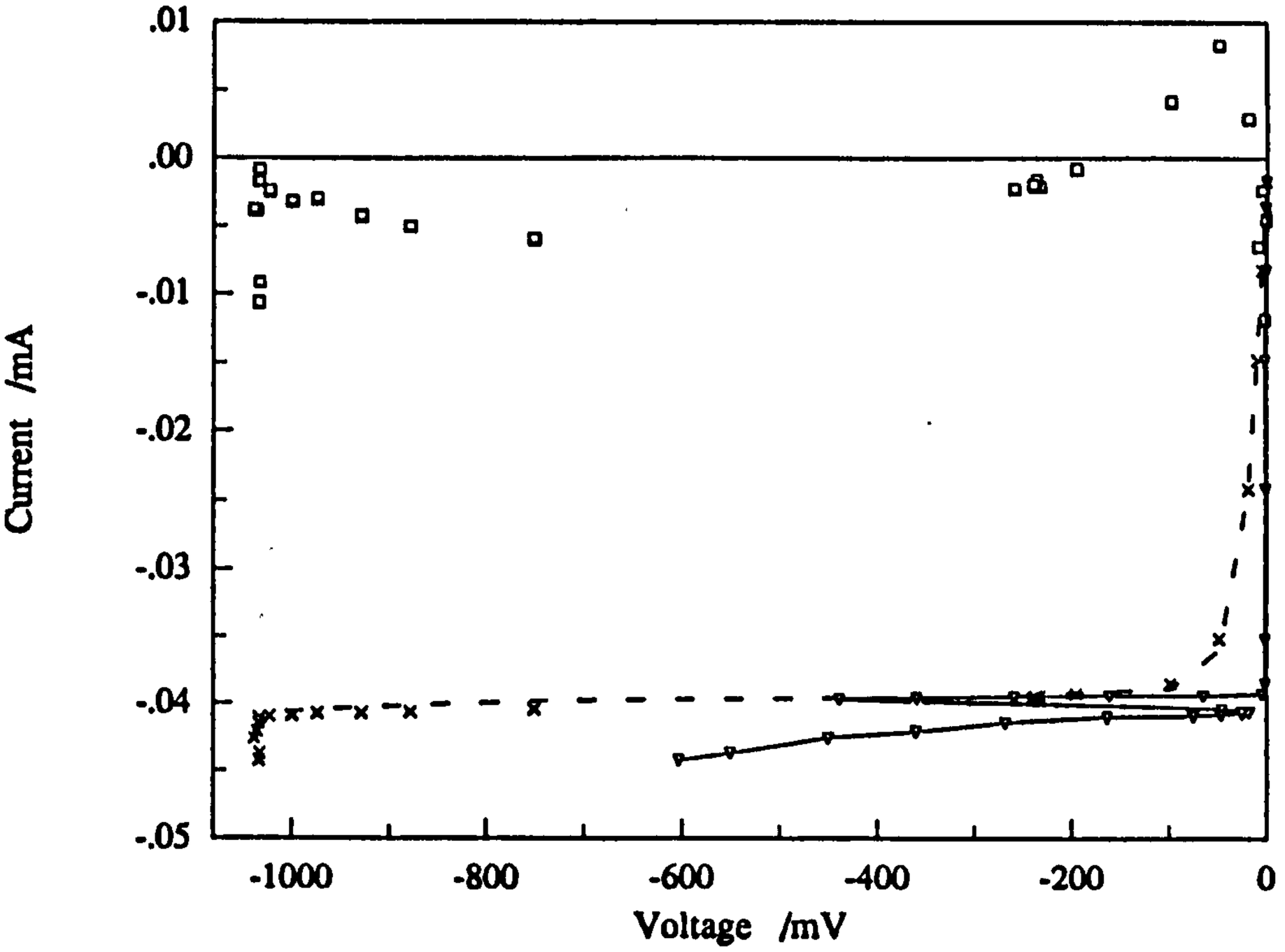

Fig. 4.16: Sensor G1 in 1.9%O_2 balance N_2 at 600°C. Symbols as Fig. 4.15, I_0 = 80nA, α_c = 0.17.

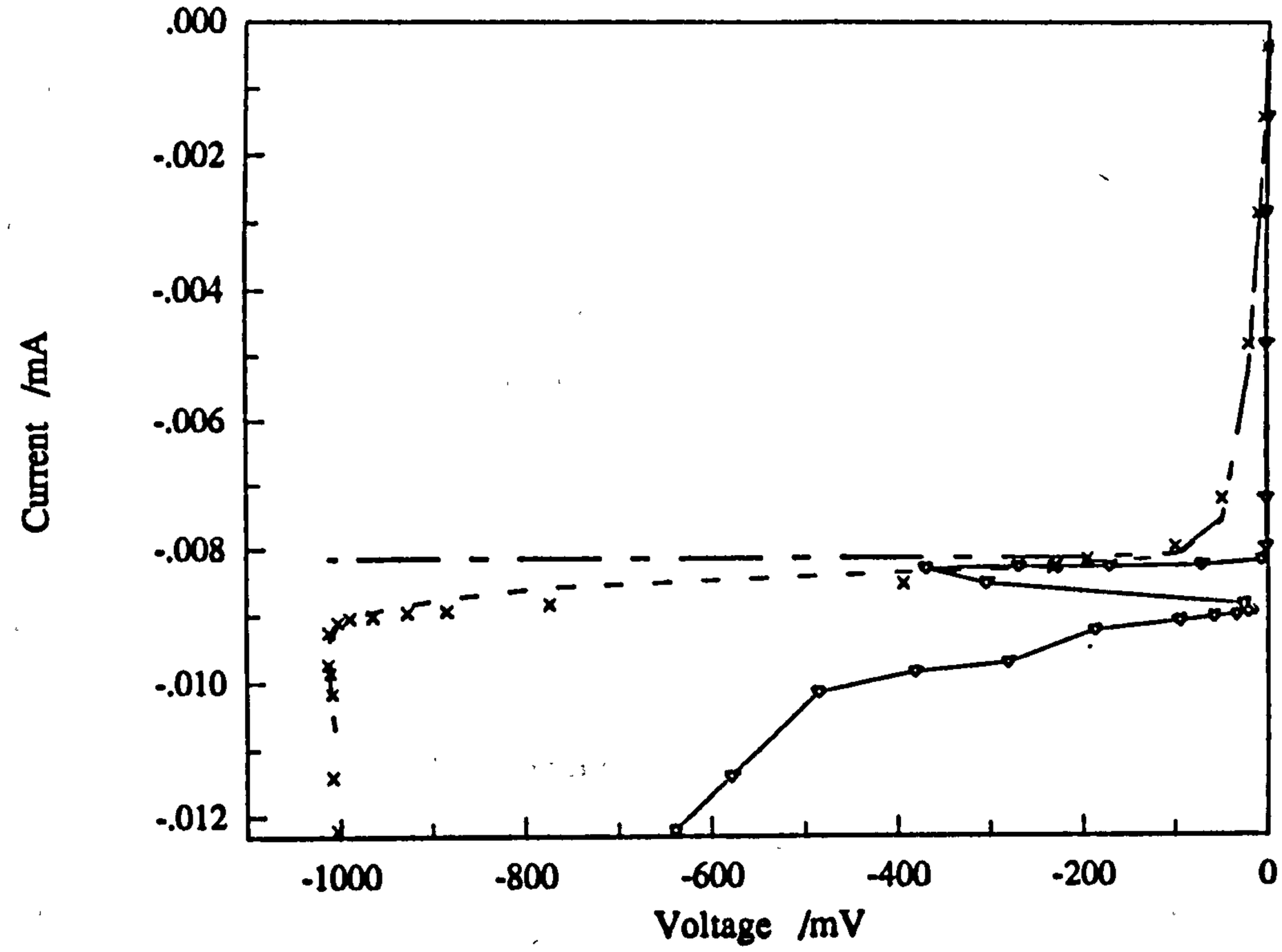

Fig. 4.17: Sensor G1 in 0.41%O_2 balance N_2 at 600°C. Symbols as Fig. 4.15, I_0 = 20nA, α_c = 0.23.

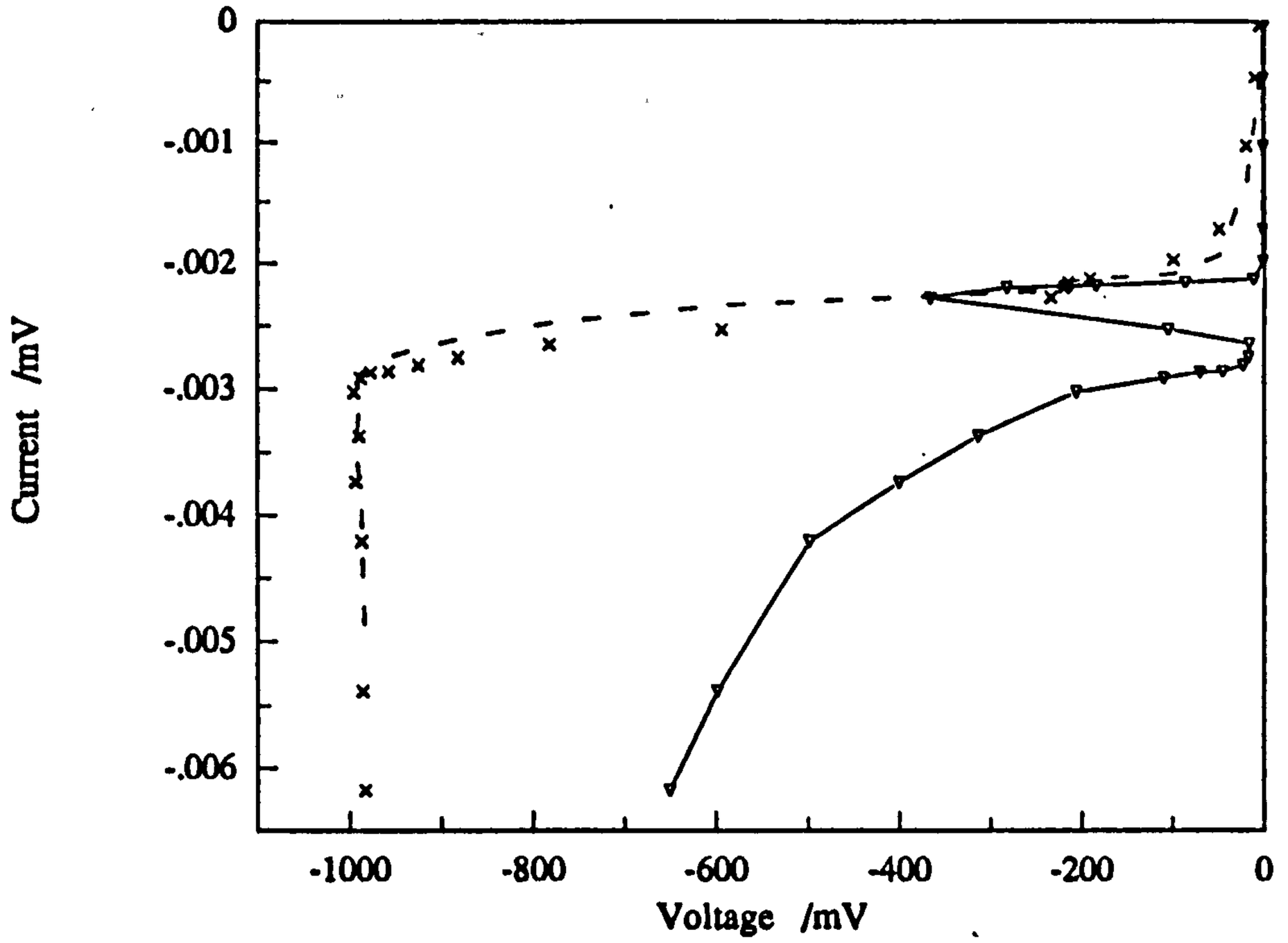

Fig. 4.18: Sensor G1 in 0.1%O_2 balance N_2 at 600°C. Symbols as Fig. 4.15, I_0 = 30nA, α_c = 0.19.

The difference between theory and experiment was usually better than 1% for oxygen concentrations of 4.1% and above which is about the accuracy with which the mass flow control valves were expected to be able to control the oxygen concentration. Also, looking at the parameters used to model the leakage current it can be seen that electrochemical leakage decreased with decreased temperature and oxygen concentration. This conforms with the expected trend for overvoltages discussed in chapter 3.

4.3) Conclusions

Eqn(4.1) was derived by taking into account all known factors affecting pump-gauge sensors except electrochemical and semipermeability leakage. At low applied voltages where leakage was minimal it was shown that eqn(4.1) could accurately model I_p vs. E_g of a pump-gauge sensor. By using a number of simplifying assumptions it was found to be possible to compensate for most of the electrochemical leakage using the Butler-Volmer equation. Using this correction a range of experimental results could be modelled to better than 1% accuracy. At temperatures below 500°C the gauge voltage did not follow the Nernst law.

Chapter 5

Advanced gas sensors: theory and tests

5.1) Theory of current due to gases containing oxygen

If a sufficiently large voltage is applied to the electrodes on a zirconia vessel, the oxygen partial pressure inside can be reduced to the extent that any oxygen-containing gas will be reduced. A number of authors including Fouletier et al (1984) and Taimatsu et al (1988) have derived theoretical equations showing the relation between current, the oxygen partial pressure and the partial pressure of gases such as H_2, H_2O, CO, CO_2, NO etc. However, these workers considered gas flowing through a zirconia tube. The situation in an amperometric sensor is slightly different. The rate at which species enter the diffusion pore equals the rate at which they are consumed within the sensor. However, this rate is limited by the rate of diffusion of the species through the pore. Mass balances can therefore be formulated using the equations for diffusion rates discussed in chapter 1.

5.1.1 The water/hydrogen system

The example of water reduction (or hydrogen oxidation) was considered first. The electrochemical reaction may be considered as:

$$H_2O + 2e^- \rightleftharpoons H_2 + O^{2-}$$

or the chemical reaction as:

$$H_2O \rightleftharpoons H_2 + \tfrac{1}{2}O_2.$$

A steady state mass balance was done on the free oxygen entering the internal volume of the sensor using eqn(1.14).

$$rO_2 = I/4F + \Gamma_{O2}(pO_2 - p'O_2) \qquad (5.1)$$

rO_2 is the rate at which oxygen enters the internal volume, pO_2 is the partial pressure of oxygen surrounding the sensor and $p'O_2$ is the partial pressure within the

sensor. Γ is the leak conductance given by: $\Gamma = DA/RT\ell$; it is a coefficient describing the rate of diffusion of gases through the pore. The diffusion coefficient (D) was estimated assuming a binary mixture of the 2 dominant gases. The method used to estimate D is presented in Appendix 1. Therefore Γ_{H2O} (for example) was calculated using D determined for a steam/nitrogen mixture. This was a necessary simplification because diffusion coefficients in complex gas mixtures are difficult to predict. Also the composition of the gas changed through the length of the pore, adding to the difficulty of finding an exact solution.

r is taken as positive for gas flowing into the sensor and I as positive for oxygen being pumped into the cell. This conforms with the convention used in this work of the internal pumping electrode being the working electrode (WE) and anodic currents on the WE being positive.

Using the same procedure as for eqn(5.1) a mass balance for water is:

$$rH_2O = \Gamma_{H2O}(pH_2O - p'H_2O). \tag{5.2}$$

A mass balance for free hydrogen gas gives:

$$rH_2 = \Gamma_{H2}(pH_2 - p'H_2). \tag{5.3}$$

The balance for all hydrogen is:

$$rH_2 + rH_2O = 0, \tag{5.4}$$

and for all oxygen it is:

$$rO_2 + \tfrac{1}{2}rH_2O = 0 \tag{5.5}$$

By expressing eqn(5.1) in terms of I and substituting in eqns(5.5) and then (5.2) it is readily shown that;

$$I = 2F\Gamma_{H2O}(p'H_2O - pH_2O) + 4F\Gamma_{O2}(p'O_2 - pO_2) \tag{5.6}$$

Rearranging eqns(5.2), (5.3) and (5.4) produces:

$$p'H_2O = pH_2O + \Gamma_{H2}/\Gamma_{H2O}(pH_2 - p'H_2) \tag{5.7}$$

$p'H_2$ is determined from the equilibrium relationship (eqn(1.29)) and substituting it into eqn(5.7) gives:

$$p'H_2O = pH_2O + \Gamma_{H2}/\Gamma_{H2O}(pH_2 - K_{H2O}P^{\frac{1}{2}}p'H_2O/p'O_2^{\frac{1}{2}})$$

rearranging gives an expression for $p'H_2O$ which when substituted into eqn(5.6) results in:

$$I = 2F\Gamma_{H2O}\left(\frac{pH_2O + \frac{\Gamma_{H2}pH_2}{\Gamma_{H2O}}}{1 + \frac{\Gamma_{H2}\,K_{H2O}\,P^{1/2}}{\Gamma_{H2O}\,p'O_2^{1/2}}} - pH_2O\right) + 4F\Gamma_{O2}(p'O_2 - pO_2) \quad (5.8)$$

Eqn(5.8) is divided into two distinct parts, the first being due to reduction of water or oxidation of hydrogen and the second being due to reduction of free oxygen (or its production). The current can therefore be calculated in two parts, the second part being identical to eqn(1.14) derived for O_2/N_2 systems.

$p'O_2$ was calculated from the following equation derived from the Nernst equation:

$$p'O_2 = pO_2 \exp(-4FE_g/RT) \quad (1.7a)$$

E_g (the gauge voltage) was used because there was no overvoltage on the gauge electrodes. It was possible for mixed potentials to prevent E_g obeying the Nernst law at low temperatures. However, Fouletier et al (1984) found that the agreement at 805°C was better than 0.4% in their tubular system.

The final equation expressing the current (without the contribution from the free oxygen) as a function of the gauge voltage was therefore:

$$I_{H2O} = 2F\Gamma_{H2O}\left(\frac{pH_2O + \frac{\Gamma_{H2}\,pH_2}{\Gamma_{H2O}}}{1 + \frac{\Gamma_{H2}\,K_{H2O}\,P^{1/2}}{\Gamma_{H2O}\sqrt{pO_2\exp\left(\frac{-4FE_g}{RT}\right)}}} - pH_2O\right) \quad (5.9)$$

The theoretical relation between current and gauge voltage at 600 and 900°C for a gas containing 10% O_2 and 10% H_2O is shown in fig 5.1.

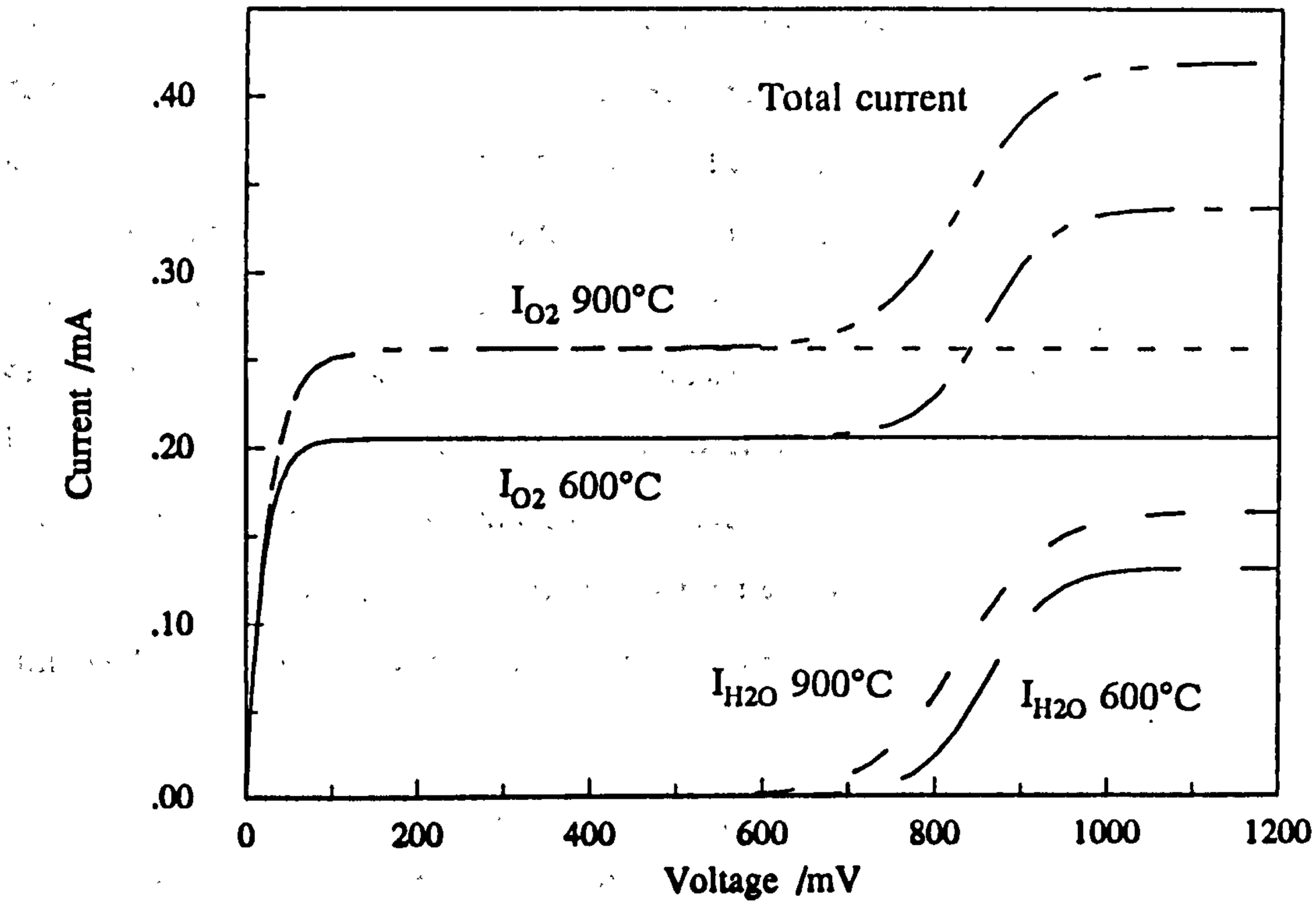

Fig. 5.1: Theoretical current voltage relationship for amperometric sensor reducing water vapour at 600°C and 900°C. H_2O and O_2 concentrations were 10%, balance N_2. Pore length was 0.7mm and θ_p was 50μm.

5.1.2 The $CO/CO_2/C$ system

Carbon dioxide reduction could follow any of 7 possible paths involving the 4 reactions listed below:

$$CO_2 + 4e^- \longrightarrow C + 2O^{2-} \quad \text{(a)}$$

$$CO_2 + 2e^- \longrightarrow CO + O^{2-} \quad \text{(b)}$$

$$CO + 2e^- \longrightarrow C + O^{2-} \quad \text{(c)}$$

$$2CO \longrightarrow C + CO_2 \quad \text{(d)}$$

The possibility of parallel and serial reactions made the prediction of reduction behaviour using only thermodynamic relationships impossible. Data about the relative rates of the reactions was required. Although there has been much work reported on the oxidation of CO on platinum electrodes using solid electrolytes there has been relatively little done on the reduction of CO_2 with such systems. Fouletier at al (1974) demonstrated reaction (b) in a flow system using a zirconia tube. The

mechanism was not well enough understood to make any assumptions about the relative rates of any parallel reactions. Single reactions therefore had to be considered by themselves starting with reaction (a).

At the temperatures of interest, carbon is a solid. From a thermodynamic point of view the activity of carbon is either zero or equal to the ambient pressure of the system (solid graphite or carbon present). Therefore, any chemical reaction involving it undergoes a sudden transition from conditions where carbon is not thermodynamically stable to conditions where it is.

The derivation of an expression for the pump current as a function of E_g followed the same lines as for water reduction and can be found in Appendix 1. The result is:

$$I_{CO2} = 4F\,\Gamma_{CO2}[pCO_2 - pO_2/K_{CO2}\exp(-4FE_g/RT)]. \qquad (A1.5)$$

The predicted current due to partial reduction only is also derived in Appendix 1.

$$I_{2CO} = 2F\Gamma_{CO2}\left(pCO_2 - \frac{pCO_2 + \Gamma_{CO}/\Gamma_{CO2}\,pCO}{1 + \dfrac{\Gamma_{CO}K_{2CO}P'^{1/2}}{\Gamma_{CO2}\,p'O_2^{1/2}}}\right) \qquad (A1.9)$$

Reduction of CO could not occur if it was not first produced by reduction of CO_2 so at least two reactions had to be considered together. All the CO_2 that diffused into the sensor was consumed, but the CO produced was both consumed by reaction (c) and lost by diffusion out of the sensor. Without detailed knowledge of the relative rates of all the reactions it was not possible to model the real situation where 2 or more reactions occurred simultaneously.

The disproportionation reaction (d) could only occur in the event of the concentrations of CO and CO_2 being away from equilibrium and $p'O_2$ being low enough to allow the formation of carbon. Because no free oxygen was involved in the reaction it is unlikely that it was electrochemically active. If reaction (d) did occur, the result would be to bring CO and CO_2 closer to equilibrium if the rates of reactions (a) and (c) were such as to remove these gases from equilibrium. The occurrence of reaction (d) would bring reaction (b) nearer to equilibrium.

The currents predicted by eqns(A1.5) and (A1.9) are shown in Fig. 5.2 for

temperatures of 600 and 900°C.

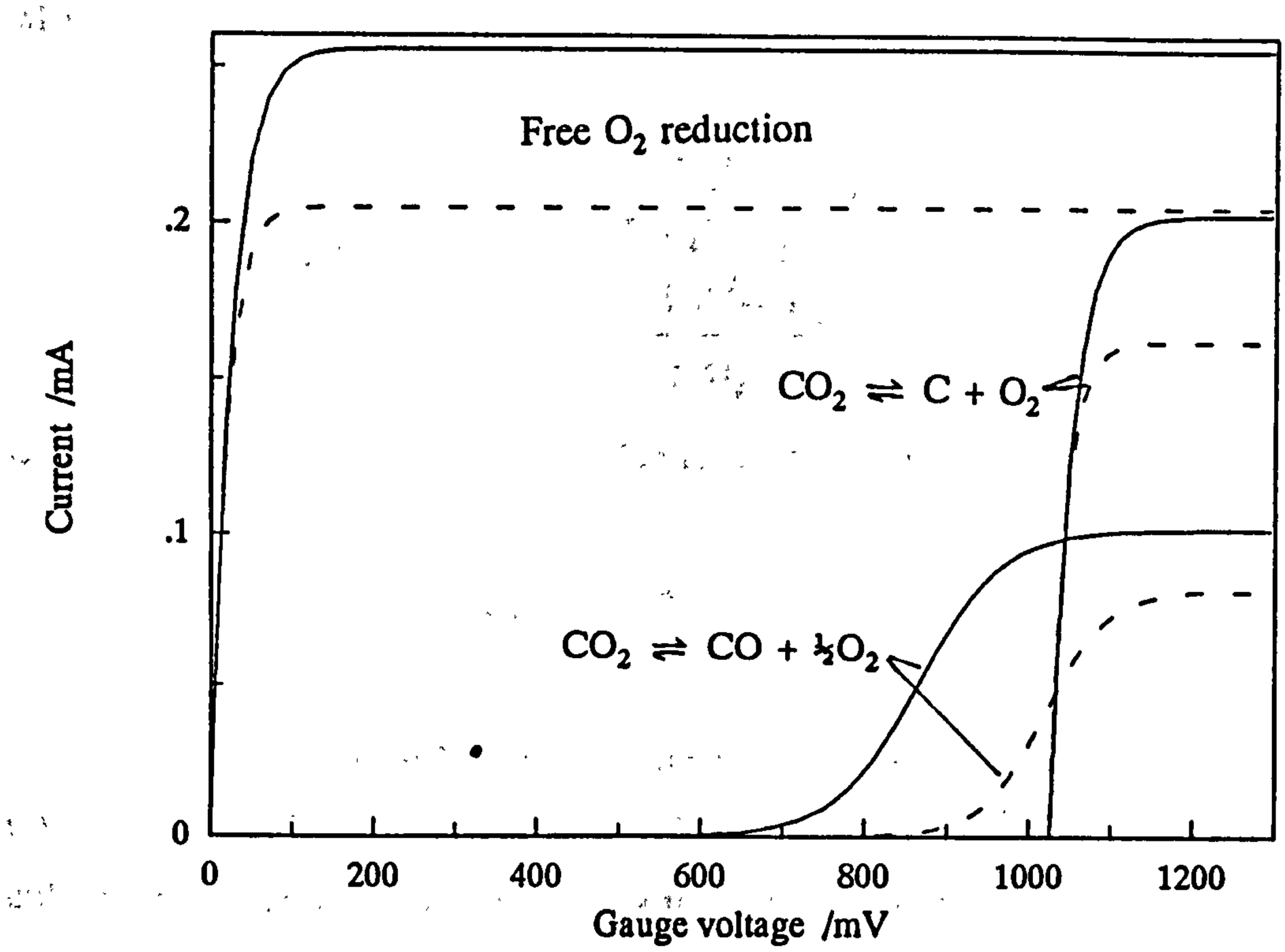

Fig. 5.2: Current predicted for reduction of 10% O_2 and 10% CO_2 in N_2 to CO and C. ——, 900°C; - - -, 600°C. The pore length was 0.7mm and θ_p was 50μm.

5.1.3 The SO_2/S system

The reduction of SO_2 could follow a number of different paths since intermediate oxides such as SO and S_2O could be involved (Barin (1989)). The direct reduction to sulphur was the only possibility considered here.

$$SO_2 + 4e^- \longrightarrow \tfrac{1}{2}S_2 + 2O^{2-} \qquad (a)$$

Sulphur in the vapour phase occurs as S_2, S_4, S_6 and S_8 (Considine (1984) and Rapp and Shores (1970)). Estimating the diffusion coefficient would therefore require a knowledge of the proportions of each species. Since the currents obtained experimentally for SO_2 reduction were high it was assumed that only S_2 was present. The current due to the reduction of SO_2 as a function of gauge voltage was derived in Appendix 1. Leaving out the current due to oxygen reduction the result is:

$$I_{SO_2} = 4\ F\ \Gamma_{SO2}\ (pSO_2 - p'SO_2) \qquad \text{(A1.14)}$$

where $p'SO_2$ is found by the equation:

$$p'SO_2 = \frac{-1 \pm \sqrt{1 + 8\dfrac{K_{SO2}^2\ \Gamma_s\ P}{p'O_2^{\,2}\ \Gamma_{SO2}}\left(pSO_2 + 2pS_2\dfrac{\Gamma_s}{\Gamma_{SO2}}\right)}}{\dfrac{4\ K_{SO2}^2\ \Gamma_s\ P}{p'O_2^{\,2}\ \Gamma_{SO2}}} \qquad \text{(A1.13)}$$

Only the root producing a positive value is valid in equation A1.13.

5.1.4 The $NO/N_2O/N$ system

The situation with NO_x was potentially the most complicated of all. Barin (1989) listed the heats of formation for 7 different NO_x compounds. NO was the only gas tested in this work so the only possible reactions were;

$$NO + 2e^- \longrightarrow \tfrac{1}{2}N_2 + O^{2-} \qquad \text{(a)}$$

$$2NO + 2e^- \longrightarrow N_2O + O^{2-} \qquad \text{(b)}$$

$$N_2O + 2e^- \longrightarrow N_2 + O^{2-} \qquad \text{(c)}$$

Assuming only reaction (a) the limiting current predicted is:

$$I_{NO} = 2FT_{NO}\left(pNO - \frac{-1 \pm \sqrt{1 + 8K_{NO}^2/p'O_2(pNO + 2pN_2)}}{4K_{NO}^2/p'O_2}\right) \qquad \text{(A1.21)}$$

The predicted current due to reaction (b) only is:

$$I_{2NO} = 2F\Gamma_{NO}\left(pNO - \frac{-1 \pm \sqrt{1 + 8\dfrac{K_{2NO}\ \Gamma_{2NO}}{p'O_2^{1/2}P^{1/4}T_{NO}}\left(pNO + 2pN_2O\dfrac{\Gamma_{2NO}}{\Gamma_{NO}}\right)}}{\dfrac{4\ K_{2NO}\ \Gamma_{2NO}}{p'O_2^{1/4}\ P^{1/4}\ \Gamma_{NO}}}\right) \qquad \text{(A1.28)}$$

5.2) Tests in $CO_2/O_2/N_2$ mixtures

In the sensors used in this work the current due to electrochemical leakage masked that due to CO_2 reduction. Fig. 5.3 illustrates the magnitude of the problem. The theoretical current due to partial CO_2 reduction only is compared to the measured current, the theoretical current due to O_2 reduction and the total theoretical current. Because the current due to leakage was difficult to predict and greater than that due to CO_2 reduction (I_{CO2}) it was not possible to isolate the contribution from I_{CO2}. With the degree of leakage illustrated in Fig. 5.3 the sensor could not measure CO_2 concentrations of less than 1%. The resolution of the sensor would improve in direct proportion to any reduction in leakage current.

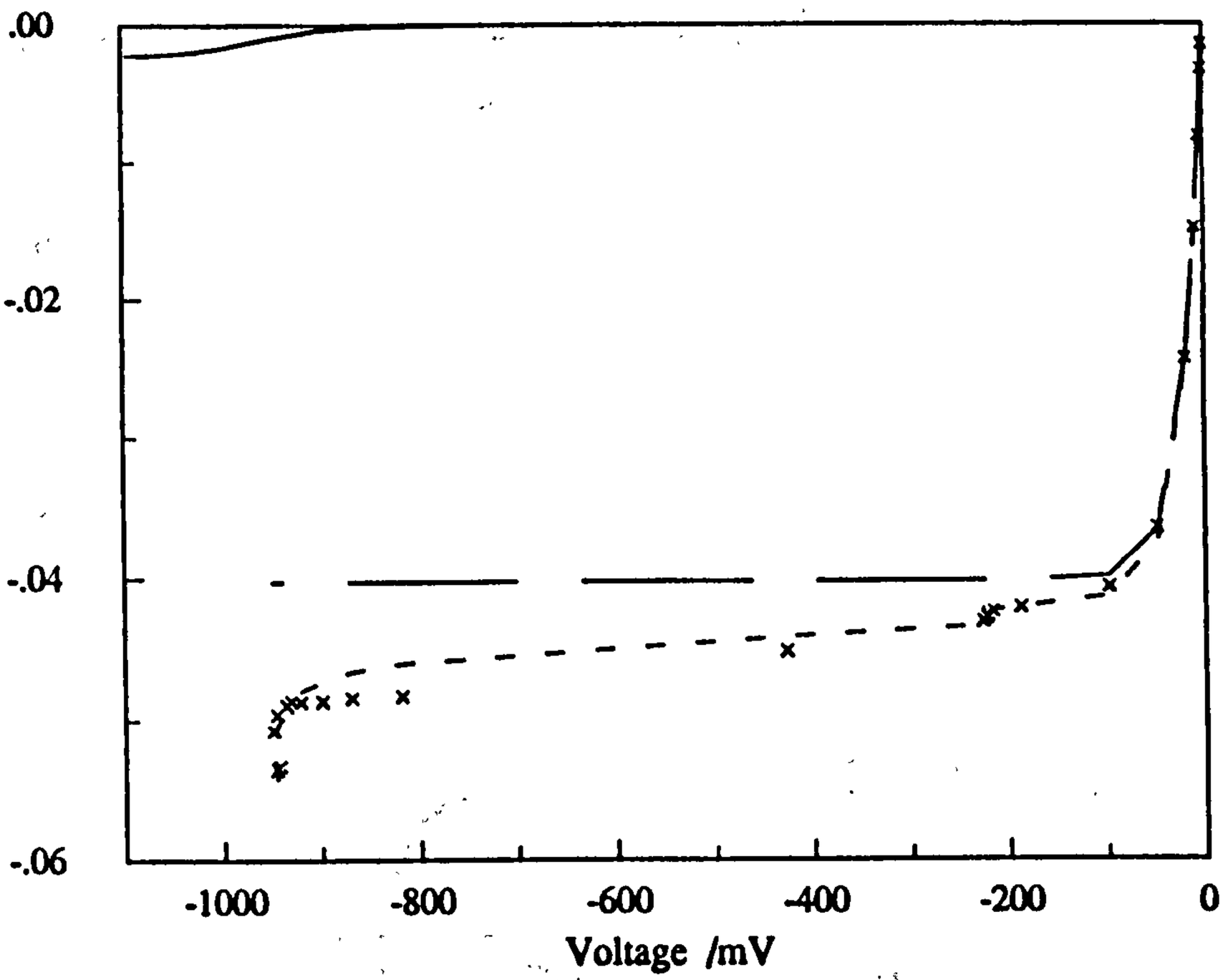

Fig. 5.3: Sensor G1 in 0.28% CO_2 and 1.89% O_2 in N_2 at 650°C. - - -, predicted using 49.6μm pore, I_0 = 0.7μA, α_c = 0.13. — –, current due to O_2 reduction only; ——, current due to CO_2 reduction only; ×, measured I_p vs. E_g.

Fig. 5.3 shows the theoretical current due to partial reduction of CO_2 only compared to the measured pumping current (I_p) and the total theoretical current.

Both were plotted against the gauge voltage (E_g) which appeared to reach a limit just below -1000mV. Figs. 5.4 and 5.5 show results measured under similar conditions. E_g reached a limiting value because a large increase in the overvoltage on the internal pumping electrode (η_c) prevented complete reduction of CO_2 before the zirconia became electronically conducting. The maximum E_g reading corresponded to 43% of the CO_2 being reduced to CO in Fig. 5.3 and 45% in Fig. 5.4. Fig 5.6 illustrates a similar set of results. The total theoretical current and the theoretical current without the component due to CO_2 reduction were extrapolated beyond the gauge voltage values measured experimentally. This was done by assuming no further increase in the internal electrode overvoltage. The contribution from electrochemical leakage therefore increased very little on the extrapolated curves. The difference between these two curves illustrates the current expected from CO_2 reduction. The greatest E_g reading corresponded to 42% of the CO_2 being reduced.

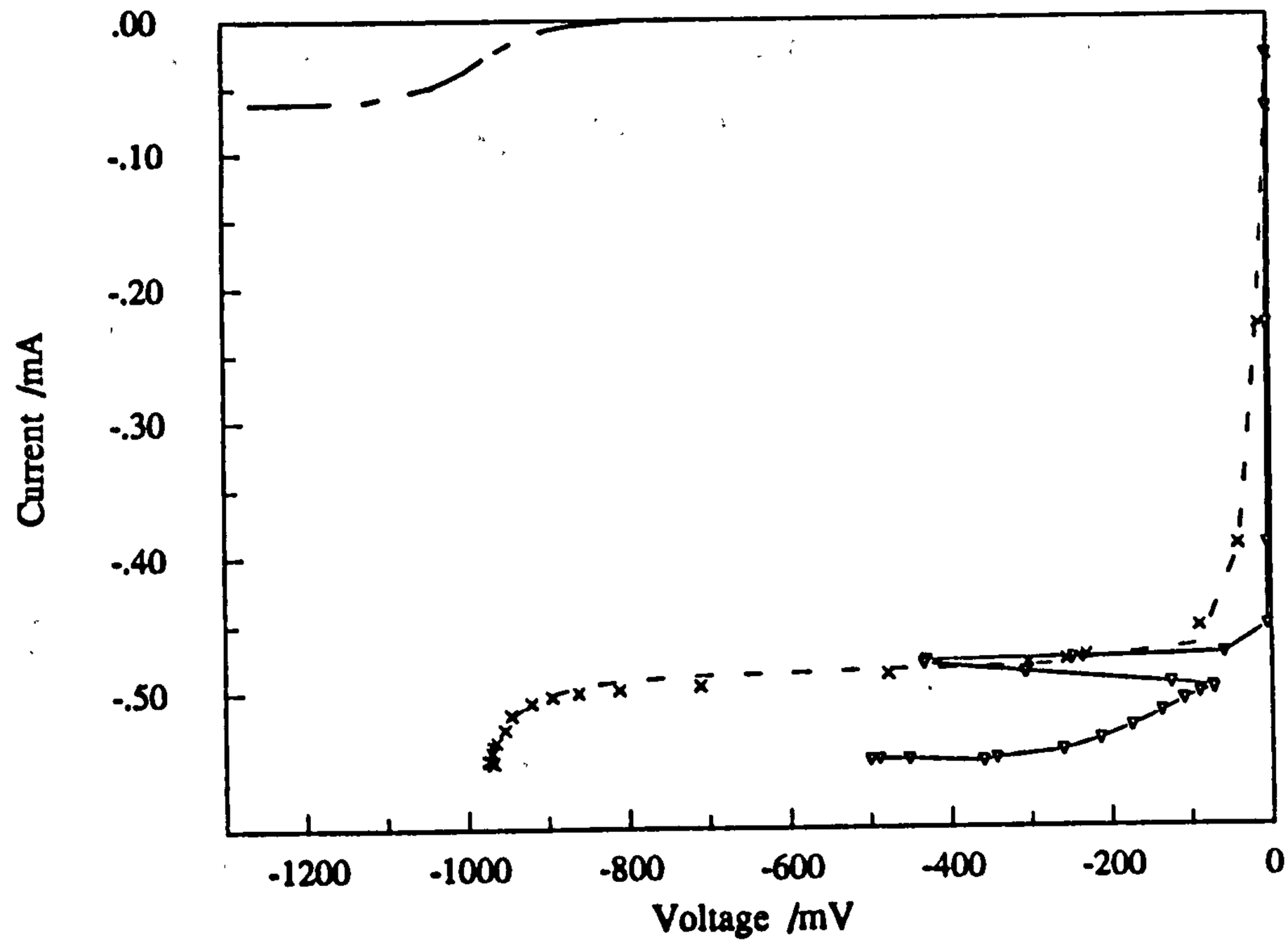

Fig. 5.4: Sensor G1 in 7.2% CO_2 and 19.4% O_2 in N_2 at 700°C. - - -, predicted using 49.5μm pore, I_0 = 1.7μA, α_c = 0.17. — –, current due to CO_2 reduction only vs. E_g; ×, measured I_p vs. E_g; –▽–, I_p vs. η_c.

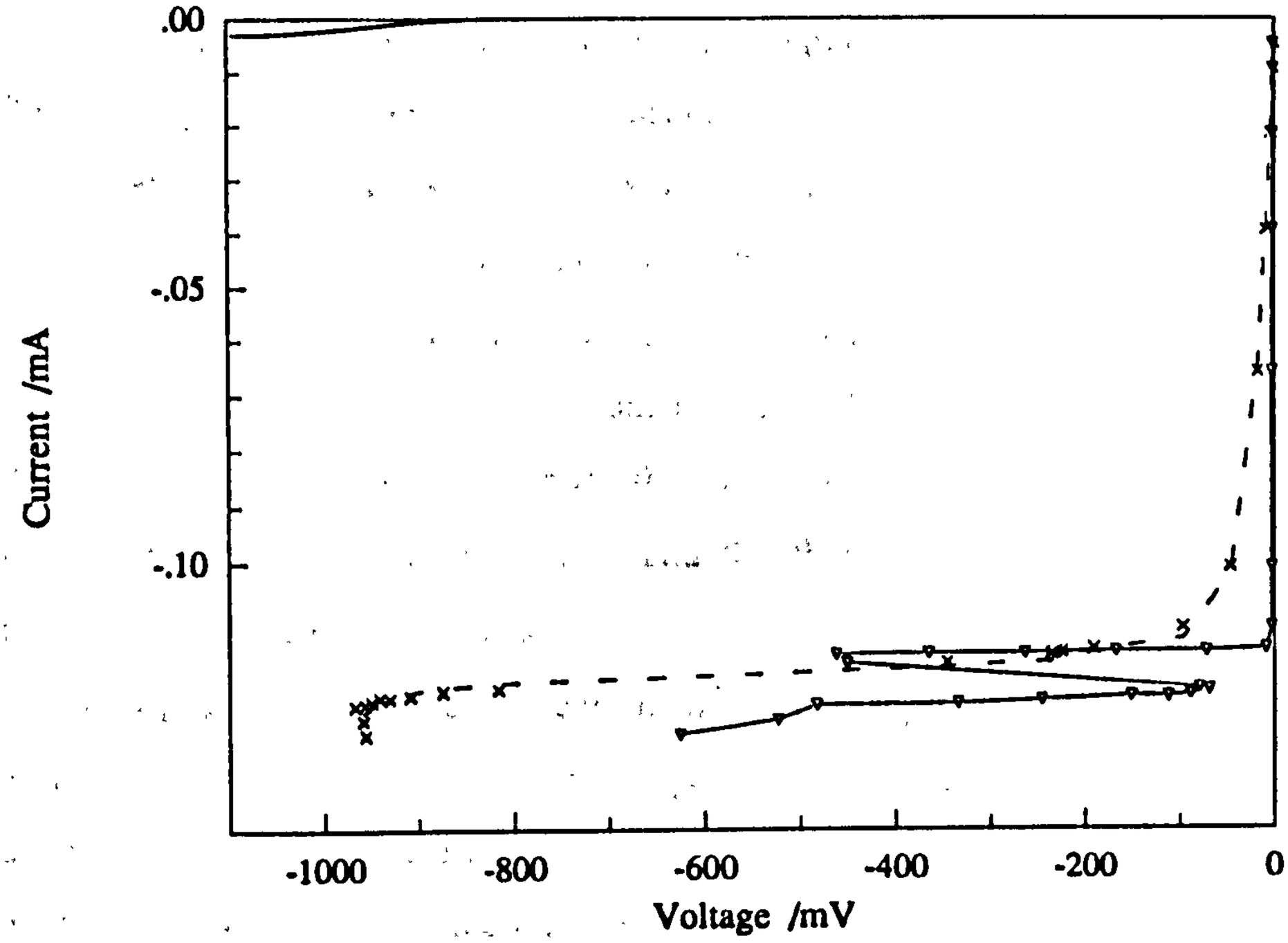

Fig. 5.5: Sensor G1 in 0.39% CO_2 and 5.12% O_2 in N_2 at 650°C. - - -, predicted using 49.6μm pore, I_0 = 2μA, α_c = 0.09. ——, current due to CO_2 reduction only vs. E_g; ×, I_p vs. E_g; -▽-, I_p vs. η_c.

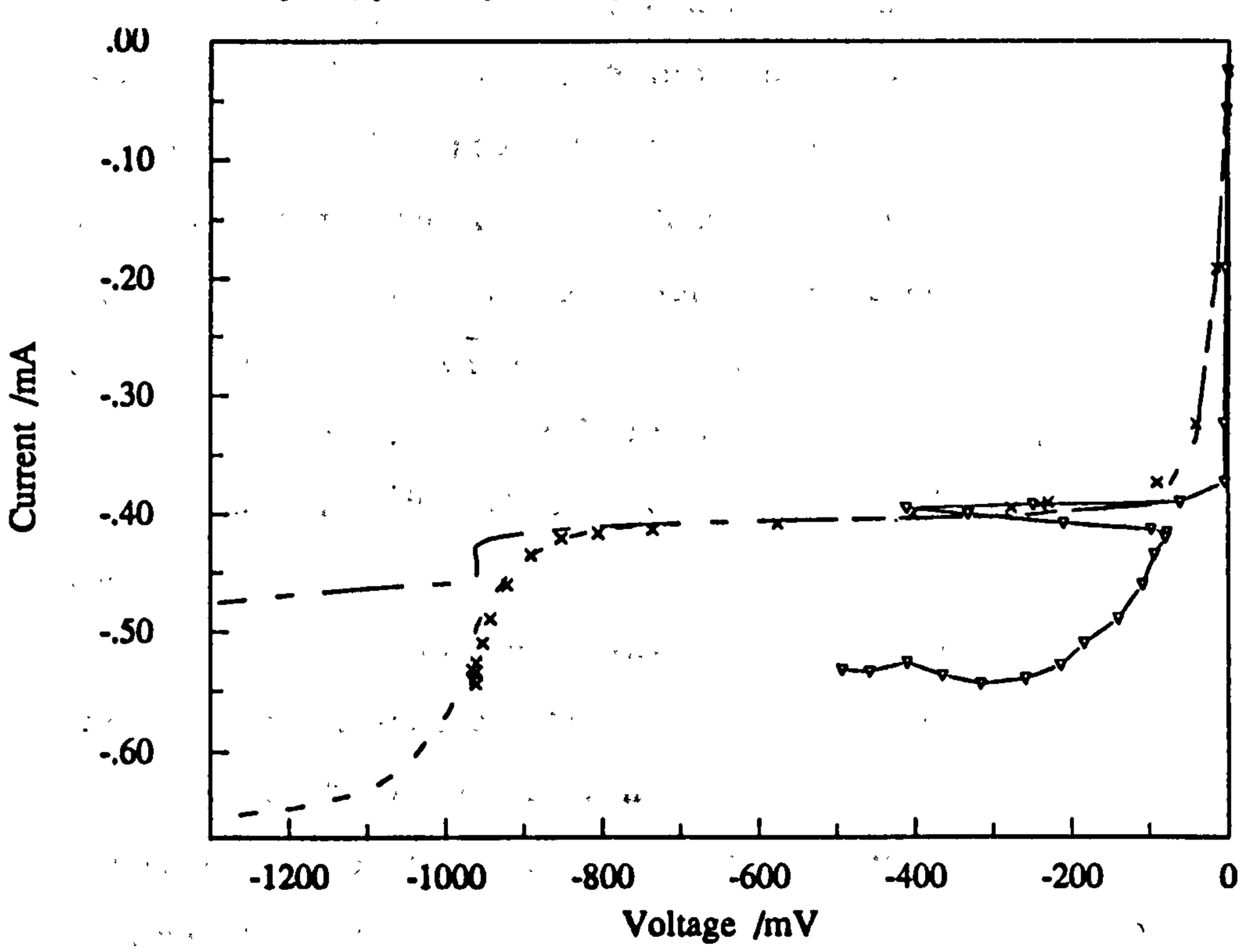

Fig. 5.6: Sensor G1 in 20.6% CO_2 and 16.6% O_2 in N_2 at 700°C. - - -, predicted using 49.5μm pore, I_0 = 0.5μA, α_c = 0.26. — –, current due to O_2 reduction and electrochemical leakage vs. E_g; ×, I_p vs. E_g; -▽-, I_p vs. η_c.

Under limited circumstances when the pumping voltage was in the range of 1100 to 1400mV, the current suddenly decreased before rising sharply again with increased applied voltage. Often it was a single pump voltage setting where the current reading was substantially below the neighbouring readings. Since the current readings were calculated using the average of many readings it is unlikely that it was caused by instrument error. The phenomena was only observed between 650 and 700°C. Also, when the current dropped the gauge voltage increased. Figs. 5.7 and 5.8 show examples of such behaviour and the theoretical currents due to CO_2 reduction to CO and C are illustrated.

It is possible that the dip in current was caused by carbon formation on the internal pump electrode. Although the gauge voltage indicated an oxygen potential 100mV lower than that where carbon formation was thermodynamically possible it may still have occurred for three reasons.

- The gauge electrodes may not have obeyed the Nernst law and the oxygen potential within the sensor may have been lower than that indicated. Perfilyev and Fadeev (1984) found that platinum electrodes in CO/CO_2 mixtures gave slightly incorrect Nernst readings at all temperatures tested. Fouletier et al (1974) showed that at temperatures between about 700 and 900°C the Nernst potential on platinum electrodes provides an accurate indication of the oxygen partial pressure in the gas phase. They also found that CO_2/CO mixtures reached equilibrium. In a different apparatus Mizusaki et al (1990) found that at 800°C, the inclusion of platinum painted surfaces in the gas stream leading to the electrode brought CO/CO_2 mixtures closer to equilibrium.
- It is possible that the oxygen activity on the pump electrode was lower than that on the gauge because of the overvoltage on the former.
- It is possible that the electrochemical leakage current produced a small overvoltage on the internal gauge electrode and thereby reduced the potential difference across it.

The theoretical curves in Figs. 5.1, 5.7 and 5.8 show that there is a very narrow band where reduction of CO_2 to C is possible but the resultant current is lower than that due to reduction of CO_2 to CO. Therefore a change in mechanism

from reaction (b) to reaction (a) could cause a dip in current. However, the dip in observed current was greater than that due to partial CO_2 reduction (40μA in Fig. 5.6) so the proposed change in reaction route seems unlikely. It is also unlikely that the dip was entirely due to increased electrode resistance caused by the formation of carbon on its surface. Such a mechanism would have been associated with a decrease in E_g instead of an increase.

It must therefore be concluded that oxygen was chemically consumed by the process causing the dip. The most likely explanation was thought to be disproportionation of CO followed by partial oxidation of the resulting carbon. These two reactions (d) and (c) were presumed not to be electrochemically active while partial reduction of CO_2 (reaction (b)) was. Etsell and Flengas (1972) and Gur and Huggins (1992) noticed that carbon does not always form even when the CO concentration is high enough to make it thermodynamically possible. Carbon formation may require a nucleus before it can start. If this supersaturation occurred in the sensor the CO concentration could have built up to a high level before a nucleus of carbon formed. The CO would then rapidly disproportionate and the resulting carbon may have reacted with the oxygen entering from the diffusion pore. Strong evidence for this theory comes from Yentekakis and Vayenas (1988) who found that CO can decompose under certain conditions forming C that reacts rapidly with gaseous O_2.

As the pump voltage was further increased, the current increased little and the overvoltage on the pump electrode increased considerably. It is therefore likely that carbon formation partially blocked the pumping electrode and increased its resistance.

The results in Fig. 5.9 show the slightly different behaviour of sensor G2 under similar circumstances. It can be seen that η_c increased as I_p decreased and there was no single current reading significantly below its neighbouring readings. Carbon formation partially blocking the pump electrode was therefore probably the only phenomena involved here.

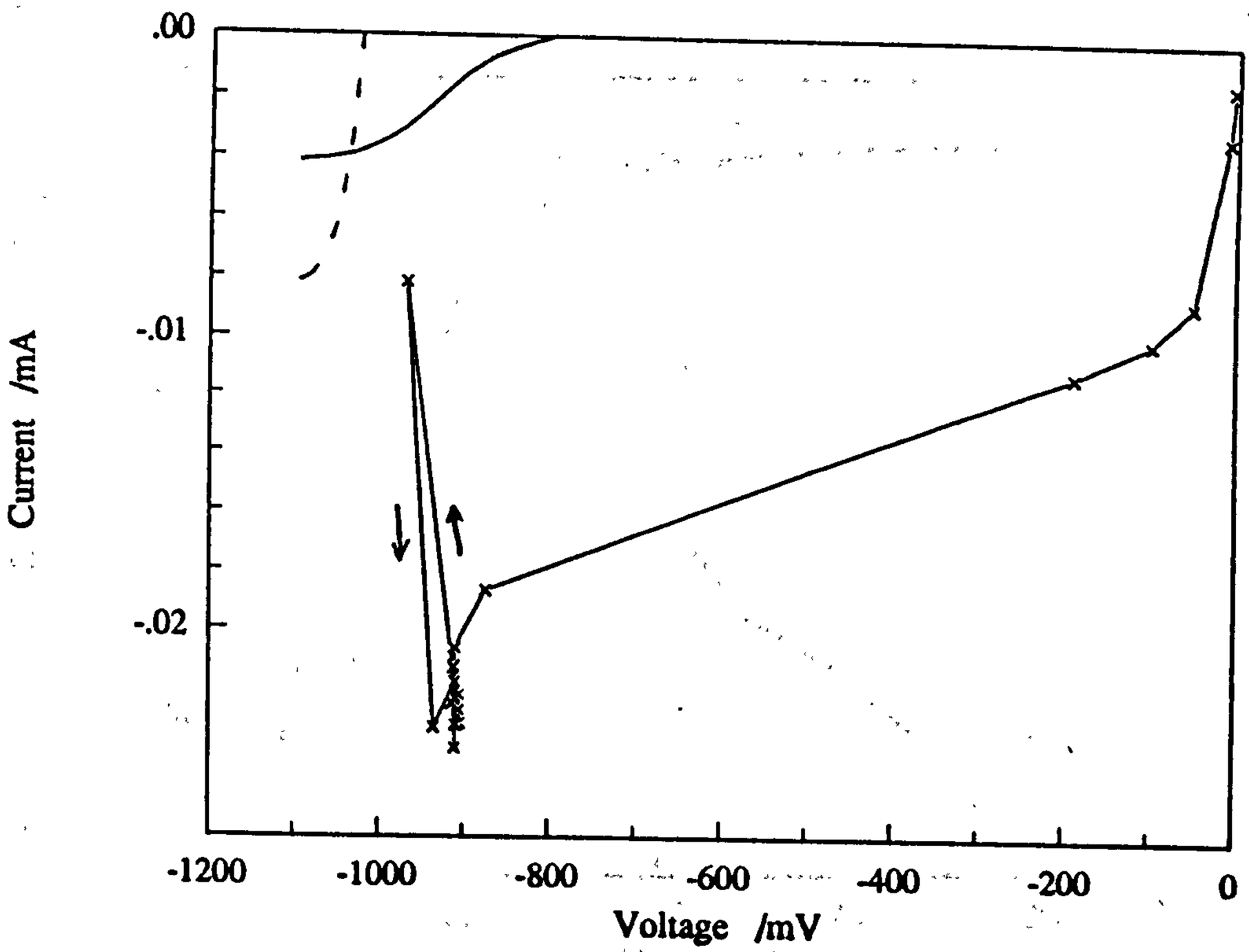

Fig. 5.7: Sensor G1 in 0.507% CO_2 and 0.408% O_2 in N_2 at 650°C. - - -, theoretical current due to complete reduction of CO_2 vs. E_g; ——, partial reduction of CO_2 vs.E_g; –×–, I_p vs. E_g.

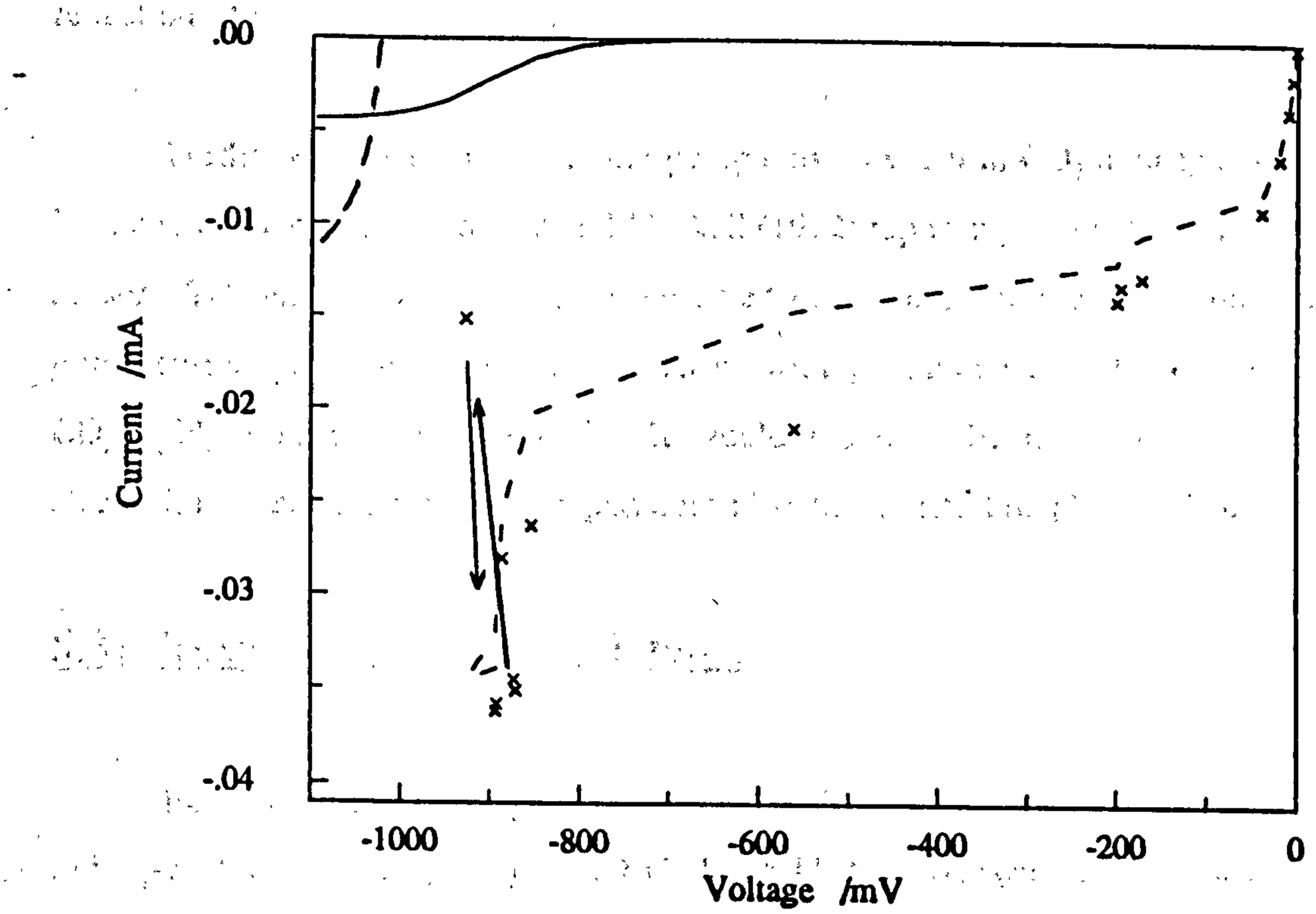

Fig. 5.8: Sensor G1 in 0.507% CO_2 and 0.408% O_2 in N_2 at 700°C. - - -, predicted using 49.5μm pore, I_0 = 0.5μA, α_c = 0.21. —— and - - -, theoretical currents due to partial and full reduction of CO_2 respectively vs. E_g; ×, I_p vs. E_g.

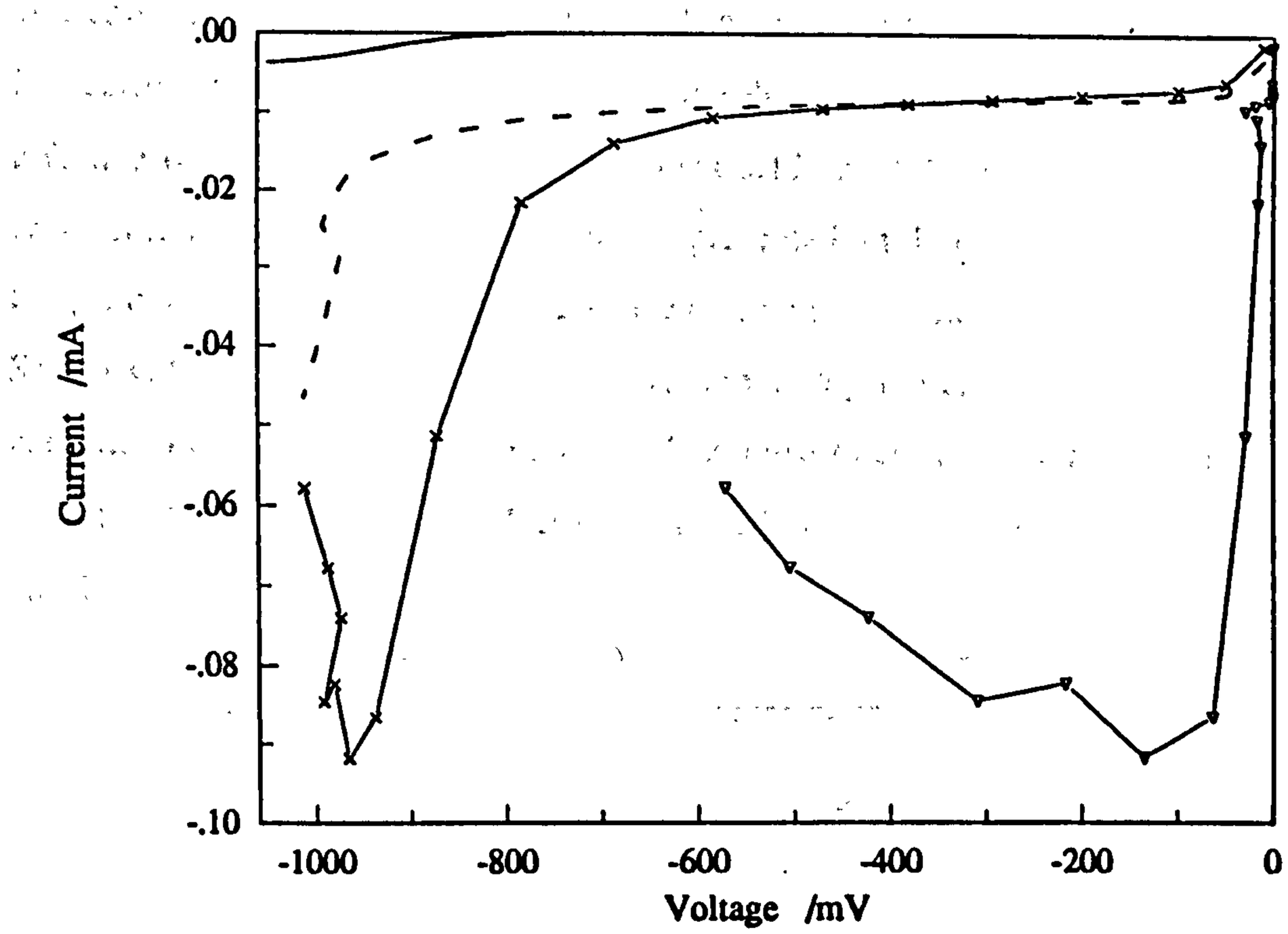

Fig. 5.9: Sensor G2 in 2.31% CO_2 and 1.856% O_2 in N_2 at 700°C. - - -, total theoretical current assuming θ_p = 22μm, I_0 = 70nA, α_c = 0.32; ——, partial reduction of CO_2; –×–, I_p vs. E_g.

Further examples of dips in the pump current when in CO_2 atmospheres can be found in the paper by Copcutt and Maskell (1992) reporting results from an earlier sensor. Takahashi et al (1985) also presented results indicating a slight dip in the pump current of their amperometric sensor with platinum electrodes operated in $CO_2/O_2/N_2$ atmospheres at 700°C. It would therefore be interesting to test if electrodes of materials other than platinum also experience this phenomenon.

5.3) Tests in $SO_2/O_2/N_2$ mixtures

Fig. 5.10 shows the high currents that resulted when sensor G1 was operated in SO_2-containing atmospheres at 750°C. Fig 5.11 illustrates earlier results using the sensor at 600°C in a lower SO_2 concentration. Although the measured current was closer to the theoretical current it was still much higher than expected. Note that in both figures the theoretical curves show results assuming ten times the SO_2

concentration actually fed to the sensor. It could have been suspected that the SO_2 had corroded the platinum wire blocking the diffusion pore and thus increasing the effective pore diameter. The results in Figs 5.12 and 5.13 disprove this. Fig 5.12 represents results taken just after those presented in Fig 5.11 but at the lower temperature of 500°C. At low voltages the current approaches the theoretical current. Sensor G2 had no wire blocking its pore and also produced higher than expected currents in SO_2 atmospheres (Fig 5.13). The most likely explanation was therefore considered to be electronic conductivity induced in the YSZ by the sulphur diffusing into it.

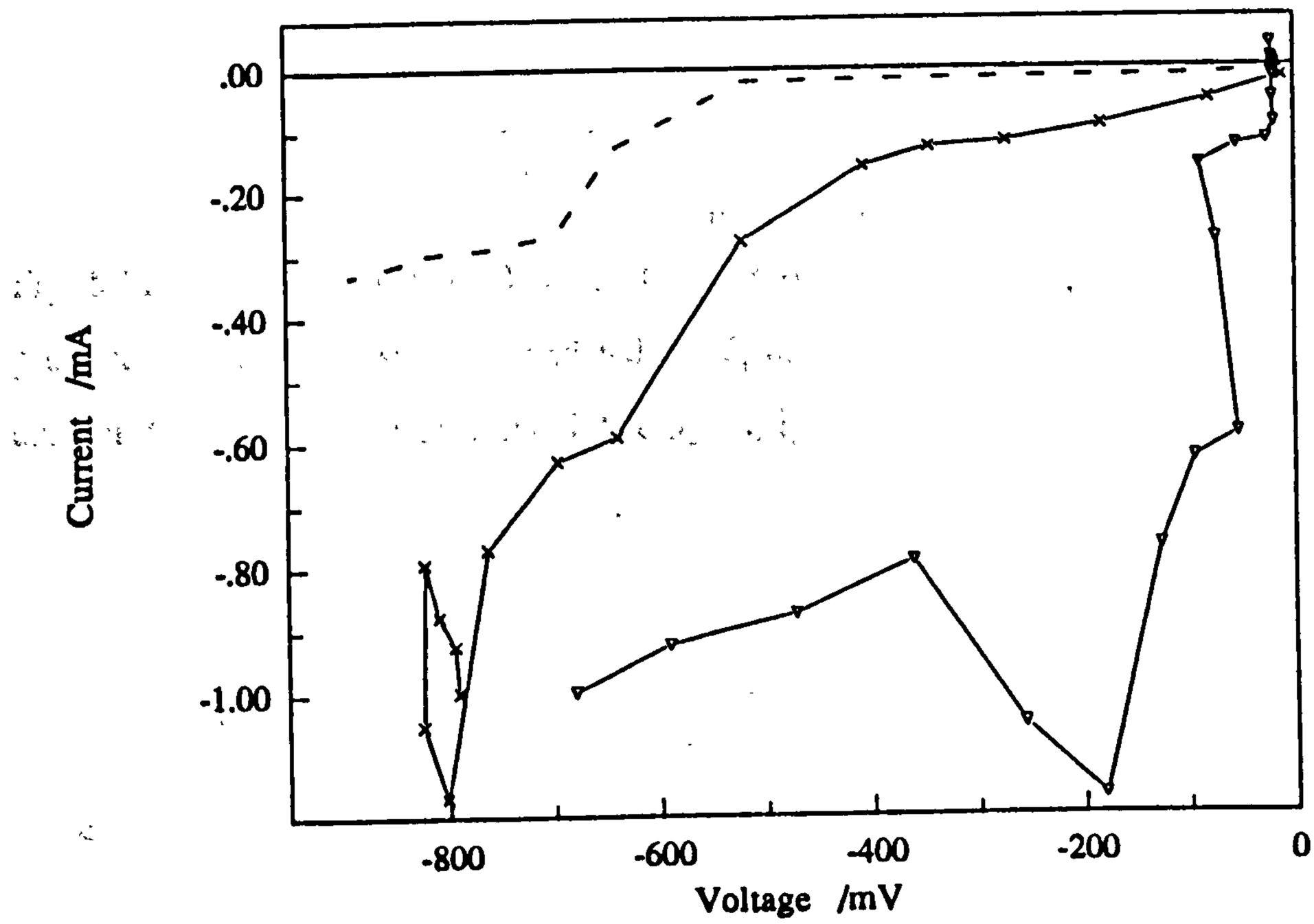

Fig. 5.10: Sensor G1 in 1.41% SO_2 and 0.402% O_2 in N_2 at 750°C. - - -, theoretical current due to reduction of O_2 and 14.1% SO_2, I_0 = 1.2μA, α_c = 0.22; –∇–, I_p vs. η_c; –×–, I_p vs. E_g.

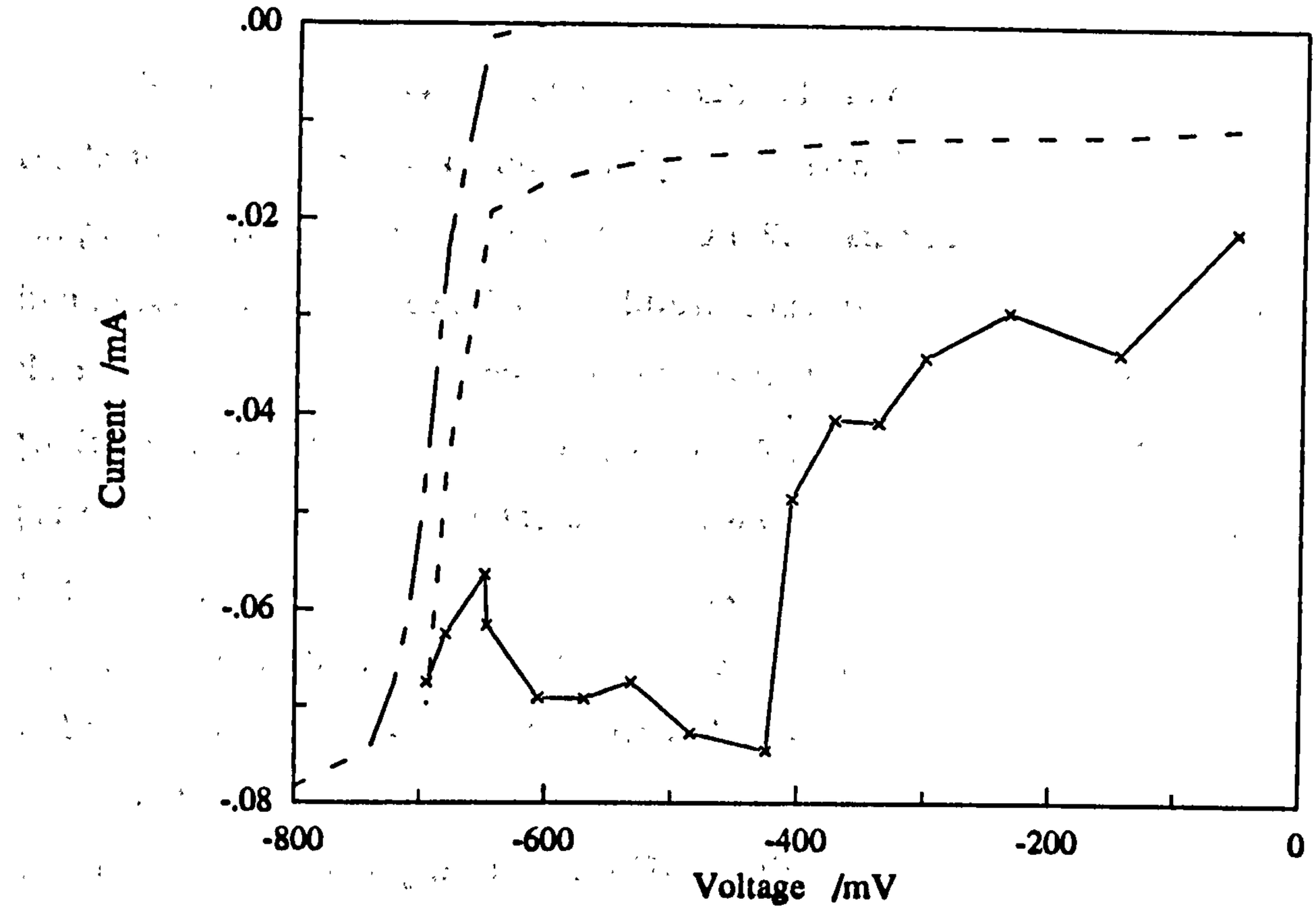

Fig. 5.11: Sensor G1 in 0.48% SO_2 and 0.407% O_2 in N_2 at 600°C. - - -, predicted assuming 4.8% SO_2 and using 56μm pore, I_0 = 0.2μA, α_c = 0.2. — -, current due to reduction of 4.8% SO_2 only; ×, I_p vs. E_g.

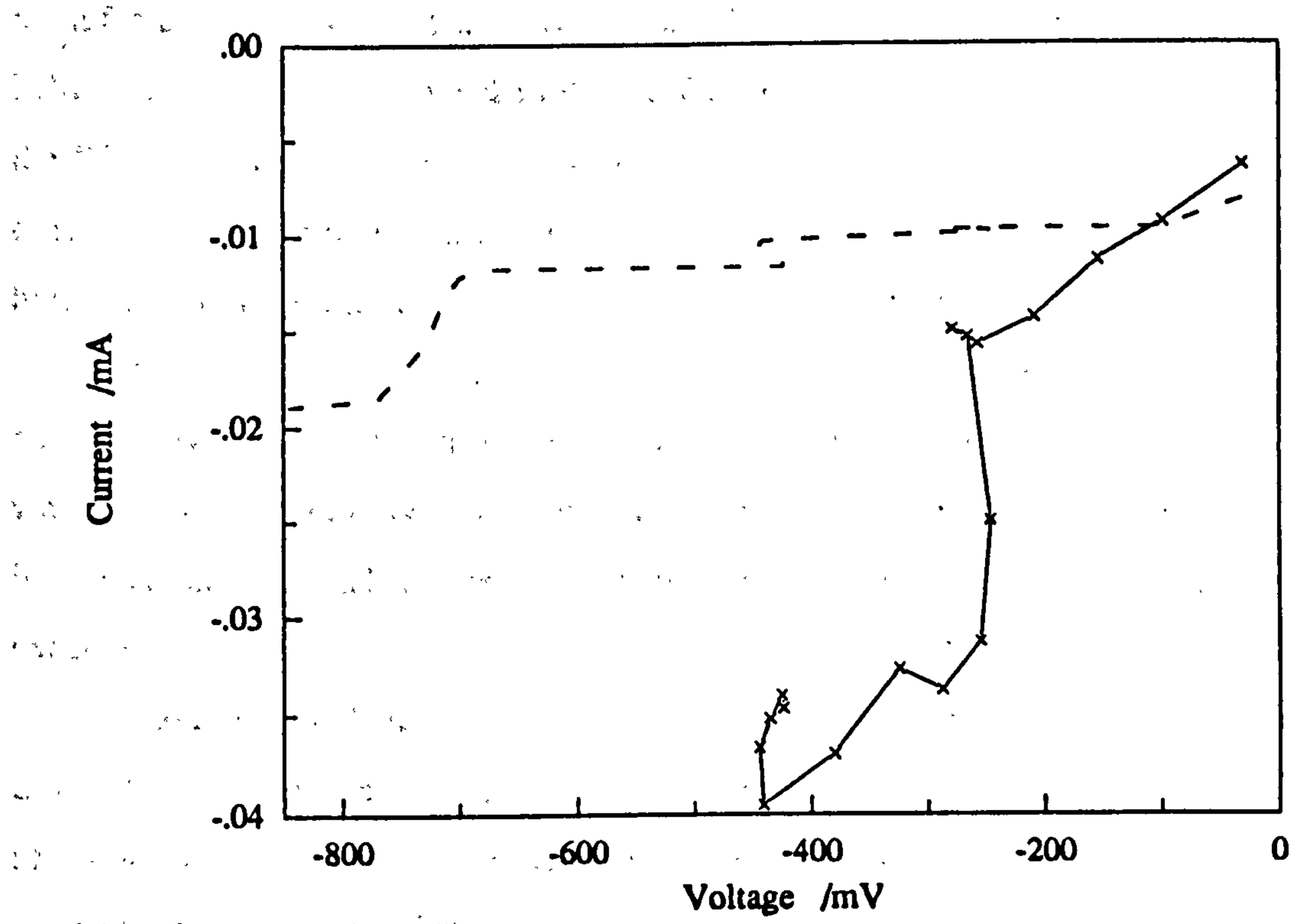

Fig. 5.12: Sensor G1 in 0.48% SO_2 and 0.407% O_2 in N_2 at 500°C. - - -, total theoretical current including contribution due to reduction of SO_2 using 56μm pore, I_0 = 1.2μA, α_c = 0.22. –×–, I_p vs. E_g.

Iwase et al (1984) found that a CaS electrode caused increased n type conductivity in a sample of high purity calcia stabilized zirconia particularly at temperatures below 1300°C. Mehrotra et al (1988) studied the diffusion of sulphur into zirconia and concluded that the diffusion rate is 3 orders of magnitude lower than that of oxygen. The significance of this is that sulphur will enter the zirconia while the sensor is operated in sulphur atmospheres and continue to affect the performance some time after the sensor is moved into sulphur free atmospheres. Results from sensor G2 support this idea; it continued to draw large pump currents after the flow of SO_2 was stopped (Fig. 5.13). Also electronic conductivity seems to be induced by very low concentrations of SO_2.

A bottle of pure SO_2 was connected to a flow control valve attached to the test rig and tests were begun on sensor G1. At first the valve was set to pass no SO_2 and only the valves connected to the air and nitrogen supplies were set to pass gas. Fig. 5.14 shows the results under this circumstance where no more than a trace of SO_2 could have been present in the atmosphere surrounding the sensor. The valve manufacturer claims that the valves have a leak rate of less than 1×10^{-3} ml/s of helium (section 2.2.4). Since the nitrogen flow rate was 1.25 ml/s it is probable that the SO_2 concentration was well below 0.08%. At first the sensor passed currents only slightly above those expected if there had not been a trace of SO_2 present. At higher voltages the currents increased very rapidly and the gauge voltage decreased.

The electronic conductivity induced by the SO_2 was much less than the ionic conductivity of the YSZ. The current observed in Fig. 5.10 represented about 1000Ω while R_u was previously determined to be between 3 and 4Ω at 750°C. The instrumentation available was not capable of detecting the small change in R_u expected.

Vayenas and Saltsburg (1979) and Chen and Saltsburg (1986) studied the $SO_2/SO_3/O_2$ system and concluded that in some circumstances the potentiometric response was controlled by mixed potentials and competitive adsorption of the different gases on the electrode surface. Mixed potentials are caused by two electrochemical reactions competing to determine the potential of an electrode. In the SO_x system the above authors considered the competing reaction to be:

$$SO_3 + 2e' + V_O^{\cdot\cdot} \rightleftharpoons O_O^x + SO_2.$$

They found that the open circuit electrode potentials were determined by pO_2 in the usual way when

$$pSO_2\ pO_2^{½} < K_{Pt}.$$

ie. the cell obeyed Nernst's law. However, when

$$pSO_2\ pO_2^{½} > K_{Pt}$$

the potentials were also controlled by pSO_2 and the term K_{Pt} that they called the electrode constant (Pt electrodes). The proposed mechanism was the formation of SO_3 on the electrode which adsorbed strongly and blocked adsorption sites. The result was a potentiometric response that indicated a lower pO_2 than that present in the gas phase. Chen and Saltsburg found K_{Pt} to be 1.5×10^{-3} $atm^{3/2}$ at 600°C and 9.1×10^{-5} $atm^{3/2}$ at 500°C. The product $pSO_2\ pO_2^{½}$ was 3.0×10^{-4} $atm^{3/2}$ on the external electrodes during the tests reflected in Figs. 5.11 and 5.12. SO_3 formation was therefore expected at 500°C with the consequential reduction in oxygen potential and reduced E_g. At 600°C no reduction in E_g was expected and it did reach the theoretical values at the highest applied voltages. The increase in current near -400mV may have been due to the slow response of the electrodes. This slow response is illustrated by the large difference between the currents measured during opposing voltage sweeps shown in Fig. 5.13 (650°C).

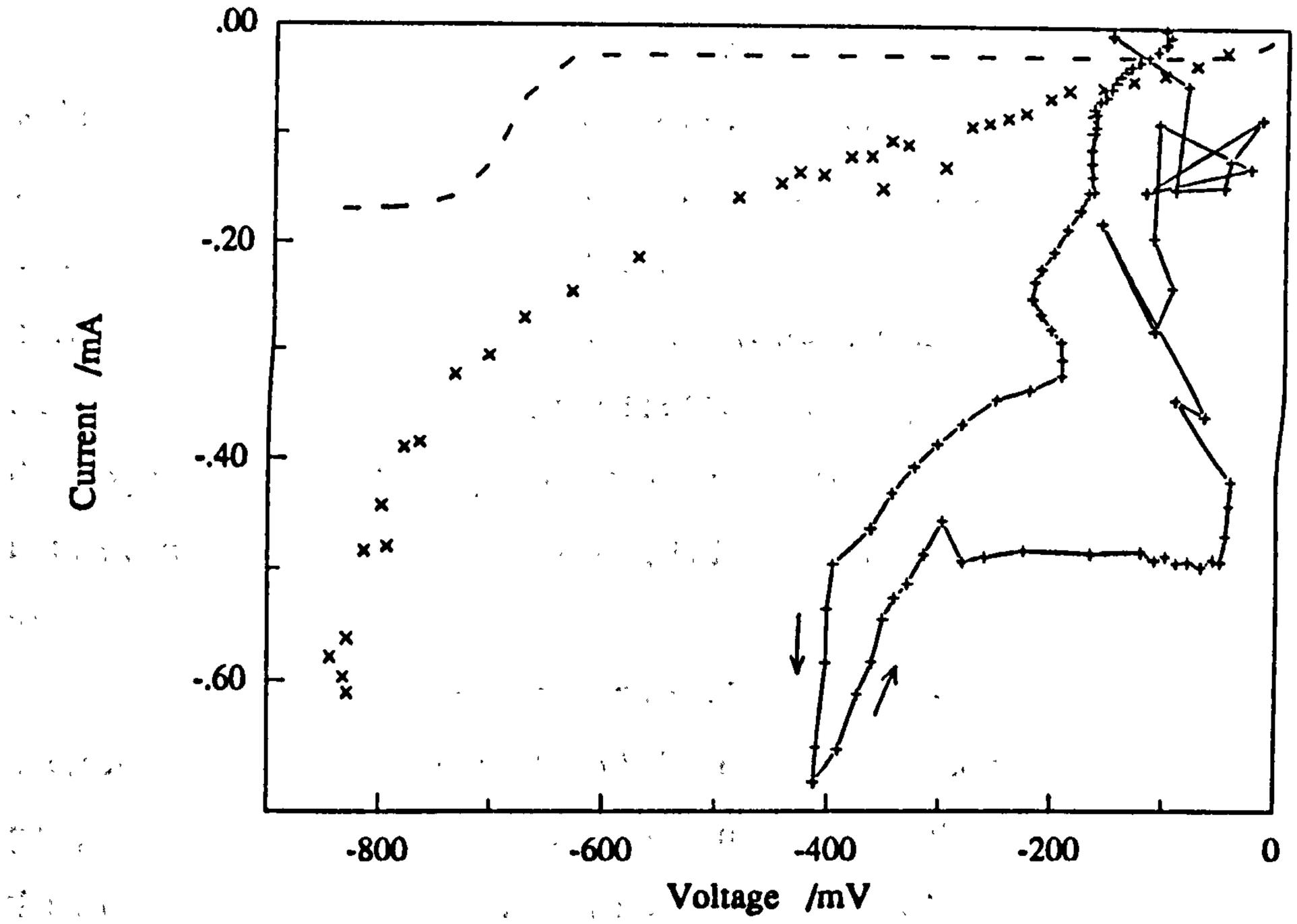

Fig. 5.13: Sensor G2 in trace SO_2 and 5.97% O_2 in N_2 . - - -, current predicted assuming 50% SO_2 and 22.3μm pore. ×, I_p vs. E_g at 750°C; –+–, 650°C; both measured using cyclic voltammetry (CV) at 0.2mV/s.

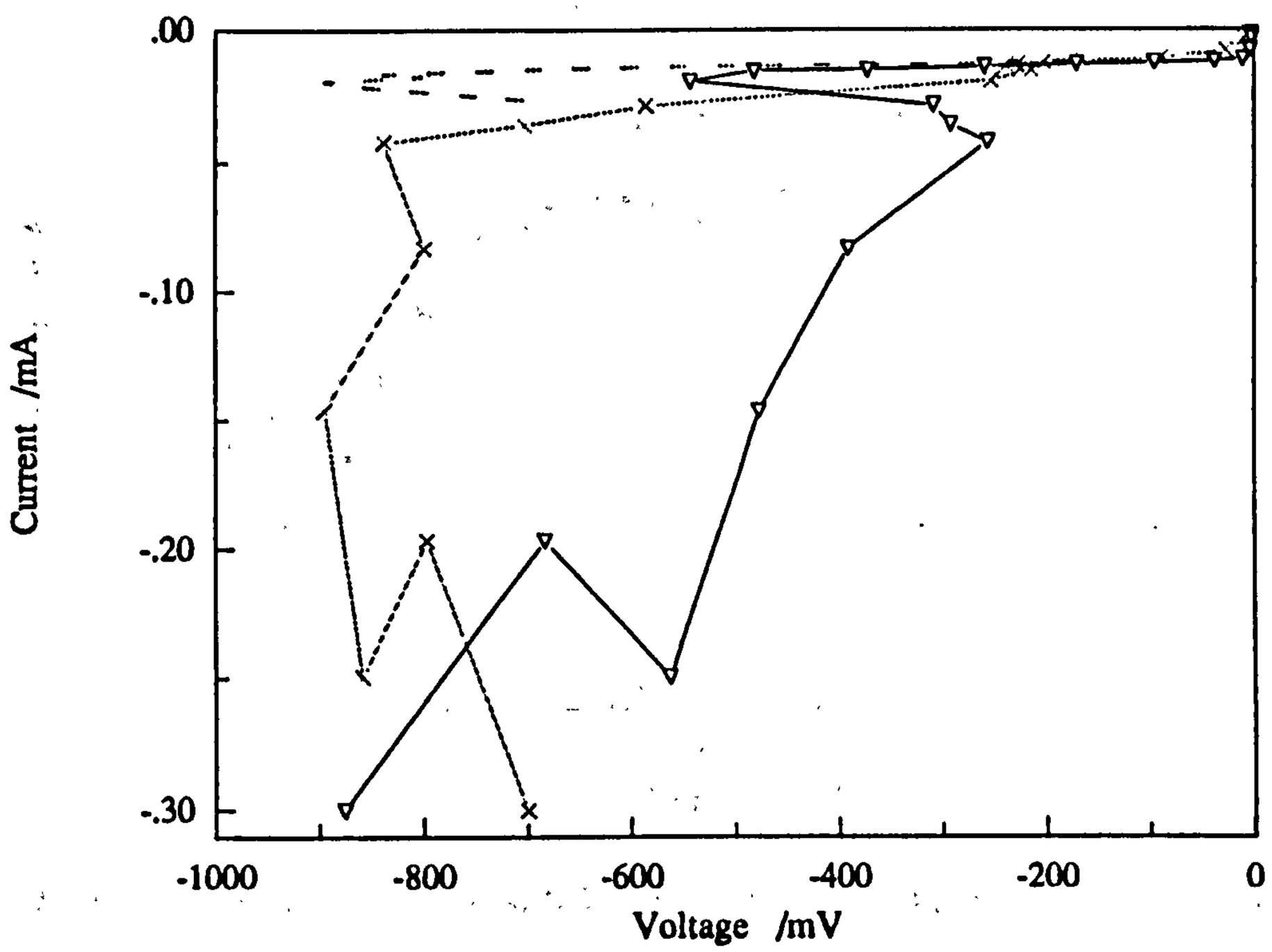

Fig. 5.14: Sensor G1 in trace SO_2 and 0.41% O_2 in N_2 at 600°C. - - -, total theoretical current using 56μm pore, I_0 = 0.2μA, α_c = 0.2. –×–, I_p vs. E_g; –∇–, I_p vs. η_c.

Tests were performed to see if the sensor could detect O_2, SO_2 and CO_2 in a single sweep of applied voltage starting at zero potential. Fig. 5.15 illustrates one set of results. A hump in the current occurred when E_g was 200mV below the value where an increase was expected due to SO_2 reduction. A large increase in current occurred about 200mV before the increase expected due to CO_2 reduction. Previous results (Fig. 5.11 and 5.13) showed that at 650°C the gauge voltage could be smaller than expected. Since the magnitude of the observed steps in Fig. 5.15 was similar to that expected for each gas it was concluded that this device could be developed to determine all 3 gases.

An interesting feature on the return voltage sweep was that the current on the internal pump electrode changed from being cathodic to anodic while the gauge and pump voltages still indicated reducing conditions. Since this transition occurred at the gauge voltage where it was suspected that SO_2 reduction began it must be assumed that it was due to the re-oxidation of the sulphur within the sensor.

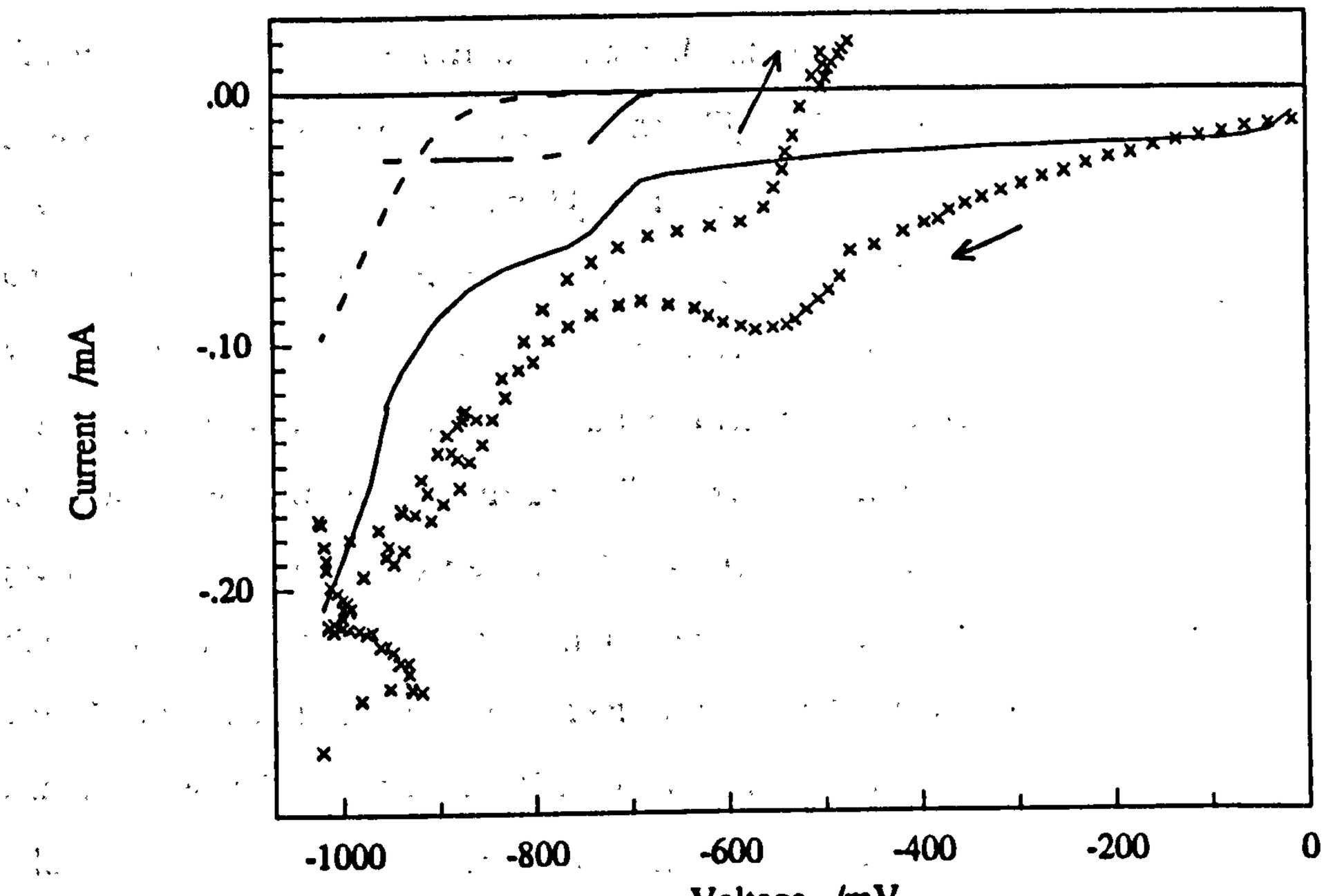

Fig. 5.15: Sensor G2 in 0.98% SO_2, 78.8% CO_2 and 4.22% O_2 in N_2 at 650°C. - - -, predicted current due to CO_2 reduction vs. E_g; — –, predicted current due to reduction of SO_2; ——, total theoretical current using 22μm pore, I_0 = 1μA, α_c = 0.2 and assuming 9.8% SO_2. –×–, I_p vs. E_g measured using CV at 0.2mV/s.

Sensors G1 and G2 both failed after brief usage in $SO_2/O_2/N_2$ mixtures. Sensor G2 failed because the pump electrodes developed a very high resistance after 6 days. It was suspected that the sulphur produced by the reducing conditions within the sensor reacted with the platinum electrodes ($Pt + S \rightleftharpoons PtS\uparrow$) as postulated by Steele et al (1981) and Whelan and Borbidge (1988).

Sensor G1 cracked during its 9th day of operation in SO_2 atmospheres probably because while testing in 4.6% SO_2 at 750°C the pump current oscillated with currents exceeding +100 and -100mA. The positive excursions of the current may have created large pressures within the sensor. Oscillations also occurred in CO-containing atmospheres and are discussed again in the next section.

5.4) Tests in $CO/CO_2/O_2/N_2$ mixtures

In $CO/CO_2/O_2/N_2$ mixtures at low temperature (below 500°C) the current on the internal pumping electrode remained cathodic even when the electrode was positive relative to the external electrode. Fig. 5.16 shows that the effect was more prominent when there was more O_2 in the initial feed gas than CO. When the O_2 concentration was lower there was not such a clear plateau in the current but a gauge voltage of just over +250mV was required before oxygen could be pumped into the sensor in both cases. A negative current meant that oxygen was flowing from the internal to the external electrode. This was the case when E_g was zero. The probable explanation is as follows. CO is strongly adsorbed onto the platinum and dominates the adsorption sites on the external electrode. Free oxygen is also adsorbed but not as strongly and reacts with the CO before its concentration on the surface approaches that of the CO. However, the diffusion pore limits the rate at which CO can reach the internal electrode. The rate of reaction of CO and O_2 on this electrode at 450°C is obviously great enough to consume all the CO. In both cases presented in Fig. 5.16 there was a stoichiometric excess of O_2. Since CO and O_2 have similar diffusion coefficients there was sufficient O_2 inside the sensor to oxidise all the CO. The excess oxygen is reduced at the internal electrode to supply the external electrode that cannot get enough by adsorption because the CO is blocking the sites.

To stop the current flowing a potential had to be applied. This potential is directly related to the anomalous emf studied by Okamoto et al (1981). They found that the anomalous emf decreased with increased temperature and that phenomena was mirrored in this work (Fig. 5.17).

In both sweeps shown in Fig. 5.16 the current started to rise rapidly just before E_g reached -600mV. Most probably, this was due to CO_2 reduction which only starts at a potential of -900mV relative to air. The external gauge electrode must therefore have had an oxygen potential approaching -300mV relative to air. This conforms with the above theory that strong CO adsorption on the external electrodes causes an anomalous depletion of oxygen adsorbed on them. With increased temperature the difference between the adsorption energies of CO and O_2 on platinum decreases and the anomalous emf also decreases.

When E_g was in the range -600 to -700mV (Fig. 5.16) the current oscillated. Okamoto also observed oscillations when the CO concentration was high which it would have been when E_g was -600mV. Oscillations in CO/CO_2 systems have been widely studied. Eiswirth et al (1990) proposed that they are caused by nonlinear dynamics in the rate of reaction. They support the conclusion by Matsushima (1978) that CO oxidation on Pt proceeds via the Langmuir-Hinshelwood mechanism: ie. $CO_{ads} + O_{ads} \rightarrow CO_2$. It has been observed that the surface of the Pt undergoes a facetting process during CO oxidation which increases the reaction rate (Sander and Imbihl (1991)). Similar phenomenon may have caused the oscillations observed during SO_2 reduction (previous section).

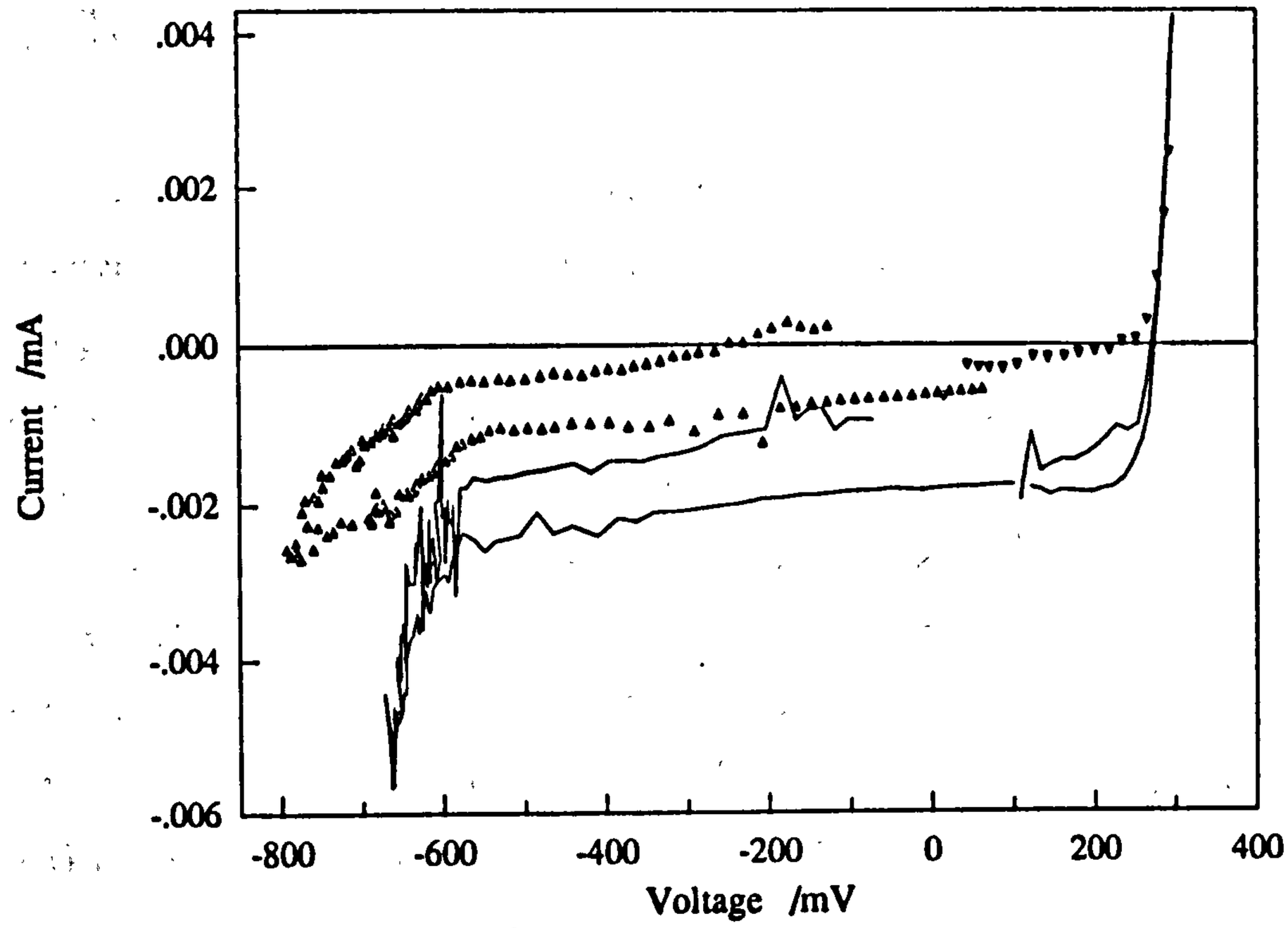

Fig. 5.16: Sensor G2 in 0.38% CO, O_2 and N_2 at 450°C. ——, I_p vs. E_g in 0.65% O_2; ∇ and Δ, I_p vs. E_g in 0.33% O_2, measured using CV mode at 0.1mV/s.

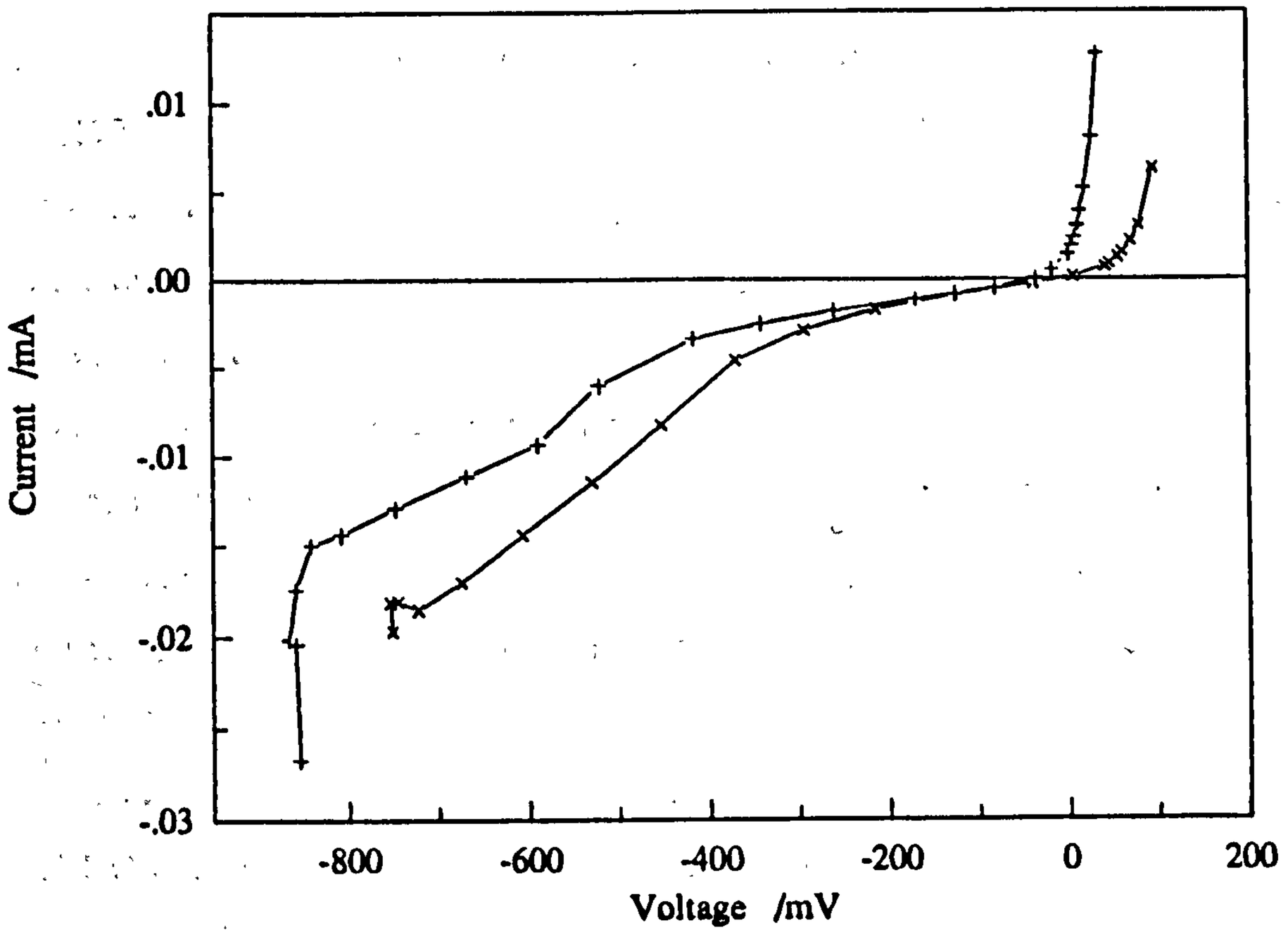

Fig. 5.17: Sensor G2 at 700°C. -+-, I_p vs. E_g in 0.052% CO and 0.36% O_2; -×-, I_p vs. E_g in 0.38% CO and 0.33% O_2.

5.5) Tests with nitric oxide

Large quantities of NO_x are produced by numerous combustion processes but the concentration, even in the stack gas, is never very high. The main requirement for NO_x sensors is therefore for devices that can detect 1000 ppm and less. NO comprises 98% of the NO_x produced by petrol engines (Gur and Huggins (1979)) so the available supply of 100ppm NO in N_2 was used exclusively in this work.

The oxygen concentration of the test gases had to be kept low to allow the current due to NO reduction to be distinguished from those due to oxygen reduction and electrochemical leakage. Fig. 5.18 shows a set of results compared to the theoretical currents with and without the contribution due to NO reduction. If eqn(A1.21) for full NO reduction ($NO + 2e^- \longrightarrow \frac{1}{2}N_2 + O^{2-}$) was used it predicted complete reaction at relatively large oxygen partial pressures. The results in Figs. 5.18 to 5.20 show that this did not occur. If eqn (A1.28) for partial reduction was used it still predicted reduction at oxygen pressures higher than those observed but the agreement with experiment was closer. It was therefore assumed that the reaction mechanism included the formation of N_2O as an intermediate product. Pancharatnam et al (1975) also concluded this. It is suspected that N_2O was formed first by electrochemical reduction and it then immediately decomposed at the temperatures used for testing the sensors. The decomposition was either electrochemical or the oxygen released chemically was reduced electrochemically. Usui et al (1989a) tested a similar sensor in N_2O atmospheres and found that their sensor passed a current that was close to that predicted if complete reduction of N_2O occurred. Without a gauge cell they were unable to tell at what internal oxygen partial pressure reduction began or was completed. The thermodynamic data (Fig. 1.10) also predicts that N_2O will be extremely unstable.

To calculate the currents due to NO reduction in this work eqn (A1.28) for partial NO reduction was used but an additional electron was transferred because of the immediate decomposition of the N_2O.

At higher temperatures electrochemical leakage becomes much more significant and the results do not agree as well with theory. However, an interesting feature becomes more evident. It is the remarkable stability of the gauge voltage

reading at a value near -200mV while the overvoltage on the internal pumping electrode experiences more than an order of magnitude increase. This demonstrates that NO is not reduced until pO_2 is reduced to a critical level. This conforms with several studies of the catalytic reduction of NO that have shown that the rate is inversely proportional to pO_2; in essence the oxygen poisons the ability of platinum to reduce NO_x (Gur and Huggins (1979), Pancharatnam et al (1975), and Gessner et al (1988)).

Tests were not performed on single discs in $NO/N_2/O_2$ mixtures but they were performed in $CO/CO_2/N_2$ mixtures (section 3.3.2). The results in this section showed that σ_e decreased as pCO increased and then σ_e increased markedly as pCO increased beyond a certain level. It is possible that the peak in η_c was caused by a similar phenomenon in the $NO/N_2/O_2$ system.

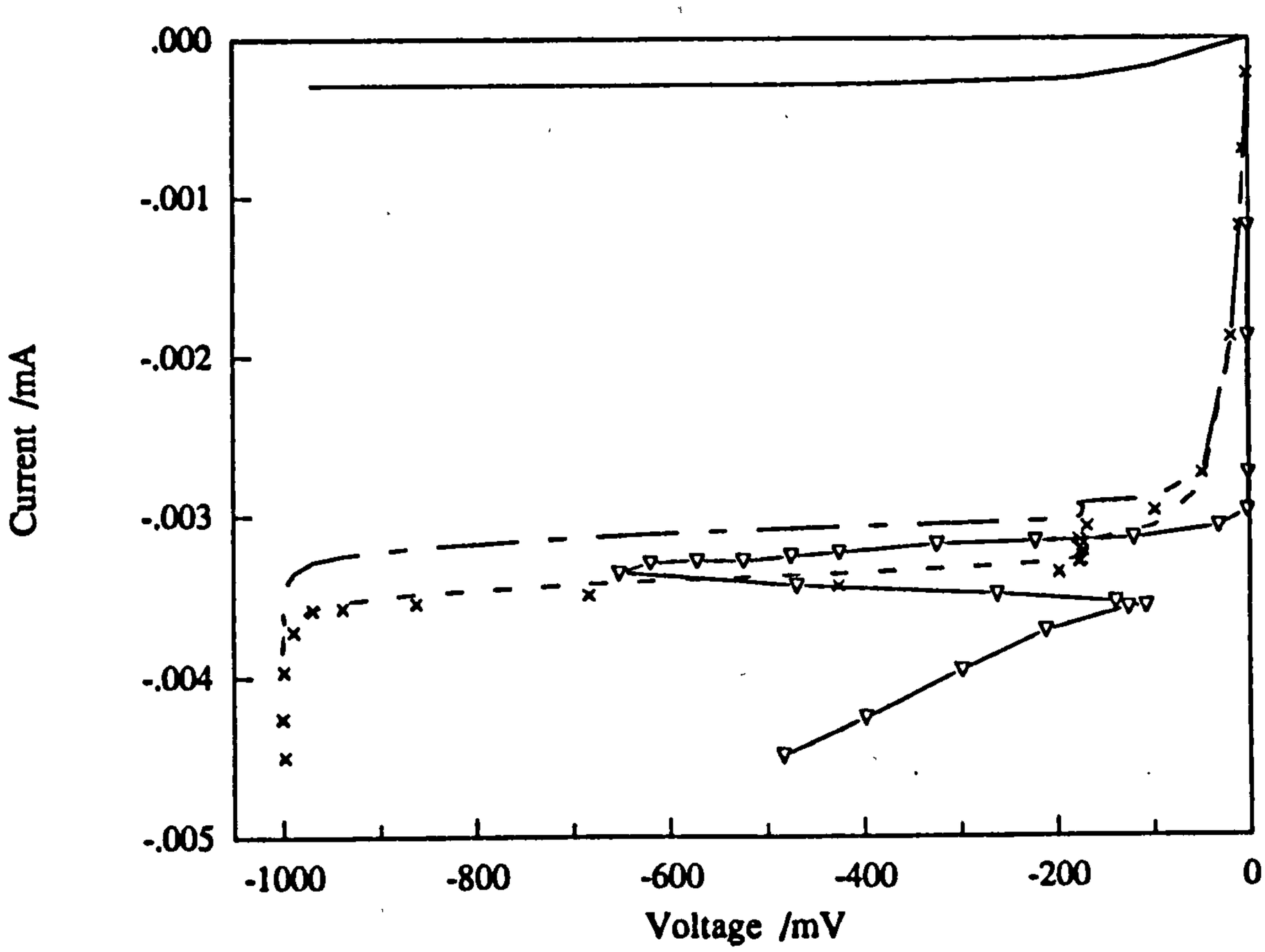

Fig. 5.18: Sensor G1 in 0.01%NO and 0.139%O_2 in N_2 at 500°C. - - -, current predicted using θ_p 52.5μm, I_0 = 20nA α_c = 0.15; — –, predicted without contribution from NO; ——, current due to NO only. ×, I_p vs. E_s; ▽, I_p vs. η_c.

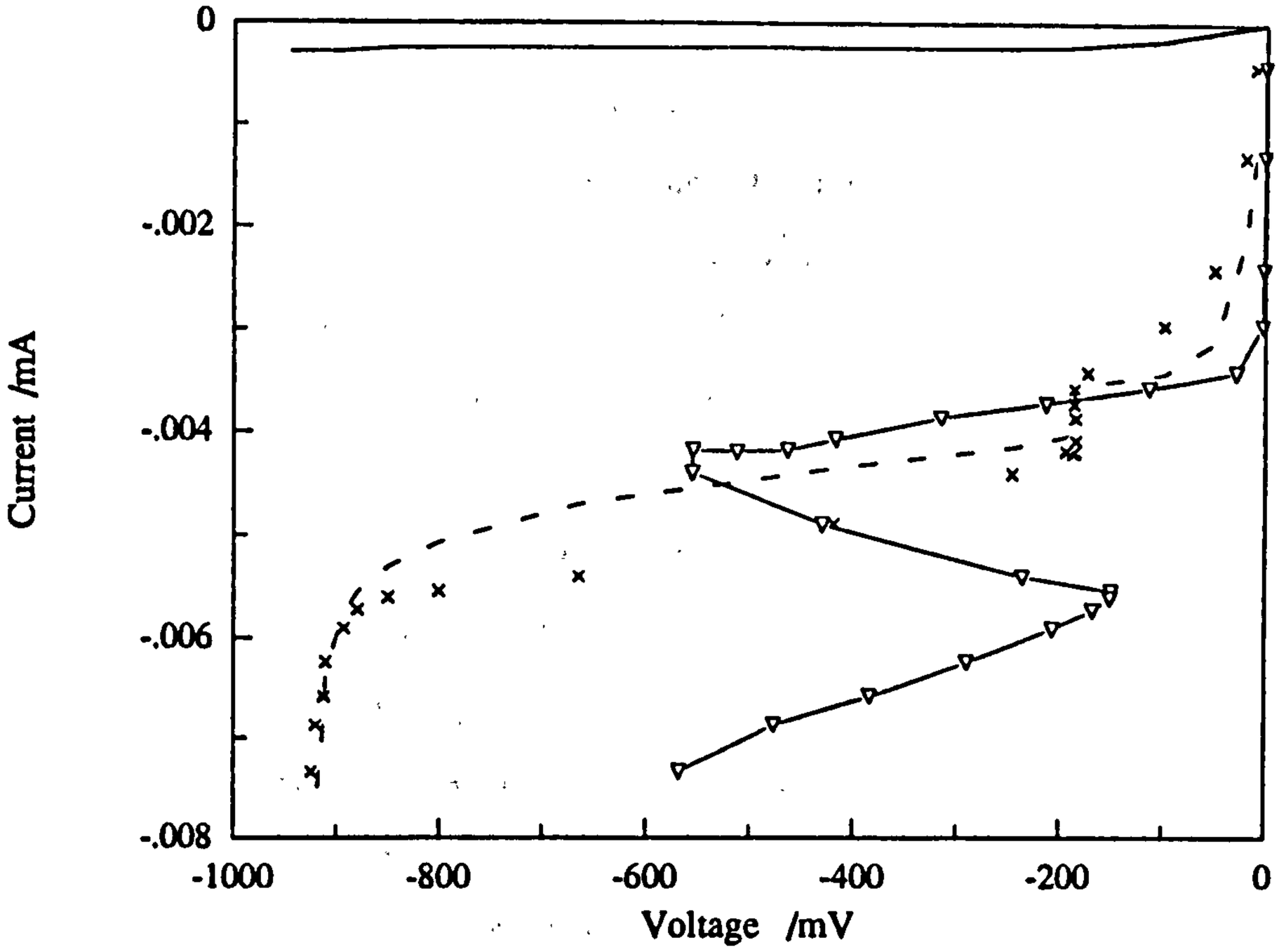

Fig. 5.19: Sensor G1 in 0.01%NO and 0.139%O_2 in N_2 at 600°C. - - -, current predicted using θ_p = 53μm, I_0 = 100nA α_c = 0.15; ——, due to NO only. ×, I vs. E_g; ▽, I vs. η_c.

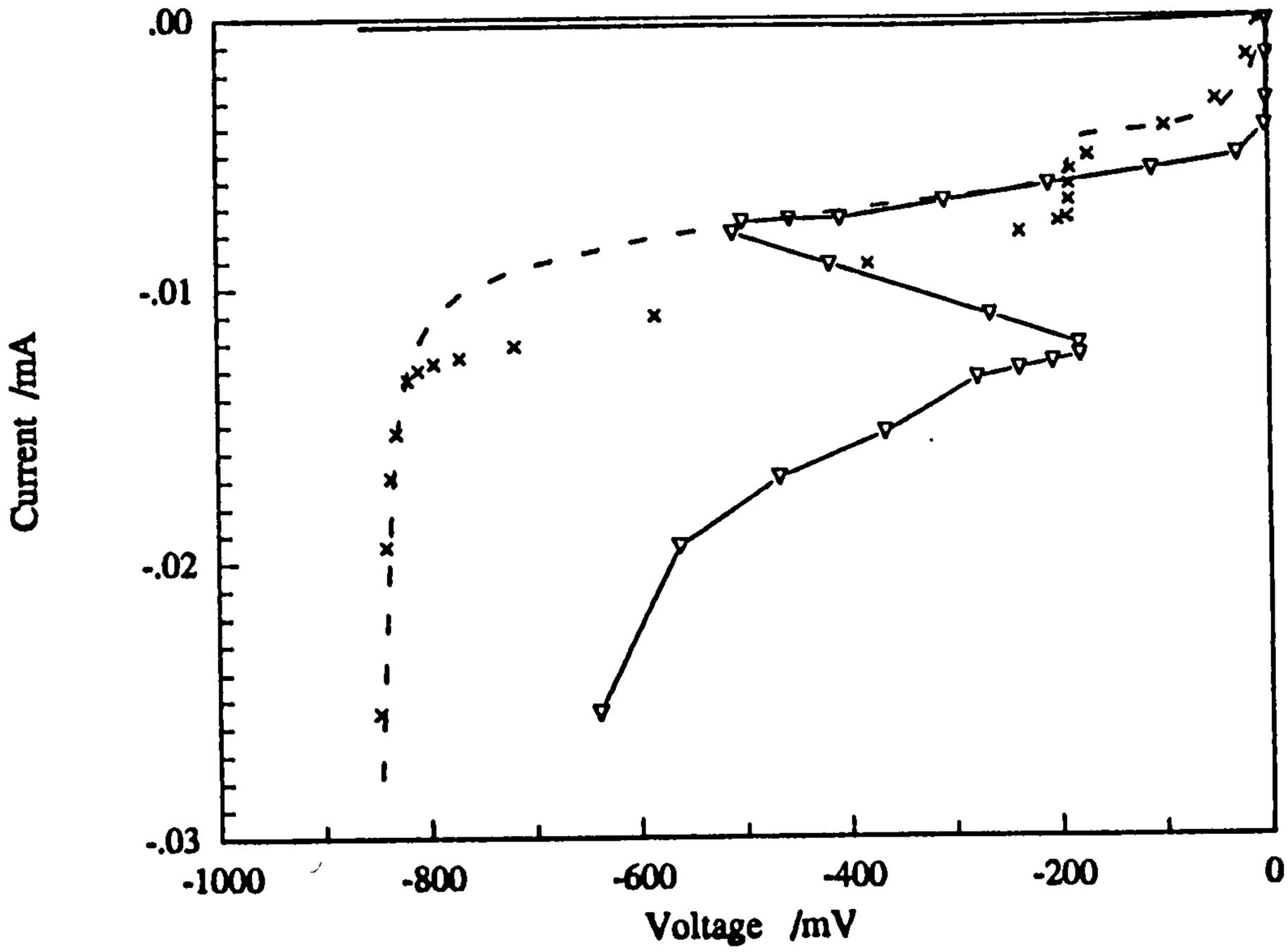

Fig. 5.20: As Fig. 5.19 but at 700°C. Symbols as Fig. 5.19 except I_0 = 20nA and α_c = 0.25.

Extensive tests were done with sensor G2 in NO mixtures and Figs 5.21 and 5.22 illustrate a few of the results. The peak in η_c is still evident but is smaller than in G1. The width of the peak (along the current axis) is of the same magnitude as that expected due to NO reduction. There is some evidence of a small step in current as a function of gauge voltage in Fig. 5.22 but the stability of E_g during this step seen on sensor G1 is not apparent on sensor G2. The difference was believed to be due to the platinum wire blocking the pore of G1. At the entrance to the pore where the oxygen partial pressure was relatively high, the platinum would have catalysed the oxidation of the nitrogen. NO_x compounds would therefore enter the sensor even if they had not originally been present in the gas supplied to the sensor. This would explain why a peak in η_c was observed in nearly all sets of results from sensor G1 while in sensor G2 it was usually observed when NO was in the gas supplied to the sensor and the oxygen partial pressure was low. Fig. 5.23 is one exception. The theoretical current with and without the contribution due to partial CO_2 reduction are plotted, but the latter is only just visible at the point where the current increases sharply. The results suggest that a small amount of NO may have been formed on the external electrodes and diffused to the pore entrance.

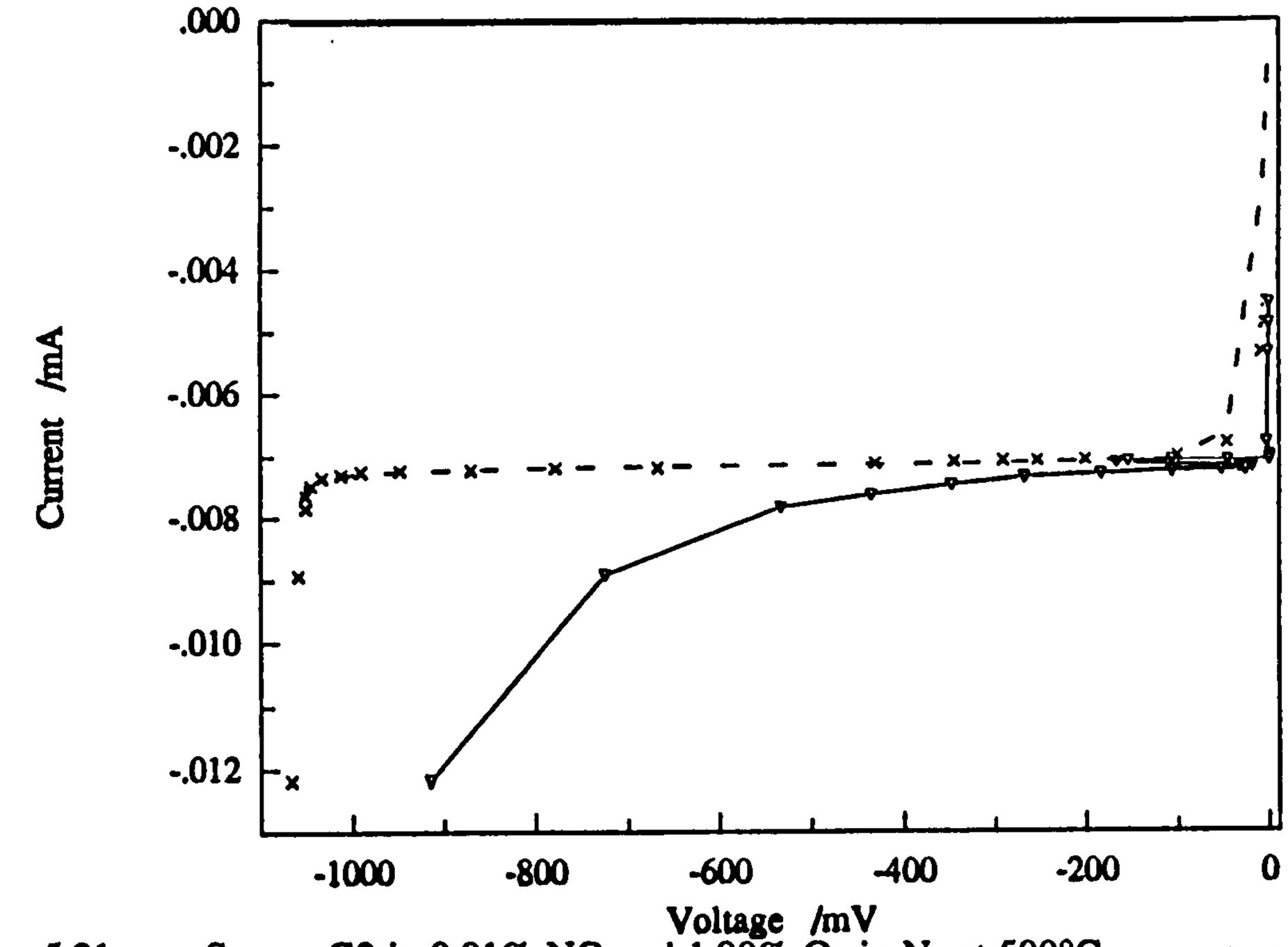

Fig. 5.21: Sensor G2 in 0.01% NO and 1.90% O_2 in N_2 at 500°C. - - -, current predicted using θ_p = 22.1μm pore, I_0 = 10nA α_c = 0.15; ——, current due to NO reduction only. ×, I_p vs. E_g; -▽-, I vs. η_c.

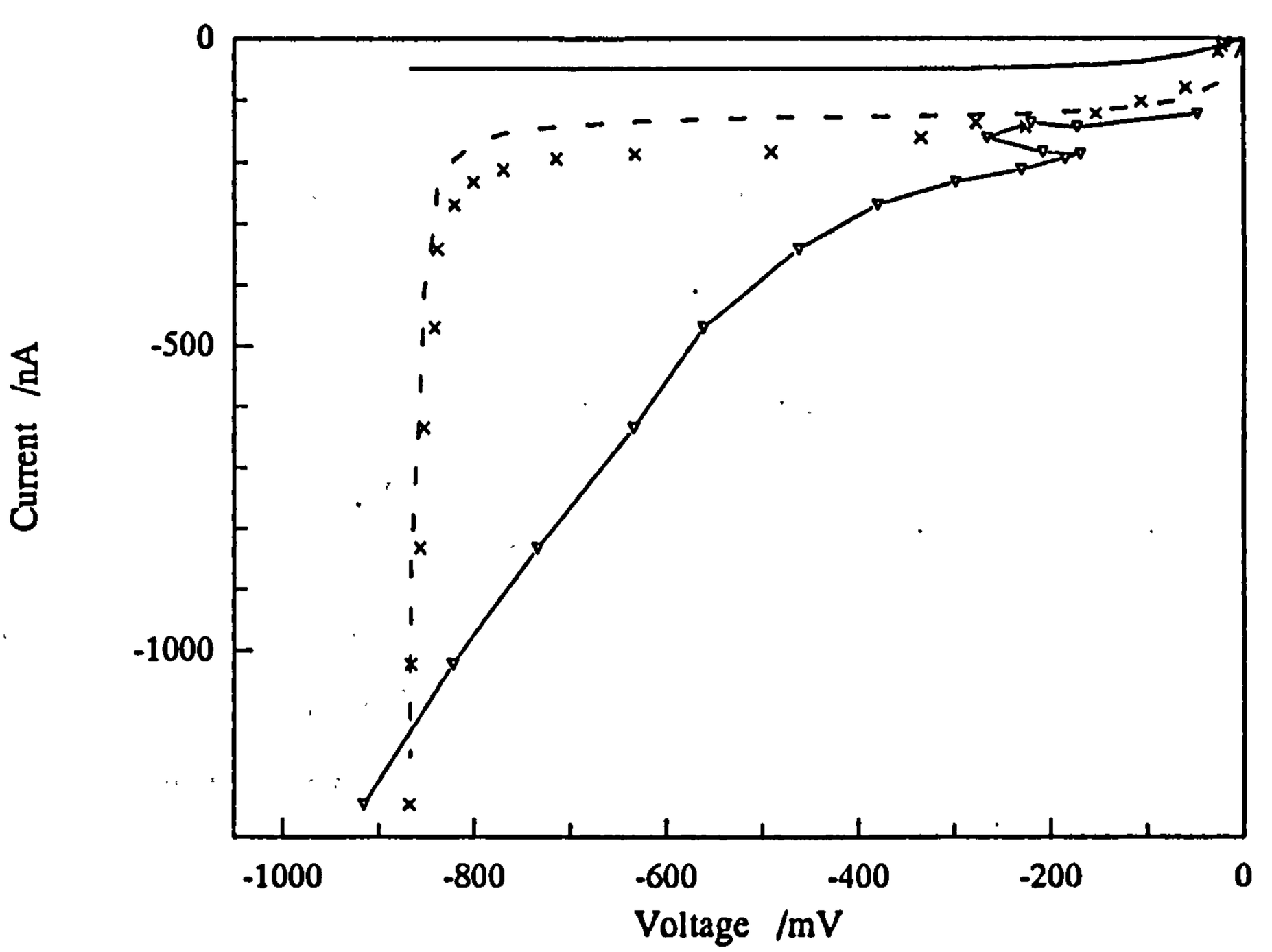

Fig. 5.22: Sensor G2 in 0.01% NO and 0.021% O_2 in N_2 at 450°C. - - -, current predicted using θ_p = 22.1μm pore, I_0 = 0.2nA α_c = 0.3; ——, current due to NO reduction only vs. E_g. ×, I_p vs. E_g; -▽-, I vs. η_c.

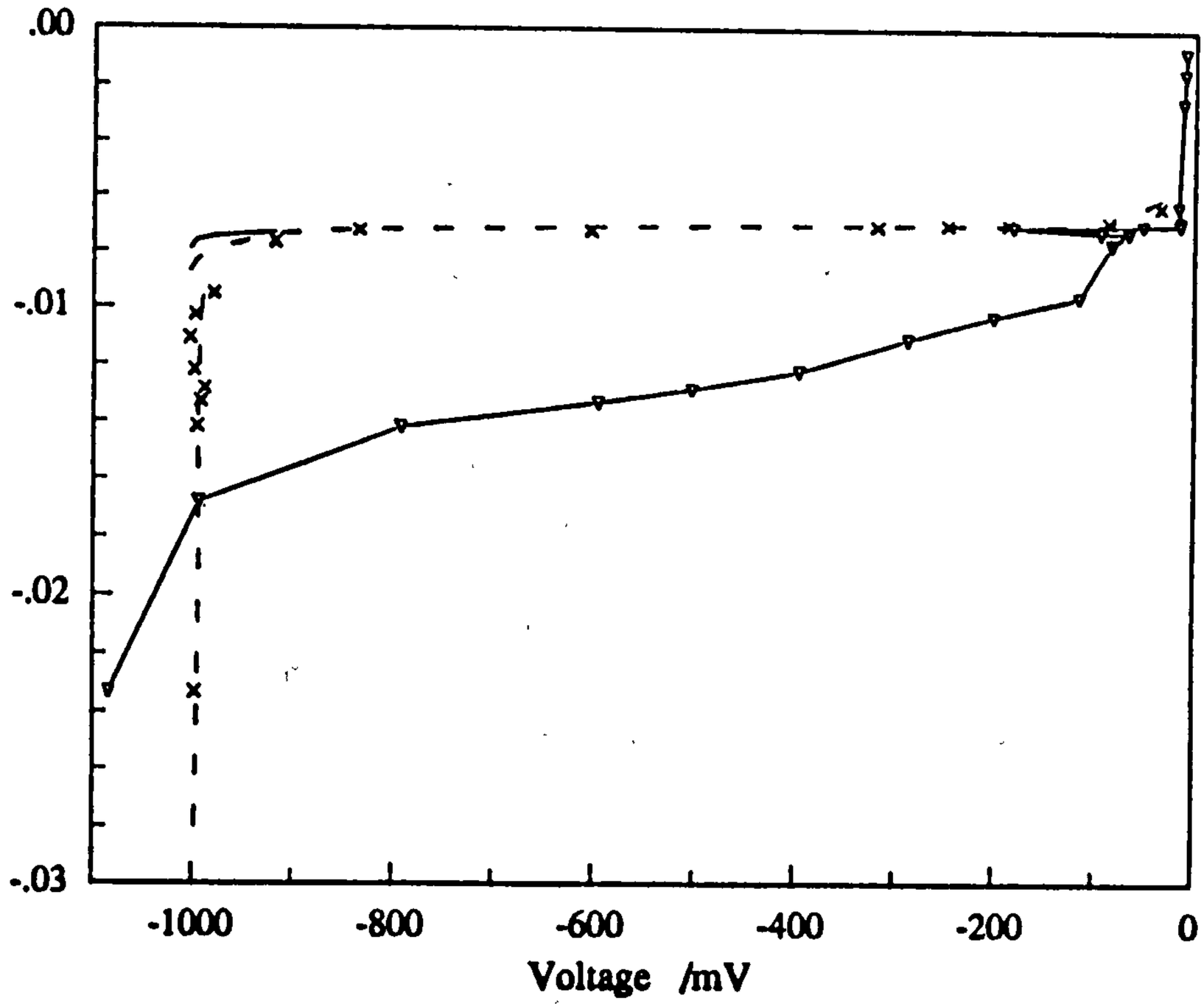

Fig. 5.23: Sensor G2 in 2.31% CO_2 and 1.86% O_2 in N_2 at 500°C. - - -, current predicted using θ_p = 22.2μm pore, I_0 = 8nA α_c = 0.22; ——, predicted without current due to CO_2 reduction vs. E_g. ×, I_p vs. E_g; -▽-, I vs. η_c.

The gauge voltage reading where the sharp step in current occurred was recorded at a range of temperatures and external oxygen partial pressures using sensor G1. Note that NO was not added to the feed gas. A test was done to determine if the temperature dependence of the step voltage correlated with the thermodynamic stability of the reaction:

$$NO \rightleftharpoons N_2O + \tfrac{1}{4}O_2.$$

Table 5.1 shows the results. It was assumed that the N_2, NO and O_2 were in equilibrium at the pore entrance outside the sensor. Eqn(A1.28) was then used to determine the percentage of the NO that would be reduced by the sensor at the gauge voltage where the step occurred. Table 5.1 shows this theoretical percentage NO reduction as a function of temperature and surrounding oxygen concentration (balance N_2).

Table 5.1

Gauge voltage at which step increase in current occurred and theoretical percentage reduction in pNO at that voltage.

Temperature °C	Air		5.25% O_2		0.41% O_2	
	E_g /mV	Theoretical % pNO reduction	E_g /mV	Theoretical % pNO reduction	E_g /mV	Theoretical % pNO reduction
750	285	73	260	59	233	25
700	259	70	254	59	236	31
650	249	72	247	62	235	36
600	232	71	238	64	231	42
550	215	71	226	66	228	47
500	191	67	212	67	222	52

An extensive search of the Gibbs free energy tables in Barin (1989) did not reveal any other reaction (in the solid or gaseous phase) that matched the observed trend in stability. Fig. 1.10 shows the results of converting some of this data to oxygen potentials. This result helps confirm that it was indeed partial NO reduction that caused the step in current and the peak in η_c. Table 5.1 shows that the correlation was not as good when pO_2 was low. The most likely explanation is that a very low NO concentration was produced by the platinum at the pore entrance and this small amount of NO was easily reduced inside the sensor.

Tests were performed to see if sensor G2 could be used to detect three gases: O_2, NO and CO_2: Fig. 5.24 shows one set of results. The pump currents after the addition of CO_2 to the gas mixture were larger, but the increase was small and the gauge voltage did not reach potentials where significant CO_2 reduction was expected to occur. These disappointing results could have been due to the low operating temperature.

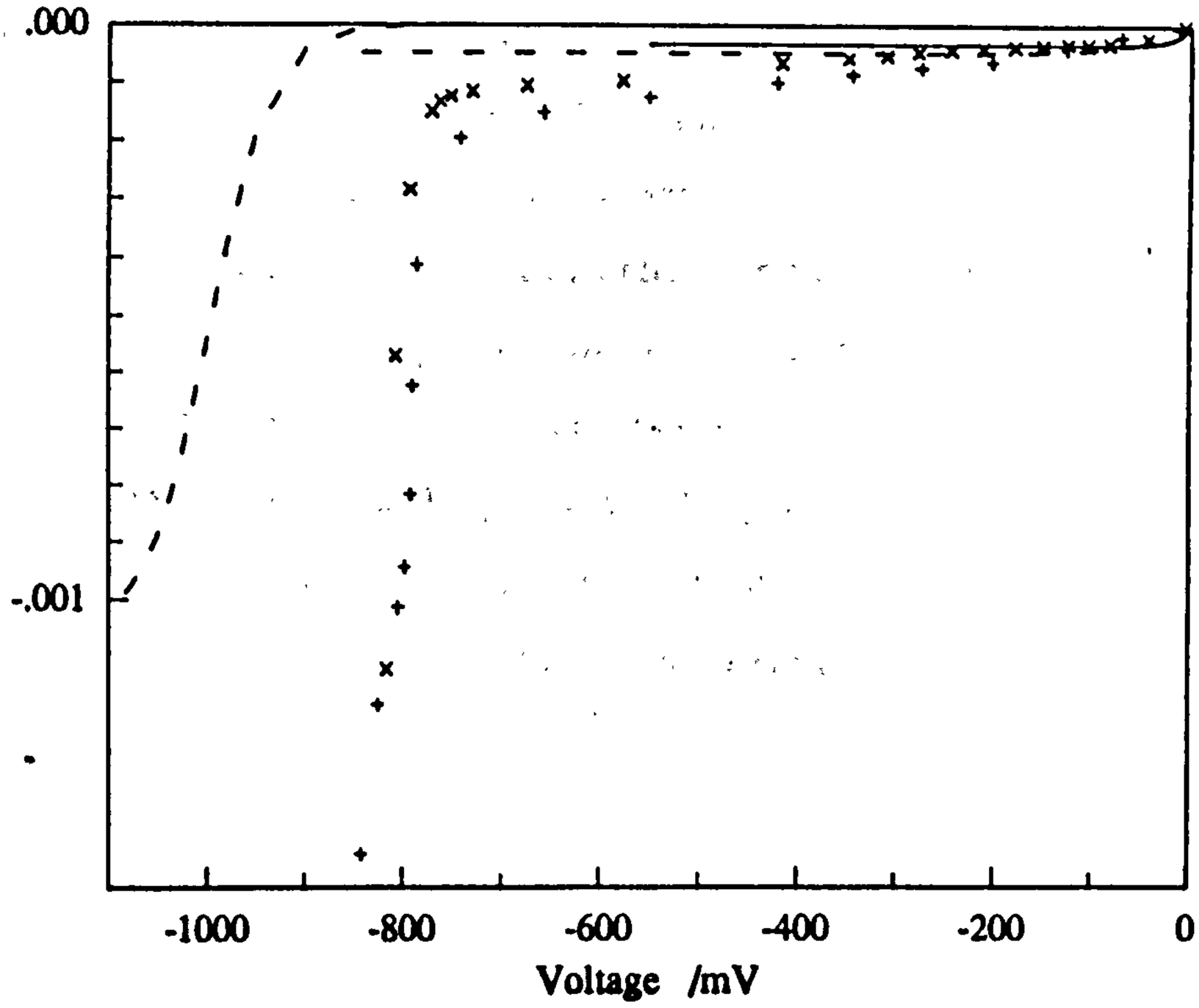

Fig. 5.24: Sensor G2 at 450°C. ×, 0.01% NO and 0.01% O_2 in N_2; +, 0.01% NO, 0.77% CO_2 and 0.01% O_2 in N_2. - - -, current predicted using θ_p = 22μm pore (two curves, one for NO reduction only and one for CO_2 reduction). ——, current due to O_2 reduction only. ×, I_p vs. E_g; +, I vs. η_c.

5.6 Conclusions

The theory for the reduction of several oxygen-containing gases in a pump-gauge sensor was derived using thermodynamic relations. The pump current predicted by these equations was then compared to experimental results. It was found that the sensors did not behave exactly as predicted, but this may have been mostly due to electrochemical leakage.

In $NO/O_2/N_2$ mixtures the NO was reduced over a smaller range of pO_2 values than predicted. In $CO_2/O_2/N_2$ mixtures η_c increased to the extent that the CO_2 could not be reduced before semipermeability of the YSZ became a problem. Large leakage currents also masked the expected increase in I_p due to CO_2 reduction. An interesting dip in I_p was sometimes observed in these mixtures. It was postulated that this was due to disproportionation of CO that had built up in the sensor followed

by rapid combustion of the carbon that formed. In $CO/O_2/N_2$ mixtures an anomalous voltage effect was observed. It was suspected that the diffusion barrier had a similar effect to the catalyst layer of the anomalous CO sensor of Okamoto et al (1980). It was suspected that SO_2 caused electronic conductivity in the YSZ. Corrosion of the platinum electrodes by NO and SO_2 was shown to be a problem.

Tests were performed to see if the sensors could detect three gases within a mixture: O_2, NO and CO_2 in N_2 and O_2, SO_2 and CO_2 in N_2 mixtures were tested. The results were not conclusive but it was believed that a sufficiently developed sensor could determine all three gases in the above mixtures simultaneoulsy.

Chapter 6

Advanced sensors: considerations

6.1 Sensor durability

Sensor G1 was used continuously for more than 3 months in a wide range of gases at temperatures between 350°C and 750°C. Figs. 6.1 - 3 are a direct comparison of its performance at different ages. Fig. 4.14 illustrates its performance in air at 500°C when 5 days old. Fig. 6.1 illustrates the results from the same sensor except that it had nearly 5 weeks of use and 0.4% of CO_2 was added to the air. The difference between the predicted and measured current multiplied by 10 (represented by □ and plotted on both figures) showed that the current characteristics hardly changed. The overvoltages (represented by ▽) decreased with age if anything.

Fig. 6.2 illustrates the results at an age of 7 weeks. The overvoltage on the internal pumping electrode increased to the extent that it prevented the sensor achieving a limiting current plateau at 500°C; therefore Fig. 6.2 presents data measured at 600°C. Fig. 4.13 shows the results in air at 600°C when 5 days old for comparison. The pore diameter required to model the data increased from 49.8μm to 54.2μm and the exchange coefficient (α_c) modelling the leakage increased from 0.07 to 0.14. The only difference between the first 5 weeks of use (Fig. 6.1) and the last 2 weeks (Fig 6.2) is that the sensor was used in nitric oxide containing atmospheres for 5 days during the last 2 weeks.

Fig. 6.3 shows the results after a further 2 weeks of operation in NO-containing gases. The effective pore diameter increased to 55.6μm, the overvoltages increased again and the leakage current had also increased (modelled by an I_0 of 0.6μA instead of 0.4μA).

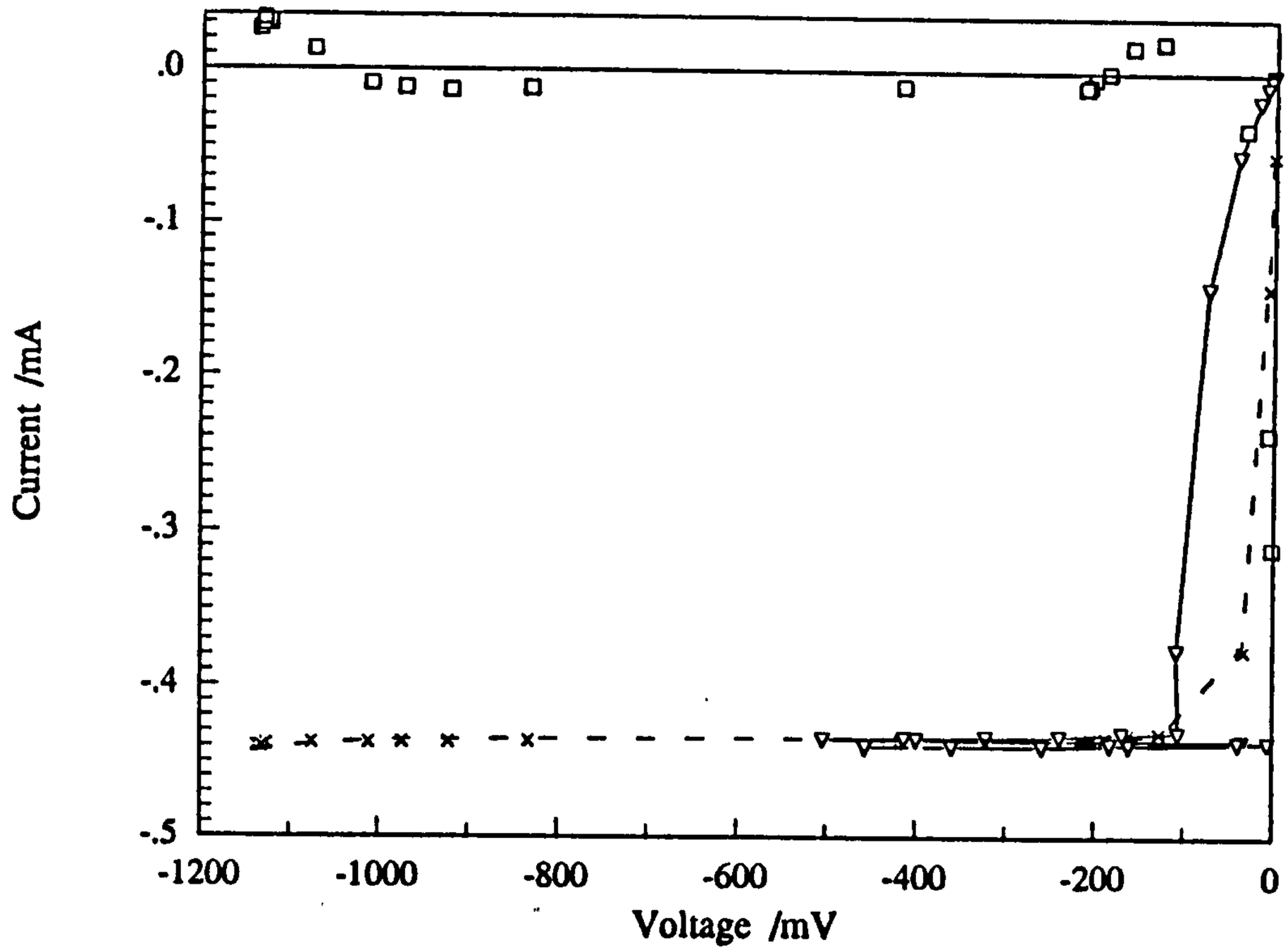

Fig. 6.1: Response of sensor G1 in air at 500°C when aged 5 weeks. x, measured I_p Vs. E_g; - - -, theoretical current vs. E_g, $\theta_p = 49.8\mu$, $I_0 = 0.6\mu A$, $\alpha_c = 0.07$. –∇–, overvoltage on internal pumping electrode; □, error × 10.

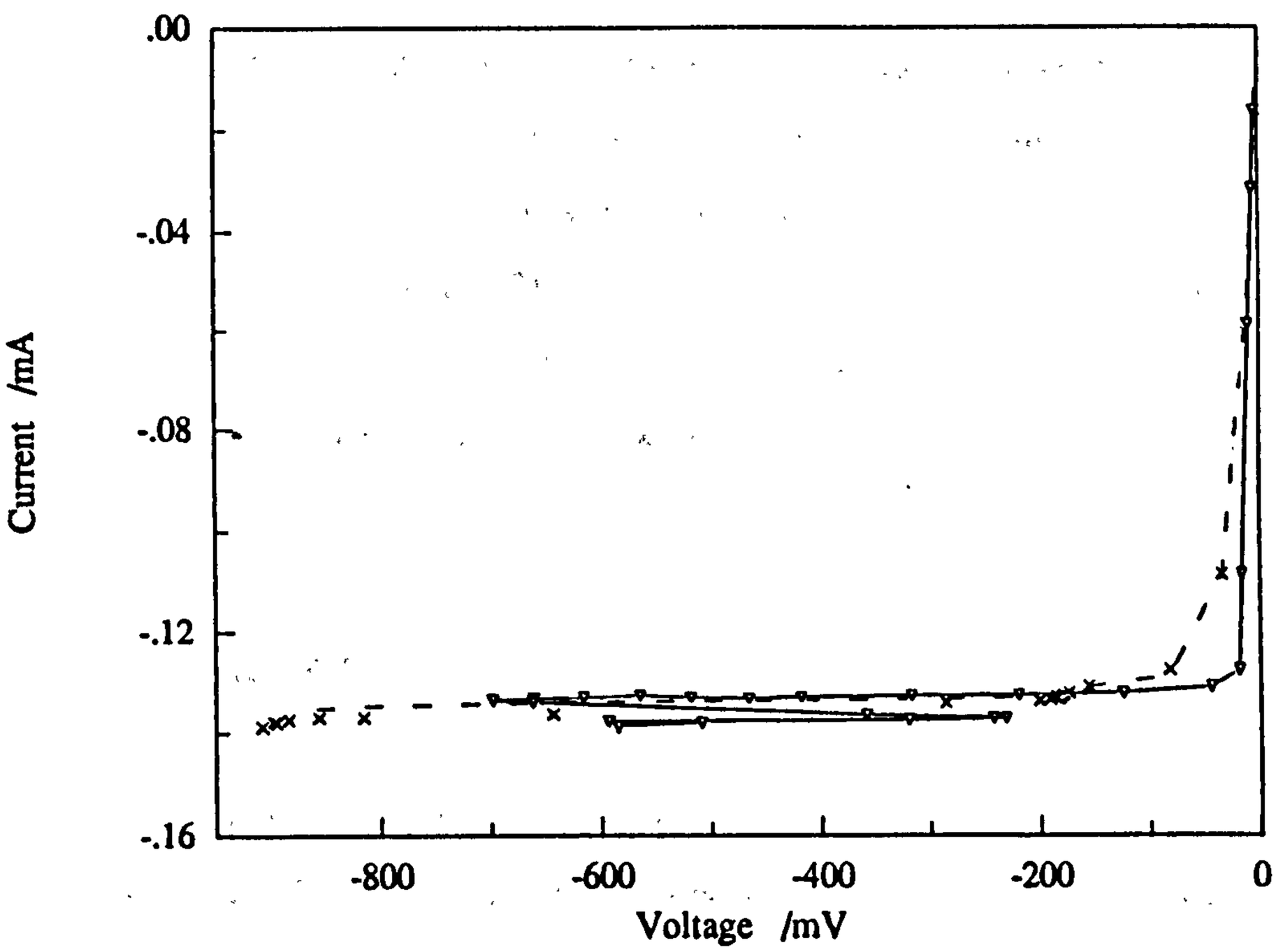

Fig. 6.2: Sensor G1 aged 7 weeks in air at 600°C. x, measured I_p vs. E_g; - - - , theoretical current vs. E_g, $\theta_p = 54.2\mu$, $I_0 = 0.4\mu A$, $\alpha_c = 0.14$. –∇–, I_p vs. η_c.

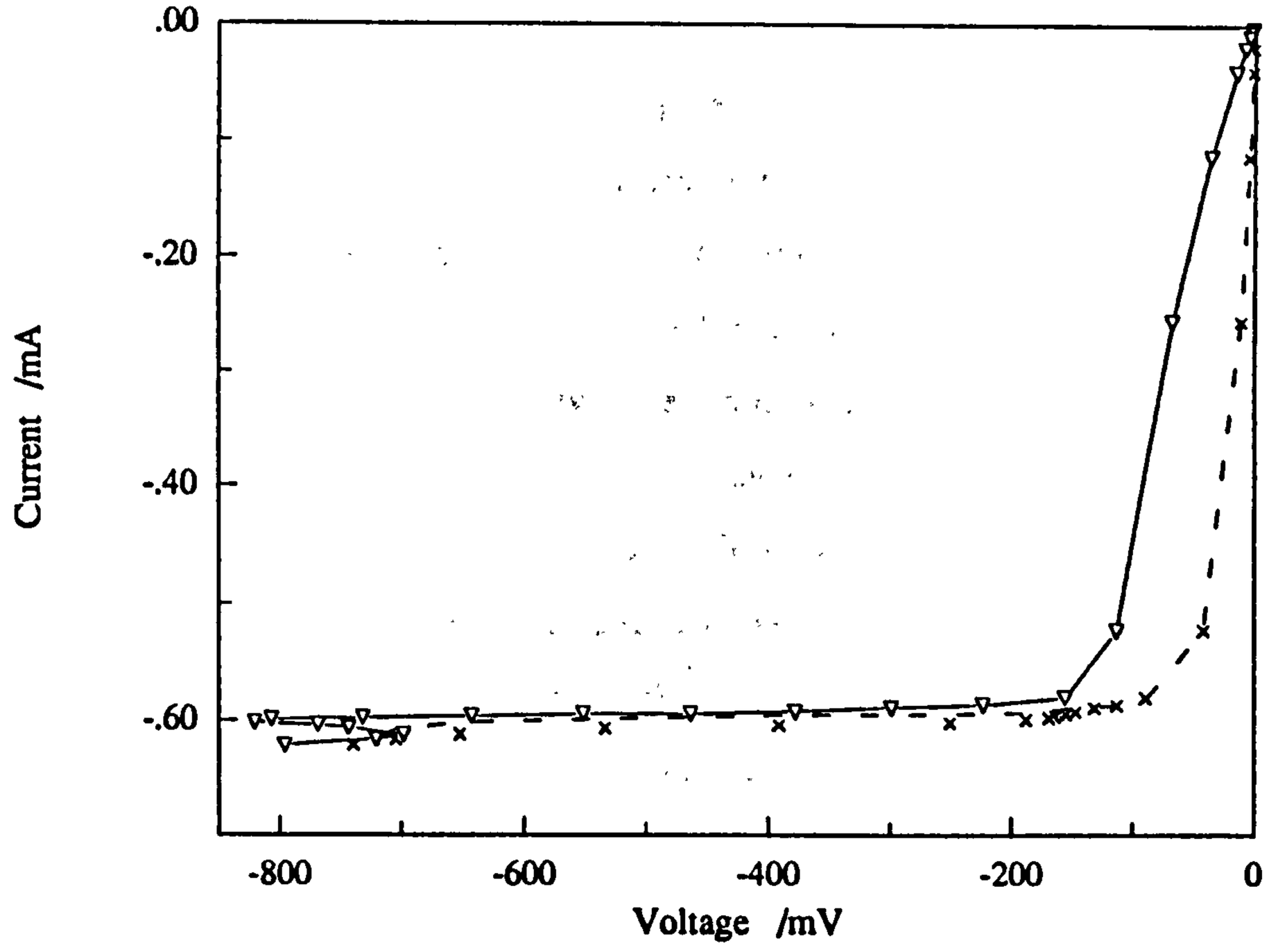

Fig. 6.3: As Fig. 6.2 but sensor aged 3 months. θ_p = 55.2μ, I_0 = 0.6μA, α_c = 0.13.

Extrapolating from the results for 5 days and 5 weeks indicates that the sensor should have had a lifetime of many years. It therefore seems likely that the deterioration was caused by the low NO concentrations (.01% and less) used before the final 2 tests (Figs. 6.2 and 6.3). The NO probably reacted with the platinum causing the electrode activity to decrease. It could have also reacted with the platinum wire blocking the diffusion pore which would explain the increased limiting current.

6.2) Response rates

Fig. 6.4 shows the results of two cyclic voltammetry (CV) scans on sensor G2 at 700°C in air. The slow scan at 0.1mV/s showed little difference between the forward and reverse sweeps at gauge voltages less than -800mV. At greater values where trace impurities of CO_2 and H_2O are expected to be reduced there is a greater difference between the sweeps. The fast scan (10mV/s) shows a large difference

between the sweeps. The difference between fast and slow scans is more evident in Fig. 6.5 which reflects results measured at 550°C. At 0.1mV/s the CV scan corresponds closely with the theoretical curve but at 10mV/s there is a large difference. The peak at -80mV is presumably due to the reduction of oxygen adsorbed on the platinum electrodes. The peak was an order of magnitude smaller than the peak observed when using silver electrodes (Fig. 4.8).

The results in Fig. 6.6 demonstrate that even 1mV/s was too fast a scan to achieve close agreement with theoretical curve. Therefore if a multi-gas sensor were to operate by scanning the pumping or gauge voltage it would have to scan at less than approximately 0.2mV/s. That would take more than 1½ hours to scan 1000mV. This very slow response is probably due to the capacitive nature of the electrodes.

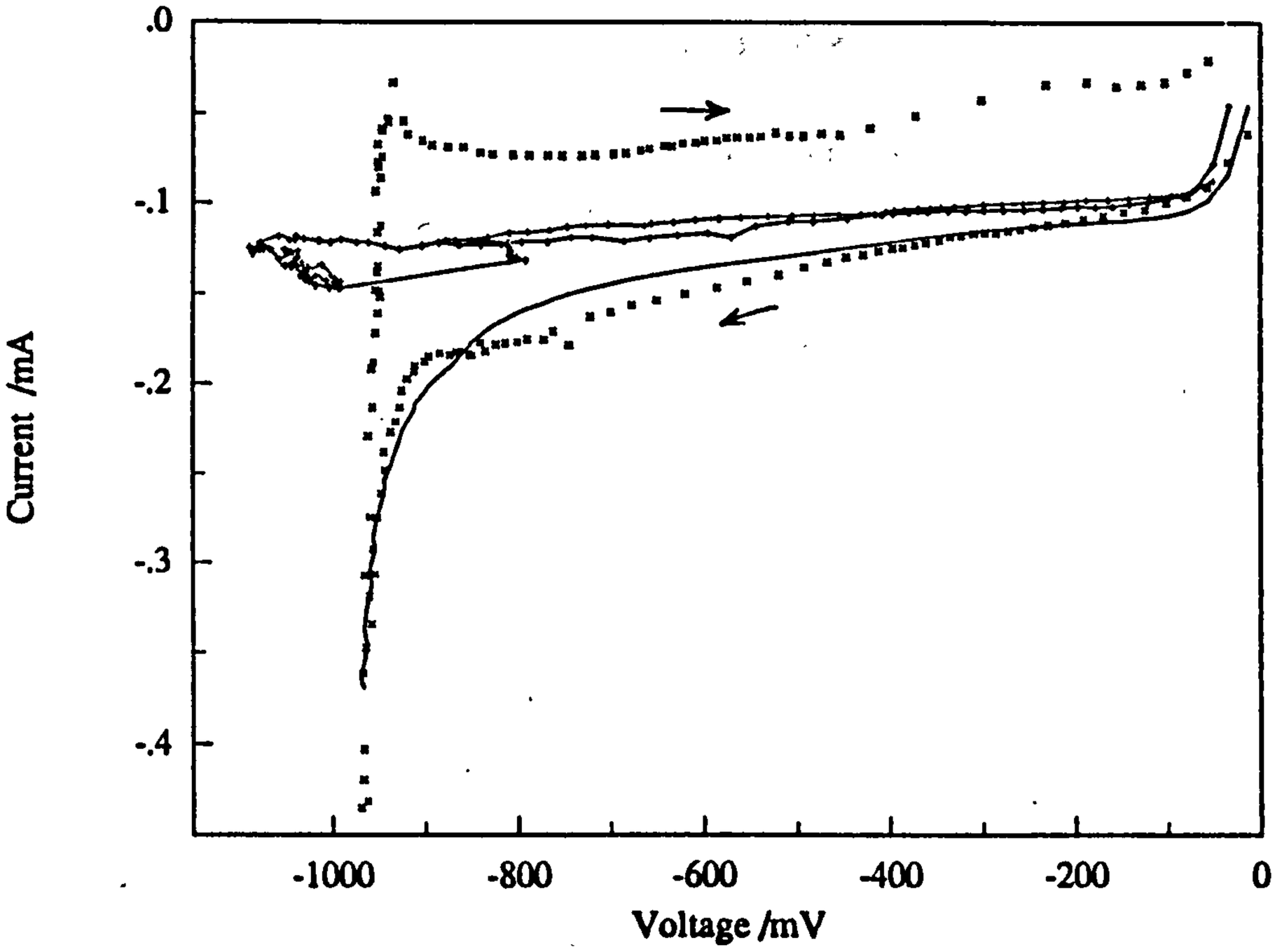

Fig. 6.4: CV scan on sensor G2 in air at 700°C. x, 10mV/s; -+-, 0.1mV/s; ——, theoretical current, θ_p = 22.0μm, I_0 = 3μA, α_c = 0.22.

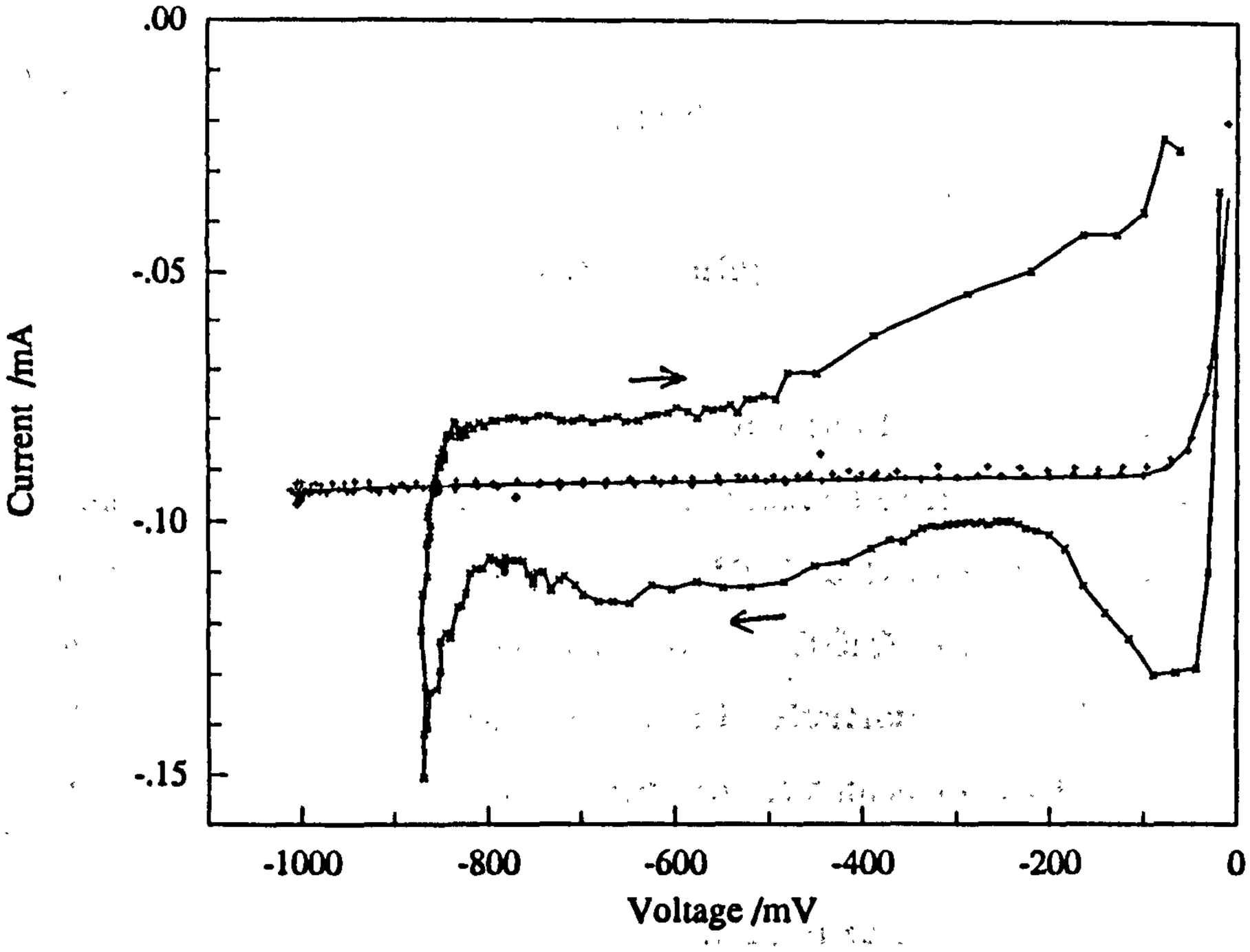

Fig. 6.5: CV scan on sensor G2 in air at 550°C. –x–, 10mV/s; +, 0.1mV/s; ——, theoretical current, $\theta_p = 22.1\mu$, $I_0 = 0.5\mu A$, $\alpha_c = 0.09$.

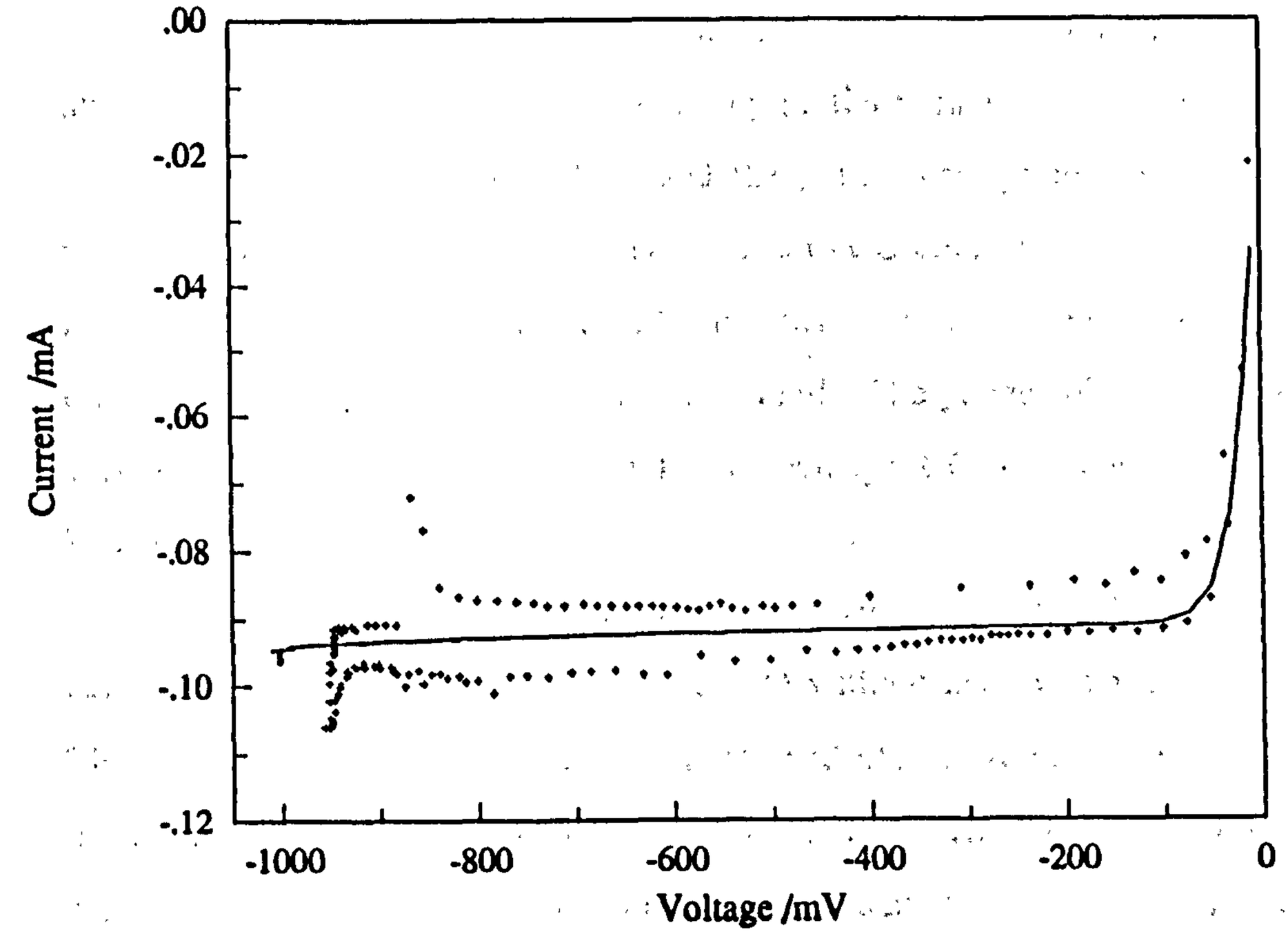

Fig. 6.6: CV scan on sensor G2 in air at 550°C. As Fig. 6.5 but only scan shown was at 1mV/s.

6.3) Zirconia multi-gas sensor

6.3.1 Operating modes

In theory, scanning the pumping voltage of a solid electrolyte pump-gauge sensor in a complex gas mixture would produce a series of plateaus in the pumping current. At a gauge voltage of about -150mV only free oxygen would be reduced. At -250mV NO would also be reduced. At -800mV SO_2 would be reduced and at -900mV CO_2 would be partially reduced. Therefore all the above gases could be determined quantitatively and qualitatively. A number of problems need to be solved before such a sensor could be built.

If a CO_2 sensor were to be operated in such a way that it reduced CO_2 to carbon, then the carbon would build up within the sensor. The carbon would have to be oxidized out periodically. This would add significant complication to the sensor's control system and electrochemical oxidation (reverse pumping) would have to be done with care to avoid creating large pressures within the sensor. An alternative would be to operate so that only partial reduction to CO was achieved.

A sensor control unit that used the gauge voltage to ensure that a fixed proportion of the CO_2 (eg. 30%) was reduced to CO could be used. The current due to CO_2 reduction would be small but this would not be a problem if the electrochemical leakage current was also small. The gauge cell would also require accurate calibration to ensure that the percentage CO_2 reduction was accurately known.

Sensing H_2O in the presence of CO_2 presents a major problem. As Fig. 1.10 illustrates, there is no way of reducing H_2O without also reducing CO_2 to carbon. The intermittent mode of operation mentioned above would therefore have to be used. Fig. 1.10 also shows that the potentials at which CO_2 and H_2O are reduced are very similar (Dietz (1982)). Very careful interpretation of high quality results would be required to distinguish between the two. Such results could probably only be obtained by slowly increasing the gauge voltage over the appropriate voltage range. This would mean that it would take hours to perform an analysis.

For detecting oxygen-containing gases other than H_2O there is another possible mode of operation that could increase the detection rate. That would be to operate a number of matched sensors at different gauge potentials. For instance an array of sensors could be used with the gauge potentials set to the values suggested at the beginning of this section. By calibrating the array each gas could be determined simultaneously. Also the capacitance of the electrodes would be eliminated from the response time of the indidual sensors. The array could therefore probably achieve a response time in the order of a second.

6.3.2 Electrodes

The electrodes for a multi-gas sensor require a high activity if they are to reduce gases such as CO_2 fully. They also require strong resistance to corrosion as the results in section 5.4 illustrated.

There are numerous materials that could be tested as possible electrode materials. Silver showed promise because it produced high current densities and it adhered well to zirconia. However, it adsorbs large amounts of oxygen and has a low melting point.

Gold electrodes could improve corrosion resistance but their poor adherance to zirconia is a problem. Current densities also tend to be low.

6.3.3 Limiting electrochemical leakage

As discussed above, electrochemical leakage needs to be reduced to a very low level if a sensor is to be able to distinguish between widely different concentrations of different gases. Most practical applications will fall into this category. Reducing electrochemical leakage is therefore a high priority for developing a multi-gas pump-gauge sensor.

6.4) Proposed lean burn sensor

It was shown in section 3.4 that when the current through a zirconia cell was above a certain level (dependent upon the exchange current of the electrodes) the cathodic overvoltage was significantly larger than the anodic overvoltage. Section 3.4 applied to O_2/N_2 mixtures. In section 3.5 it was shown that the difference was smaller in CO/CO_2 mixtures. This feature could be used to make an oxygen sensor for combustion products capable of an unambiguous reading in rich- and lean-burn conditions. This problem was discussed in section 1.4.1.

Decreasing the length of the 3-phase boundary of the anode, and thus increasing the overvoltage on it, would have very little effect on the performance of an amperometric sensor used in excess-air conditions. On the other hand such a change should greatly decrease the current, for a similar applied pump voltage, when operating in the fuel-rich region. Additional benefit would also result by lowering the operating temperature.

Thus these modifications should result in a sensor showing a linear current vs. oxygen partial pressure characteristic in the excess-air region and a current close to zero through the fuel-rich region. The activity of the anode could be reduced by simply making it smaller. Alternatively, a porous layer could be used that would have the dual purpose of protecting the electrode as well as reducing its activity. Another possibility would be to use different materials for the cathode and anode. The anode material would need a high activity in high pO_2 atmospheres and a low activity in low pO_2 atmospheres.

Chapter 7

Conclusions

7.1) The fundamental O_2 sensor

As a foundation for later work on extending the technology of the zirconia amperometric oxygen sensor to other gases, its performance in O_2/N_2 mixtures was studied first. A thorough understanding of the operating principles was obtained from a study of the literature and an analysis of the results from a unique 5 electrode sensor.

7.1.1 Electrolyte resistance

The electrolyte resistance was measured and shown to be a minor factor limiting the performance of zirconia amperometric sensors. The resistance of the electrolyte could be predicted more accurately than that of the electrodes so attention was directed to the latter. The onset of electronic conductivity limited the voltage that could be applied to the YSZ sensors.

7.1.2 Electrode overvoltages

The overvoltages on the internal pumping electrodes of amperometric sensors were shown to be relatively large under some circumstances. For instance their magnitude was a factor in determining the minimum operating temperature of the sensors. Also, large overvoltages prevented the complete reduction of CO_2 in the pump-gauge sensors. Attention was therefore given to the mechanisms by which overvoltages formed.

Study of the literature revealed that several steps where probably significant. At low oxygen concentrations the dissociative adsorption of oxygen and diffusion of

the adsorbed oxygen atoms on the electrode surface were probably controlling. Evidence for this was plateaus in the cathodic current which were also observed in this work. The absence of current plateaus in the anodic regime helped confirm this idea.

At higher O_2 concentrations electrochemical reaction of adsorbed oxygen atoms at the three phase boundary (TPB) was believed to be controlling. Evidence for this was a $pO_2^{-\frac{1}{4}}$ dependence of electrode resistances on oxygen partial pressure: also observed under some circumstances in this work.

At high overvoltages the increased electronic conductivity of the zirconia was believed to increase the effective width of the TPB. Evidence for this was an increase in current at high applied voltages above that expected if the previous two mechanisms were controlling.

A mathmatical model that incorporated all the above rate limiting mechanisms was not found. The Butler-Volmer equation was therefore used as a first approximation for modelling electrode current-voltage characteristics.

7.1.3 I vs. E characteristics of amperometric sensors

The fundamental equations governing the behaviour of amperometric sensors were derived and tested. It was found that the experimental behaviour could be accurately modelled using eqn(4.1) in combination with compensation for electrochemical leakage. Oxygen concentrations could be determined with better than 1% accuracy for concentrations between 0.4 and 21%. By reducing the temperature to minimize electrochemical leakage, greater accuracy was achieved. However, response speed decreased and the gauge cell deviated increasingly from the Nernst equation as the temperature was decreased below 500°C.

Electrochemical leakage caused non-ideal behaviour of the sensors and was an extremely complicated function of the operating conditions. It was therefore not possible to accurately account for it. Consequently, attention was given to its source and its minimization. It was shown to be governed mainly by the resistance of the small electrode (called the ETPB) formed where the electronic contact to the internal electrodes exited the sensor body. Covering the ETPB with glass was shown to help

but not to eliminate the problem. Glass-sealed sensors suffered less leakage than the metal-sealed sensors even when glass was used to cover the external surface of the metal. More work on methods for sealing sensors was required.

7.2) New sensors

7.2.1 Lean-burn sensor

Based on the results on single electrodes, a design for a lean-burn sensor was proposed. In O_2/N_2 mixtures where the oxygen activity was high, the anodic overvoltage was shown to be much lower than the cathodic overvoltage for the same magnitude of anodic or cathodic current respectively. In $CO/CO_2/N_2$ mixtures where the oxygen activity was low the difference was much less. Therefore, by making the anodic overvoltage dominant, an approximate distinction could be made between the two types of gas mixture.

The proposed design consisted of a standard amperometric sensor with an active internal pumping electrode and an external pumping electrode (operated anodically) with a much lower activity. The activity of the anode would be set so that it could pass sufficient current for normal operation in fuel-lean conditions. In fuel-rich conditions where its conductance would be much lower it would only allow a small current to pass. The sensor would therefore pass a current proportional to oxygen concentration in lean-burn conditions and a much smaller current in rich-burn conditions. The size of this current would be strongly dependent on operating temperature.

7.2.2 Multi-gas sensor

The operating principle of the multi-gas sensor was tested in $CO_2/O_2/N_2$, $NO/O_2/N_2$ and $SO_2/O_2/N_2$ gas mixtures. The multi-gas sensor showed great promise as a nitric oxide detector. It was found that the NO was reduced over a very narrow band of gauge voltages. Corrosion of the platinum electrodes was shown to be a

problem. Also, to measure the low NO concentrations that most practical applications would require, a sensor with very little electrochemical leakage would be required.

High overvoltages hindered its operation as a multi-gas sensor, particularly for CO_2 sensing. An insight into why this occurred was seen in chapter 3 where it was shown that the activity of Pt electrodes was lower in CO/CO_2 atmospheres. Silver and gold electrodes showed the same trend.

The consequence of the high overvoltages in CO/CO_2 mixtures was that CO_2 could not be completely reduced before electronic conductivity caused a large increase in current. Therefore no current plateau with a magnitude proportional to CO_2 concentration was seen. Attempts were made to increase the activity of the internal pumping electrode relative to the size of the diffusion pore but progress sufficient to produce a plateau was not made. However, if complete reduction of CO_2 were to be achieved, carbon would be deposited inside the sensor and would have to be periodically removed. It was therefore proposed that partial reduction of CO_2 to CO would be a preferable operating mode. The gauge cell could be used to determine the proportion of the CO_2 that was reduced.

Interesting results were obtained in $CO/O_2/N_2$ mixtures at temperatures below 500°C. It was postulated that a mixed potential developed on the external platinum electrodes, but that the diffusion hole prevented their development on the internal electrodes.

Zirconia was found to become electronically conducting in the presence of sulphur dioxide which created doubts about its possible use as an electrolyte for an amperometric SO_2 or SO_3 sensor. The platinum electrodes were also corroded by the SO_2. However, results obtained before these two problems rendered the sensors useless showed that SO_2 could be detected with a polarographic sensor.

It was therefore demonstrated that the principle of the multi-gas sensor was sound but more work needed to be done to reduce electrochemical leakage, to improve corrosion resistance, and to reduce the affects of sulphur on the electrolyte.

7.3) The computer controlled apparatus

A computer controlled apparatus was built. It controlled the furnace and the gas flow control valves, but most importantly it controlled an auto-ranging potentiostat/galvanostat. The apparatus was built to perform a number of electrochemical tests such as cyclic voltammetry and current interruption. Since the computer controlled all experimental variables it could be set to run unattended for weeks or months if necessary. It was also demonstrated that it could produce a wide range of accurate data with the minimum delay.

Building the computer controlled apparatus and writing the program to operate it involved a considerable investment in time. Having built the system it is now available for future use, allowing a large saving of experimental effort. However, there are useful modifications that could be made which are discussed in the next chapter.

Chapter 8

Recommendations

"Let us not be caterpillars debating

the impossibility of flight"

Michael Sky

8.1) Testing of proposed sensors

8.1.1 Lean-burn sensor

Lean-burn combustion with a very tightly controlled air to fuel ratio keeps air pollution to a minimum. The sensor designs proposed above should be tested in the flue of an experimental burner or in the exhaust of petrol engines. Facilities for doing this were not fully operational during the experimental phase of this work.

8.1.2 NO_x sensor

Tests need to be performed in a wider range of NO concentrations than those tested in this work to see how closely the sensor approaches theoretical performance. Also the corrosion of the platinum electrodes needs to be investigated more and alternative NO_x resistant materials found. Tests should also be done with NO_2 and possible other NO_x gases.

It would be interesting to build another sensor with a platinum wire blocking its diffusion pore and to test it in argon/oxygen mixtures to see if the spike in η_c attributed to NO disappears.

8.2) Design ideas for multi-gas sensors

8.2.1 Reducing overvoltages

The high overvoltages on the internal pumping electrode of the sensors tested prevented them from fully reducing CO_2. This means that a clear plateau representative of the CO_2 concentration was not observed. Therefore, methods for reducing the overvoltage (increasing electrode activity) are desired.

One idea is to use alternative electrode materials besides noble metals and noble metal cermets. Promising materials are RuO_2 (Periaswami et al (1988)) and perovskites. Many of these materials would be reduced at high pumping voltages which would add to the difficulty of finding suitable ones. For instance RuO_2 would be reduced to metal at -360mV at 1000K.

The resistance of metal electrodes can be reduced considerably by applying a large anodic current for short durations (Karpachev and Filgaev (1966)). However, the application of large anodic currents, even for short periods, to the internal electrodes of a sensor could cause a catastrophic build up of pressure within the sensor. This could be overcome by passing a cathodic current of similar magnitude simultaneously through the second internal electrode.

8.2.2 Improved electrolytes

The choice of ceramic for multi-gas sensors is important to minimize semipermeability and maximize reliability. If YSZ is used, its conductivity can be optimized by ensuring that the Al_2O_3 content is considerably higher that the SiO_2 content (Drennan and Badwal (1988)).

Tapes made by viscous plastic processing are easy to shape and can produce good quality ceramic. High purity powder with small particle size should be used and the ceramic cooled rapidly in air after sintering.

A possible electrolyte is $CaZrO_3$ which is shown in Fig. 1.10 to be more resistant to reduction than YSZ. Wang et al (1988)) reports that it is a generally

promising electrolyte with a good ionic conductivity.

Another economical alternative is mullite which Nagatani et al (1992) found to have pe of 10^{-83}atm O_2 at 1000K as opposed to 9%MgO-ZrO_2 with 10^{-48}atm. Its ionic conductivity is also lower so its use would be limited to high temperature applications, or to amperometric sensors with fine diffusion pores.

8.2.3 Hermetic seal

Another problem with constructing a cell was the formation of a good seal in the sensor. The sensor illustrated by Liaw and Weppner (1991) was made so that there was no three phase contact between the glass seal, the internal electrode and its lead and the zirconia. Their cell design has the disadvantage of being difficult to make with a small internal volume.

An idea from Van Wijngaarden et al (1988) was to sinter a slip cast block of alumina around the parts to be sealed together. Alumina is more resistant to reduction than zirconia (Kumar and Fray (1993)) but it has a larger coefficient of expansion. Van Wijngaarden et al pointed out that the dimensions of the seal had to be carefully controlled before sintering.

An approach presently being pursued in the department is to use zirconia to seal the zirconia discs together. If the internal pump electrode and the internal gauge electrode were electronically connected there would then be an electronic and an ionic connection between them. The gauge electrode would therefore become part of the pump electrode with the oxygen ions flowing through the seal from the gauge electrode to the external pump electrode. This would increase the area of the internal pumping electrode and thereby reduce the overvoltage on it. However, the gauge electrode would then have an overvoltage on it. Agrawal et al (1974) studied an equivalent tubular system with two internal electrodes and two external electrodes. They found an instant increase in the gauge voltage if the two internal electrodes were electronically connected. Therefore, the sensor would need two separate leads to its internal electrodes in order to be used as a pump-gauge. An interesting advantage of the all zirconia pump-gauge would be that the internal gauge electrode would act as a reference electrode to the internal pumping electrode. It would be

interesting to compare the results obtained for the overvoltage of the pumping electrode using this system against the system reported above where the reference electrode was outside.

8.2.4 Gas diffusion coefficients

If a pump-gauge device could be built with insignificant electrochemical leakage its accuracy for oxygen determination would be limited by the accuracy of the ammeter measuring the pump current. If the diffusion pore size could be calibrated to equal accuracy the device could be used to accurately determine gas diffusion coefficients.

8.2.5 Low temperature operation

At high temperatures the overvoltages on the pumping electrodes are relatively low (chapter 4). The largest contribution to the total pumping voltage therefore comes from the Nernst voltage as measured by the gauge cell. At lower temperatures the overvoltages on the pumping electrode become more dominant. If these overvoltages could be predicted, it would enable the low temperature operating limit of the sensor; as an oxygen gauge; to be calculated. Hetrick (1982) showed that the current is still proportional to the oxygen concentration if the gauge voltage is set at a fixed but low value. For instance if the gauge voltage were set to 20mV, the current drawn for a given oxygen concentration would decrease and the minimum operating temperature could therefore also be decreased. However, such a scheme would require the use of electrodes with better low temperature response rates and compliance with the Nernst law than platinum electrodes. Several possibilities are available: eg. Badwal et al (1984) found that $UScO_4$ could be used down to 300°C, and Periaswami et al (1988) found that RuO_2 electrodes obeyed the Nernst law down to 225°C.

8.3) Other sensor mechanisms

The anomalous emf CO sensor (section 1.4.3) has not been commercially successful, possibly because of interference from a number of other gases (Kudo and Fueki (1990)). However, the idea deserves more investigation as does the whole topic of mixed potentials. The possiblity of using a diffusion pore instead of a catalyst layer to remove the mixed potential from one electrode also deserves more investigation. Using a diffusion barrier could reveal more information about the gas mixture (such as O_2 concentration) than a catalyst layer could.

The use of sensor arrays (sometimes modelled on the nose) to overcome the problem of cross-sensitivity has attracted attention recently (de Agapito et al (1993)). An array of mixed voltage sensors could be built using a range of electrode materials and/or operating temperatures.

8.4) Experimental apparatus

8.4.1 Computer interface card

To keep the costs to a minimum a number of compromises were made while building the computer-controlled apparatus. Firstly, only one interface card was used for the input signals. The ideal solution would be to use two cards. An accurate one (at least 14 bit) is needed for accurate reading of the furnace's thermocouple. A fast one is needed for the current-interruption measurements. The two card solution is more economical since cards that are both accurate and fast are difficult to find and very expensive. Determining the IR drop with an oscilloscope is labour intensive and the 8 bit resolution of most available digital instruments limits the accuracy. IR drop determination with the program written for this work was very easy but the 0.1mS minimum sample time of the card in use limited the accuracy of these measurements. Better results would be obtained with a 12 bit card capable of sampling in less than 10μS. Such a card would enable a more accurate study of the changes in electrode resistance due to changing oxygen partial pressure, and to electronic conduction of

the electrolyte near the three phase boundary.

Using the software available at the time it was difficult to take full advantage of the computer's power and its ability to multi-task because the ADDA card used had no internal timer. The computer's clock had to be used to time the measurements. The only way found to do this was by using the interrupt 8 signal generated by the computer for its internal use. This conflicted with all the multi-tasking programs available at the time. A card with a timer generates its own interrupt and this would allow the computer to be run with an economical multi-tasking operating system. This would mean that the computer could be available for other tasks while experiments were running and long experimental runs would not have to be stopped in order to check previous results. Also, data (including the latest experimental data) could be easily transferred between applications. Possibilities such as running several tests concurrently would also be opened up. The operating system OS/2 version 2 has since been introduced and it is possible that this system could handle the above requirements.

A card that includes digital input/output lines should also be acquired so that the printer port does not have to be used to run the apparatus. This would allow the use of a printer while the computer is connected to the interface which is not presently possible.

8.4.2 Computer control program

Software is never finished and perfect, and CONTRL could be usefully upgraded in a number of ways.

One major addition that would be useful is more sophisticated detection of steady-state. In a pump-gauge sensor, the pump can easily reach steady-state before the gauge does. A facility should therefore be added where more than one value can be monitored for steady-state.

The addition of features such as the ability to apply a sinusoidal current or voltage waveform would also be beneficial.

References

Abraham F., Boivin J.C., MAiresse G. and Nowogrocki G. (1990) Solid State Ionics 40/41, 934-937.

Agrawal Y.K., Short D.W., Gruenke R. and Rapp R.A. (1974) J. Electrochem. Soc 121, 354-360.

Alcock C.B., Li B., Fergus J.W. and Wang L. (1992) Solid State Ionics 53-56, 39-43.

Anthony A-M., Baumard J.F. and Corish J. (1984) Pure and Applied Chem. 56, 1069-1094.

Azad A.M., Akbar S.A., Mkaisalkar S.G., Birkefeld L.D., and Goto K.S. (1992) J. Electrochem. Soc. 139, 3690-3704.

Badwal S.P.S. (1984) J. Electroanal. Chem. 161, 75-91.

Badwal S.P.S. (1990) Appl. Phys. A. 50, 449-462.

Badwal S.P.S. and De Bruin H.J. (1982) J. Electrochem. Soc. 129, 1921-1928.

Badwal S.P.S. and Drennan J. (1987) J. Mat. Sci. 22, 3231-3239.

Badwal S.P.S. and Nardella N. (1989) Appl. Phys. A. 49, 13-24.

Badwal S.P.S., Bannister M.J. and Garrett W.G. (1984) Advances in Ceramics 12, 598-606.

Barin I. (1989) Thermochemical data of pure substances, V.C.H. Weinheim FRG

Bates J.B. and Wang J.C. (1988) Solid State Ionics 28-30, 115-119.

Bauerle J.E. (1969) J. Phys. Chem. Solids 30, 2657-2670.

Baumard J.F., Papet P. and Abelard P. (1988) Advances in Ceramics 24, 779-788.

Benammar M. and Maskell W.C. (1989) J Phys E: Sci Instrum 22, 933-936.

Benammar M. and Maskell W.C. (1991) Sensors, Technology, Systems and Applications. Ed. K.T.V. Grattan, Adam Hilgen, Bristol.

Benammar M. and Maskell W.C. (1992a) Solid State Ionics 53-56, 75-79.

Benammar M. and Maskell W.C. (1992b) Smart Mater. Struct. 1, 134-138.

Benammar M. and Maskell W.C. (1992c) Proc. Int. School of Mat. Sci. and Tech. Ed. W. Weppner, ERICE, Italy. in press.

Benammar M. and Maskell W.C. (1993a) Applied Phys. A57, 45-50.

Benammar M. and Maskell W.C. (1993b) Sensors and Actuators B12, 195-198.

Beresnev S.M. (1991) Soviet Electrochem. 26, 1279-1286.

Bockris J.O'M. and Reddy A.K.N. (1970) "Modern Electrochemistry", vol 2, Plenum press, New York

Bonanos N., Slotwinski R.K., Steele B.C.H. and Butler E.P. (1984) J. of Mat. Sci. Lett. 3, 245-248.

Brook R.J. and Markin T.L. (1973) Fast Ion Transport in Solids, van Gost W. 533-541.

Brook R.J., Pelzmann W.L. and Kroger F.A. (1971) J. Electrochem. Soc. 118, 185-192.

Chen K. T_Y. and Saltsburg H.M. (1986) Extended Absracts 86-1 407, 589.

Colvin A.D., Rankin J.S. and Carduner K.R. (1993) Sensors and Actuators B 12, 83-90.

Considine D.M. (1984) van Nostrand Reinhold Scientific Encyclopedia of Chemistry, 4th ed, van Nostrand Co, New York.

Copcutt R.C. and Maskell W.C. (1992) Solid State Ionics 53-56, 119-125.

Copcutt R.C. and Maskell W.C. (1993) Paper presented at Solid State Ionics 9, The Hague, Eds; Boukamp B.A., Burggraaf A.J. and Schoonman J., Elsevier Science

Publishers B.V.

Danckwerts P.V. (1953) Chem. Eng. Sci. 2, 1-13.

de Agapito J.A., de Agapito L., Schneider M., Rosa R.G. and de Pedro T. (1993). Sensors and Actuators B 15-16, 105-109.

De Jong H.L. (1983) U.S. Patent 4 384 935

de Velasco A.A.A., Moseley P.T., Peat R. and Pelaez J.G. (1993) Sensors and Actuators B 15-16, 55-62.

Dietz H. (1982) Solid State Ionics 6, 175-183.

Dou S., Masson C.R. and Pacey P.D. (1985) J. Electrochem. Soc. 132, 1843-1849.

Drennan J. and Badwal S.P.S. (1988) Advances in Ceramics 24, 807-818.

Eiswirth R.M., Krischer K. and Ertl G. (1990) Appl. Phys. A 51, 79-90.

El Barhmi A., Schouler E.J.L., Hammou A. and Kleitz M., (1988a) Advances in Ceramics 24, 885-894.

El Barhmi A., Schouler E.J.L., Hammou A. and Kleitz M., (1988b) Solid State Ionics 28-30, 493-496.

Etsell T.H. and Flengas S.N. (1970) Chemical Reviews 70, 339-376.

Etsell T.H. and Flengas S.N. (1971) J. Electrochem. Soc. 118, 1890-1900.

Etsell T.H. and Flengas S.N. (1972) Metallurgical Transactions 3, 27-36.

Fouletier J. and Henault M. (1983) Solid State Ionics 9&10, 1277-1282.

Fouletier J., Fabry P. and Kleitz M. (1976) J. Electrochem. Soc. 123, 204-213.

Fouletier J., Seinera H. and Kleitz M. (1974) J. Appl. Electrochem. 4, 303-315.

Fouletier J., Seinera H. and Kleitz M. (1976) J. Appl. Electrochem. 6,

177-185.

Fouletier J., Vitter G. and Kleitz M. (1975) J. Appl. Electrochem. 5, 111-120.

Fray D.J. (1992) Chemistry and Industry 12, 445-448.

Frueham R.J., Martonik L.J. and Turkdogan E.T. (1969) Trans. Metallurgical Soc. of AIME 245, 1501-1509.

Funke K. (1988) Solid State Ionics 28-30, 100-107.

Gauthier M., Chamberland A., Belanger A. and Poirier M. (1977) J. Electrochem. Soc. 124, 1584-1587.

Gessner M.A., Nagy S.G. and Michaels J.N. (1988) J. Electrochem. Soc. 135, 1294-1301.

Goge M., Especel D., Heggestad K. and Gouet M. (1985) Transport-structure relations in fast ion and mixed conductors. Poulsen F.W., Anderson N.H., Clausen K., Skaarup S., Sorensen O.T., 6th Riso int symp on met 291-296.

Gur T.M. and Huggins R.A. (1992) J. Electrochem. Soc. 139, L95-L97.

Gur T.M., Raistrick I.D. and Huggins R.A. (1980) Solid State Ionics 1, 251-271.

Haaland D.M. (1977) Anal. Chem. 49, 1813-1817.

Haaland D.M. (1980) J. Electrochem. Soc. 127, 796-804.

Hargreaves K.J.A. and Ovenden N.A. (1990) Int. Gas Research Conf.

Heijme L., Beekman N.M., Peelman P.J. and Eijnthoven R.K. (1975) U.S. patent 3907657

Hetrick R.E., Fate W.A. and Vassel W.C. (1981) Appl. Phys. Lett. 38, 390-392.

Heyne L. (1978) 153rd meeting electrochemical society

Heyne L. and den Engelsen D. (1977) J. Electrochem. Soc. 124, 727-735.

Hughes A.E. and Badwal S.P.S. (1991) Solid State Ionics 46, 265-274.

Hughes A.E. and Sexton B.A. (1989) J. Mat. Sci. 24, 1057-1061.

Inoue T., Seki N., Eguchi K. and Arai H. (1990) J. Electrochem. Soc. 137, 2523-2527.

Ioannou A.S. and Maskell W.C (1992) Solid State Ionics 53-56, 85-89.

Iwase M., Ichise E. and Jacob K.T. (1984) Advances in Ceramics 12, 646-659.

Joyner R.W., Bowker M. and Truex T.J. (1992) Chemistry in Britain 1011.

Kamo T., Chujo Y., Akatsuka T., Nakano J. and Suzuki M. (1985) SAE technical paper series 850380

Kaneko H., Maskell W.C. and Steele B.C.H. (1987) Solid State Ionics 22, 161-172.

Karpachev S.V. and Filyaev A.T. (1966) Soviet Electrochemistry 2, 576-577.

Kilner J.A. and Brook R.J. (1982) Solid State Ionics 6, 237-252.

Kleitz M., Bernard H., Fernandez E. and Schouler E., (1981a) Advances in Ceramics 3, 310-336.

Kleitz M., Levy M., Fouletier J. and Fabry P., (1981b) Advances in Ceramics 3, 337-348.

Kleitz M., Fernandez E., Fouletier J. and Fabry P., (1981c) Advances in Ceramics 3, 349-363.

Kofstad P. (1983) "Nonstoichiometry, diffusion and electrical conductivity in binary metal oxides" Robert E. Krieger publishing co., Malabar, Florida.

Kontoulis I. and Steele B.C.H. (1991) Solid State Ionics 47, 317-324.

Kudo T. and Fueki K. (1990) "Solid State Ionics", VCH, Kodansha.

Kumar R.V. and Fray D.J. (1993), presented at "9th Int. Conf. on Solid State Ionics, The Hague.

Kuzin B.L. and Komarov M.A. (1990) Solid State Ionics 39, 163-172.

Leach C.A., Tanev P. and Steele B.C.H. (1986) J. of Mat. Sci. Lett. 5, 893-894.

Levy M., Fouletier J. and Kleitz M. (1988) J. Electrochem. Soc. 135, 1584-1589.

Li N., Tan T.C. and Zeng H.C. (1993) J. Electrochem. Soc. 140, 1068-1073.

Liaw B.Y. and Weppner W. (1991) J. Electrochem. Soc. 138, 2478-2483.

Liu M. and Khandkar A. (1990) Extended Abstracts 90-2, 1062-1063.

Logothetis E.M., Vassell W.C., Hetrick R.E. and Kaiser W.J. (1985) Transducers '85, 3rd international conference on solid-state sensors and actuators 330-332.

Makovos E.B. and Liu C-C. (1991) Sensors and Actuators B 3, 15-22.

Malpas D. (1992) Personal communication

Maskell W.C. (1987) J. Phys. E: Sci Instrum. 20, 1156-1168.

Maskell W.C. (1989) UK patent application GB 2 208 007 A

Maskell W.C. (1992) UK patent application GB 2 253 174 A

Maskell W.C. (1991) in Moseley P.T., Norris J.W. and Williams D.E. (eds) in "Techniques and mechanisms in gas sensing", Adam Hilger, Bristol Ch1, 1-45.

Maskell W.C. and Steele B.C.H. (1986) J. Appl. Electrochem. 16, 475-489.

Maskell W.C., Kaneko H. and Steele B.C.H. (1986) Proc. 2nd Int. Meeting on Chemical Sensors, Bordeaux 302-305.

Maskell W.C., Steele B.C.H. (1988) Solid State Ionics 28-30, 1677-1681.

Matsushima T. (1978) J. Catalysis 55, 337-347.

Mehrotra G.M., Nakamura A. and Wagner J.B.Jr. (1988) Advances in Ceramics

24, 797-806.

Metcalfe I.S. and Sundaresan S. (1988) AIChE Journal 34, 195-208.

Middleton H. (1990) Personal communication

Mizusaki J., Amano K., Yamauchi S. and Fueki K., (1987a) Solid State Ionics 22, 313-322.

Mizusaki J., Amano K., Yamauchi S. and Fueki K., (1987b) Solid State Ionics 22, 323-330.

Mizusaki J., Aoki M., Miyaki Y., Yamauchi S. and Fueki K. (1990) Denki Kagaku 58, 1169-1177.

Mizusaki J., Tagawa H., Miyake Y., Yamauchi S., Fueki K., Koshiro I. and Hirano K. (1992) Solid State Ionics 53-56, 126-134.

Moseley P.T. (1987) in "Solid state gas sensors" P.T. Moseley and B.C. Tofield (Ed), Adam Hilger, Bristol 139-150.

Moseley P.T. (1988) Solid State Gas Sensors, Ed. Moseley P.T. and Tofield B.C., Adam Hilger, 139-150.

Moure C., Jurado J.R. and Duran P. (1985) British Ceramics Proceedings 36, 31-43.

Nafe H. (1984) Solid State Ionics 13, 255-263.

Nagatani A., Inoue R. and Suito H. (1992) J. Applied Electrochem., 22 859.

Nakagawa N., Kuroda C. and Ishida M. (1990) Solid State Ionics 40/41, 411-414.

Nakagawa N., Yamamoto M., Kuroda C. and Ishida M. (1993) Denki Kagaku 61, 305-312.

Nakamura A. and Wagner J.B. Jr. (1986) J. Electrochem. Soc. 133, 1542-1548.

Nettleship I. and Stevens R. (1987) Int. J. High Technology Ceramics 3, 1-32.

Nguyen B.C., Lin T.A. and Mason D.M., (1986a) J. Electrochem. Soc. 133, 1807-1815.

Nguyen B.C., Rincon-Rubio L.M. and Mason D.M., (1986b) J. Electrochem. Soc. 133, 1860-1869.

Nowotny J., Sloma M. and Weppner W. (1988) Solid State Ionics 28-30, 1445-1450.

Okamoto H., Obayashi H. and Kudo T. (1980) Solid State Ionics 1, 319-326.

Okamoto H., Obayashi H. and Kudo T. (1981) Solid State Ionics 3/4, 453-456.

Ong B.G., Chiang C.C. and Mason D.M. (1981) Solid State Ionics 3/4, 447-452.

Palguev S.F., Gilderman V.K. and Neujmin A.D. (1975) J. Electrochem. Soc. 122, 745-748.

Pancharatnam S., Huggins R.A. and Mason D.M. (1975) J. Electrochem. Soc. 124, 869-875.

Park K. and Olander D.R. (1991) J. Electrochem. Soc. 138, 1154-1159.

Perfilyev M.V. and Fadeev G.I. (1984) Solid State Ionics 14, 55-59.

Periaswami G., Varamban S.V., Babu S.R. and Mathews C.K. (1988) Solid State Ionics 26, 311-317.

Perry R.H. (1984) "Chemical Engineers' Handbook", 6th ed.

Pizzini S., Bianchi M., Corradi A. and Mari C. (1974) J. Appl. Electrochem. 4, 7-16.

Radford K.C. and Bratton R.J., (1979a) J. Mat. Sci. 14, 59-65.

Radford K.C. and Bratton R.J., (1979b) J. Mat. Sci. 14, 66-69.

Rao N., van den Bleek C.M. and Schoonman J. (1992) Solid State Ionics 52, 339-346.

Rapp R.A. and Shores D.A. (1970) Physicochemical measurements in metals research Part 2, Rapp R.A., Interscience 123-192.

Ratner M.A. and Nitzan A. (1988) Solid State Ionics 28-30, 3-33.

Reetz T., Nafe H. and Rettig D. (1984) Advances in Ceramics 12, 591-597.

Robertson N.L. and Michaels J.N. (1991) J. Electrochem. Soc. 138, 1494-1499.

Saji K., Kondo H., Takahashi H., Takeuchi T., Igarashi I. (1988) J. Appl. Electrochem. 18, 757-762.

Saji K., Takahashi H., Kondo H., Takeuchi T. and Igarashi I. (1984) Proc. 4th sensor symposium. IEE of Japan. 147-151.

Sakurai K., Nagamoto H. and Inoue H. (1989) Solid State Ionics 35, 405-410.

Sander M. and Imbihl R. (1991) Surface Science 255, 61-72.

Schindler K., Schmeisser D., Vohrer U., Wiemhoffer H.D. and Gopel W. (1989) Sensors and Actuators 17, 555-568.

Schouler E.J.L. (1983) Solid State Ionics 9&10, 945-952.

Schouler E.J.L. and Kleitz M. (1987) J. Electrochem. Soc. 134, 1045-1050.

Skeaff J.M. and Dubreuil A.A. (1993) Sensors and Actuators B 10, 161-168.

Slotwinski R.K., Bonanos N. and Butler E.P. (1985) J. Mat. Sci. Lett. 4, 641-644.

Soejima S. and Mase S. (1985) SAE technical paper series 850378 53-59.

Sorensen O.T., Johannesen O. and Clausen K. (1985) Transport structure relations in fast ion and mixed con 93-117.

Steele B.C.H. (1985) Transport-structure relations in fast ion and mixed conductors 79-92.

Steele B.C.H. and Butler E.P. (1985) British Ceramics Proceedings 36, 45-

55.

Steele B.C.H., Drennan J., Slotwinski R.K., Bonanos N. and Butler E.P. (1981) Advances in Ceramics 3, 286-309.

Steele B.C.H., Kilner J.A., Dennis P.F. and McHale A.E. (1986) Solid State Ionics 18&19, 1038-1044.

Subbarao E.C. and Maiti H.S. (1983) Progress in solid electrolytes. Wheat T.A., Ahmad A., Kuriakose A.K. Energy, mines and resources, Ottawa 281-312.

Suzuki S., Sasayama T., Miki M., Yokono H., Iwanaga S. and Ueno S. (1985) Transducers '85, 3rd international conference on solid-state sensors and actuators. 333-335.

Suzuki Y., Takahashi T. and Nagae N. (1981) Solid State Ionics 3/4, 483-487.

Taimatsu H., Kaneko H. and Kawagoe M. (1988) Solid State Ionics 34, 25-33.

Takahashi H., Saji K., Kondo H., Takeuchi T. and Igarashi I. (1985) Proc 5th sensor symposium 133-137.

Tannenberger H. and Siegert H. (1969) Advances in chemistry series. Fuels cell systems _ II. Ed. Gould R.F. American chemical society 90, 281-300.

Theunissen G.S.A.M., Winnubst A.J.A. and Burggraaf A.J. (1989) J. of Mat. Sci. Lett. 8, 55-57.

Tuller H.L. and Moon P.K. (1988) Materials Sci. & Eng. B1, 171-191.

Ueno S., Ichikawa N., Suzuki S. and Terakado K. (1986) SAE no. 860409 2915-2921.

Unwin J., Walsh P.T. (1989) Sensors and Actuators 17, 575-581.

Usui T., Asada A., Ishibashi K. and Nakazawa M., (1989a) Jap. J. Appl. Phys. 28, 2046-2047.

Usui T., Asada A., Ishibashi K. and Nakazawa M., (1991) J. Electrochem. Soc. 138, 585-588.

Usui T., Asada A., Nakazawa M. and Osanai H., (1989b) J. Electrochem. Soc. 136, 534-542.

Usui T., Asada A., Nakazawa M. and Osanai H., (1989c) Jap. J. Appl. Phys. 28, L1654-L1656.

Usui T., Kurumiya Y., Nuri K. and Nakazawa M., (1989d) Sensors and Actuators 16, 345-358.

van Hassel B.A. and Burggraaf A.J. (1992) Solid State Ionics 51, 175-181.

van Hassel B.A., Boukamp B.A. and Burggraaf A.J., (1991a) Solid State Ionics 48, 139-154.

van Hassel B.A., Boukamp B.A. and Burggraaf A.J., (1991b) Solid State Ionics 48, 155-171.

van Hassel B.A., Boukamp B.A. and Burggraaf A.J. (1992) Solid State Ionics 51, 161-174.

Van Herle J. and Thampi K.R. (1993) IEA Programme, SOFC. Instrumentation & in-situ diagnostics. Chexbres, Switzerland 62-67.

van Heuveln F.H., van Berkel F.P.F. and Huijsmans J.P.P. (1993) Riso International Symposium on Materials Science, Roskilde, Denmark 53-67.

van Manen P.A., Weever R. and de Wit J.H.W. (1992) J. Electrchem. Soc. 139, 1130-1134.

Van Wijngaarden M.J.U.T., Geldenhuis J.M.A. and Dippenaar R.J. (1988) J. Appl. Electrochem.. 18, 724-730.

Vayenas C.G. and Saltsburg H.M. (1979) J. Catalysis 57, 296-314.

Vayenas C.G., Bebelis S., Yentekakis I.V., and Neophytides S. (1992) Solid State Ionics 53-56, 97-110.

Verkerk M.J., Hammink M.W.J. and Burggraaf A.J. (1983a) J. Electrochem. Soc. 130, 70-77.

Vlasov A.N. and Perfiliev M.V. (1987) Solid State Ionics 25, 245-253.

Wang C.V., Xu X. and Yu H. (1988) Solid State Ionics 28-30, 542.

Wang D.Y. and Kennedy D.T. (1985) U.S. patent 4547281

Wang D.Y. and Nowick A.S. (1979b) J. Electrochem. Soc. 126, 1166-1172.

Wang D.Y. and Nowick A.S. (1979a) J. Electrochem. Soc. 126, 1155-1165.

Wang D.Y. and Nowick A.S. (1981) J. Electrochem. Soc. 128, 55-63.

Weast R.C. (1988) "CRC Handbook of Chemistry and Physics", 6th ed., CRC Press, Florida

Wen T.L., Lu Z.Y. and Li S.F. (1988) Solid State Ionics 28-30, 475-479.

Whelan P.T. and Borbidge W.E. (1988) J. Appl. Electrochem. 18, 188-195.

Yajima T., Kazeoka H., Yogo T. and Iwahara H. (1991) Solid State Ionics 47, 271-275.

Yamamoto O., Takeda Y., Kanno R. and Noda M. (1987) Solid State Ionics 22, 241-246.

Yan Y., Shimizu Y., Miura N. and Yamazoe N. (1993) Sensors and Actuators *B 12, 77-81.*

Yentekakis I.V. and Vayenas C.G. (1988) J. Catalysis 111, 170-188.

Yentekakis I.V., Neophytides S. and Vayenas C.G. (1988) J. Catalysis 111, 152-169.

Yoshimura M. (1988) Ceramic Bulletin 67, 1950-1955.

Yoshimura M., Noma T., Kawabata K. and Somiya S. (1987) J. of Mat. Sci. Lett. 6, 465-467.

Young C.T. (1983) Progress in solid electrolytes. Wheat T.A., Ahmed A., Kuriakose A.K., Energy, mines and resources, Ottawa 549-580.

Zaromb S. and Stetter J.R. (1984) Sensors and Actuators 6, 225-243.

Appendix 1

Current due to gas reduction

A1.1 Carbon dioxide reduction

Complete CO_2 reduction

It was shown in section 5.1.1 that the current due to the reduction of free oxygen and H_2O is equal to the sum of the currents due to each separate component. Therefore, it is only necessary to derive an expression for the current due to reduction of the oxygen containing gas and only one mass balance is required.

The rate of reduction of CO_2 directly to carbon (r_a) was derived from a steady state materials balance of carbon dioxide entering the sensor.

$$r_a = \Gamma_{CO2}(pCO_2 - p'CO_2) \qquad (A1.1)$$

where Γ_{CO2} is given by $DA/RT\ell$ (D calculated for CO_2 in N_2). pCO_2 is the CO_2 partial pressure surrounding sensor, and $p'CO_2$ is the CO_2 partial pressure within the sensor.

It can be assumed that the rate of electrochemical reduction equals the rate of diffusion of CO_2 into the sensor at steady state. The carbon formed remains on the internal pumping electrode inside the sensor so there is no term for diffusion of products.

The equilibrium relationship for the reaction

$$CO_2 \rightleftharpoons C + O_2$$

is:

$$K_{CO2} = pO_2 / pCO_2. \qquad (A1.2)$$

Using eqn(A1.2) and the Nernst equation (1.7) allows the calculation of $p'CO_2$ that

is in equilibrium with the oxygen activity created by the electrochemical pumping.

$$p'CO_2 = pO_2/K_{CO2} \exp(-4FE_g/RT). \quad (A1.3)$$

If $p'CO_2$ is found to be greater than pCO_2 then no CO_2 will diffuse in and no reaction occurs. When $p'O_2$ falls below a critical value, the equilibrium value of $p'CO_2$ falls below pCO_2 and suddenly the reduction begins. The rate of this reduction is found by substituting eqn(A1.3) in (A1.1) and is:

$$r_a = \Gamma_{CO2}(pCO_2 - pO_2/K_{CO2} \exp(-4FE_g/RT)). \quad (A1.4)$$

By applying Faraday's law an equation for the resultant current is obtained.

$$I_{CO2} = 4F\,\Gamma_{CO2}(pCO_2 - pO_2/K_{CO2} \exp(-4FE_g/RT)). \quad (A1.5)$$

Partial CO_2 reduction

If the partial reduction of CO_2 to CO is the only reaction to occur then the rate is determined by the rate of diffusion of CO out of the sensor as well as the diffusion rate of CO_2 into it. The rate of reduction (r_b) is found from the material balance:

$$r_b = \Gamma_{CO2}(pCO_2 - p'CO_2) = \Gamma_{CO}(p'CO - pCO) \quad (A1.6)$$

rearranging the middle and right hand parts gives:

$$p'CO_2 = pCO_2 - \Gamma_{CO}/\Gamma_{CO2}(p'CO - pCO) \quad (A1.7)$$

The equilibrium relationship for the reaction

$$CO_2 \rightleftharpoons CO + \tfrac{1}{2}O_2$$

is:

$$K_{2CO} = pCO\ pO_2^{1/2}/pCO_2\ P^{1/2}. \quad (A1.8)$$

By assuming equilibrium conditions inside and outside the sensor p'CO and pCO respectively can be determined using the Nernst equation as before. r_b can then be found by substituting the new expression for $p'CO_2$ into the middle part of the mass balance relation. Performing the substitutions and then applying Faraday's law produces the following expression for the current.

$$I_{2\infty} = 2F\Gamma_{\infty 2}\left(pCO_2 - \frac{pCO_2 + \Gamma_{\infty}/\Gamma_{\infty 2}\, pCO}{1 + \frac{\Gamma_{\infty} K_{2\infty} P^{1/2}}{\Gamma_{\infty 2}\, p'O_2^{1/2}}}\right) \qquad (A1.9)$$

$p'O_2$ is determined using the Nernst equation (1.7a) again. The partial pressure of CO surrounding the sensor (pCO) can either be assumed to be zero with little loss of accuracy in most cases, or calculated assuming equilibrium using eqn(A1.8).

<u>CO_2 and CO reduction in parallel</u>

Reduction of CO can only begin when it has been produced by CO_2 reduction. Therefore, to determine the rate of the former reaction (r_c) both reactions must be considered in parallel. All the CO_2 that diffuses into the sensor is consumed by reaction (b). The CO produced is both consumed by reaction (c) and lost by diffusion out of the sensor. The mass balance therefore becomes:

$$r_b = \Gamma_{CO2}(pCO_2 - p'CO_2) = \Gamma_{CO}(p'CO - pCO) + r_c$$

If equilibrium is assumed as above, the solution turns out to be the same as eqn (A1.5). This is because assuming equilibrium means that all the CO is consumed before it can diffuse out of the sensor. Parallel reactions would therefore only produce different results if CO were to be metastable under the conditions within the sensor.

<u>A1.2 Sulphur dioxide reduction</u>

Sulphur melts at 200 C and boils at 444 C. It is therefore treated as a gas in the following derivation. It was assumed that no SO_3 was formed at any stage. A mass balance for the materials entering and leaving the sensor is:

$$r_s = \Gamma_{SO2}(pSO_2 - p'SO_2) = 2\Gamma_S(p'S_2 - pS_2) \qquad (A1.10)$$

The equilibrium relationship for the reaction

$$SO_2 \rightleftharpoons \tfrac{1}{2}S_2 + O_2$$

is:

$$K_{SO2} = pS_2^{1/2}\, pO_2/pSO_2\, P. \qquad \text{(A1.11)}$$

By rearranging eqn(A1.11) and substituting into eqn(A1.10), $p'SO_2$ is calculated to be:

$$p'SO_2 = -\frac{2\Gamma_{S2}}{\Gamma_{SO2}}\left(\frac{K_{SO2}^2\, pSO_2^2\, P}{p'O_2^2} - pS_2\right) + pSO_2 \qquad \text{(A1.12)}$$

Solving the quadratic equation that results from rearranging eqn(A1.12) produces:

$$p'SO_2 = \frac{-1 \pm \sqrt{1 + 8\dfrac{K_{SO2}^2\, \Gamma_s\, P}{p'O_2{}^2\, \Gamma_{SO2}}\left(pSO_2 + 2pS_2\dfrac{\Gamma_s}{\Gamma_{SO2}}\right)}}{\dfrac{4\, K_{SO2}^2\, \Gamma_s\, P}{p'O_2{}^2\, \Gamma_{SO2}}} \qquad \text{(A1.13)}$$

The internal partial pressure of oxygen, $p'O_2$, was determined using the Nernst relation, and pS_2 using eqn(A1.11). By applying Faraday's law to the mass balance equation the current due to SO_2 reduction was determined:

$$I_{SO_2} = 4\, F\, \Gamma_{SO2}\, (pSO_2 - p'SO_2) \qquad \text{(A1.14)}$$

where $p'SO_2$ was determined using the positive result from eqn(A1.13).

A1.3 Nitric oxide reduction

Complete reduction

If the reaction

$$NO \rightleftharpoons \tfrac{1}{2}N_2 + \tfrac{1}{2}O_2 \qquad \text{(A1.15)}$$

is the only reaction involving NO to occur, and assuming equilibrium, the limiting current is determined by starting with the mass balance:

$$r_{NO} = \Gamma_{NO}(pNO - p'NO) = 2\,\Gamma_{NO}(p'N_2 - pN_2). \qquad \text{(A1.16)}$$

Rearranging gives:

$$p'NO = pNO - 2(p'N_2 - pN_2). \qquad (A1.17)$$

The equilibrium relationship for reaction (A1.15) is:

$$pN_2 = K_{NO}^2 \, pNO^2 / pO_2. \qquad (A1.18)$$

Substituting eqn (A1.18) into eqn (A1.17) to eliminate $p'N_2$ and rearranging produces the quadratic in p'NO:

$$\frac{2K_{NO}^2}{p'O_2} p'NO^2 + p'NO - pNO + 2pN_2 = 0 \qquad (A1.19)$$

Therefore:

$$p'NO = \frac{-1 \pm \sqrt{1 + 8K_{NO}^2/p'O_2 (pNO + 2pN_2)}}{4K_{NO}^2/p'O_2} \qquad (A1.20)$$

Obviously p'NO could only be determined using the real positive root, if one existed, for the above equation. The value found for p'NO can then be used in eqn (A1.16) and the resulting current determined using Faraday's law.

$$I_{NO} = 2F\Gamma_{NO}\left(pNO - \frac{-1 \pm \sqrt{1 + 8K_{NO}^2/p'O_2 (pNO + 2pN_2)}}{4K_{NO}^2/p'O_2}\right) \qquad (A1.21)$$

Another approach taken was to ignore the diffusion of nitrogen out of the sensor and to solve;

$$r_c = \Gamma_{NO}(pNO - p'NO) \qquad (A1.22)$$

by determining p'NO using the equilibrium relationship (eqn (A1.18)) only.

Partial reduction

Assuming only the reaction

$$NO \rightleftharpoons \tfrac{1}{2}N_2O + \tfrac{1}{4}O_2 \qquad (A1.23)$$

the mass balance is;

$$r_{2NO} = \Gamma_{NO}(pNO - p'NO) = 2\,\Gamma_{N2O}(p'N_2O - pN_2O) \qquad (A1.24)$$

Rearranging gives:

$$p'NO = pNO - 2\,\Gamma_{N2O}/\Gamma_{NO}\,(p'N_2O - pN_2O). \qquad (A1.25)$$

The equilibrium relationship is:

$$pN_2O = K_{2NO}\, pNO^2 / pO_2^{1/2}\, P^{1/2}. \qquad (A1.26)$$

Substituting A1.26 into A1.25 and rearranging produces the quadratic in p'NO:

$$p'NO^2\, 2K_{2NO}\Gamma_{N2O} / (\Gamma_{NO} p'O_2^{1/2} P^{1/2}) + p'NO - pNO - 2\Gamma_{N2O} pN_2O / \Gamma_{NO} = 0$$

Therefore:

$$p'NO = \frac{-1 \pm \sqrt{1 + 8\dfrac{K_{2NO}\,\Gamma_{2NO}}{p'O_2^{1/2} P^{1/2} \Gamma_{NO}}\left(pNO + 2pN_2O\dfrac{\Gamma_{2NO}}{\Gamma_{NO}}\right)}}{\dfrac{4K_{2NO}\Gamma_{2NO}}{p'O_2^{1/2}\, P^{1/2}\, \Gamma_{NO}}} \qquad (A1.27)$$

The current for the partial reduction of NO was found by substituting the real positive value found for p'NO into eqn(A1.24) and applying Faraday's law.

$$I_{2NO} = 2F\Gamma_{NO}\left(pNO - \frac{-1 \pm \sqrt{1 + 8\dfrac{K_{2NO}\,\Gamma_{2NO}}{p'O_2^{1/2} P^{1/2} \Gamma_{NO}}\left(pNO + 2pN_2O\dfrac{\Gamma_{2NO}}{\Gamma_{NO}}\right)}}{\dfrac{4\,K_{2NO}\,\Gamma_{2NO}}{p'O_2^{1/2}\, P^{1/2}\, \Gamma_{NO}}}\right) \qquad (A1.28)$$

A1.4 Estimation of diffusion coefficients

A number of relations have been developed for estimating the diffusion coefficients of binary gas mixtures. Diffusion in more complex mixtures was very difficult to estimate so in this work the two dominant gases were assumed to be the only ones controlling.

The Fuller, Schettler, and Giddings relation (Perry (1984)) was used whenever possible.

$$D_{ab} = \frac{10^{-3} T^{1.75} \left[(M_a + M_b)/M_a M_b\right]^{1/2}}{P\left[(\Sigma v)_a^{1/3} + (\Sigma v)_b^{1/3}\right]^2} \qquad A1.29$$

where D_{ab} is the diffusion coefficient for the gas mixture of a and b in [cm^2/s], P is

the ambient pressure in atmospheres. M_a and M_b are the relative molecular masses of gases a and b respectively. Σv is the atomic diffusion volume. The value of Σv for some common gases has been measured and reported. Values for NO and sulphur could not be found in the literature so another relation had to be used.

The method chosen was the Wilke and Lee relation (Reid et al (1987)).

$$D_{ab} = \frac{[3.03-(0.98/M_{AB}^{1/2})]\,(10^{-3})\,T^{1.5}}{P\,M_{AB}^{1/2}\,\sigma_{AB}^{2}\,\Omega_D} \qquad \text{A1.30}$$

where $M_{ab} = 2[(1/M_A) + (1/M_B)]^{-1}$

$\sigma = 1.18V_b^{1/3}$

V_b = liquid molar volume at boiling point [cm^3/mol]

$\sigma_{AB} = (\sigma_A + \sigma_B)/2$

$$\Omega_D = \frac{1.06036}{(T^*)^{0.15610}} + \frac{0.193}{\exp(0.47635T^*)} + \frac{1.03587}{\exp(1.52996T^*)} + \frac{1.76474}{\exp(3.89411T^*)}$$

$T^* = T(k/\varepsilon_{AB})$

$(\varepsilon/k_{AB}) = [(\varepsilon/k_A)(\varepsilon/k_B)]^{1/2}$

$(\varepsilon/k) = 1.15Tb$

Tb = Boiling point (at 0.1MPa)

For polar gases a correction was required.

$$\Omega_D = \Omega_D + \frac{0.19\left(\frac{1940\mu_D^2}{V_bT_b}\right)^2}{T^*}$$

where μ_D = dipole moment.

Appendix 2

The computer interface and potentiostat

An overview of the complete computer controlled furnace, gas mixing apparatus and potentiostat/galvanostat was presented in Fig. 2.7. The following is a detailed description of each part.

A2.1 Digital interface

The centronics port of the computer has a 25pin D plug that can send and receive 0 - 5V digital signals. The port was used to output 10 signals that performed the various switching applications required by the circuit. Table A2.1 lists the pins on the plug, what they operated and the colour of the wire connected to the plug. The pins not listed were not used.

A2.2 Analogue interface

The analogue input of the first ADDA card failed; however, the card was retained and its analogue output (DA) channel was used to send the 0 - 5V command signal to the gas flow control valves via the interface discussed in section A2.4.

The details of how the second ADDA card was connected are shown in Table A2.2. The pins not listed were not used.

Table A2.1

Connections to the centronics port.

Pin	Function	Colour
1	Galvanostat or potentiostat	Brown/green
2	Gas valve select	Brown
3	Gas valve select	Green
4	Voltage range select	Yellow/brown
5	Current range select	Green
6	Current range select	White
7	Current range select	White/yellow
8	Voltage range select	Black
9	Furnace on/off	Red
10	-	Blue
11	-	Yellow
12	-	Pink
13	-	Grey
15	-	Red/blue
16	Interrupt relay	Grey/pink
18-25	Earth	Purple

Table A2.2

14bit ADDA conversion card connections

Pin	Function	Colour
2	Command signal to potentiostat (E_{set})	Black
3	Earth	Yellow
4	SE voltage	Green
5	Voltmeter 1	Pink/grey
6	RE voltage	Blue/red
7	Valve 4 reading	Green/brown
8	Valve 2 reading	Green/white
9	Primary voltmeter	Blue
10	-	Brown
11	Room temperature	Red
15	-	Blue
16	Voltmeter 2	Purple
19	Current reading	White
20	Valve 3 reading	Brown/yellow
21	Valve 1 reading	Pink
22	2.45 voltage reference	Yellow
23	Thermocouple reading	Green
24	Earth	Grey

A2.3 15V power supply

This used the simple circuit illustrated in Fig. A2.1. A KBU4B (4 ampere) bridge rectifier rectified the output from a mains transformer. 10 000μF capacitors were connected to smooth the rectified output from each side of the centre-tapped output. Voltage regulation at +15V and -15V was achieved by fixed voltage regulators rated at 3A and 1A respectively. -15V units rated at more than 1A were not available so 2 were used with the output from the second supplying only the negative arm of the booster amplifier of the potentiostat. 0.33μF capacitors were connected across the leads of these regulators to minimize radio frequency (rf) noise.

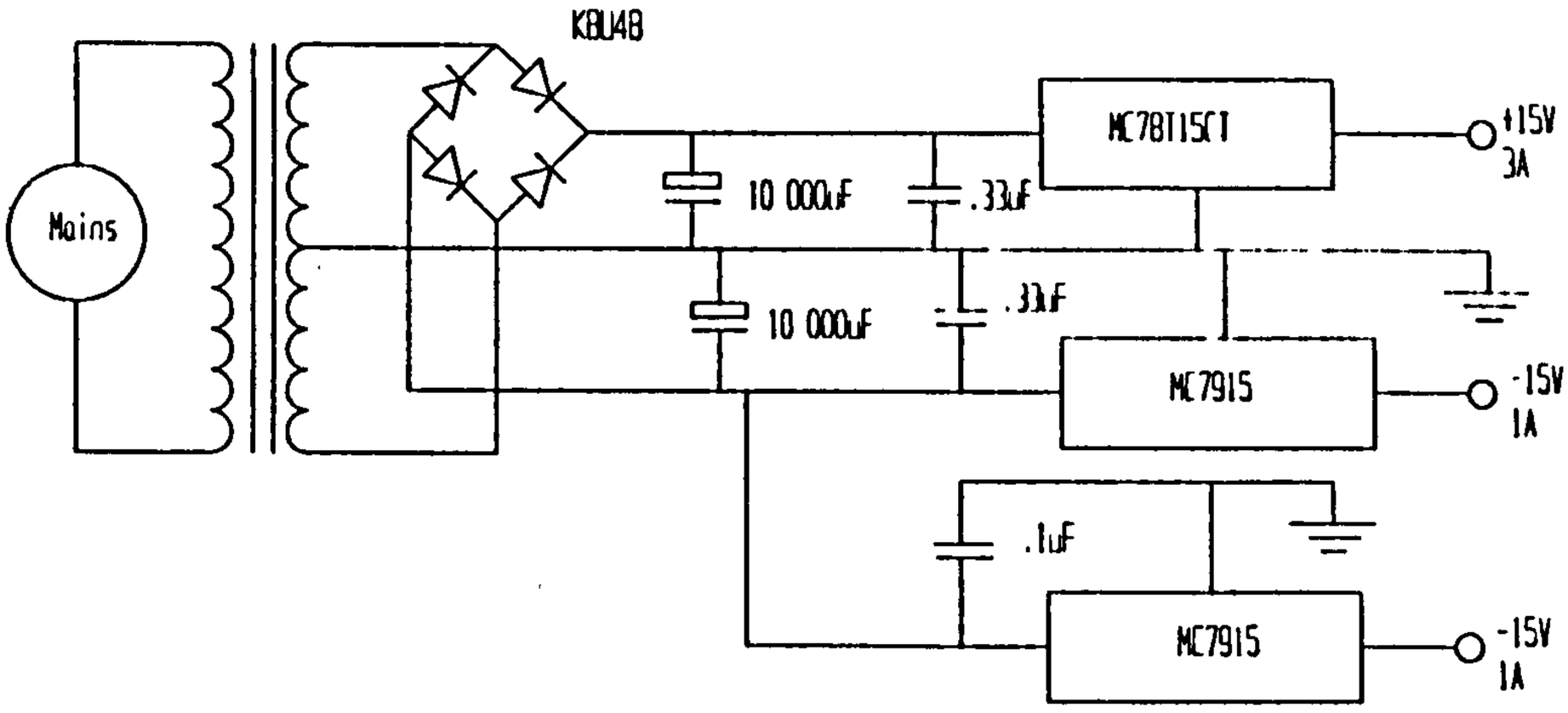

Fig. A2.1. 15 volt bipolar power supply circuit

A2.4 Gas flow control circuit

The gas flow control valves (5850TR from Brookes) had a built in circuit that allowed their flow rate to be set by a 0 - 5 volt command and they sent back a 0 - 5 volt signal reflecting the flow rate achieved. An interface circuit was therefore built that allowed the computer to send and receive these two signals (Fig. A2.2). The figure shows the three plugs to which 3 valves could be connected. All three

plugs were identical but the figure reflects different information on each. There was provision for a fourth valve but it was not fitted.

The DG508ACJ is a transistorized relay that allows a signal to be switched to any one of 8 outputs. The 0 - 5V command from the computer DA card was connected to the common drain (terminal 8). The switch to which the command was sent was selected by two digital inputs to pins 1 and 16 (see Table A2.1).

The TL074CN consists of 4 high impedance input op-amps on a single chip. It was connected to operate as a sample and hold circuit.

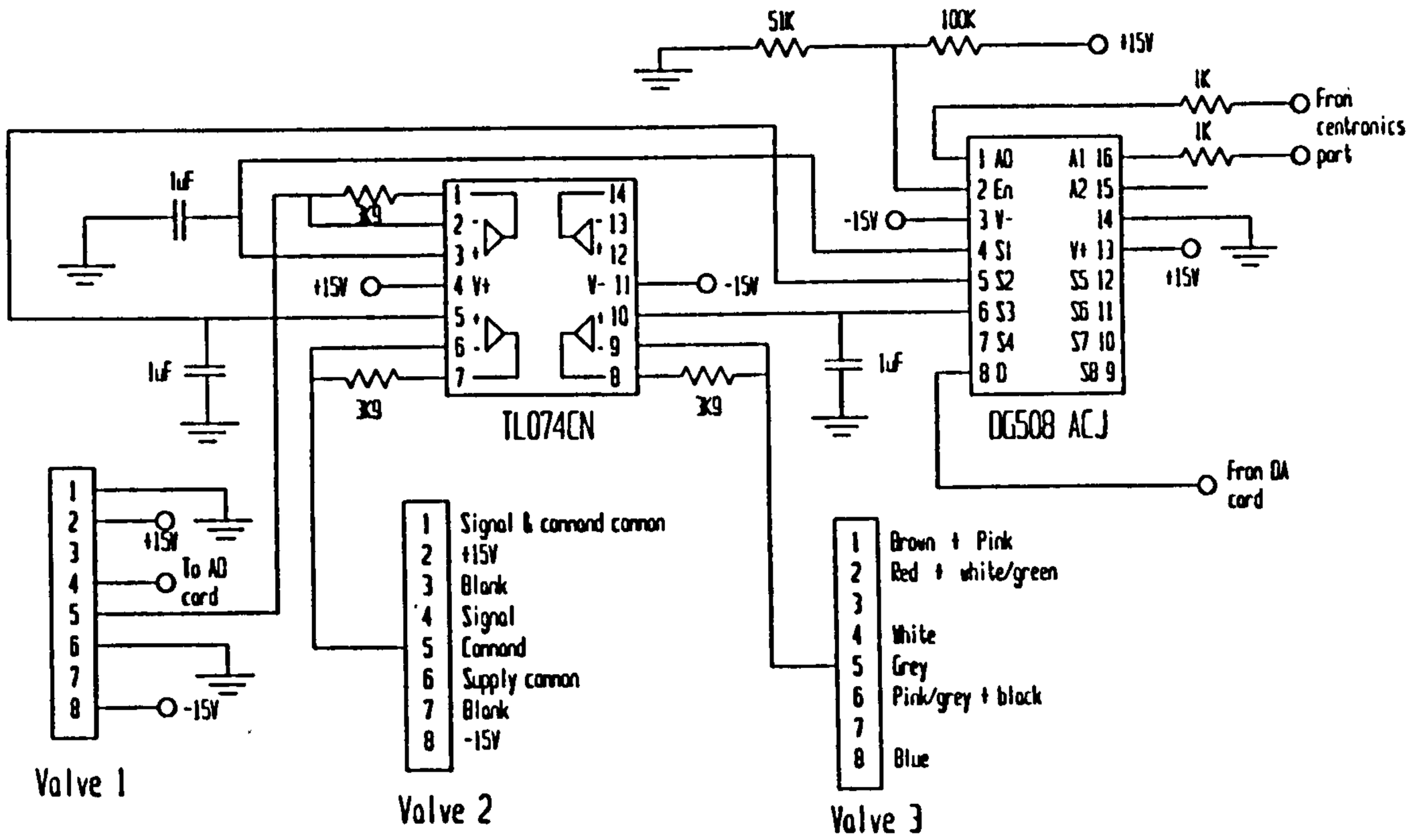

Fig. A2.2. Valve control circuit

A2.5 Furnace control circuit

The solid state zero switching relay shown in Fig. A2.3 was used to control the power to the furnace. Originally this switch was operated via the two terminals marked 'Furnace controller' in the figure. The controller was a PD unit fitted by the manufacturer. It measured the furnace temperature using the K type thermocouple embedded in the wall of the furnace. In order to allow the computer or the Eurotherm controller to control the furnace temperature the circuit shown in Fig. 2.3

was built.

In the bottom position of the switch primary control of the furnace was from *the centronics port of the computer. However, the digital signal was buffered by a* 220kΩ resistor so that it could only turn on the furnace if the controller was also signalling on. The controller therefore had to be set about 50°C above the highest temperature required. This was a useful safety feature and was the switch position normally used. However, if temperatures above 950°C were required, the Eurotherm controller had to be disabled. This was done by selecting the bottom position of the switch. The Eurotherm controller then had to be set below the minimum expected temperature. The middle position of the switch gave the Eurotherm controller full control which was useful if there was a any problem with the computer control. The two preset resistors were adjusted so that all three switch positions operated as just described.

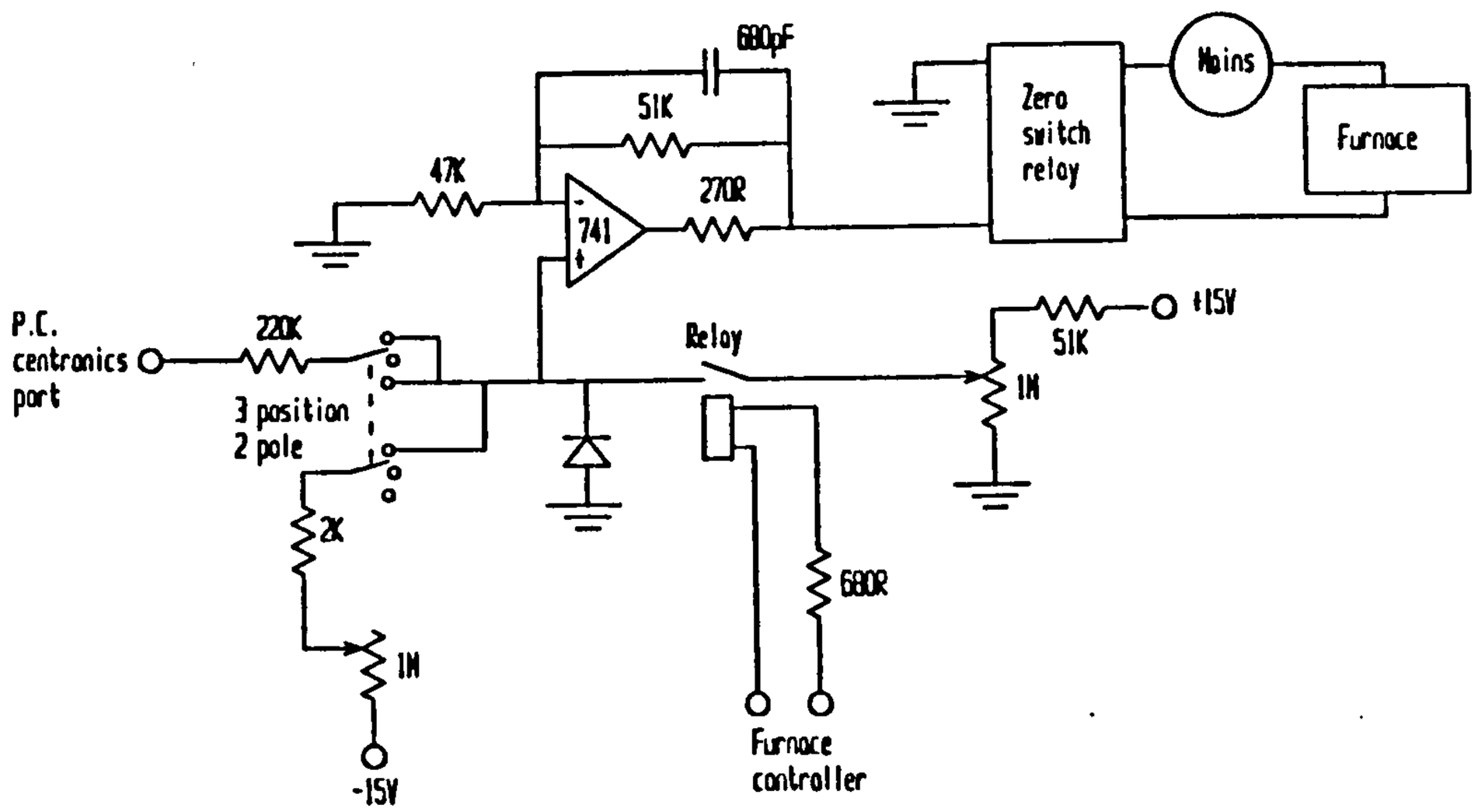

Fig. A2.3. Furnace control circuit.

The computer calculated the furnace temperature using the reading of an R type thermocouple positioned near the sensor under test. To do this it used the circuit shown in Fig. 2.4 to determine the temperature of the cold junction of the thermocouple. The LM35 chip was mounted near the cold junction and gives an

output of 10mV/°C. This signal was amplified 10 times and passed to the AD card as shown. The computer then calculated the compensation required for the thermocouple.

The greatest possible accuracy was desired for the furnace temperature so considerable care was taken with the circuit that amplified the thermocouple voltage (top of Fig. 2.5). A high quality op-amp (MAX430) with a very low offset voltage (1μV) was used and it was mounted as close as possible to the furnace in a metal box. A precision bandgap device was used to supply 2.45 volts and produce an output offset when the thermocouple was at room temperature. This was to make maximum use of the -9.5 to +9.5V span of the AD card. High precision resistors with a temperature coefficient of 15ppm were used to set the gain. Care was also taken to avoid earth loops and the non-inverting input was connected directly to the point used as a zero reference by all the circuits (shown a triangle symbol). (The three bar symbol was used for connections that were not necessarily direct to the zero reference point.) The program also read the temperature often and averaged the results in two stages to eliminate any interference (see section A3.3).

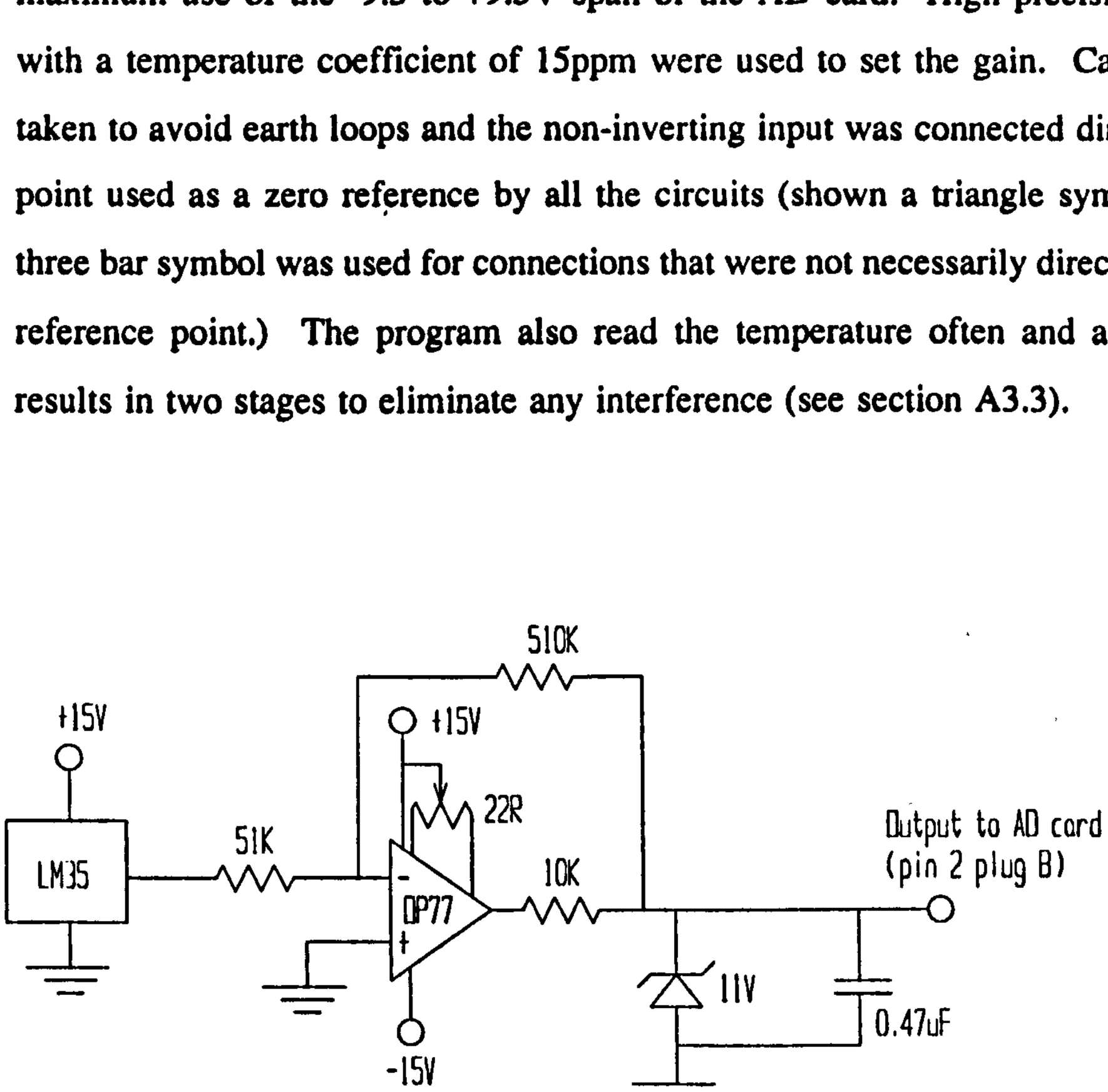

Fig. A2.4. Thermocouple cold junction temperature sensor and amplifier.

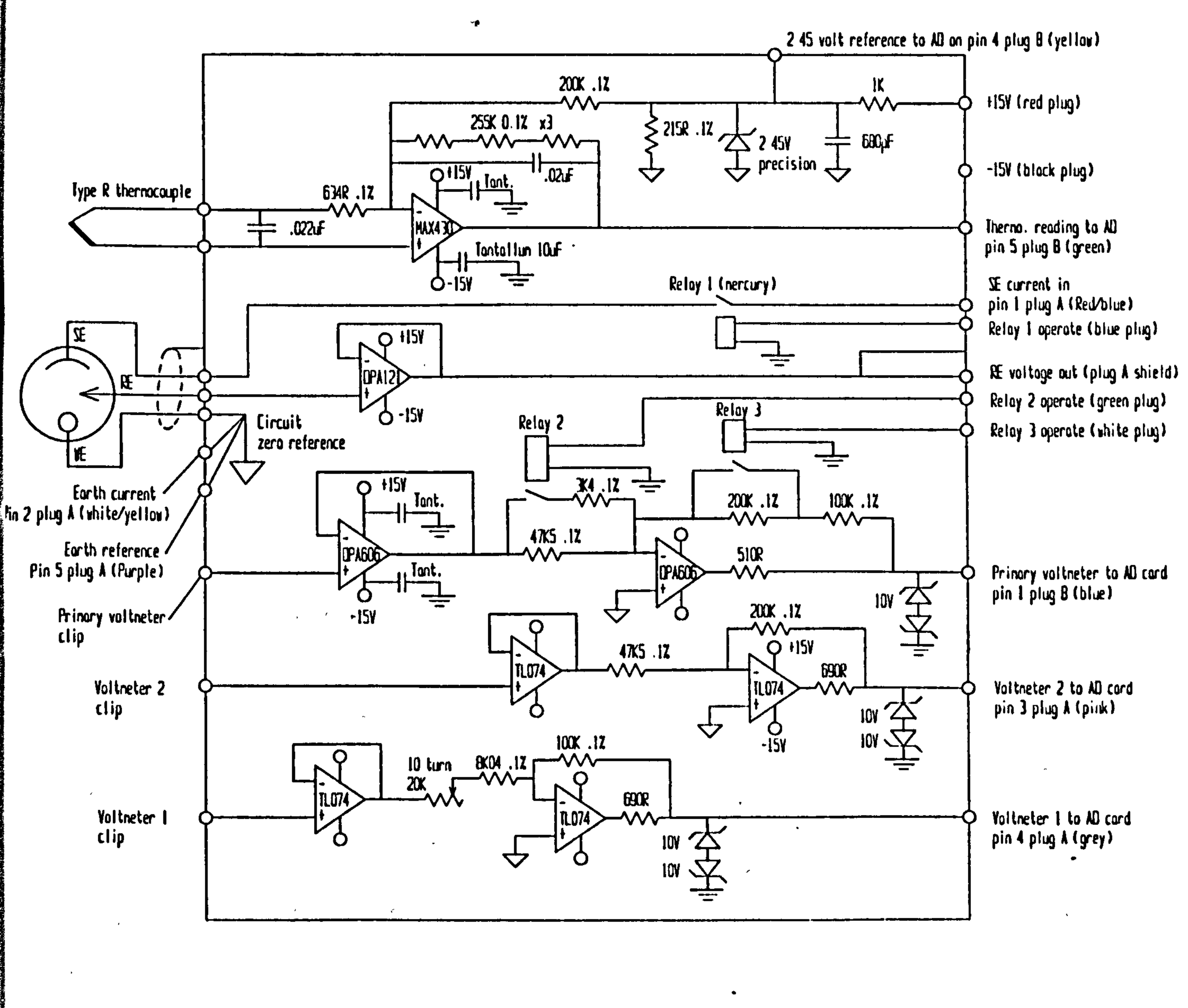

Fig. A2.5. Circuits in low-level signal buffer box mounted near the furnace entrance.

A2.4 The potentiostat/galvanostat

The potentiostat/galvanostat was built in two parts. The low-level signals from the sensor were amplified using circuits mounted in the metal box (Fig. 2.5) that was positioned as close as possible to the furnace. This was to minimize noise picked up by leads carrying low-level signals. The remainder of the circuit was housed in the main box (also metal but larger).

The signal conditioning box (Fig. 2.5) held the current interrupting relay (relay 1) and the buffer amplifier for the RE. The output of the op-amp was connected to the box and to the alloy steel tubes that shielded the platinum wires running into the furnace. This was done to provide the maximum possible shielding for the signal from the RE.

Three voltmeters were also built into the signal conditioning box. The primary voltmeter had 4 possible ranges selected by relays that were operated via the circuit shown in Fig. A2.7. All voltmeters had zener diodes connected to their outputs to prevent voltages greater than ±12V reaching the ADDA card. The card gave erroneous readings on all channels if this occurred.

The remainder of the potentiostat/galvanostat is shown in Fig. A2.6. The buffered signal from the RE was passed to a voltage comparator (OPA121) via a network that selected between 4 possible voltage ranges. The non-inverting input of the OPA121 was connected to a circuit that compensated for its input off-set voltage. There was a selection of three negative feed-back capacitors that could be selected to give the desired combination of frequency response and noise immunity.

The output from the voltage comparator was passed to a booster amplifier operated in the voltage follower mode. The output from both circuits was passed to an array of span resistors used to select the current range. If potentiostatic mode was selected (it was in Fig. 2.6) the voltage across the span resistors was amplified by the differential op-amp INA105. The output from this op-amp was passed to the AD card. If galvanostatic mode was selected using relays 4 and 6 then the circuit connected to the RE had no function. The 5 low current span resistors were connected directly to the output of the voltage comparator (OPA121) to minimize

noise in these ranges. Relay 5 was used to ensure that the differential amplifier measured the voltage across the span resistor selected. Fig. 2.7 shows how relay 5 was operated by a summing amplifier connected to the relays that selected the 3 high current span resistors.

The galvanostat operated by using the differential amplifier to feed a current through the span resistors.

Because a wide range of currents needed to be measured, provision was included for switching load resistors. Eight resistors switched by relays were used ranging from 5Ω to 2MΩ which gave maximum current readings of between 3.6μA and 1.4A. The computer program converted all readings directly into milliamps automatically.

Although relays switch much more slowly (2ms) than transistorised switches, they have a low resistance once connected and a high current carrying capacity. Both features were essential for the high current ranges so relays were used for all current ranges. Relays were also used to allow the circuit to be changed from a potentiostat to a galvanostat for the same reason. A mercury relay was used for the current interruption switch since they are immune to contact bounce.

A facility was added to change the range of voltages that could be set by the potentiostat. Four ranges were made giving maximum voltage settings of between 100mV and 4500mV. Again, the resistors were selected using relays.

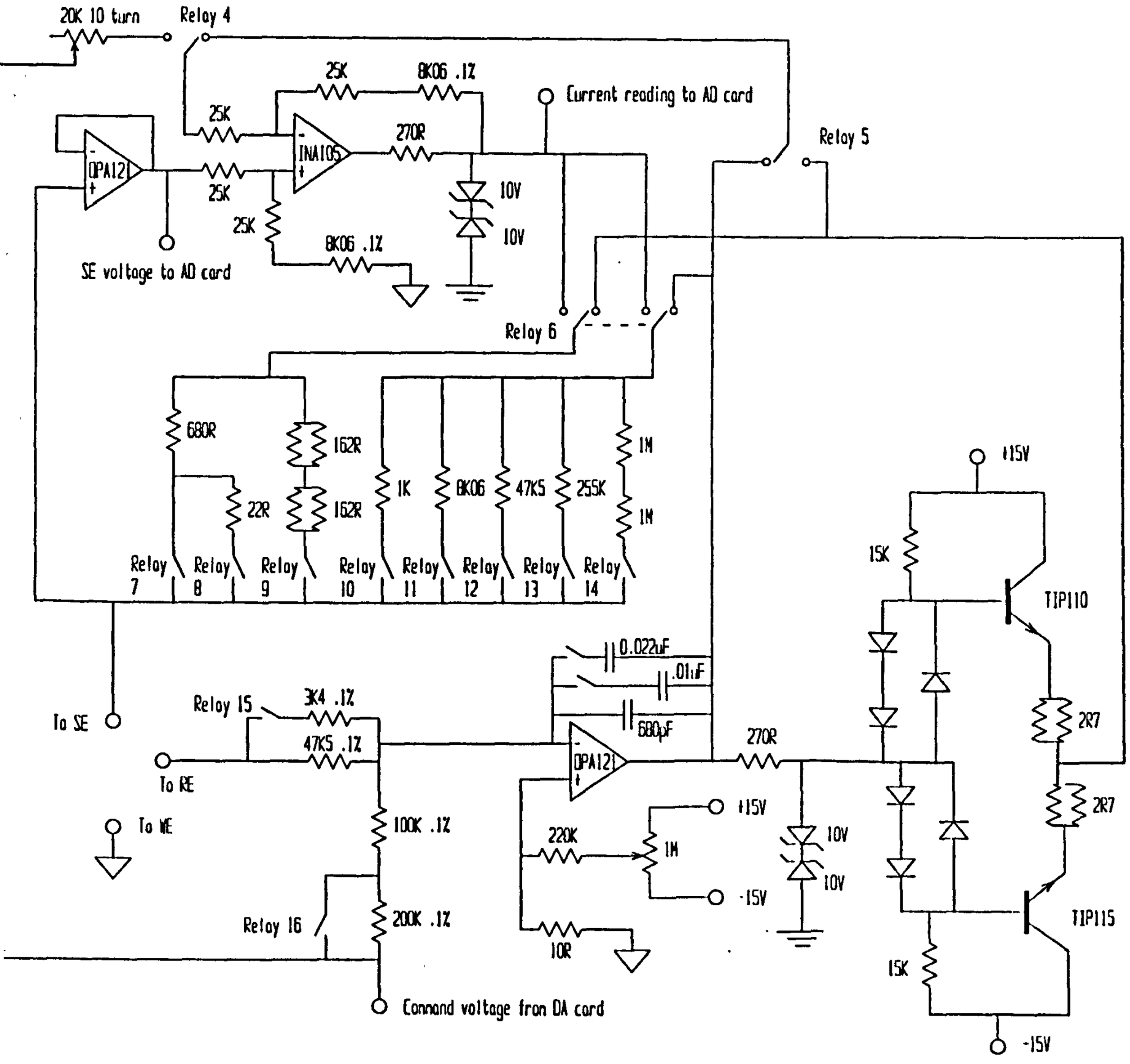

Fig. A2.6. Main potentiostat/galvanostat circuit.

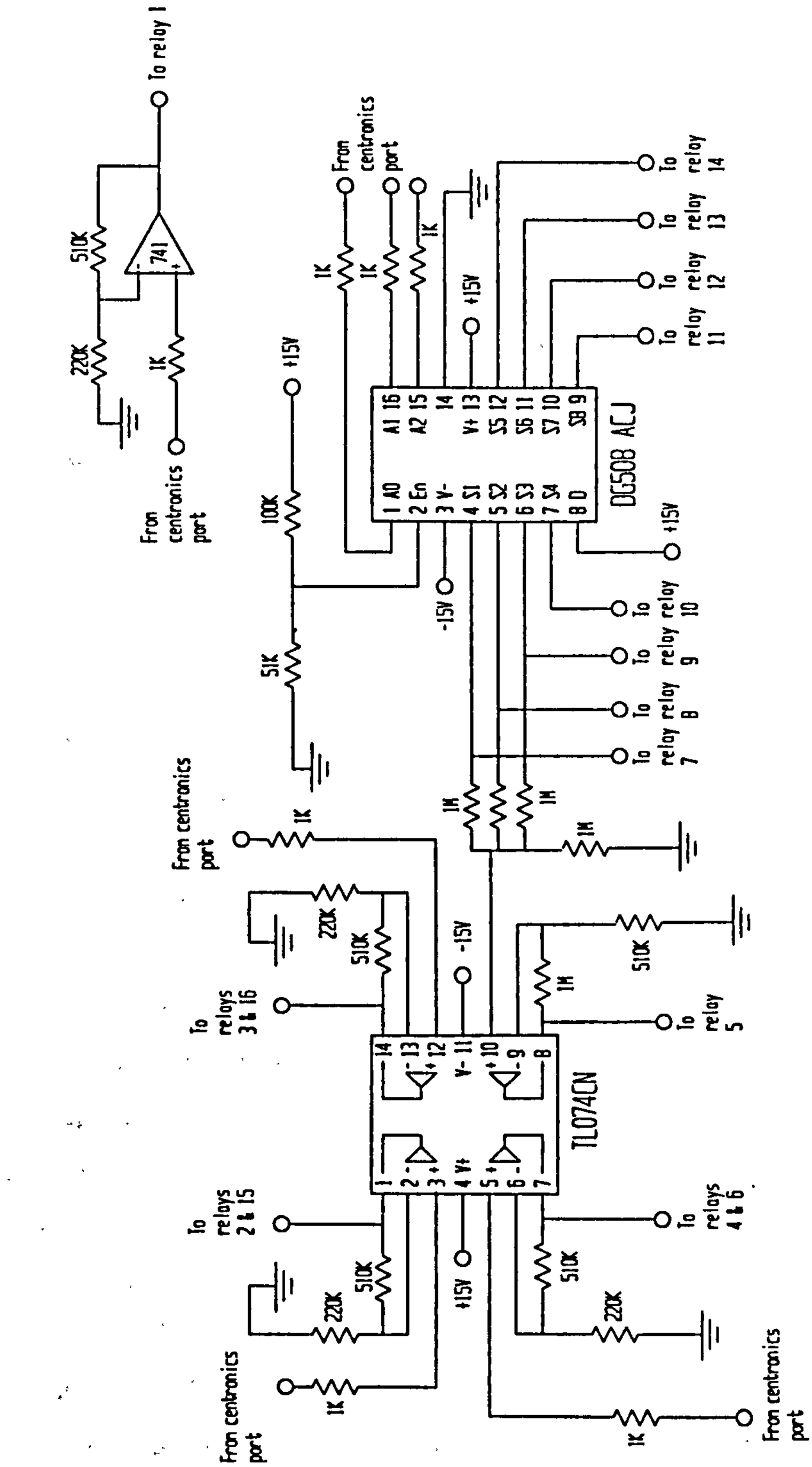

Fig. A2.7. Circuit for operating the relays in the interface.

Appendix 3

The control program (CONTRL)

3.1 Program design philosophy

CONTRL was written in Turbo Pascal v5.5 with a few Turbo Assembler v1.2 procedures included. Turbo Pascal was chosen for its low price, reliable operation, speed of code compilation and the large range of available tools including a built-in debugger. Turbo Assembler was used for procedures that had to be performed as quickly as possible.

The codes for programs are often difficult to understand and revise. Since the effort required to write the program was large, much attention was paid to making the program code as easy to follow as possible. With this in mind, all variables and procedures were given meaningful names. Also the length of the procedures was kept as short as possible.

There are two methods by which computers generally perform timed operations; polling and interrupts. Polling involves the computer checking its internal clock at frequent intervals to see if it is time to perform the operation. (In this section interrupts refers to hardware interrupts which are different to software interrupts). Interrupts are signals either generated by the computer's clock or by some other device. The central processing unit (CPU) has a special terminal for it to be informed when an interrupt has occurred. On receiving the interrupt signal the CPU stops what it is doing as quickly as it can and services the interrupt. This facility in effect enables the CPU to perform two or more completely separate tasks in parallel. This has several advantages but also has some pitfalls. The main advantages are that the CPU usually has less to do and timing accuracy is higher for a given CPU work-load. One pitfall is that if the computer is servicing an interrupt when a new interrupt arrives, the new one is delayed until the old one is finished. It is therefore important to keep the tasks performed by the program during an interrupt to a minimum. Under normal circumstances the computer should spend a

very small proportion of its time processing interrupts. Also the maximum rate at which interrupts can be performed is slower than the maximum for polling. Finally, the software for interrupts is more difficult to write. It was decided to use interrupts to perform all except the fastest timed measurements. This was done to allow the control program to do as much processing of the experimental data as possible while waiting for interrupts. Polling at the ADDA card's maximum speed was used immediately after current interrupts.

All the procedures in the program that are called by the interrupt routine are marked because the computer crashes if the integrated debugger is used to step into such a routine. The stand-alone debugger must be used for that. Also, interrupt procedures must not perform any task that uses further interrupts (such as writing to the screen or disc).

3.2 Program structure

Turbo pascal allows large programs to be split into units. CONTRL is written in three units: GRAFTIL, CONTEX and CONTRL. These units should be compiled in the order given. An assembly program call CLOCK is also part of CONTRL. It reprograms the computer's clock to operate at the speed required by CONTRL using interrupt 8.

CONTRL requires 3 files of data. The first is DEFAULT.DAT which contains a range of data such as the factors by which to multiply the digital readings in order to obtain the true analogue value. Where possible, calibration of the interface circuit was achieved by setting coefficients in DEFAULT.DAT rather than introducing a variable resistor into the circuit. This reduced costs and improved accuracy due to reduced temperature dependence. The claimed temperature coefficient for the 0.1% resistors used in the circuits was 15 ppm/°C which was better than that of readily available variable resistors.

The other data files are MACRO.DEF and MACRO.DAT. Both hold settings used in the macro mode of operation. When macro mode is started it reads MACRO.DAT and when all the desired settings have been chosen they are all stored in MACRO.DAT.

3.3 Furnace control

The furnace temperature was calculated by converting the digital reading to a microvolt reading and then converting to temperature using a functional representation from Coates (1978).

CONTRL took 10 readings of the furnace temperature at the rate of one every 0.4 seconds. It then averaged those readings and took a room temperature reading from which it calculated the furnace temperature. It then calculated the percentage of full power needed to achieve the desired furnace temperature. The algorithm used was based on PID control except that the derivative component was calculated by predicting the furnace temperature at a future time. A more accurate estimate of the actual furnace temperature was arrived at by taking a moving average of the averages calculated every 4 seconds. A moving average is calculated using the formula:

$$\text{New value} = Y \times \text{old value} + (1-Y) \times \text{last reading.}$$

3.4 Gas valve control

Every 400ms CONTRL changed the valve that received the command voltage. This required first changing the selection on DG508 (Fig. A2.2) and then setting the required voltage on the DA card. Before doing this it read the signal voltage of the previously connected valve.

If the command and signal voltage did not agree within 1% of full scale CONTRL printed a warning message so that the leakage, pressure setting or other fault could be attended to.

3.5 Potentiostat/galvanostat control

The default setting for the mercury relay (relay 1) was open and it was only closed when a current needed to be passed through the cell under test. It was hoped that this would help protect the cell and the potentiostat.

Appendix 4

Operating instructions for CONTRL

A4.1 Getting started

CONTRL is started by typing in its name. It is designed to do a number of things automatically when first started. This includes controlling the furnace according to preset values. The furnace interface, potentiostat and other interfaces therefore should be switched on before starting the program. A screen showing the values of various settings and readings is also displayed initially. At the bottom of this screen is a list of basic instructions for operating the program.

A4.2 Creating a results file

One of the first things the program does is to create a file on the hard disk in which to store the results. This file is given a file name that starts with the letter R and then a single number to represent the year (2 for 1992). It then has 2 digits for the month and two for the day. This means that when the result files are listed in alphabetical order the latest results are presented at the bottom of the list. If the program had been run previously on the same day the program detected this and asked for a letter to follow the digits. The first time the program is run it sets this letter to "a". By typing an "a" at the prompt, the second set of results for that day is stored in the same file following the first set. If any other letter is entered a new results file is created. A typical results file name is R20424A.PRN for the first set of results started on the 24th April 1992.

A4.3 The default settings file

The next task for the program was to read a file that contained a range of default settings for the furnace and the potentiostat. These settings can be changed

at any time by changing them as described below and then pressing F9. All the new settings were saved at once.

The first screen that comes up when the program starts is called the reporting screen. It consists of a range of headings under which are tables of continuously updated readings. It is designed for monitoring the performance of the system, and nothing can be changed while this screen is displayed. To change the furnace settings the F3 key must be pressed. A graph showing the furnace temperature history appears and a menu with the values that can be changed also appears. The value that will be changed if a value is typed in is displayed in a different colour to the other values. To move to the other values use the up or down arrow.

A4.4 Setting the valve flow rates

To get the valve setting menu press F5 at any time. It operates in the same way as the furnace control menu.

A4.5 Performing cyclic voltammetry

To perform a CV press F6. A menu appears and the axis for the graphic presentation of the results also comes up. The menu operates as the others. The menu also includes a switch to allow the results to be saved to disk or not as desired. To toggle this switch select it on the menu with the arrow keys and then use the space bar. When all the settings have been changed to the desired values "g" must be pressed to start the cycle. Pressing any key will immediately make the program disconnect the cell and stop the sweep.

CONTRL needed to know the rate at which the voltage changes so it asked for the voltage rise rate (in mV/s). If a positive value was given, the voltammogram started with the voltage increasing (ie. becoming more anodic on the working electrode) and it decreased first if a negative value was given. The voltage set before the cell was switched on was called the initial voltage and the program also asked for this. The amplitude of the waveform was set by a variable called the voltage scan. If the scan rate was positive initially it was changed to a negative value when the voltage reached offset + voltage scan. It then changed back to positive when the

voltage reached offset - voltage scan. Although offset voltage and initial voltage were often both zero, the program allowed them to be set to any value independently. A stroke was the name chosen for the process where the voltage moved from the offset to the upper or lower limit of the scanned voltage, or visa versa. Four strokes therefore made a complete cycle and the program allowed the number of strokes to be set.

If a record of the results is required, the menu option about saving results must be on.

A mode called slow CV is also available. In this mode the two voltmeters are also read and the current range will select the appropriate scale. These extra operations additional to those performed by normal CV mode require extra time so slow CV mode is only appropriate for scan rates of less than 10mV/s.

A4.6 Steady state mode

This mode allows a fixed voltage or current to be applied until the current or voltage respectively comes to a steady state. It can also be used to monitor the open circuit voltage until that comes to steady state. It is selected with F7 while F8 allows the setting of a batch of up to 30 steady states. F8 does not store the results showing the progress to steady state while F7 does. When the program detects steady state it performs a current break and stores the results. To cause a current break before steady state has been detected by the program press "b". Pressing any other key will immediately make the program disconnect the cell and stop the run.

A4.7 Macro mode

Macro mode is a powerful system that enables the program to do any of the functions described above in any order and as many times as required. It is limited to 10 000 hours of operation or the free space on the hard disc. To set a macro running press F4. A screen comes up that allows all the parameters for any operation to be set. The screen comes up with the settings read from a file called "Macro.def". All these settings can be changed as needed. When everything has been set for the first operation the settings are stored on disc by pressing "Home" or "Page Down".

Home will read the next operation from Macro.def while "Page Down" will copy the previous one. There is a page counter at the bottom of the screen to indicate how many operations have been set. More than 33 000 pages can be set. When all the operations have been set, bring up a new page and select function 9 (ending). The Macro will immediately start operating. To exit it before it has finished press "x".

If the program stops while performing a macro (eg. due to a power failure) the macro can be started again from where it last saved the results. First check the results file and count the number of operations performed. Then copy the file where the data for the macro is stored (Macro.dat) to Macro.def (having backed up the old Macro.def first if necessary). Restart CONTRL, press F4 and then press "End" once for every operation already saved. Then press "Home" until all the operations have been read from macro.def and the macro starts running.

A4.8 Using the results.

The results in the results file were saved in a format ready to be imported into a spreadsheet. This made it easy to review and perform detailed processing on the results after each experimental run. CA SuperCalc version 5.1 was chosen as a suitable spreadsheet. The command for importing the example results file would be {//Import Coma separated values} and then {C:\tp5\prog\R20424A.PRN}. The spread-sheet with all the results in it would then be stored as R20424A.CAL using the save command.

The spreadsheet files thus created were saved using the date of creation as the file name as explained above. So the file R20912A.CAL would be the sheet (created with CA SuperCalc) containing the first set of data collected on the 12/9/1992. It would also contain details of the subsequent processing of the data so these spreadsheet files became more important than the original results files, and were therefore carefully backed-up.

Appendix 5

Example calculations

A5.1 High voltage reduction of YSZ

A single experiment was performed where high voltages were applied to the electrodes on a single YSZ disc and the amount of oxygen released by the reduction of the YSZ was measured: see section 3.2.3.

White spot nitrogen (low oxygen content) was connected to a 150ml/min mass flow valve (calibrated at 273K) which was set to 100% flow rate and air was connected to a 5ml/min valve that was set to 3% flow rate. The expected mole fraction of oxygen flowing into the atmosphere surrounding the YSZ cell was therefore:

$$X_{O2} = 0.209 \times 0.15 / (0.15+150)$$
$$= 0.000209.$$

The concentration of oxygen leaving the system was measured with a potentiometric sensor at 735°C. The reading on this sensor was 149.3mV while 0.1 and 0.2mA were flowing through the cell. Using the Nernst equation and assuming the pressure on both sides of the sensor was 101325pa the measured mole fraction of oxygen was calculated as:

$$X_{O2} = .209 \times \exp(.1493V \times 4 \times 96485 Cequiv^{-1}/(*.3144 Jmol^{-1}K^{-1} \times 1008K))$$
$$= 0.000216.$$

The difference of 3.3% is well within the expected experimental error considering the low flow rate through the valve controlling the air.

When the current through the cell was 5mA the potentiometric sensor read 144.4mV which corresponds to $X_{O2} = 0.0002705$. To calculate the number of electrons that flowed per mole of oxygen reduced (n) a mass balance was done on oxygen.

$$\text{Out flow} = \text{In flow} + O_2 \text{ released by reduction}$$

Using a basis of 1 second, assuming the total flow rate is unchanged by the extra

oxygen and by applying Faraday's law this becomes:

$$N\,X_{O2}(out) = N\,X_{O2}(in) + I / n\,F.$$

At low currents the YSZ is not reduced so the current (I) would be zero for the purposes of the above mass balance. The value of I used was therefore; total current - current where YSZ was beginning to be reduced; 0.1mA was assumed. N is the total moles of gas that flow in a second and was determined using the ideal gas equation:

$$N = P\,V / R\,T$$

where V is the volume that flows in a second $(150.15/6 \times 10^7)m^3$. Substituting this into the mass balance results in:

$$X_{O2}(out) = X_{O2}(in) + IRT/nFPV.$$

Using a value of 8 for n in the above equation produces reasonable agreement with the measured oxygen concentration.

$$X_{O2}(out) = .000216 + 0.0049\times8.314\times273/(8\times96450\times101325\times150/6\times10^7)$$

$$= 0.000274.$$

Appendix 6

Selected physical property data

Table 6.1

Gibbs free energy of formation and melting points of selected oxides (Barin (1989))

Compound	Melting point /°C	Gibbs free energy /kJmol^{-1}			
		600K	800K	1000K	1200K
ZrO_2	2715	-982.029	-944.714	-907.940	-871.337
Al_2O_3	2072	-1487.31	-1424.89	-1361.33	-1295.05
Bi_2O_3	825/860	-412.2	-353.3	-295.7	-294.8
CaO	2614	-572.1	-551.6	-531.1	-509.8
Y_2O_3	2410	-1728.2	-1670.9	-1614.5	-1558.5
$CaZrO_3$	2550	-1595	-1539.6	-1484	-1428
CO_2	-56.6	-395.139	-395.527	-395.810	-396.007
CO	-199	-164.494	-182.494	-200.261	-217.796
SO_3		-342.658	-321.945	-293.571	-260.47
SO_2	-72.7	-300.294	-298.383	-288.640	-274.011
H_2O	0	-214.081	-203.595	-192.713	-181.572
NO	-163.6	82.8	80.3	77.8	75.2
N_2O	-90.8	126.9	141.8	156.6	171.1

Table 6.2

Coefficient of linear expansion, melting point and boiling point at 0.1Pa of selected metals (Weast (1988)).

Metal	Expansion coeff. $\times 10^{-6}$	Melting point /°C	Boiling point at 0.1Pa /°C
Gold	14.2	1064.434	1237
Nickel	13	1453	1373
Platinum	9	1772	1882
Silver	19	961.93	906
Zirconia	10-11	2715	
Alumina	8	2072	